Design of high efficiency turbomachinery blades

Hamakhan, Idres Azzat

Design of High Efficiency Turbomachinery Blades

by

Idres Azzat Hamakhan

B.Sc. (First Class Honours) in Mechanical Engineering

University of Salahaddin, Kurdistan, 1997

MSc in Materials and Applied Mechanics

University of Salahaddin, Kurdistan, 2002

Dissertation submitted to the School of Engineering and Material Sciences,

Queen Mary , University of London

in partial fulfillment of the requirements for the Degree of

Doctor of Philosophy

in

Mechanical Engineering

Supervised by:**Professor T. Korakianitis**

November 2009

School of Engineering and Materials Science

Queen Mary, University of London

PhD THESIS

DECLARATION

This thesis entitled

Design of High Efficiency Turbomachinery Blades

was composed by me and is based on my own work. Where the work of others has been used, it is fully acknowledged in text, captions and illustrations. This thesis has not been submitted for any other qualification.

Name: Idres Azzat HAMAKHAN

Signed:

Date:

Abstract

The prescribed surface curvature distribution (PSCD) direct blade design method, which was developed by Korakianitis, offers novel and unique advantages in aerodynamic performance and surface heat transfer distribution for the design of turbomachinery blades and isolated airfoils, blades or wings. This dissertation has introduced modified equations in the two-dimensional (2D) and extensions in the three-dimensional (3D) PSCD blade design method, and has used the method to illustrate its aerodynamic and heat transfer advantages in several test cases.

2D modifications include polynomial functions, similar to polynomials developed by Korakianitis, connecting the main part of the blades with the leading and trailing edge circles. The 3D design method, which was presented by Wegge and Korakianitis for the first time, include application of the method to describe the blade parameters with Bezier curves in the radial direction in order to obtain 3D blades. The use of the overall method is illustrated in turbine, compressor and wind turbine blade geometries.

The ability of the method is illustrated at design and off-design conditions with new designs and redesigns of seven test cases and at various flow incidences. The commercial code packages GAMBIT (grid generation), and FLUENT and ANSYS12 (flow solvers) are used to compute the flow around the blades using various grids and turbulence models. These calculations indicate all redesigned test cases remove flow disturbances and separation bubbles generated by surface curvature discontinuities. The effects of surface curvature distribution on convective heat transfer are illustrated.

The main contributions are the following: modifications of the exact forms of the polynomials; modifications of the exact location of the match points of the leading and trailing edge circles; increase in the number of control points of the Bezier curves; application of the same method to work on compressor blades and isolated airfoils; and application of the method to several test cases.

Acknowledgment

I would like to express my deep and sincere gratitude to my first supervisor, Professor Theodosios Korakianitis (a.k.a. Professor T. Alexander) for his guidance and support throughout my research time. His patience, support and kindness with his vast knowledge in research played a crucial role in the development of this method for design of turbomachinery blades. I thoroughly enjoyed working under him and would like to thank him for making my graduate school experience a valuable one. I would like to thank my second supervisor Professor C. J. Lawn for his continued support, guidance and encouragement. I am very grateful to Professor Tony Arts at von Karman Institute for providing me with his experimental data for surface heat transfer distribution for the VKI-L89 cascade.

Special thanks for Kurdistan Government especially Mr. Nechirvan Barzani, the Prime Minister and Salahaddin University, College of Engineering, Department of Mechanics, for their supporting financially this work . I would like to thank my favorite friends Dr. Nuree Othman and Mala Fayaq Chuchani for making this study successful. I am particularly indebted to Dr. Dara Jaff and Dr. Anwar Othman who encouraged me during my PhD study.

I am very grateful to Dr. Yubing Shi for continuous help and advice. I would like to thank Dr. Raymond Lam and Mr. Allem Million for their help in installing computer programs and IT support during my studies. I would like to thank my friends at University (Dr. Akbar Rahideh, Mr. Amzari and Mr. Yankai) who helped me in programming. Special thanks for my PhD friends (Paula and Anna) for their helping during my research time.

Unfortunately, I lost my dad, Azzat, and my elder brother, Faris, in a car accident during my PhD research 2006-2007. This PhD study is in reality from my dad's support and I do not know how I can thank him. The only thing that I can perhaps do for him is to present him the honour of this work credibility. I would like to say again thank you dad, and I promise I will never forget your advise and your

continuous support.

I would like to thank my mam, Khanm, for her patience, continuous support and gave me the strength to get through this incredible journey. I am grateful to my wife, Nishtiman Mohammed who put up with the lifestyle dictated by my studies, bravely endured me while I was pursuing my dreams, and without her support, it would not be possible to start, continue and accomplish my study abroad. Her presence in both pleasant and unpleasant conditions of my life made it possible to improve my self confidence.

Contents

Abstract 2

Acknowledgment 4

Table of contents 6

List of nomenclatures 9

List of figures 16

List of tables 24

1 Introduction **25**

1.1 Airfoil and blade geometry in energy conversion systems 25

1.2 Motivation and the purpose of this thesis 27

1.3 Outline of the thesis 30

2 Background **33**

2.1 Energy balance and the Euler equation 33

2.2 Blade notation and definitions 35

2.3 Velocity diagrams and their parameters 38

2.3.1 The work or loading coefficient, ψ 40

2.3.2 The flow coefficient, ϕ 41

2.3.3 The Reaction, R_n 42

2.4 Blade design characteristics 43

2.4.1 Tangential lift coefficient 43

2.4.2 Axial dimensions and number of blades 45

2.4.3 Choice of stagger angle 46

2.4.4 Selection of number of stages 47
2.5 Blade design methods 48
2.6 Flow analysis with CFD 53
2.6.1 Models for turbulence and transition 54
2.6.1.1 Modes of transition 56
2.6.1.2 Transition models 58
2.7 Loss mechanisms 68
2.7.1 Two-dimensional loss mechanisms 71
2.7.1.1 Boundary layer loss 72
2.7.1.2 Shock loss 72
2.7.1.3 Mixing loss 72
2.8 Surface-curvature and surface-velocity distributions 74
2.8.1 Theoretical evidence 75
2.8.2 Experimental evidence 76
2.9 The 2D PSCD blade design method 78
2.9.1 Introduction 78
2.9.2 Trailing edge thickness - the trailing edge circle 80
2.9.3 Trailing edge polynomial (y_3) 82
2.9.4 Main curvature-mapped part of the blade (y_2) 85
2.9.5 The leading edge circle and front part of the blade (y_1) 86
2.9.6 Procedures of the executable program 89
2.9.7 Validation, reproduction and redesign with the PSCD blade design method 90

3 Leading edge effects in gas turbine expander blades 98
3.1 Introduction 98
3.2 Aerodynamic effects of leading edge geometry 100
3.3 Design and off-design performance 109
3.4 Conclusion 118

4 3D stacking effects in gas turbine expander blades 120

4.1 Introduction 120

4.2 3D flow analysis 124

4.3 Blade shape parameterization 126

4.4 Blade stacking, design and off-design performances 128

4.5 Conclusion 135

5 Surface curvature distribution effects on heat transfer of turbine blades 148

5.1 Introduction 148

5.2 Blade geometry and surface heat transfer effects 151

5.3 Conclusions 165

6 PSCD applied to the design of compressor and fan blades 167

6.1 Introduction 167

6.2 Blade design methodology 170

6.3 Design and off-design condition 171

6.4 Blade shape parameterization and stacking 189

6.5 Conclusions 196

7 Wind turbines and isolated airfoils 199

7.1 Introduction 199

7.2 The PSCD method applied to isolated airfoils 201

7.3 Results and discussion 202

7.4 Conclusions 205

8 Conclusions 209

9 Recommendations 212

References 213

List of nomenclatures

Latin

A	cross sectional area (figure 2.3), representative of leading edge suction side (figure (2.23)
a	coefficient (section 2.9.3 and equation 2.26)
B	representative of point P_{s1} (figure 2.22)
b_x	axial chord length (figure 2.4, sections 2.2, 2.4.1, 2.9.2, 2.9.3 and equations 2.2,2.3)
C	curvature (equation 2.5, sections 2.9.2, 2.9.4 and figures 2.14, 2.21, 2.27, 3.2, 3.15, 5.2, 5.7, 7.3), with prime , slope of curvature (equations 2.6, sections 2.3.3, 2.9.3, 2.9.4, 2)), absolute velocity (figures 2.3,2.2, 2.5, 2.6, 2.8, sections 2.2, 2.5, 2.3, 2.3.1, 2.3.3), representative of the starting point of construction lines (figure2.22), with subscript θ, tangential velocity (section 2.8.1)
C_f	skin friction coefficient, $C_f = \tau_w / 2u^2{}_\infty \rho_\infty$, (figures 3.6, 5.6, 5.11, 6.12)
C_x	axial velocity (figures 2.3, 2.5, 2.6 and sections 2.3.2,4.2)
C_u	Tangential velocity (sections 2.2, 2.5, 2.3.1, 2.3.3, 4.2 and figures 2.3 and 2.5)
C_r	radial velocity (sections 2.8.1, 2.3.3, 4.2)
C_L	tangential loading coefficient (equation 2.25)
c	blade chord (section 2.2 and figure 2.4)
E_γ	dissipation source term (section 2)
$F_{\theta t}$	blending function (section 2)
h	enthalpy (sections 2.5, 2.7, 2.3.1, 2.3.3, 4.2, figures 2.1, 2.12, 2.8), with subscript t surface heat transfer coefficient (figure 5.8)
i	height (figure 2.10)
K	acceleration parameter (section 2)

M	Mach number (figures 2.15,2.16,3.7,3.8,3.9,3.10, 3.11,3.12, 4.6, 4.7, 4.9, 4.10,4.12,4.13, 5.8, 6.4, 6.5, 6.6, 6.7, 6.8 and 6.9), (equation 2.22)
n	nozzle (figures 2.3 and 2.10))
o	opening or throat width (figures 2.4, 2.20, section 2.2
p	pressure (figures 2.12, 2.8, sections 2.7, 2.4.4, 2.9.5)
P	point or node on suction and pressure segment surfaces of the blade (figures 2.4, 2.19, 2.20, 2.22 and sections 2.9.2, 2.9.3, 2.9.4, 2.9.5)
P_γ	production source term (section 2)
P_{θ_t}	source term (section 2)
r	local radius (equation 2.5, figures 2.3, 2.2, and sections 2.8.1, 2.9.2, 2.9.5)
rr	rotor (figures 2.3, 2.10, 2.5 and section 2.3.3)
R	gas constant (equation 2.22)
Re_θ	momentum thickness Reynolds number (section 2)
Re_{θ_t}	transition onset momentum thickness Reynolds number (section 2)
Re_{θ_c}	critical momentum thickness Reynolds number (section 2)
$\tilde{Re}_{\theta t}$	local transition onset momentum thickness Reynolds number (section 2)
R_n	actual reaction for velocity diagram (section 2.3.3)
R_T	viscosity ratio (section 2)
R_y	wall-distance based turbulent Reynolds number (section 2)
S, $\dot{S}$	entropy and entropy rate, in units of [W/(m^2.K)]
S	tangential pitch of the blade (figure 2.4 and section 2.2), with superscript dot entropy creation rate per unit surface area (equation 2.23, 2.21), entropy (equation 2.22), non-dimensional surface length (with b_x) (figures 2.28, 3.5, 3.13, 3.14, 4.8, 4.11, 4.14, 5.4, 5.5, 5.8, 5.10, 5.11, 6.10, 6.11, 6.14)
u	mean rotor speed (figures 2.3, 2.5, 2.7 and sections 2.5, 2.3.1, 2.3.2, 2.3.3, 4.2)
(r, θ, z)	cylindrical coordinates (section 2.8.1)

x, y	variable distances (sections 2, 2.9.2, 2.9.3, 2.9.4 and 2.9.5, 2.9.4)
(X, Y)	non-dimensional (with b_x) distances (figures 2.14, 2.15, 2.16, 2.19, 2.20, 2.21, 2.22, 2.23, 2.24, 2.25, 2.26, 2.27, 2.28, 2.29, 3.1, 3.2, 3.3, 3.1, 3.7, 3.8, 3.9, 3.10, 3.11, 3.12, 3.15, 4.5, 4.6, 4.7, 4.9,4.10, 4.12, 4.13, 5.1, 5.2, 5.3, 5.4, 5.7 and 5.8)
(xC, yC)	non-dimensional curvature distances (section 2.9.4)
u_∞	local free-stream speed
W	relative blade velocity (figures 2.3, 2.2, 2.6) and sections 2.3, 2.3.1, axial blade width of a stage (figure 2.10), with dot, power (section 2.5)
c_p	specific heat at constant pressure (section 2.4.4)
w	throat width (equation 2.23)
Y	stagnation pressure loss coefficient (equations 2.17, 2.18), energy loss coefficient (section 2.7)
S_t	Stanton number (figure 5.4)
T	time scale (section 2), temperature (section 2, 2.4.4), with subscript q torque (section 2.5 and figure 2.2)
T_u	free stream turbulence intensity (section 2)
t	Bezier variable span (section 2.9.4), trailing edge thickness (equation 2.23
y', y'', y'''	first, second and third derivatives of function y (section 2, 2.9.3, 2.9.4)
Z	stagnation pressure loss factor (section 2.7)

Greek

α	flow angle (figures 2.3, 2.4, 2.5, 2.19, and equations 2.2, 2.24,2.25)
β	angle of the blade surface (figures 2.4, 2.22 and sections 2.9.1, 2.9.2, 2.9.3)
C_μ	constant (equation 2.8)
δ	with star, displacement thickness of boundary layer, in metres [m] (equation 2.23, figures 2.14,

	2.28, 3.5, 3.6, 3.13, 3.14, 4.8, 4.11, 4.14, 5.5, 5.10, 6.10, 6.11, 6.14)
Δ	finite difference operator (equation 2.4 and sections 2.3.1, 2.3.3)
η	efficiency (section 2.7)
ϵ	dissipation rate (section 2.6)
γ	intermittency factor (section 2), specific heat ratio (equation 2.22)
ϕ	local angle (figure 2.4), flow
	coefficient (sections 2.3.2, 4.2 and figure 2.7)
k	coefficient (sections 2.9.3, 2.9.5),
	turbulent kinetic energy (sections 2, 2.6)
ν	kinematic viscosity (equation 2.8)
λ	with subscript θ pressure gradient parameter (section 2),
	stagger angle (figures 2.4, 2.22, 4.1, 4.2, sections 2.4.3, 2.9.2)
θ	angle for specifying points on leading and trailing edge circles, (sections 2.9.2
	and 2.9.5), momentum thickness boundary layer (section 2, equation 2.23)
μ	molecular viscosity (section 2)
μ_t	turbulence viscosity (section 2, equation 2.8)
ψ	work coefficient (sections 2.3.1, 4.2 and figure 2.7)
ρ	density (section 2)
σ	solidity (section 2.2)
τ	shear stress (section 2.8.1)
υ	velocity (section 2.7)
ω	specific dissipation rate (section 2), rotational speed (figure 2.2)
ξ	energy loss coefficient (section 2.23), with subscript s entropy loss
	coefficient (section 2.7)

Subscripts

0	stagnation condition (figures 2.12, 2.8 and sections 2.7, 2.3.3, 4.2)

$0, 1, 2, ...$	with xC_s, yC_s, xC_p, yC_p, points on the blade curvature (figure 2.21and section 2.9.4), with letter a, No. of coefficients (sections 2.9.3 and 2.9.5)
$1, 2$	with flow quantity, cascade inlet and outlet (figures 2.3, 2.4, 2.5, section 2.2, 2.4.1, 2.9.3)
$1, 2$	with P_s *and* P_p, points on line segments for suction and pressure sides (figures 2.4, 2.20 and 2.22), stage numbers (figures 2.3, 2.10)
$1, 2, 3, 4$	with k, constants (section 2.9.3, 2.9.5)
BL	with subscript of δ and θ boundary layer (section 2)
sc, pc	construction line for suction and pressure sides (section 2.9.5)
s	suction side (figures 2.4, 2.20, 2.21, 2.22, 2.23 sections 2.9.2, 2.9.3, 2.9.4, 2.9.5, 2.9.5)
p	pressure side (figures 2.4, 2.20, 2.21, 2.22, 2.23 sections 2.9.2, 2.9.3, 2.9.4, 2.9.5, 2.9.5)
in	inlet (section 2.5)
ex	exit (section 2.5)
si	simple (section 4.2)
∞	free stream
is	isentropic (figures 2.12, 3.7, 3.8, 3.9, 3.10, 3.11, 3.12, 4.6, 4.7, 4.9, 4.10,4.12, 4.13 and section 2.4.1, 5.8, 6.4, 6.5, 6.6, 6.7, 6.8, 6.9)
t	tip (figures 2.3, 2.10)
h	hub (figures 2.3, 2.10)
u	with C and W tangential direction of velocity, (sections 2.5, 2.8.1, 2.3.1, 2.3.3, 4.2) and (figures 2.3, 2.5)
w	wall
te	trailing edge (section 2.9.2)
le	leading edge (section 2.9.5)
c	center of trailing edge circle (section 2.9.2, figure 2.19)

rr	rotor (figures 2.3, 2.10 and section 2.3.3)
ss	stator (figure 2.10)
se	stage (section 2.3.3)
st	static (section 2.7 and figure 2.8)
sm, sk	with P, points on suction side of the blade,(figures 2.4, 2.20, 2.22, sections 2.9.3, 2.9.5, 2.9.5)
pm, pk	with P, points on pressure side of the blade,(figures 2.4, 2.20, 2.22, sections 2.9.3, 2.9.5, 2.9.5)

Symbols and operators

d	derivative operator (equations 2.5,2.6, sections 2, 2.8.1, 2.9.3)
∂	partial derivative operator (section 2.8.1)
∇	gradient operator (section 2.8.1)

Acronyms

A1	redesigned Eppler 387 blade (figures 7.1, 7.3 and 7.4)
B	sample blade, with subscripts 1 (figures 3.7, 3.8, 3.9), with subscript 3 (figures 3.10, 3.11, 3.12), with subscriptions 1,2,3 (sections 3.2)
h-S	enthalpy - entropy
LE	leading edge (figures 2.21 and 2.22)
C	redesigned compressor blade, with subscript 1 (figures 6.4, 6.5, 6.6), with subscript 2 (figures 6.7, 6.8, 6.9 and with subscript 3 (figure 6.15)
CF	central difference (section 2.9.4)
CFD	computational fluid dynamic (section 2.6)

2D	two dimensional
3D	three dimensional
HD	Hodson-Dominy
H	redesigned NASA and VKI blades, with subscript 1 (figures 5.1, 5.2, 5.3, 5.4), with subscript 2 (figures 5.7, 5.8) and with subscripts 1,2 (section 5.2)
I1,I4,I9	reproduce and redesigned HD blades, forth and ninth iterations to produce improved blades (figures 2.24, 2.25, 3.1, 3.2)
PSCD	prescribed surface curvature distribution
QMUL	Queen Mary College, University of London
S1	redesigned VKI blade (figure 2.26, 2.28)

List of Figures

2.1 Processes occurring in an axial flow turbine. (p_0 and T_0 variation is similar to h_0) ; (p_{st} and T_{st} variation is similar to h_{st}) (from [11]) . . . 34

2.2 Flow through rotor (from [12]) 34

2.3 Left, axial flow turbine stage (from [13]); Right, velocity diagram (from [12]) 36

2.4 Cascade geometry and notation(from [5]) 37

2.5 Turbomachinery blade rows and their velocity diagrams (constant u and C_x): a- Simple velocity diagrams for an axial turbine stage, b- simple velocity diagrams for an axial compressor stage (from [12]) . . 39

2.6 General velocity diagram (from [12]) 40

2.7 Design point for reaserch turbines (from [15, 16]) 40

2.8 Enthalpy-entropy diagram for a turbine expansion (from [12]) 42

2.9 Diagrammatic variation of loss with blade solidity (from [12]) 44

2.10 Left, axial flow turbine stage (from [13]); Right, Typical axial dimension of a compressor stage (from [15]) 45

2.11 Separation bubble effects on suction side velocity distribution(from [69]) 58

2.12 Enthalpy-entropy diagram for cascade flow (from [94]) 69

2.13 Structure of supersonic trailing edge flow (from [97]) 73

2.14 Performance of typical turbine cascade; Left, surface-curvature distributions. Right, boundary-layer displacement thickness (freestream turbulence 15%) (from [5, 12]) 74

2.15 Tested and computed Mach-number distributions: a- Surface Mach number distributions, b- Computed Mach number contours (increment 0.05) (from [6, 12]) 77
2.16 Effect of curvature discontinuity caused by the leading edge circle. Tested and computed Mach number distributions for HD turbine cascade (from [6, 12]) 77
2.17 Change in blade shape to resolve leading edge spike (from [27]) 80
2.18 Mach number distributions for HD and redesign of the blade with inverse method including spikes, dips (from [27]) 80
2.19 The nominal stagnation point on the trailing edge which is from outlet flow angle 81
2.20 Relationship between the throat o parameter and the neighbouring blade 84
2.21 Sample of curvature distribution of the whole suction side of the blade. 86
2.22 Some parameters near the leading edge of the blade 87
2.23 Leading edge circle, leading edge suction and pressure surfaces of the blade and construction lines. A= Leading edge suction side, B= Point P_{s1}, C= Starting point of construction line, D= Point P_{p1}, E=Leading edge pressure side F= Construction line for suction side, G= construction line for pressure side 89
2.24 Isentropic Mach number test results for both of the original and reproduced HD blade 93
2.25 Isentropic Mach number distributions from viscous calculations for both the HD and reproduced blades 93
2.26 Blade geometries for the original cascade (from [107]) and redesigned S1 blade 94
2.27 Surface curvature distributions for the original cascade investigated by Kiock (from [107]) and reproduced S1 blade 94

2.28 a-Surface Mach number distributions for the Kiock(from [107]) and redesigned S1 blades. b-Boundary layer displacement thickness calculations 95
2.29 a- Mach contours for original cascade investigated by Kiock (from [107]) . b- Mach contours for the redesigned S1 blade 96
2.30 Distributions of the total rate of entropy creation on the suction side of the Kiock and redesigned S1 blades 97

3.1 Original and redesigned leading edge for both of HD and I1, I4, and I9 blades 102
3.2 a- Surface curvature distributions for all blades (HD, I1, I4, I9). b- Isentropic surface Mach number distributions of the reproduced HD blade and redesigned I4 and I9 blades 103
3.3 a- Mach contours for the original HD blade. b- Mach contours for the redesigned I9 blade 104
3.4 a- Isentropic surface Mach number distributions of the HD and I1 blades. b- Viscous Mach number distributions for the HD and I9 blades 105
3.5 a-Surface Mach number distributions for the HD and redesigned I9 blades. b-Boundary layer displacement thickness calculations 106
3.6 a-The rate of entropy creation on the suction side of the HD and I9 blades. b- Skin friction calculations on the suction side of the HD and I9 blades 107
3.7 a- Isentropic surface Mach number distribution at design condition 0°. b- Mach contours at design condition 0°, increment 0.05 108
3.8 a- Isentropic surface Mach number distribution at off-design condition +5°. b- Isentropic surface Mach number distribution at off-design condition -5° 109

3.9 a- Isentropic surface Mach number distribution at off-design condition +10°. b- Isentropic surface Mach number distribution at off-design condition -10° 110
3.10 a- Isentropic surface Mach number distribution at design condition 0°. b- Mach contours at design condition 0° of the B3 blade, increment 0.05 111
3.11 a- Isentropic surface Mach number distribution at off-design condition -5°. b- Isentropic surface Mach number distribution at off-design condition +5° 112
3.12 a- Isentropic surface Mach number distribution at off-design condition -10°. b- Isentropic surface Mach number distribution at off-design condition +10° 113
3.13 a- Surface Mach number distributions for B1 and B3 blades. b- Boundary layer displacement thickness calculations 114
3.14 a- Surface Mach number distributions for B1 and B3 blades. b- Boundary layer displacement thickness calculations 115
3.15 Surface curvature distributions of blades B1 and B3 117

4.1 a- Throat to pitch ratio from hub to tip. b- Stagger angle variation from hub to tip 128
4.2 Hub to tip non-dimensional surface curvature control points of the suction side of the blade, a- $XC2s$, b-$YC1s$, c-$YC2s$, d-$YC3s$, e-$YC4s$, f-$XC5s$ 131
4.3 Hub to tip non-dimensional surface curvature control points of the suction side of the blade, a- $YC1p$, b-$YC2p$, c-$YC3p$, d-$XC5p$ 133
4.4 Sample of blade stacking: a- Non-radial stacking 3D blade shape. b- Radial stacking 3D blade shape 136
4.5 Blade stacking: a- Center of gravity, b- Trailing edge, and c- Leading edge 138

4.6 Hub: a- Isentropic surface Mach number distribution at design incidence. b- Mach contours at design condition 139
4.7 Hub: a- Isentropic Mach number distribution at off-design incidence -5°. b- Isentropic Mach number distribution at off-design incidence +5° 140
4.8 a- Surface Mach number distributions for hub at design and off-design conditions. b- Boundary layer displacement thickness calculations . . 141
4.9 Mean: a- Isentropic Mach number distribution at design incidence. b- Mach contours at design condition 142
4.10 Mean: a- Isentropic Mach number distribution at off-design incidence -5°. b- Isentropic Mach number distribution at off-design incidence +5° 143
4.11 a- Surface Mach number distributions for the mean section at design and off-design conditions. b- Boundary layer displacement thickness calculations 144
4.12 Tip: a- Isentropic Mach number distribution at design incidence. b- Mach contours at design condition 145
4.13 Tip: a- Isentropic Mach number distribution at off-design incidence -5°. b- Isentropic Mach number distribution at off-design incidence +5° 146
4.14 a- Surface Mach number distributions for tip section at design and off-design conditions. b- Boundary layer displacement thickness calculations 147

5.1 Blade geometries. a- NASA and H1 blades. b- VKI and H2 blades . . 152
5.2 Surface curvature distributions for the NASA stator and redesigned H1 blade 156
5.3 a- Mach contours for the NASA blade, increment 0.005. b- Mach contours for the H1 blade, increment 0.005 157
5.4 a- Surface pressure distributions. b- Surface Stanton number distributions 158

5.5 a-Surface Mach number distributions for the NASA and redesigned H1 blades. b-Boundary layer displacement thickness calculations . . . 159
5.6 a-The rate of entropy creation on the suction side of the NASA and H1 blades. b- Skin friction calculations on the suction side of the NASA and H1 blades 160
5.7 Surface curvature distributions for the VKI NGV and redesigned H2 blade 161
5.8 a- Isentropic surface Mach number distributions. b- Surface heat transfer coefficients,h_t ,W/m^2K 162
5.9 a- Mach contours for the VKI blade, increment 0.025. b- Mach contours for the redesign H2 blade, increment 0.025 163
5.10 a-Surface Mach number distributions for the VKI and redesigned H2 blades. b-Boundary layer displacement thickness calculations 164
5.11 a-The rate of entropy creation on the suction side of the VKI and H2 blades. b- Skin friction calculations on the suction side of the VKI and H2 blades 165

6.1 Illustration of compressor blade design with the PSCD method 171
6.2 Blade geometries for MAN GHH 1-S1, C1 and C2 blades 171
6.3 Blade geometries for Sanger and C3 blades 172
6.4 a- Isentropic Mach number distributions at design incidence. b- Mach contours at design condition 177
6.5 a- Isentropic Mach number distributions at off-design incidence -4°. b- Isentropic Mach number distributions at off-design incidence +4° . 178
6.6 a- Isentropic Mach number distributions at off-design incidence -7°. b- Isentropic Mach number distributions at off-design incidence +5° . 179
6.7 a- Isentropic Mach number distributions at design incidence. b- Mach contours at design condition 180

6.8 a- Isentropic Mach number distributions at off-design incidence -4°. b- Isentropic Mach number distributions at off-design incidence +4° . 181
6.9 a- Isentropic Mach number distributions at off-design incidence -7°. b- Isentropic Mach number distributions at off-design incidence +5° . 182
6.10 a-Surface Mach number distributions for the Steinert and C2 blades at design and negative incidences. b-Boundary layer displacement thickness calculations 183
6.11 a-Surface Mach number distributions for the Steinert and C2 blades at design and positive incidences. b-Boundary layer displacement thickness calculations 184
6.12 a-The rate of entropy creation on the suction side of the Steinert and C2 blades. b- Skin friction calculations on the suction side of the Steinert and C2 blades 185
6.13 a- Isentropic Mach number distributions for design and redesign blades. b- Mach contours for Sanger cascade at design condition 186
6.14 a-Surface Mach number distributions for the Sanger and C3 blades at design condition. b-Boundary layer displacement thickness calculations 187
6.15 a-Mach contours for C3 blade. b-The rate of entropy creation on the suction side of the Sanger and C3 blades 188
6.16 Stagger angle variations from hub to tip 190
6.17 Hub to tip non-dimensional surface curvature control points of the suction side of the blade, a- $YC1s$, b-$YC2s$, c-$YC3s$, d-$YC4s$ 193
6.18 Hub to tip non-dimensional surface curvature control points of the pressure side of the blade, a- $YC1p$, b-$YC2p$, c-$YC3p$, d-$YC4p$ . . . 195
6.19 Blade stacking : a- Center of gravity, b- Trailing edge, and c- Leading edge 197
6.20 Stacking of the 3D compressor stator blade along the center of gravity 198

7.1 Blade geometries for the Eppler 238 and redesigned A1 blades 203

7.2 Part of the structured grid for the Eppler 387 204
7.3 Sample of curvature distributions for the Eppler 387 and redesigned A1 airfoils 205
7.4 Pressure distributions for the Eppler 387 and redesigned A1 airfoils . 206
7.5 Mach contours around the whole blade and the shown separated area of the Eppler 387 207
7.6 Mach contours around the whole blade and the shown separated area of the redesigned A1 airfoil 208

List of Tables

3.1 Stagnation pressure losses Z at design and off-design conditions . . . 117

3.2 Stagnation pressure losses at design and off-design conditions,$Y_t = \frac{P_{01}-P_{02}}{P_{02}-P_2}$ 117

3.3 Suction-side diffusion ratio at design and off-design conditions 117

4.1 Output parameters for stator from 3D streamline curvature (hub-tip) 127

6.1 Stagnation pressure losses at design and off-design conditions 176

6.2 Output parameters for stator from 3D streamline curvature (hub-tip) 190

Chapter 1

Introduction

1.1 Airfoil and blade geometry in energy conversion systems

World energy resources and consumption have become a matter of ever more public interest over the past decades. The political, social and ecological issues regarding the use and supply of energy will most likely remain a vital concern for many years to come. One of the main objectives in saving energy resources is to reduce energy consumption by increasing efficiency of energy conversion and utilization. As the gas turbine is the most common device for power reduction and energy conversion, improvements of its efficiency would be a major contribution to energy resource savings. A thorough understanding of the role of the gas turbine component is important to those involved in the design and/or performance assessment of gas turbine engines. The gas turbine engine is a complex machine involving operation at extremes of pressure and temperature and it is one of the most popular engine that has a great application in the energy conversion systems.

In many industry sectors, turbomachinery, or more broadly speaking rotating machinery, plays a vital role. Rotating machines change the state of working fluids (pumps or compressors), convey or transport fluids (fans and pumps), extract energy

(turbines) and create propulsion (propellers). Performance, efficiency, reliability and rapid delivery have always been important, but todays world conditions intensify the pressures designers face since rotating machines play a critical role in power generation and various forms of transportation. Their is a limiting factor regarding cost, efficiency and emissions during the design process of gas turbine engines. In the energy industries, most of our power is produced by gas, steam and water turbines. Steam turbines extract power in nuclear and coal-fired power plants. Land-based gas turbines is also run on natural gas and, in some cases, oil. In the other side wind turbine production, which is still relatively small in volume, has increased dramatically in recent years, with the largest machines being 6 megawatts (MW) in size and having rotors approaching 130 meters in diameter [1].

In the transportation industry, turbomachinery plays an equally important role. For air travel, the rotating machinery used on commercial aircraft which is called the gas turbine aircraft engine. Its key rotating components include the fan, which can be seen when boarding the plane, as well as the compressor and the turbine. For transportation at sea and on the ground, diesel engines in ships, trucks and an increasing number of cars use turbo-chargers to improve their performance and efficiency. These engines also use electric-driven fans and pumps, which must be optimized, since available electrical power is limited. Efficiency of the automatic transmission torque converter another rotating machinery component comprised of a pump, a stator and a turbine is critical to vehicle fuel efficiency. Turbomachinery plays an important role in other industries as well.

Compressors and pumps are important to the chemical, process, and oil and gas industries, and are even key components in large industrial air conditioning systems. In the medical industry, heart pumps must be designed to be compact and to minimize blood damage. Each rotating machine type has one or more key design challenges. Efficient blade geometry and cooling due to high temperatures are problematic in gas turbines and compressors. Cavitation is an issue in pumps. Non-ideal gas behavior in steam turbines and refrigerant compressors must be con-

sidered. Several design, performance or production factors are common among turbomachine types. Reliability and safety require accurate prediction of steady and transient thermal, aerodynamic and structural loads for stress and fatigue life predictions. However, excessive safety and strength features are likely to make the machine too expensive or too heavy; these features also can preclude other competing requirements such as efficiency. Operational cost and emission issues have recently intensified the pressure to produce efficient machines.

All above uses for gas turbine engines, including stationary and rotating blades, make the design of the blade geometry is challenging and requires a methodology that produce high efficient blades based on aerodynamic performance, surface heat transfer, mechanical integrity, noise reduction and overall cost. It is concluded that design of high efficient blade geometry, to produce highly aerodynamic performances (pressure distributions and isentropic Mach number), is a core to predict the other properties such as heat transfer, mechanical integrity, and noise phenomenon. In other words, any improvement on aerodynamic performance reflects to improve the overall efficiency of the engine.

1.2 Motivation and the purpose of this thesis

Besides various blade design methods for turbomachinery blade, several specific factors motivated this thesis. First among them is the spikes and dips in the surface pressure or Mach number distributions of the most of the turbomachinery blades and wind airfoil in the open literature, which is mostly a function of the discontinuity in the local surface curvature or slope of the local surface curvature. Various techniques and equations have been used in an attempt to remove these spikes, which have not been successful, except for the the presecribed surface curvature distribution (PSCD) blade design method developed by Korakianitis [2–9]. The modifications in the PSCD method developed by Korakianitis and described in this thesis enhance the ability of this method to produce high efficiency turbomachinery blades and

isolated airfoils.

The streamwise blade surface curvature distribution has a great effect on boundary layer development, blade aerodynamic performance, and surface heat transfer distribution. This surface curvature distribution is different from the usual definition of blade surface smoothness, which also affects boundary layer development, aerodynamic performance, and heat transfer distribution. Other existing line and surface design programs do not address this blade surface curvature distribution effect (they usually introduce slope of curvature discontinuities at the knots joining the lines, or the lines joining the surface segments).

The aim of this thesis is to modify the PSCD blade design method, which was developed by Korakianitis, to design all high efficiency turbomachinery blades (compressor and turbines), wind turbine airfoil and investigate its effects at design and off-design conditions and surface heat transfer distribution. The blade design method has been enhanced with two polynomial equations, which are exponential and similar in nature to those proposed in [8], to specify the leading and trailing edge parts of the blade; and expanding the smoothness on the rest of the blade with increasing the number of control points of the Bezier spline, which they have an effective influence of the overall blade performance. The effects on design and off design conditions are also discussed to show the influence of the continuous surface curvature on blade performance, to remove the flow disturbances, separation bubbles and improve the boundary layer development on the blade surface. The influence of the continuous surface curvature of the blade heat transfer is also discussed, on the improvement of the boundary layer development on the surface of the blade. In the following the contributions of this thesis have been briefly summarized:

- Use of the PSCD method to design high efficiency turbomachinery blades for all the above uses.

  The flow around the turbomachinery blade is complex and unsteady. The complexity and three-dimensional flow around the blade mostly depend on

the shape of the blade. The 2D shape of the blade is specified by joining lines, and the overall surface results in a specified surface curvature distribution. With the usual line-joining methods there is a discontinuity in the slope of curvature between line segments. These curvature or slope of curvature discontinuities result in local kinks in surface pressure or Mach number distribution, and in order to produce a high efficiency blade the discontinuities need to be removed. Two modified polynomial equations are introduced in this thesis, which are of similar form to the exponential polynomials introduced in [8]. These polynomials enhance application of the PSCD method near the leading and trailing edge of the blades. Overall the separate lines joined to form the suction and pressure surface of the blades have continuity of point, first, second and third derivative everywhere along the surface of the blades, including the joints with the leading and trailing edge shapes (circles).

- Modifications to the original PSCD blade design method, which was initially applied to axial gas turbine expanders, to apply to compressor and isolated airfoils.

  In the original PSCD method the suction surface of turbine blades has to pass perpendicularly through the point where the surface touches the throat diameter. The throat diameter is defined form the trailing edge circle of the adjacent blade. The pressure surface development is analogous, but instead of the throat point and perpendicular, an arbitrary point and surface angle are introduced on the pressure surface. The procedure is similar for compressor blades: the throat point moves closer to the leading edge, and is defined form the leading edge circle of the next blade. The pressure surface development for compressors is exactly analogous to that of turbines. In the case of isolated airfoils there is no adjacent blade, and both the suction and pressure surfaces are defined with an arbitrary point and surface angle, one on the suction side, and a second on the pressure side (where the latter point and angle on the

pressure side is exactly analogous to that of the pressure side of turbines).

- Sample applications of the 2D method to 3D blades.

  The through-flow code proposed in [10] has been used to design 3D variations of inlet and flow angles in sample multi-stage turbomachines. The original code was modified to use general velocity diagrams instead of simple velocity diagrams. The 3D outputs of the through-flow code are combined with 3D variations of key geometric blade design parameters to design 3D blades. These 3D geometric parameters are described with Bezier curves, as originally introduced in [8]. Various sample cases are presented.

- Investigations of surface curvature distribution effects on convective blade surface heat transfer.

  The surface curvature distribution affects boundary layer development, and therefore it also affects aerodynamic and heat transfer performance. Removing the discontinuities in slope of surface curvature and thus smoothing the blade surface results in removing spikes and dips in the surface Stanton number (and thus surface heat transfer coefficient). As a result the local heating rate can be decreased, reducing local cooling requirements, and correspondingly resulting in higher engine efficiency. This aspect illustrates an additional efficiency feature of the PSCD method, as originally claimed in [2–9].

1.3 Outline of the thesis

A brief outline of the thesis is presented below.

- Chapter 2 presents the background of blade design methods. It starts with the description of energy balance and Euler equation for turbomachinery blades. It describes the fundamentals and characteristics of blade design methods. Velocity diagrams and their parameters has also been described. Effects of surface

curvature discontinuity on aerodynamic and surface heat transfer distributions have been presented through theoretical and experimental evidences. Flow analysis with computational fluid dynamics (CFD) and models for turbulence and transition are described. Two dimensional loss mechanisms for turbomachinery blades are presented. The detailed descriptions of the PSCD blade design method have been described for turbomachinery blades and isolated airfoil. Computerized blade design procedures with an executable MATLAB program are presented. Reproduction and comparison has been shown for the original and redesigned blades such as Hodson-Dominey (HD) and Kiock blades and others in the following chapters.

- Chapter 3 describes the leading edge effects in gas turbine expander blades. It includes reproduction of one sample blade at design and off design conditions and the surface curvature effects on removing the flow disturbances and separation bubble around the leading edge. More than one blade has been designed to explain the effect of the surface curvature on the design of high efficiency blade with different incidence values. A comparative example between analytical and experimental data is also presented in this chapter.

- Chapter 4 describes three dimensional stacking effects in gas turbine expander. It presents the background of the three dimensional blade design method and flow analysis. Blade shape parameterization, stacking lines, design and off-design effects are also discussed. The guidance to design three dimensional (3D) blades through stacking second dimensional blades at center of gravity, leading and trailing edge points from hub to tip are presented.

- Chapter 5 presents the effect of the surface curvature method on local convective heat transfer. Comparison of calculation with experiments of surface Stanton numbers for two test cases (NASA and VKI blades) are presented. Modified blades have been produced with the PSCD method. The effect of surface curvature on improving heat transfer (lowering the local Stanton num-

ber) by removing spikes and dips in surface curvature and corresponding spikes and dips in Stanton number or local surface heat transfer coefficient has been discussed. Comparisons have been made between experimental results on the original NASA and VKI blades, and computations on the original and modified blades.

- Chapter 6 describes application of the PSCD blade design method for compressor and fan blades. Reproduction of two compressor test cases and comparison with experimental data are presented. Design and off-design effects are also discussed in this chapter.

- Chapter 7 describes application of the PSCD blade design method for isolated (wind turbine) airfoils. The effect of surface curvature on one wind turbine airfoil (Eppler 387) performance has been discussed. A modified Eppler airfoil has been designed, and a comparison of computational results between the original and modified airfoils is presented.

- Chapter 8 and 9 consist of the conclusions and recommendations.

Chapter 2

Background

2.1 Energy balance and the Euler equation

The principal aim of this section is to present a useful equation, known as the Euler equation, which is an energy balance in thermodynamics (energy change is equal to enthalpy change through the stage) and fluid dynamics (energy change in the stage is equal to change in angular momentum through the stage times angular velocity). This Euler equation is the most useful equation in turbomachinery design, and it combines principles of mass flow continuity, steady flow energy transfer, momentum changes and the associated reaction forces.

Turbine blades are affected by the pressure and temperature of the gas. Through those blades the fluid energy is converted into mechanical energy. As the fluid goes through the turbine, all properties, as well as stagnation pressure and stagnation temperature, change. Figure 2.1 shows enthalpy changes through a turbine stage. The high-temperature high-pressure fluid is expanded through stationary vanes called nozzles. In uncooled turbine nozzles the stagnation temperature does not change from inlet to outlet, but there is a small stagnation pressure drop due to friction. Work is extracted from the flow by the rotor blades, which results in a corresponding stagnation enthalpy and stagnation temperature drop, followed by the corresponding stagnation pressure drop.

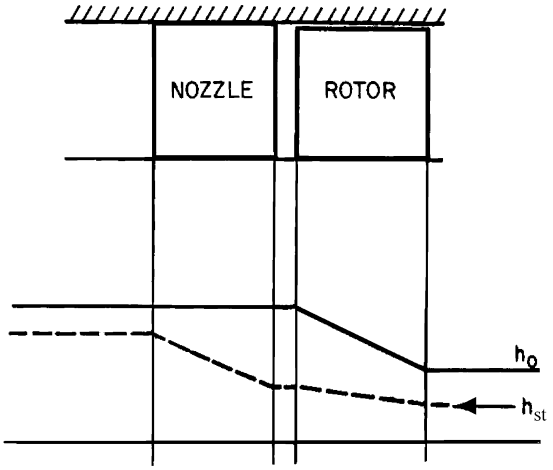

Figure 2.1: Processes occurring in an axial flow turbine. (p_0 and T_0 variation is similar to h_0) ; (p_{st} and T_{st} variation is similar to h_{st}) (from [11])

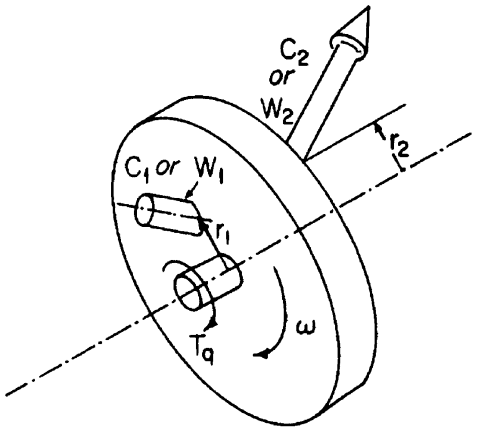

Figure 2.2: Flow through rotor (from [12])

The Euler equation is derived by considering a turbomachine stage as an actuator disk, rotating at angular velocity ω as shown in figure 2.2. The fluid enters the actuator disk at radius r_1 with absolute velocity C_1 and leaves at another radius r_2 with absolute velocity C_2.

The force on the fluid is equal and opposite to the force on the blade, and it can be specified through the change of momentum between the flow entering and leaving the rotor. Wilson and Korakianitis [12] mentioned that the radial and axial components are important for the design of bearings and the analysis of vibrations, but only the tangential component of the force can produce a change in enthalpy through work transfer. The following equations [12] are used to describe the Euler

equation for adiabatic turbomachines. It is determined from the torque on the rotor and energy transfer through it as follows:

$T_q = \dot{m}\left(r_1 C_{u,1} - r_2 C_{u,2}\right)$

energy transfer $= T_q \omega = \dot{m}\omega\left(r_1 C_{u,1} - r_2 C_{u,2}\right)$

$$\frac{W_{ex} - W_{in}}{\dot{m}} = \left(u_1 C_{u,1} - u_2 C_{u,2}\right)$$

The power through the stage is determined by the energy-rate balance, coupling power with enthalpy changes:

$$\frac{W_{ex} - W_{in}}{\dot{m}} = \left(h_{0,2} - h_{0,1}\right) = \left(u_1 C_{u,1} - u_2 C_{u,2}\right) \tag{2.1}$$

Equation 2.1 is known as the Euler equation for turbomachines. It is evident that the stagnation pressure and stagnation enthalpy drop in a turbine is directly proportional to the rate of change of tangential velocity and blade speed.

2.2 Blade notation and definitions

The description of the turbomachinery stages, for simplicity, is started with its projections at a certain radius as shown in figure 2.3. For a turbine the stage has a nozzle row followed by a rotor row. Cascade projections are drawn in an essentially similar manner for mixed and radial flow machines.

The corresponding velocity vectors are indicated in the above Fig. 2.3. Each velocity triangle is composed of absolute C, relative W and blade u velocities. Also the important axial (subscript x) and tangential (subscript u) velocity components are indicated. For 3D geometries the flow stations between blade rows, 1,2 etc are designated as shown in figure 2.3, while for 2D velocity diagrams shown later the inlet to the stator and the outlet of the rotor are given the designation 2, while the outlet of the stator and the inlet to the rotor are given the designation 1.

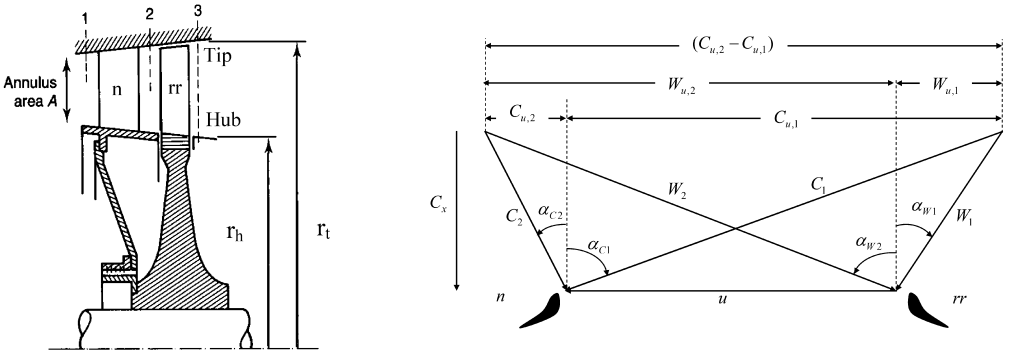

Figure 2.3: Left, axial flow turbine stage (from [13]); Right, velocity diagram (from [12])

Absolute flow angles are designated α, with a subscript C or W for absolute and relative flow angles, while blade angles are designated β. The sense in which these angles are drawn is important. In this work, the angles are measured with respect to the axial direction, shown in Fig. 2.3. Obviously, the inflow angle and outflow angle have different signs, as we define an angle to be positive counter-clockwise above the axial direction. This follows the usual industry convention for axial machines of measuring these angles. Therefore, throughout this thesis, and for typical turbine geometries, inflow angles are positive, while outflow angles are negative (except for very unusual velocity diagrams, for instance for a wind turbine blade rotor this notation would give a negative inlet flow angle).

A more detailed 2D projection for representative turbine blade rows is presented in Fig. 2.4, from [5]. The purpose of Fig. 2.4 is to represent the notation which is commonly used for 2D blade geometries and their parameters, and which will be followed in this thesis.

Fig. 2.4 is drawn for stationary blade rows, using α to represent the flow angles, but the approach would be similar for stators (with absolute flow velocities) and for rotors (with relative flow velocities).

The chord, designated by c, is defined as the length of the perpendicular projection of the blade profile onto the chord line. It is approximately equal to the linear distance between the leading edge and the trailing edge [14]. The angle between

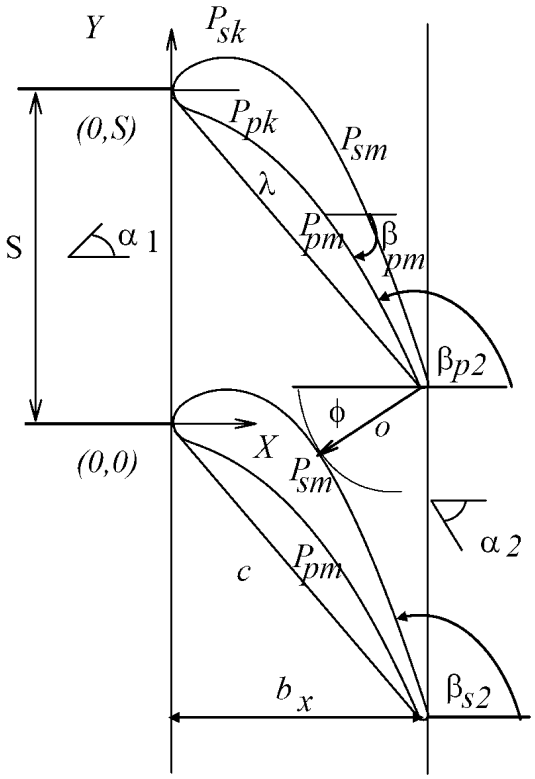

Figure 2.4: Cascade geometry and notation(from [5])

the chord and the axial direction is defined as λ, the stagger angle of the blade which starts non-dimensionally between zero and one. As can be seen, λ usually is negative in turbine geometries (and positive in compressor geometries). For the purposes of this work , the axial length of the blade, b_x is defined as the length of the projection of the blade, as set in the turbine, onto a line parallel to the turbine axis [14](from zero to one). In the 2D segments the non-dimensional blade length b_x is always equal to 1.0; while the dimensional value of b_x in actual blades may vary from hub to tip in 3D blades. The stagnation points for the leading and trailing edges of the blade can be described as a function of inlet and outlet flow angles.

The distance between two nominal stagnation points of two adjacent blades is defined as the spacing, S or pitch. It is an important parameter in the design process, which in 3D geometries it is defined by the number of blades. In 2D geometries S divided by axial chord b_x is defined as the pitch-to-axial-chord ratio S/b_x, which is an important 2D blade-design parameter connected to tangential lift coefficient C_L and inlet and outlet flow angles as shown below. The reciprocal of this ratio is called

solidity, $\sigma \equiv b_x/S$.

The throat diameter o, is defined as the smallest distance from any point on the pressure surface to the adjacent suction surface. It is the "throat", minimum size, of the passage presented to the flow, and in a correctly designed subsonic blade passage is from the trailing edge circle on the pressure side to the suction side of the next blade [5]. The value of o is related to the mass flow rate, the exit flow angle, and Mach number at throat of the blade. The ratio of o/S is an input parameter in 2D blade passages.

2.3 Velocity diagrams and their parameters

The flow through the blades of turbomachines is represented by velocity vectors and the corresponding velocity diagrams. The diagrams shown for the velocity vectors are those for the mean flow at a specified radius at entry to, or at exit form, a stator or a rotor, or both. The velocity diagrams do not show the flow directions within stator and rotor passages and around blades. The use of the Euler's equation [12] in the interpreting velocity diagrams enables the relative enthalpy change obtainable in any given diagram to be estimated on sight. It means the Euler equation couples the thermodynamic energy change to the momentum changes in fluid dynamics, which are related to the velocity diagrams.

Figure 2.5 illustrates a single stage of the turbine (a combination of stator ["nozzle"] and rotor blades) and compressor and their corresponding velocity diagrams. The flow enters the stator with an absolute velocity C_2 and leaves it with absolute velocity C_1. The flow enters the rotor of the same stage with relative velocity W_1 and leaves it with relative velocity W_2. There are two popular velocity diagrams in the literature [12], the simple (repeating) one and the general three-dimensional velocity diagrams. In the simple velocity diagrams both axial velocity and rotor peripheral speed are assumed constant through the stage of the turbine. The tangential velocities ($C_{u,1}$, $C_{u,2}$, $W_{u,1}$ and $W_{u,2}$) are also shown in figure 2.5. Simple

velocity diagrams are specified at the mean radius for both stator and rotor blades for turbine and at the tip radius for compressor. The flow directions are indicated in the velocity diagrams. In the general velocity diagram (figure 2.6), the peripheral speed and the axial velocity vary as a function of radius from hub to tip.

For preliminary design it is appropriate to start with the simple 2D velocity diagrams at mean radii of the blades for turbine and at tip radii for compressor. This means that, unlike in 3D diagrams, in 2D diagrams the flow velocities are identical at the inlet and outlet of the stage.

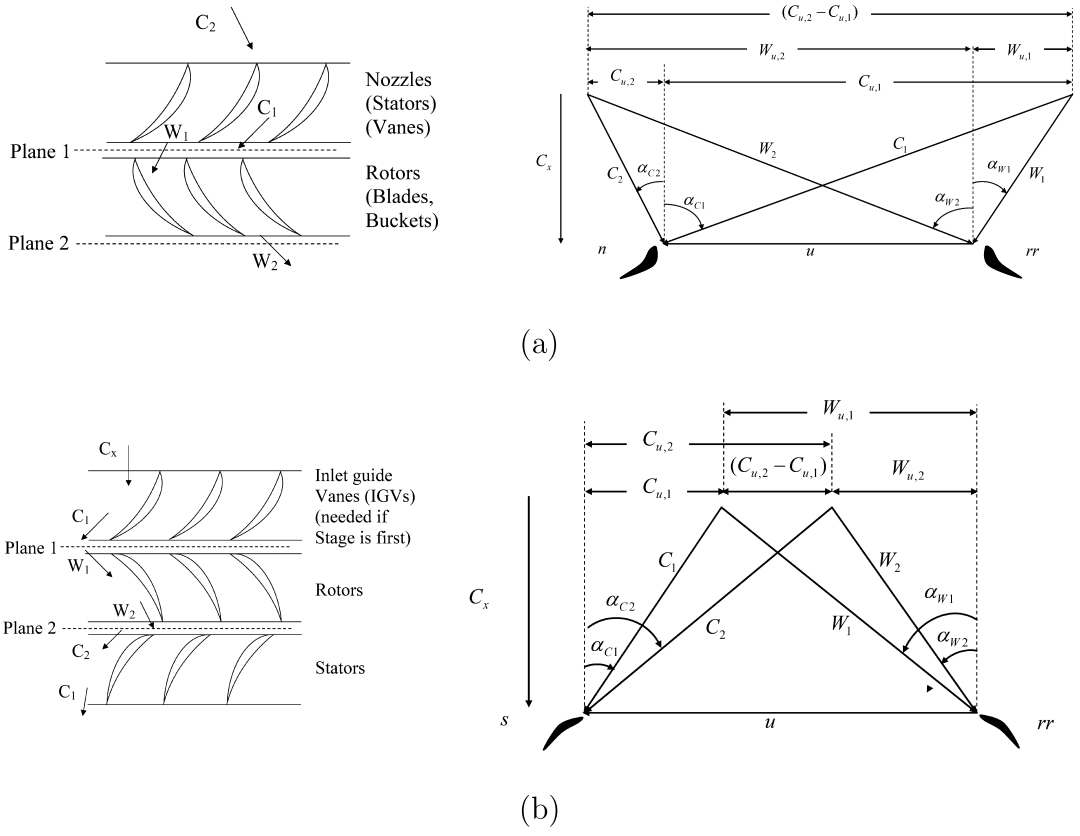

Figure 2.5: Turbomachinery blade rows and their velocity diagrams (constant u and C_x): a- Simple velocity diagrams for an axial turbine stage, b- simple velocity diagrams for an axial compressor stage (from [12])

The three major non-dimensional parameters including loading coefficient ψ, flow coefficient ϕ and reaction R_n, are used to sketch the velocity diagrams as indicated in the following. These parameters are a dominant keys on specifying the regions of low and high efficiencies for axial flow turbines as shown in figure 2.7. It is noted

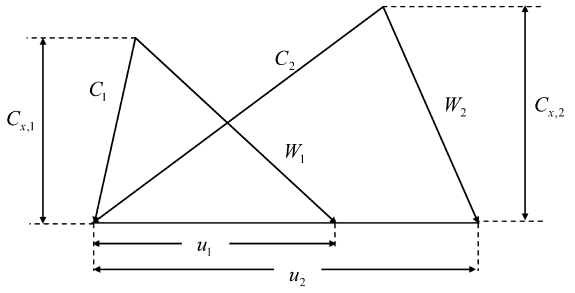

Figure 2.6: General velocity diagram (from [12])

that the work coefficient should be greater than 1 and the flow coefficient for high efficiency turbines in the range of 0.3 to 1.4 [15, 16]. In this thesis, these values are kept to produce high efficiency turbomachinery blades with the 3D blade through flow design method.

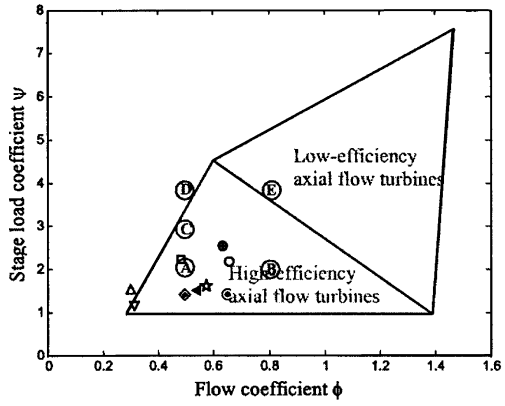

Figure 2.7: Design point for reaserch turbines (from [15, 16])

2.3.1 The work or loading coefficient, ψ

For simple velocity diagrams specification of the loading coefficient ψ requires the following assumptions: constant axial velocity C_x; constant mean radius $r_m = \frac{1}{2}(r_h + r_t)$; and identical velocity vectors C_2, C_1 and W_1, W_2 for both the stator and rotor in the subsequent "repeating" stages. The velocity diagram can be made from the combination of the two velocity triangles for the stage.

Five factors affect stage efficiency: thermodynamic variables; speed and size; velocity triangles; properties of the working substance; and losses. The effect of

these parameters on ϕ, ψ and R_n is discussed in reference [17]. Given the other constraints, the shape of the velocity triangle is the most important parameters that affects the total to total isentropic efficiency.

The loading coefficient [12] can be specified as:

$$\psi \equiv \frac{-\Delta_1^2 h_0}{u^2} = -\left[\frac{\Delta_1^2 \left(uC_u\right)}{u^2}\right]$$

For simple diagrams,

$\psi = -\left[\frac{\Delta_1^2 \left(C_u\right)}{u}\right]$

The work coefficient is positive for turbine and negative for pumps, compressors and fans. For simple 2D diagrams the loading coefficient is reduced to a graphical representation as the ratio of the distance between the apexes of the absolute and relative velocity triangles to the rotor blade speed [12]. With work coefficient above 2.5 the turbine is called highly loaded or high-work, but for values of loading coefficient less than one the turbine is called lightly loaded. This variable by itself is not enough to specify the aerodynamic characteristics of flow in turbine stages. The flow deflection through the blade row requires two more parameters which are called flow coefficient ϕ and reaction R_n.

2.3.2 The flow coefficient, ϕ

The flow coefficient is defined as the ratio of the axial velocity to the rotor blade speed,

$$\phi \equiv \frac{C_x}{u}$$

The flow coefficient is constant through the rotor and the stator in simple 2D velocity diagrams. In the general 3D velocity diagram both values of axial velocity C_x and blade rotor speed u vary from hub to tip.

2.3.3 The Reaction, R_n

The reaction can be defined as the ratio of the change in static enthalpy to the change in stagnation enthalpy of the flow passing through the rotor (in adiabatic stages the stagnation enthalpy change through the rotor is equal to that through the stage):

$$R_n = \left[\frac{\Delta h_{st}}{\Delta h_0}\right]_{rr} = \frac{\Delta h_{st,rr}}{\Delta h_{0,se}}$$

The reaction is a measure to show how much the rotor blade contributes to the overall decrease in static enthalpy in the turbine stage. The reaction is a useful parameter in the turbomachinery design and it is possible to form the relationship in-terms of the various velocities and flow angles associated with the stage. This parameter is always in a percentage value for example 50% reaction turbine. With this parameter the velocity diagram can be sketched. For the simple 2D diagrams (illustrated for turbine expansion in Fig.2.8), the reaction [12] reduces to:

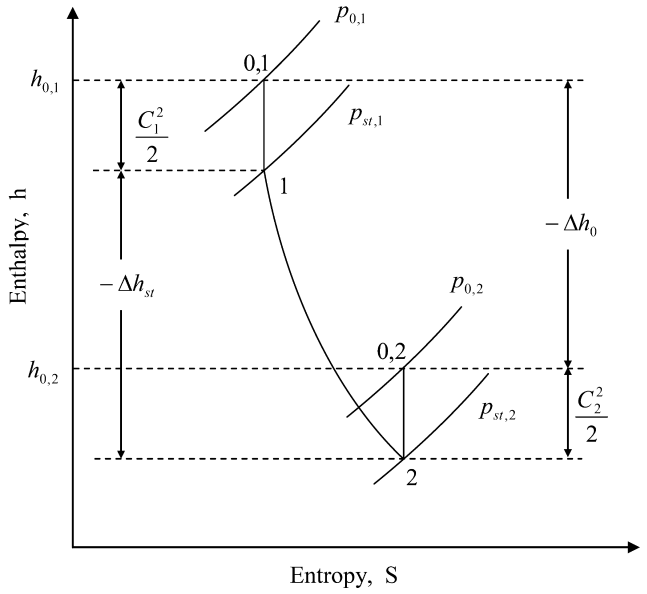

Figure 2.8: Enthalpy-entropy diagram for a turbine expansion (from [12])

$$R_n \equiv \frac{\Delta h_{st}}{\Delta h_0} = 1 - \frac{\left(C_2^2 - C_1^2\right)/2}{u_2 C_{u,2} - u_1 C_{u,1}}$$

This simple 2D formula is valid for turbines, compressors, and for general velocity diagrams, and it graphically is represented by the location at which the bisector between the apexes of the absolute and relative velocity triangles intersects vector u.

In general 3D velocity diagram u_1 is not equal to u_2, and $C_{x,1}$ is not equal to $C_{x,2}$, but for simple velocity diagram $u_1 = u_2$ and $C_x = C_{x,1} = Cx, 2$. Also, in general velocity diagram,

$C_1^2 = C_x^2 + C_{u,1}^2 + C_r^2 \qquad\qquad C_2^2 = C_x^2 + C_{u,2}^2 + C_r^2$

In this work, the general velocity diagram is used to specify three major design parameters including loading coefficient, flow coefficient and reaction that are used to make velocity diagrams for blades at hub, mean and tip, and then specifying the flow angles for each blade.

2.4 Blade design characteristics

2.4.1 Tangential lift coefficient

The choice of the blade pitch S is important in the design process of turbine blades. Pioneer publications by Zweifel [18] and some years later by Ainley and Mathieson [19] specify rules for the choice of optimal blade spacing, aiming for minimum losses. In this context two main competing phenomena have to be considered. The first one, a low blade pitch is associated with increasing profile losses due to high values of the blade wetted surface. The second one, high blade pitch is associated with higher aerodynamic loading which may lead to flow separation, implying higher aerodynamic losses.

Zweifel (1945) introduced an aerodynamic loading coefficient, which is indicated in the literature with his name. The Zweifel loading coefficient is defined as the ratio between the peripheral force actually obtained from the change of momentum, if the deflection diagram is given, and the force obtained from an ideal pressure distribution, featuring the value of the cascade inlet total pressure on the pressure surface and the outlet static pressure on the suction surface.

$$C_L = \frac{\text{tangential aerodynamic force}}{\text{tangential blade area} \times \text{ outlet dynamic head}}$$

Figure 2.9 illustrates this effort to optimize blade pitch by minimizing losses. By

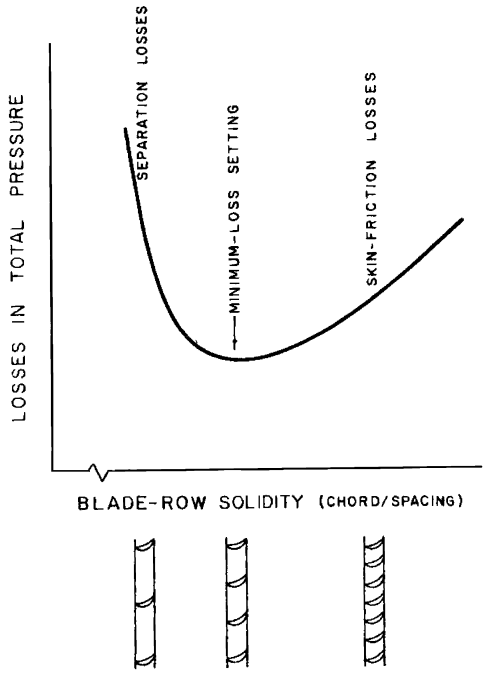

Figure 2.9: Diagrammatic variation of loss with blade solidity (from [12])

evaluating C_L in various turbine cascades in the early 1970's Stewart and Glassman [20] indicated that for minimal drag to lift ratio this coefficient assumed values between 0.9 and 1.0 for accelerating profiles featuring high deflections. Today, in the gas turbine industry a major trend is to design blade that have high tangential loading coefficient. In fact, increasing the blade spacing and the deflection reduces the number of parts and is thus associated with reduced manufacturing and maintenance costs. The current value for tangential lift coefficient is between 0.9 and 1.2 [12]. In fact, the higher the value of the tangential lift coefficient C_L, the harder it is to control the Mach number or pressure distributions of the blade surfaces. For this work, the following equation [5, 8] has been used to specify the value of the tangential lift coefficient, and use it to design the 3D blade geometry as a function of radius from hub to tip.

$$C_L = 2\,(S/b_x)\cos^2\alpha_2\,(\tan\alpha_1 - \tan\alpha_2) \tag{2.2}$$

The value of b_x/S represents the axial solidity which is smaller than the value of solidity $\sigma \equiv c/S$. The solidity is defined as the ratio of the chord to the pitch of

the blade. Both these interrelated parameters are important to control the shape of the blade geometry.

2.4.2 Axial dimensions and number of blades

Fig. 2.10 shows the cross section of a typical turbine and compressor stages which can be used to estimate their axial lengths. The selection of the axial dimensions of both stages are based on the value of the aspect ratio (height-to-chord ratio) h/c. The value of the aspect ratio, for the turbine, which is varied from about 0.8 to 10, but for the compressor, which is varied from 1 to 3. The number of blades is based on user inputs of the tangential lift coefficient and aspect ratio for both of the stator and rotor. The number of blades is open to the designer to choose. Axial turbines [12] have been built with:

- 1 to 24 blades for wind turbines,
- 3 to 30 blades for water turbines, and
- 11 to 110 blades for gas (including steam) turbines

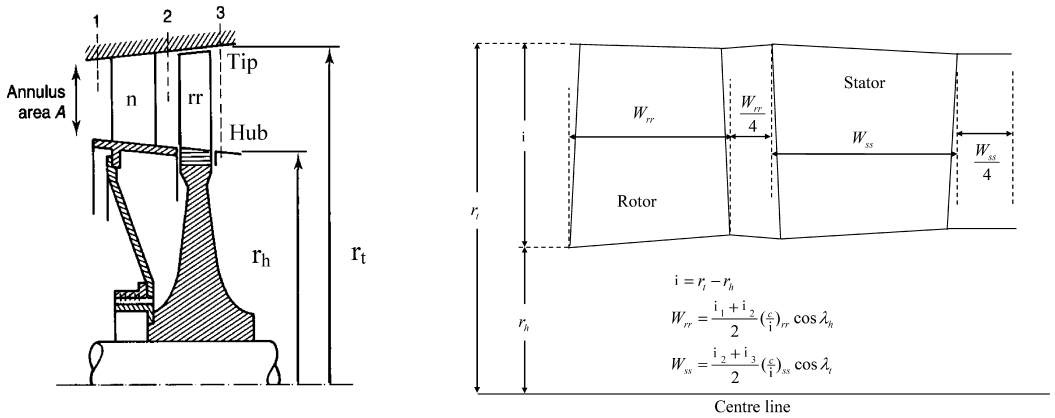

Figure 2.10: Left, axial flow turbine stage (from [13]); Right, Typical axial dimension of a compressor stage (from [15])

There are different ideas in the selection of blade numbers in turbine blade rows. Cohen [13] mentioned that the use of prime numbers for rotor blades is less common than used to be the case. This is the result of developments in mechanical design

which have result in the ability to replace damaged rotor blades in the field without the need for re-balancing the rotor system. He also explained that it is desirable to avoid numbers with common multiples for the blades in successive rows to reduce the likelihood of introducing resonant forcing frequencies. One method of doing this is to choose an even number for the stator blades and a prime number for the rotor blades.

The number of stator and rotor blades play a major role for achieving lightweight aero engines. The designer, based on the aspect ratio, has a wide choice to select the number of blades, and the size of the blades, which greatly affect the size of the machine. Stationary industrial machines have a small number of larger blades due to decrease in the overall cost and increase in the accuracy of the relative profile; but aero engines use a larger number of smaller blades in order to keep the size of the engine smaller. The amount of secondary losses and vibrations are affected by this selection of aspect ratios.

2.4.3 Choice of stagger angle

The stagger angle or setting angle λ is tangential to both the trailing and leading edge of the blade (Fig. 2.4) and it is related to the axial chord, b_x, and the blade chord, c, by

$$\cos \lambda = \frac{b_x}{c} \tag{2.3}$$

This equation is used in the preliminary design of the blade. The overall blade orientation is specified by stagger angle, which helps to specify the passage blade shape for turbomachines. The value of the stagger angle as well as the inlet and outlet flow angles and the ratio of the axial chord to the chord of the blade affect the overall blade shape. We restrict our attention to the design of high Mach number but subsonic blades. In the design process of the blades the stagger angle is not arbitrary, but it varies around a "nominal" value by (10 to 30)^o over which it is possible to design a continuously converging blade passage from inlet to outlet.

For a continuously converging passage from inlet to outlet the throat occurs at the trailing edge of the next blade (Fig. 2.4).

In this work, the stagger angle is an input parameter, which in addition to the turning of the flow through the passage of the blade and the aerodynamic loading along the blade affects the front or aft loading of the blade [6]. There is still no accurate data in the open literature to help choose the stagger angle. The only guide for low speed turbine has been published by Kacker and Okapuu [21]. In design of compressor blade the throat area is in the front part of the blade and it is measured from the adjacent blade to the around the middle of the suction surface of the next blade.

2.4.4 Selection of number of stages

The number of stages of turbomachines are affected by the major non-dimensional parameters including work coefficient ψ. This parameter generally indicates how many stages are required for turbomachine. A low value of work coefficient requires a higher number of stages for a given overall turbine output. For an industrial gas turbine, where the size and weight of the turbomachine is of little importance, it is desirable to design blades with relatively low work coefficient and relatively lower aerodynamic losses. For aircraft engines, which have tight restrictions in both size and weight, the designer should select relatively higher values of work coefficient. Mattingly [15] mentions that a single stage turbine requires work coefficient greater than 2.0 and results in negative reaction, which makes it impossible to achieve high aerodynamic efficiency.

In the blade design process, the number of stages is specified by assuming a first guess of about 0.9 for the polytropic efficiency [12], and computing the resultant overall stagnation enthalpy drop through the turbine. The decrease in stagnation enthalpy in a turbine stage depends on its application and the importance of low weight. In a multi-stage design this would result in a distributed total temperature

drop along the stages:

$$\Delta h_0 = c_p \, (T_{0,in} - T_{0,ex})/(\text{number of stages}) \tag{2.4}$$

Wilson and Korakianitis [12] use a guideline about 1.8 for the work coefficient for single-stage high-pressure turbine at the mean diameter. Higher work coefficients at the mean diameter of stages of pressure ratio of 8:1 or above result in hub work coefficients of 4.0 to 5.0 or higher. Typically, the work coefficient is $-0.5 \leq \psi \leq -0.3$ for compressor stages and $1.0 \leq \psi \geq 2$ for turbine stages.

2.5 Blade design methods

The goal of any blade design method is to find a geometry that satisfies flow requirements with minimum loss, tolerable mechanical stresses, minimum disturbances downstream and upstream, and in the case of compressors adequate stall margin, among others. The design of blade geometries is a very important step for the design of efficient turbomachines, as the blade design process directly influences the blade-row efficiency and thus the overall machine efficiency. A major challenge in the design of turbomachinery blades is simultaneously satisfying the aerodynamic design requirements and the mechanical and geometric restrictions imposed on the blades.

Early blade design methods were based on specifying a thickness distribution around a camber line. In this method, for specifying turbine and compressor shapes, straight line, circular arc or parabolic camber lines were used, and then the thickness distribution was added to these camber lines for both the suction and the pressure sides of the blade. Examples of this method [12, 22] are designs of NACA compressor airfoils (NACA-65 series) and other series of NACA profiles for turbines by Dunavant and Erwin [23]. This method did not provide enough flexibility to control both the suction and pressure surfaces in order to obtain a desirable aerodynamic performance.

After the 1950s, most turbine blades have been designed by specifying the shape of the suction and pressure surfaces of the blade. Thus the passage was defined by the blades and the resultant blade thickness was obtained. Dunham [24] and Pritchard [25] used parametric methods to describe the blade surface geometry. In these methods segments of lines are joined in a variety of points along the blade surfaces. The way in which the line segments are joined generates shapes that look smooth to the eye, but they cause local flow accelerations and decelerations as will be explained below.

Various categories for blade design methods exist: direct; inverse, semi-inverse, full-inverse or full optimization methods [26]; analysis and design modes [27]; optimization and design methods; and others. The definitions of what is semi-inverse, full-inverse etc methods vary in the literature. In this thesis, the direct design has been defined as a process in which the blade geometry is specified and the resultant aerodynamic performance on that geometry is calculated; and the inverse method has been defined as a method in which the desired blade performance is specified and the geometry that would accomplish such performance is calculated.

Both methods have relative advantages and disadvantages. In the direct method, it is relatively easy to fulfill mechanical and geometric constraints, where the complete geometry is specified; but it is usually laborious (in previous method) to obtain the desired distribution of pressure or velocity along the profile with this method. On the other hand, it can be difficult to get an acceptable geometry with an inverse method, where the velocity is prescribed and the geometry calculated [28]. The inverse design method [29] is based on the velocity or pressure distribution along the streamwise blade shape, and it requires multiple variations of the velocity distribution until an acceptable profile geometry is obtained. The inverse design method has also difficulties in both of the leading and trailing edges, due to mathematical singularity at the stagnation points [28, 30]. The inverse method ends up with blades with zero thickness at the trailing edge, which are impossible to manufacture. This last difficulty makes the inverse method acceptable for some compressor

blade geometries of thin trailing edge, but unacceptable for turbine geometries that have thicker trailing edges. The thicker turbine trailing edge, firstly is required to cover the cooling process of this part of the blade that has a positive effect on the total losses [31] and secondly, to control the circulation effect on the rear part of the blade [32]. In addition to that, Pritchard [25] mentioned that the inverse method requires a lot of data, need additional smoothing, control the camber line instead of controlling the surfaces, can not handle every case, and are time consuming, or the geometric parameters are hard to quantify.

Korakianitis has worked on the design of airfoils by the direct method. In his first attempt [2] he specified five points along the blade surface (excluding the trailing edge and the leading edge points) and two slopes on each surface. In the leading edge region he used two thickness distributions added perpendicularly to two parabolic construction lines. He concluded that the blade aerodynamic performance, judged by the shape of the blade surface Mach number distribution, is very sensitive to changes in the slope of the curvature of the blade.

In follow on work Korakianitis in a series of improvements to blade design methods [2–9] proposed a direct design method based on specifying blade surface-curvature distribution. He concluded that aerodynamic and heat transfer performances of turbomachinery blades are determined by the surface curvature distribution and mentioned that the changes in the local slope of curvature are more important than the (x,y) location of the blade shape, and that blade quality-assurance methods should not be point-by-point comparisons of geometric accuracy, but should be based on measurements of streamwise surface curvature distributions instead. These affect the aerodynamic and heat transfer performance (avoiding local separation bubbles and removing spikes in the Nusselt number). Details will discussed in the following chapters.

The conclusion for the method is that blade surfaces with continuous slope of curvature, or third derivative continuity in the spline knots, result in smooth Mach number and pressure distributions, and thus can be used to avoid flow separation,

and lead to improved heat transfer characteristics and better overall blade designs [5–9]. Slope of curvature continuity means that the surface curvature C, as well as its slope along axial distance x, $C' = dC/dx$ along the blade profile length, must both be continuous. This requires continuous third derivatives of the line segments $y(x)$, i.e. continuous $y''' = d^3y/dx^3$, as illustrated by the following two equations [2,3,5–8] for curvature and its slope.

$$C = \frac{1}{r} = \frac{(d^2y/dx^2)}{\left[1 + (dy/dx)^2\right]^{(3/2)}} \tag{2.5}$$

$$C' = (dC/dx) = \frac{d^3y/dx^3\left(1 + (dy/dx)^2\right) - 3\,(dy/dx)\,(d^2y/dx^2)^2}{\left(1 + (dy/dx)^2\right)^{5/2}} \tag{2.6}$$

$$\text{where} \qquad y = y(x), \qquad y' = \frac{df(x)}{dx}, \qquad y'' = \frac{d^2f(x)}{dx^2}, \qquad y''' = \frac{d^3f(x)}{dx^3}$$

Tiow and Rooij [33, 34] mentioned that the direct design method does not provide any guidance to the designer to control the shape of the blade, and they say the direct design method always requires designer's experience and is more laborious. However, this is only true if one is not considering the blade surface curvature distributions. Corral and Pastor [35] used a parametric design method to remove the leading-edge separation bubbles in a turbine blade geometry for which extensive experimental data have been published (the Hodson-Dominy blade (HD blade) [36–38], which is also used as an example later on in this thesis). Corral and Pastor [35] failed to remove the leading-edge difficulties with keeping the leading edge region as in the original shape and report "...it is specially difficult to match the original geometry because of i.e. discontinuity in the airfoil, which is not explicitly take into account in our method". As will be shown later in this thesis, the PSCD blade design method can be used in a direct design method to remove the leading edge separation regions from the HD, VKI and other blades.

Gas turbine blades are three dimensional objects operating in unsteady and complex flow fields. This complexity forces designers to simplify the three dimensional

blade-design problem to a series of two dimensional problems in the streamwise direction, and to assume that the blade operates in steady-flow conditions. The three dimensional variation of inlet and outlet flow angles is determined by streamline curvature calculations [8, 39–42], and they vary from hub to tip. Depending on design choices of blade aspect ratio (h/b) and the three-dimensional distribution of the centers of gravity of the two-dimensional sections, two-dimensional blade shapes are stacked to build the three dimensional geometry. The blade design manufactures have different sequences to design their blades, but all of them follow essentially the above overall procedure. Numerical optimization methods have been successfully used for a variety of design problems. However, application to aerodynamic blade shape optimization problem still remains as a hard challenge. The application of three dimensional blade-to-blade and through flow calculation methods in design process of turbomachine are restricted to consideration of limited Mach numbers, minimizing the number of stages, or maximizing work per stage while keeping high efficiencies. In most turbomachinery design systems a meridional through flow calculation is the backbone of the design process. It is fast, reliable and easy to use to design multi-stage blade rows for turbomachinery. Initial blade design components are based on the assumption of steady quasi-three-dimensional axisymmetric flow in a series of meridional planes (through-flow analysis in the axial-radial directions). These analysis are based on the general S1/S2 theory of Wu [43]. Blade shapes are then designed by quasi-three-dimensional analysis in a series of meridional-tangential planes. In the design process of turbomachinery blades, the design of annuals passage and blade shapes with both methods are crucial points before analyzing three-dimensional(3D) Navier-Stokes simulations. The through flow [44–49] and blade-to-blade [50, 51] design methods treat the three dimensional (3D) flow through a series of second dimensional blade sections and stacked based on the center of gravity [51–57] or trailing and leading edge positions [57–59] to build up three dimensional blade geometry. Design of blade geometry sections, using quasi-three-dimensional, is a typical way to design 3D blade geometry, and it is quite efficient

when it compares to fully-3D Navier-Stokes simulations [51].

In this thesis we use the 3D streamline curvature through-flow method proposed in [8, 10] to specify multi-stage 3D velocity diagrams in a series of streamlines from hub to tip. The original method used simple velocity diagrams, and was modified to include general velocity diagrams. The overall method is based on derivation of the radial-equilibrium equation assuming that the radial components of velocity do not contribute to friction, but accounts for losses in the streamwise direction. The resultant equation is coupled with the enthalpy rise per streamline in each stage. The performance of each stage is analyzed by assuming loss models for the total pressure drops in stators, and total-to-total polytropic efficiency for each stage. These loses can be applied in each individual streamline, accounting for losses as a function of geometry, using various models published in the open literature. Further details about this method can be found in [8, 10].

2.6 Flow analysis with CFD

This section presents the role of computational fluid dynamics (CFD), in the simulation of flow over blades. CFD is helpful in many applications and used extensively in industry because it is more economical than physical testing. Fluent is a tool that can provide models for a lot of fluid flow problems: compressibility, turbulence (laminar or turbulent flow), time dependency (transient or periodic), transport phenomena (chemical reaction), etc. The software uses both the Euler and the Navier-Stokes equations which take into consideration the conservation of mass , momentum and energy for many kinds of flows representing engineering applications. GAMBIT (mesh generator) and FLUENT and ANSYS12 (flow solvers) have been used throughout whole thesis to calculate flow behaviour and surface heat transfer distribution.

GAMBIT, which is a pre-processing tool linked to Fluent, is used for mesh generation. The blade geometry data points from MATLAB are imported into

GAMBIT and joined together to make the blade. The selection of mesh affects the convergence of the equations, and it cannot remove any geometry-generated flow difficulties that are exist in the model: the accuracy of the elements in the mesh is increased to decrease the errors or to increase the iterations. The higher the number of iterations, the closer the solution gets to the converged solution for the sparse matrix inversion [60]. The selection of mesh elements depends on the geometry and the representation of the viscous model. The quality of the mesh has been checked through the skewness value and the aspect ratio. The structured and unstructured meshes or mixed mesh (structured and unstructured or triangles) were used to show the ability of the turbulence model in predicting flow behaviour and surface heat transfer distribution.

FLUENT is a state-of-the-art computer program for modeling fluid flow and heat transfer in complex geometries, using Finite Volume Method (FVM). The program provides complete mesh flexibility, solving the flow problems with unstructured meshes that can be generated around complex geometries. Different turbulence models are used in FLUENT [60]. In the following subsections suitable turbulence models for whole cases, which include the transition phenomena, have been used.

FLUENT-ANSYS 12 provide several turbulence models to analyze the flow but in this thesis only the modified low-Reynolds turbulence model [61] and SST $k-\omega$ transition model [62–64] have been used. Both turbulence models, which are described in the following section, have a significance effect in predicting transition phenomena in turbomachinery blades and wind turbine airfoils.

2.6.1 Models for turbulence and transition

Turbulent flows are characterized by velocity fields which fluctuate rapidly both in space and time. Since these fluctuations occur several orders of magnitude it is computationally very expensive to construct a grid which directly simulate both the small scale and high frequency fluctuations for problems of practical engineering

significance. Two methods can be used to eliminate the need to resolve these small scales and high frequencies; Reynolds Averaging and Filtering. In the Reynolds Averaged approach all flow variables are divided into a mean component and a rapidly fluctuating component and then all equations are time averaged to remove the rapidly fluctuating components. For the continuity equation the new equation is identical to the original equation, except that the transported variables now represent the mean flow quantities. These new terms are known as the Reynolds stresses, and the solution of the Reynolds Averaged Navier-Stokes (RANS) equation initially involves the construction of suitable models to represent these Reynolds Stresses. One approach to this problem is to treat the time averaged terms as additional viscous stresses produced by turbulence in the flow. In the Boussinesq approach the Reynolds Stresses are assumed to have a form identical to the viscous stresses in the momentum equation, apart from that the Reynolds Stresses are isotropic, which is known to be untrue in many cases. The problem then reduces to finding an expression for eddy viscosity.

An alternative approach to Reynolds averaging is filtering. The idea behind this approach is to filter the time-dependent Navier-Stokes equation in either Fourier (wave-number) space or configuration (physical) space. This filtering process effectively filters out the turbulent eddies whose scales are smaller than the filter width, which is usually taken to be the mesh size. As with Reynolds averaging however, the filtering process creates additional unknown terms which must be modeled in order to provide closure to the set of equations. This approach is known as Large Eddy Simulation (LES). All LES simulations require a lengthy time-dependent run so that statistics of the mean flow quantities can be gathered. LES and DNS are suitable tools for transition predictions, although the proper specification of the external disturbance level and structure poses substantial challenges. Unfortunately, these methods are far too costly for engineering applications and they are currently used as research tools and substitutes for controlled experiments [64].

Despite its complexity, transition should not viewed as outside the range of RNS

methods. The challenge to a proper engineering model is therefore mainly in the formulation of a model that can be implemented into a general RANS environment. Flow transition plays an important role in the design and performance of turbomachinery applications and aerospace devices where the wall shear stress or the wall heat transfer or a combination of both is of interest. majority of boundary layer flows in turbomachines and wind airfoil devices involve the flow transition under the effects of various factors, such as freestream turbulence, pressure gradient and separation, Reynolds number, Mach number, turbulent length scale, wall roughness, streamline curvature, heat transfer [65]. Typically, the transition over the blade surface and the change in the properties related to the transition process can have a strong influence on the operation and performance. It has been known that early transition can prevent the separation(stall) of the suction side boundary layer and consequently lead to significant reduction in total pressure loss. Various modes exist in the open literature by which transition is generally believed to occur will discuss in the following section. The primary modes are often refereed to as a natural transition, bypass, and separated flow transition.

2.6.1.1 Modes of transition

1. Natural transition

   A modern natural transition process described by Schlichting [66]. This type of transition, based on a number of theoretical and experimental observations, is known to involve several important stages. These are brief descriptions [67]: 1- The laminar boundary layer, at a critical value of the momentum thickness Reynolds number, becomes susceptible to small disturbances and develops an instability in the form of a two dimensional Tollmein-schlichting wave. 2- Loop vortices with large fluctuations are developed and grown as a result of three dimensional instabilities which are amplified within the boundary layer. 3- Finally, the turbulent spots are formed as a result of the highly fluctuation portions of the flow. Then it grows and convects downstream within the

laminar layers to coalesce eventually into a fully developed flow.

2. Bypass transition

   For transition at high free-stream turbulence levels, the first and possibly second stages of the natural transition process are completely bypassed such that the turbulent spots are directly produced within the boundary layer by the influence of the freestream disturbances [67]. It is argued that linear stability is irrelevant for bypass transition and to date no one has been able to detect Tollmein-schlichting waves for transition in favorable pressure gradients [67]. A theory which needs to be concerned, for this mode, with the process involved in the production, growth and convection of turbulence spots. By pass transition from practical standpoint is often considered to start when the skin friction deviates from the laminar value. this has been shown to be the location where the first turbulent spots appear [68].

3. Separated flow transition

   When a laminar boundary layer separates, transition may occur in the shear layer of the separated flow as a result of the inviscid instability mechanism. In this case, the shear layer may reattach as a result of enhanced mixing caused by the turbulent flow. This reattachment forms a laminar-separation/turbulent-reattachment bubble on the surface [67]. This type of transition can occur behind the boundary layer trip wires and as result of separation due to a strong adverse pressure gradient. This mode of transition is common in gas turbine and may occur in an "overspeed" region near a leading edge of the blade on either the suction or pressure side, or both, or near the point of minimum pressure point on the suction side. The bubble length depends on the transition process within the shear layer and may involve all of the stages listed for natural transition. Because of this, it is generally accepted that the freestream turbulence level plays a large role in determining the length of the separation bubble. Traditionally, separation bubbles have been classified

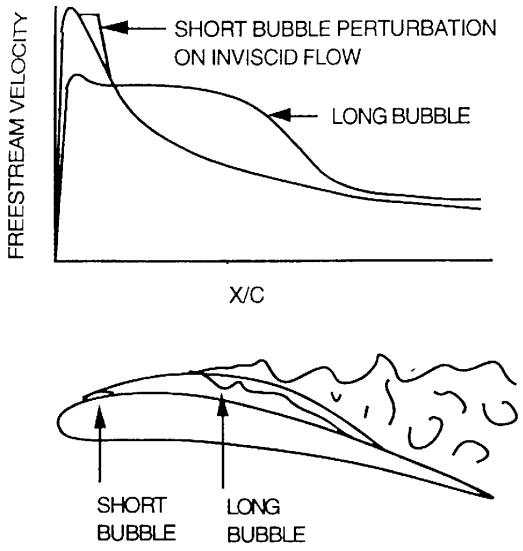

Figure 2.11: Separation bubble effects on suction side velocity distribution(from [69])

as long or short based on their effect on the pressure distribution around an airfoil [67] as shown in fig 2.11. Short bubbles reattach shortly after separation and only have a local effect on the pressure distribution. Long bubbles can completely alter the pressure distribution around an airfoil. Since long bubbles produce large losses and large deviations in exit flow angles, they should be avoided [67].

2.6.1.2 Transition models

In general, there are three main concepts used to model transition. The first approach is based on the stability theory. The successful technique is the so-called e^n method [70]. It is based on the local linear stability theory and the parallel flow assumption in order to calculate the growth of the disturbance amplitude from the boundary layer neutral point to the transition location. This method is not compatible with the current CFD methods because the typical industrial Navier-Stokes solutions are not accurate enough to evaluate the stability equation [71]. In addition, since it is based on the linear stability theory, it cannot predict the transition due to non-linear effects such as high freestream turbulence or surface roughness.

Therefore, this method is strictly used for the case of natural transition.

The second approach is the use of conventional turbulence models. One way is to switch on the turbulence model, or eddy viscosity, at an experimentally predetermined transition location. This method has advantages and disadvantages and ignores the transition physics and the importance of the transition zone completely. Especially for flows where the transitional region covers a large portion of the flow field, as observed in many low pressure turbine experiments, this practice can lead to severe errors in the solution. Another way is to use the low Reynolds number turbulence models. However, the ability of most of low Reynolds turbulence models to predict transition seems to be an questionable. This is because the calibration of the damping functions is based on reproducing the viscous sublayer behavior which include the wall distance parameter $y+$ where

$$y+ \equiv \frac{Uy}{\nu} \tag{2.7}$$

This makes the problem to predict the separation flow and reattachment point a singularity problem (divide by zero) [72–76]. These models cannot be generalized for all types of transitional flow. In order to generalize these models to correctly predict the flow affected by transition, more special treatments are needed in turbulence models [77].

The third approach to predict transition, which is favored by the turbomachinery industry, is to use the concept of intermittency to blend the flow from laminar to turbulent regions. The intermittency is the fraction of time that the flow is turbulent during the transition phase, which is zero in the laminar region and becomes unity in the fully turbulent region, so that the start and development of transition can be controlled by the intermittency [64, 71, 78–83]. From experimental observations, the development of intermittency is quite general for the steady boundary layer on a flat plate and therefore the onset location and growth rate of transition can be correlated. For the onset location, most correlations usually relate the freestream turbulence

intensity, Tu_∞, and the pressure gradient to the transition momentum thickness Reynolds number. A typical correlation is that of Mayle [67], which is based on a large number of experimental observations. Another popular correlation is the model of Abu-Ghannam and Shaw [84], which additionally accounts for the influence of the pressure gradient. The development of transition is usually expressed as a function of the intermittency factor such as the law of Dhawan and Narasimha [78]. The development of intermittency is previously described algebraically by the Dhawan-Narasimha law and the onset and end of transition are determined by the correlation. However, this law is not appropriate for general applications, which are mostly under the effects of non-zero pressure gradients and high freestream turbulence levels, because it is valid only for the flow with zero pressure gradient and natural transition. The intermittency can more generally be obtained as a solution of the intermittency transport equation. For example, the intermittency transport model of Steelant and Dick [79] is derived from the intermittency distribution of Dhawan and Narasimha along the streamline direction. Another example is based on the concept of local variables, which was formulated by Menter [64, 80, 81] in terms of a generalized intermittency variable. The concept of intermittency can be successfully incorporated with the turbulence model in many ways, such as the framework of Steelant and Dick [79] in which the intermittency is incorporated into two sets of strongly coupled equations of conditionally averaged Navier-Stokes equations. This approach is too complex and not compatible with current CFD codes in which only one set of Navier-Stokes equations is involved. As a result, transitional flows are mostly modeled within a Reynolds Averaged Navier-Stokes (RANS) framework, and usually linked with the turbulence model by modifying some terms in the turbulence model. For instance, the intermittency obtained from the Dhawan-Narasimha law is incorporated into the turbulence model by Baek [77]. Other examples are Suzen and Huang [82], Menter [64, 80, 81] and Lodefier [83, 85] who use the transport equation for intermittency incorporated into the turbulence model.

Many researchers [61, 70, 73–75, 85–91] have confirmed the ability of both tur-

bulence models (low-Reynolds $k-\epsilon$ combined with $k-\omega$ SST transition models) in predicting fluid flow behavior and surface heat transfer distribution around turbomachinery blades and isolated airfoils. This thesis used two turbulence modeling concepts. The first approach is the low-Reynolds number turbulence model, and the second approach is the use of the experimental correlations (e.g. SST $k-\omega$ transition model). A brief description for these models are described as follows:

1. **Low-Reynolds Turbulence model**

   The preferred method for predicting transition with unstructured/parallelized CFD codes is to use a low-Reynolds number two-equation turbulence model without any subsequent coupling to an empirical correlation. This is because these models are relatively easy to implement (they dont require any search algorithms) and in some cases are capable of predicting transition even in 3D flows [70, 71]. Low-Reynolds number turbulence models employ damping functions that are designed to predict viscous sublayer behaviour so that wall functions are not required. In order to predict transition they rely on the diffusion of turbulence from the freestream into the boundary layer and the interaction of this freestream turbulence with the model source terms. A modified low-Reynolds-number $k-\epsilon$ proposed by Chen [61] has able to capture the separated flow and reattachment point around an isolated airfoil.

   The modified low-Reynolds k-e turbulence model includes the modification to the turbulent viscosity, the pressure-velocity correlation term and the boundary conditions of the dissipation rate. This method proposed a more general damping function into the turbulent viscosity without introducing a y^+ parameter to avoid singularity and predicting the re-attachment point (i.e. separation) in the flow. The modifications inside this model are as follows.

Turbulent viscosity term

Generally, LRN turbulence models introduce a damping function f_μ in their turbulent viscosity calculation terms to consider the LRN effect in the near-wall region. The general form for the turbulent viscosity is

$$\mu_t = \rho C_\mu \frac{k^2}{\epsilon} f_\mu \tag{2.8}$$

where the damping function f_μ is defined that its value decreases from the unity to almost zero as the wall is approached. The proposed damping function, for the above equation, which is in the form of

$$\begin{aligned} f_\mu =& \{1 + \frac{3.45}{\sqrt{R_T}}\} \times [1 - \exp\{-1.85 \times 10^{-3} \times \\ & R_y - 1.05 \times 10^{-4} R_y^2\}]^{3/2} \end{aligned} \tag{2.9}$$

where the Reynolds numbers $R_y = \frac{\sqrt{ky}}{\nu}$ and $R_T = \frac{k^2}{\nu}$ are introduced to consider the low Reynolds-number effect instead of y^+.

This proposed formula does not involve y^+. The introduced Reynolds number, R_y, into the damping function is used to describe the low Reynolds effect inside the boundary layer. As y decreases on approaching the wall, R_y decreases resulting in decrease in f_μ. Thus the viscosity is damped. Furthermore, unlike y^+, R_y is still non-zero value above the reattachment point. This feature of the proposed damping function overcomes the singularity problem for reattached flow(i.e. predicting separated transition flow), which is caused by the use of y^+ in the damping function.

Pressure-velocity correlation term

The pressure-velocity correlation term, for LRN turbulence model, must to be considered for near wall boundary layer and separated flow. Some of the LRN turbulence models use this term but still they have y^+ in their correlation term in the form of

$$\prod = \frac{0.05}{f_\mu\{1 - \exp^{-y^+}\}} \times \frac{\mu_t}{\sigma_k}\frac{\partial^2 k}{\partial x_j^2} \tag{2.10}$$

The correlation term in this form again has the problem with the parameter of y^+ in the reattachment point. To overcome this problem, Chen [61] used Poissson's equation for the pressure fluctuation. This gives the idea of modeling correlation term based on Wilcox suggestion [92], which said the correlation term should probably depend on the mean flow strain. So the proposed correlation term for LRN model in the form of

$$\prod k = f_{\prod k}\mu_t k^{1/2}\frac{\partial}{\partial x_j}\{\frac{\partial U_i}{\partial x_j} + \frac{\partial U_j}{\partial x_i}\} \tag{2.11}$$

where U is the mean velocity and x is the distance length scale. The term $\frac{\partial}{\partial x_j}\{\frac{\partial U_i}{\partial x_j} + \frac{\partial U_j}{\partial x_i}\}$ represents the mean flow strain while $\mu_t k^{1/2}$ represents the turbulence feature. Coefficient $f_{\prod k}$ is an empirical function. It is determined from the experimental data, and it can be improved with more experimental data and different shapes. It was introduced mainly because of the magnitude of the main strain rate is much smaller than that of the pressure velocity correlation term. The formula of this empirical function is modelled as

$$f_{\prod k} = \frac{R_y}{1.45 \times 10^-4 R_y 2 + 6.65 \times 10^{-4} R_y + 7.5 \times 10^{-3}} \tag{2.12}$$

These functions provide a modifying influence on the $k - \epsilon$ model in the very near wall region, thus extending the validity of the equations clear through the

viscous sublayer to the wall. These terms obviously play an important role in predicting the separation region [61]. Luo and Lakshminarayan [75] confirmed that most of the LRN $k-\epsilon$ models depends on y^+ which make them inaccurate for predicting transition and separated flow. There is another turbulence models of LRN k-e model did not contain y^+, but it is not asymptotically consistent in the near wall region [93].

However, most of the low-Reynolds k-e turbulence models are found to predict excessive levels of turbulent energy in stagnation regions. To cover this problem, the proposed correction by Kato and Launder [60] is activated, to reformulate the turbulent energy production term. this has been done parallel to the Chen's modification. The aerodynamic performance of the case of Eppler wind turbine airfoil has been found with this model. Further descriptions for this model can b found in [61].

2. **SST $k-\omega$ transition turbulence model** This transition model, coupled with SST $k-\omega$ turbulence model [62], is based on two transport equations. The first one is the intermittency equation used to trigger the transition process. This equation is developed on the concept of non-zero freestream intermittency, and allows the turbulent eddies from the freestream to disturb the laminar boundary layer. The second equation is formulated in terms of the transition momentum thickness Reynolds number, $Re_{\theta t}$, to avoid additional non-local operations introduced by the quantities used in the correlations. The general transport equation [64, 70, 71, 80, 81] for the intermittency factor,γ, can be written as

$$\frac{\partial \rho u_j \gamma}{y} = P_{\gamma 1} - E_{\gamma 1} + P_{\gamma 2} - E_{\gamma 2} + \frac{\partial}{\partial x_j}\left[\left(\mu + \frac{\mu_t}{\sigma_\gamma}\frac{\partial \gamma}{\partial x_j}\right)\right] \tag{2.13}$$

This transport equation contains two production terms $P_{\gamma 1}$ and $P_{\gamma 2}$ and two

dissipation terms $E_{\gamma 1}$ and $E_{\gamma 2}$ which are defined as follows:

$$P_{\gamma 1} = F_{length} C_{a1} \rho S \left(\gamma F_{onset}\right)^{C_\alpha}, \quad E_{\gamma 1} = C_{e1} P_{\gamma 1} \gamma, \quad P_{\gamma 2} = C_{a2} \rho \Omega \gamma F_{turb}$$

$$E_{\gamma 2} = C_{e2} P_{\gamma 2} \gamma$$

where S is the strain rate magnitude, Ω is the vorticity magnitude, F_{length} is the empirical correlation that controls the length of the transition region. The production $P_{\gamma 1}$ is formulated as a function of F_{onset} which is controlled by the following functions [64, 70, 71, 80, 81]:

$$\begin{aligned} F_{onset} &= max\left[F_{onset2} - F_{onset3}; 0\right], \quad F = exp\left[-\left(\frac{R_T}{4}\right)^4\right] \\ F_{onset2} &= min\left[max\left[F_{onset1}; F_{onset1}4\right]; 2.0\right], \quad F = \frac{Re_\nu}{2.193 Re_{\theta c}} \\ F_{onset3} &= max\left[1 - \left(\frac{R_T}{2.5}\right)^3; 0\right], \quad Re_\nu = \frac{\rho S y^2}{\mu}, \quad R_T = \frac{\rho k}{\mu \omega} \end{aligned} \tag{2.14}$$

where Re_ν is the vorticity Reynolds number, Re_T is the viscosity ratio, y is the normal distance from the nearest wall, k is the turbulence kinetic energy, ω is the specific turbulence dissipation rate and $Re_{\theta c}$ is the critical momentum thickness Reynolds number. The equation for the transition momentum thickness Reynolds number is designed to capture the nonlocal influence of the turbulence intensity which changes due to the decay of the turbulence kinetic energy in the freestream. It is formulated by treating the transition momentum thickness Reynolds number Re_θ as a transported scalar quantity,$\tilde{Re}_{\theta t}$, as shown in the following equation [64, 71, 81]:

$$\frac{\partial \rho \tilde{Re}_{\theta t}}{\partial x_j} = P_{\theta t} + \frac{\partial}{\partial x_j}\left[\sigma_{\theta t}\left(\mu + \mu_t\right)\frac{\partial \tilde{Re}_{\theta t}}{\partial x_j}\right] \tag{2.15}$$

The source term $P_{\theta t}$ [64, 81] is defined as follows:

$$
\begin{aligned}
P_{\theta t} =& C_{\theta t}\left(\frac{\rho}{T}\right)\left(Re_{\theta t}-\tilde{Re}_{\theta t}\right)(1-F_{\theta t}),\\
T =& \frac{500\mu}{\rho U^2},\quad F_{\theta t}=min\left[max\left[F_{wake}\cdot e^{-\left(\frac{y}{\delta}\right)};1.0-\left(\frac{C_{e2}\gamma-1}{C_{e2}-1}\right)\right];1.0\right]\\
F_{wake} =& e^{-\left(\frac{Re_\omega}{10^5}\right)^2},\quad Re_\omega=\frac{\rho\omega y^2}{\mu},\quad \delta=\frac{50\Omega y}{U}\delta_{BL},\quad \delta_{BL}=\frac{15\theta_{BL}}{2},\quad \theta_{BL}=\frac{\tilde{Re}_{\theta t}\mu}{\rho U}
\end{aligned}
$$

where U is the local velocity magnitude, T is the time scale for dimensional reasons and $F_{\theta t}$ is the blending function for turning off the influence of the production term $P_{\theta t}$ inside the boundary layer. The model constants are $C_{a1}=2.0$, $C_{e1}=1.0$, $C_{a2}=0.06$, $C_{e2}=50.0$, $C_{\alpha}=0.5$, $\sigma_{\gamma}=1.0$, $\sigma_{\theta t}=2.0$ and $C_{\theta t}=0.03$. The onset of transition is determined from the empirical correlation of the transition momentum thickness Reynolds number, which is formulated as a function of the pressure gradient parameter, λ_θ, and the acceleration parameter, K, as follows [64, 71, 81]:

$$
\begin{aligned}
Re_{\theta t} =& 803.73\left(Tu+0.06067\right)^{-1.027}F\left(\lambda_\theta,K\right),\\
F\left(\lambda_\theta,K\right) =& \begin{cases} 1-F_\lambda e^{-\frac{Tu}{3.0}} & \lambda_\theta\leq 0\\ 1+F_K\left(1-e^{-\frac{Tu}{1.5}}\right)+0.556\left(1-e^{-23.9\lambda}\right)e^{-\frac{Tu}{3.0}} & \lambda\theta\geq 0\end{cases},\\
\lambda_\theta =& \frac{\theta^2}{\nu}\cdot\frac{dU}{ds},\quad K=\frac{\nu}{U^2}\cdot\frac{dU}{ds},
\end{aligned}
\tag{2.16}
$$

where Tu is the local turbulence intensity and θ is the momentum thickness. The functions, $F\left(\lambda_\theta,K\right)$, and the streamline acceleration, dU/ds, can be computed as follows [64, 71, 81]:

$$
\begin{aligned}
F_\lambda =& -10.32\lambda_\theta - 89.47\lambda_\theta^2 - 265.5\lambda_\theta^3, \\
F_K =& 0.0962\left(K\cdot 10^6\right) + 0.148\left(K.10^6\right)^2 + 0.0141\left(K\cdot 10^6\right)^3, \\
\frac{dU}{ds} =& \frac{u}{U}\cdot\frac{dU}{dx} + \frac{\nu}{U}\cdot\frac{dU}{dy},
\end{aligned}
$$

This model has been calibrated for use in accordance with the SST turbulence model [64, 71, 81] as follows:

$$
\begin{aligned}
\tilde{P}_k =& \gamma_{eff} P_k, \\
\tilde{D}_k =& min\left(max\left(\gamma_{eff}; 0.1\right); 1.0\right) D_k,
\end{aligned}
$$

where P_k and D_k are the production and destruction terms from the turbulence kinetic energy equation in the original SST turbulence model and γ_{eff} is the effective intermittency [64, 81] obtained from:

$$
\begin{aligned}
\gamma eff =& max\left[\gamma; \gamma_{sep}\right], \\
\gamma_{sep} =& min\left[8.0 max\left[\left(\frac{Re_\nu}{2.193 Re_{\theta c}}\right) - 1; 0\right] F_{reattach}; 5.0\right] F_{\theta t}, \\
F_{reattach} =& exp\left[-\left(R_y/15\right)^4\right],
\end{aligned}
$$

The SST model is modified by using the following blending function [64, 71, 81] f_1:

$$
\begin{aligned}
f_1 =& max\left[f_{1,orig}; f_3\right], \\
f_3 =& exp\left[-\left(R_y/120\right)^8\right], \quad R_y = yk^{1/2}/\mu
\end{aligned}
$$

where $f_{1,orig}$ is the original blending function responsible for switching between the $k-\omega$ and $k-\epsilon$ models.

2.7 Loss mechanisms

The standard means of defining loss is as the result of any flow feature that reduces the efficiency [94]. The most common definition of efficiency is the isentropic definition, which for a turbine compares the actual work output to the isentropic work output (and for a compressor it compares the actual work in to the ideal work in). For a turbine (where station 1 is the inlet and 2 is the outlet),

$$\eta_t \equiv \frac{(h_{01} - h_{02})}{(h_{01} - h_{02s})} \approx \frac{(T_{01} - T_{02})}{(T_{01} - T_{02s})}$$

and for a compressor (where station 1 is the inlet and 2 is the outlet),

$$\eta_c \equiv \frac{(h_{02s} - h_{01})}{(h_{02} - h_{01})} \approx \frac{(T_{02s} - T_{01})}{(T_{02} - T_{01})}$$

This definition implies that only rises in entropy can reduce the efficiency and since entropy is only generated by heat transfer or flow irreversibility, "the only rational measure of loss in an adiabatic machine is entropy creation", Denton [94]. The measurement and computation of entropy should thus be the goal of loss mechanism research. The advantages of using entropy to investigate loss are that it is independent of the frame of measurement and that it can be converted to efficiency if only one other property of state is known:

$$\eta \equiv \frac{1 - \left(\frac{P_{02}}{P_{01}} e^{\frac{S_2 - S1}{R}}\right)^{\frac{\gamma - 1}{\gamma}}}{1 - \left(\frac{P_{02}}{P_{01}}\right)^{\frac{\gamma - 1}{\gamma}}}$$

The disadvantages are that it cannot be measured directly and that only changes

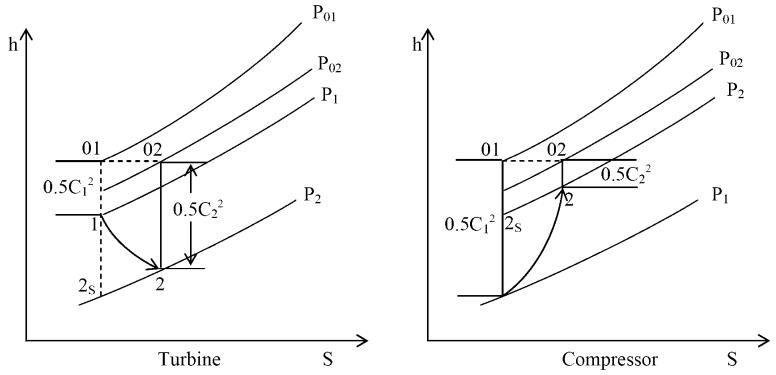

Figure 2.12: Enthalpy-entropy diagram for cascade flow (from [94])

in entropy have any meaning, necessitating the measurement of reference conditions. Using standard thermodynamic relations [95], the fractional changes in two properties of state are required to calculate a change in entropy:

$$\frac{S_2 - S_1}{R} = \left(\frac{\gamma}{\gamma - 1}\right) ln\left(\frac{T_{02}}{T_{01}}\right) - ln\left(\frac{P_{02}}{P_{01}}\right)$$

An entropy loss coefficient [94] can then be defined by

$$\zeta_s \equiv \frac{T_2\,(S_2 - S_1)}{h_{02} - h_2}$$

There are, however, a wide variety of definitions of loss coefficient for a blade row: probably the most common is the stagnation pressure loss coefficient; referring to fig. 2.12 it is defined for a turbine by

$$Y \equiv \frac{P_{01} - P_{02}}{P_{02} - P_2} \tag{2.17}$$

and for a compressor by

$$Y \equiv \frac{P_{01} - P_{02}}{P_{01} - P_1} \tag{2.18}$$

These latter definitions are easy to measure in a cascade, and they are widely

used. They are related to efficiency drop for constant total temperature. This definition of loss coefficient cannot be used for a rotating blade row. A more useful definition for design purposes is the energy loss coefficient [94]. Referring to fig. 2.12, it is defined for a turbine by

$$Y \equiv \frac{h_2 - h_{2s}}{h_{02} - h_2}$$

and for a compressor by

$$Y \equiv \frac{h_2 - h_{2s}}{h_{01} - h_1}$$

where the isentropic final enthalpy, h_{2s}, is the value in an isentropic expansion or compression to the same final static pressure as the actual process.

An additional loss factor is defined as:

$$Z \equiv \frac{P_{01} - P_{02}}{P_{01}} \tag{2.19}$$

where this is the ratio of stagnation pressure drop from inlet to outlet divided by stagnation pressure at the inlet, valid for both compressors and turbines.

There are three fundamental processes that generate entropy, and hence loss: viscous friction, heat transfer and non-equilibrium processes [94]. To provide a clearer physical insight into the flow field, however, loss is more conveniently divided into the various components of the two-dimensional and three-dimensional losses, even though it is often extremely difficult to distinguish between them. Although the three-dimensional losses are much larger than the two-dimensional losses, the two-dimensional losses are much better understood. This thesis describes only two dimensional (streamwise) loss mechanisms. Mass-averaged stagnation pressure loss has been calculated from CFD and compared with the experimental data.

Entropy generation in boundary layers, which will present in the following section, has been calculated for the suction side of the most test cases parallel to the mass-averaged stagnation pressure loss to show how implementations and modifica-

tions inside the surface-curvature direct blade design method affect the aerodynamic performance and surface heat transfer distribution and produce high efficiency turbomachinery blades. Denton [94] mentioned that because of difficulties of predicting transition, separation bubbles and base pressure coefficients the error estimation for two dimensional cascade would be within %20. However, with using the LRN and SST $k-\omega$ transition turbulence models a quantitative estimates of loss for turbine and compressor blades are approximately accurate. These are because of better predicting transition and separation phenomena with the existing two turbulence models than the previous turbulence models. The calculation of mass-averaged stagnation pressure loss from CFD can be briefly described as follows. In FLUENT and ANSYS 12 the mass-averaged total pressure is defined by

$$\bar{P}_t = \frac{\int_A (\rho P_t \mid \overrightarrow{v} \cdot \hat{n} \mid) \, dA}{\int_A (\rho \mid \overrightarrow{v} \cdot \hat{n} \mid) \, dA} \tag{2.20}$$

where $\bar{P}_t$ is the total pressure, A is the area of the inlet or outlet, $\overrightarrow{v}$ is the velocity vector, ρ is the fluid density, and $\hat{n}$ is a unit vector normal to the surface. Then the normalized mass-average pressure loss coefficient can be calculated from the above equations 2.17 and 2.18.

2.7.1 Two-dimensional loss mechanisms

The loss in a two-dimensional flow field through a blade row can be sub-divided into:

1. Boundary layer loss: Generated by shear stresses in the boundary layers.
2. Shock loss: Generated by shock waves in the flow field at high Mach numbers.
3. Mixing loss: Generated by mixing of the flow field behind the blade trailing edge.

2.7.1.1 Boundary layer loss

Entropy is generated in a boundary layer due to shear stresses acting on the flow: this process is effectively a conversion of viscous shear work into heat [94]:

$$\dot{S} = \int_0^{\delta} \frac{\tau}{T} \frac{dV}{dy} dy \tag{2.21}$$

Most of the entropy generation thus occurs in the inner part of the boundary layer where the shear stress is largest: in turbulent boundary layers most of the entropy is generated in the viscous sublayer and turbulent wall region.

2.7.1.2 Shock loss

Entropy creation in a shock wave is due to heat conduction and high viscous normal stresses, which occur within a thickness of a few molecular paths. For weak normal shock waves the corresponding entropy rise [96] is

$$\frac{S_2 - S_1}{R} \approx \frac{2\gamma}{3\left(\gamma + 1\right)^2} \left(M_1^2 - 1\right)^3 \tag{2.22}$$

giving a very small entropy rise a cross a weak shock. Denton [94] mentioned that this equation is equally applicable to oblique shock waves when provided Mach number is interpreted as the component of Mach number perpendicular to the shock front.

2.7.1.3 Mixing loss

Any shear stress in a flow generates entropy: boundary layer loss is caused by shear stress in the boundary layer and mixing loss by the shear stress that occurs when two flows mix together. For two-dimensional flows, mixing usually only occurs in the wake or when boundary layers separate from the blade surface [94]. Although it is only a relatively short-lived phenomenon as the flow eventually mixes out completely, it is a major contributor to the total loss, since it is normally associated with turbulent flows where the effective viscosity is very large. In particular, at high

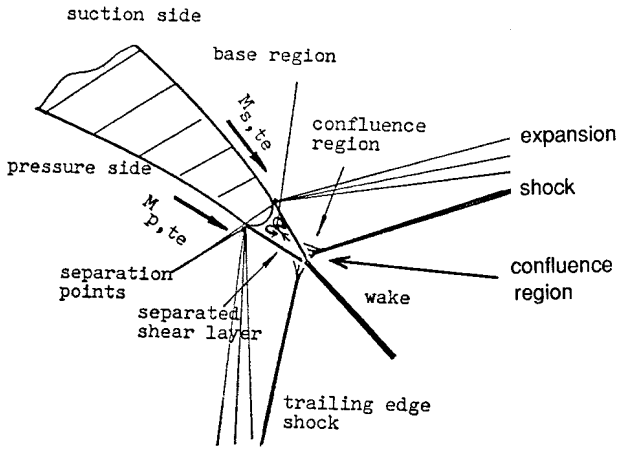

Figure 2.13: Structure of supersonic trailing edge flow (from [97])

Mach numbers the intense viscous dissipation immediately behind the trailing edge generates considerable entropy, Figure 2.13.

Just behind the trailing edge, there is a small, roughly triangular, region of approximately uniform pressure, termed the base pressure. Shear layers where the velocity rises rapidly up to the freestream value surround this region and expansion waves, caused by the change in flow direction, begin at the points where the flow separates from the blade surface. The confluence region occurs where the flows from the suction and pressure surfaces meet: the changes in flow direction generate shock waves if the flow is supersonic. Although it is difficult to quantify the local entropy generation, a control volume approach can be used quite successfully to calculate the total mixing loss, since mixing always results in uniform flow conditions. Numerical predictions should thus also be relatively accurate, since they are based on the same conservation equations. A theoretical incompressible model [94] has been developed to predict the mixing loss coefficient as follows:

$$\zeta = -\frac{C_{pb}t}{w} + \frac{2\theta}{w} + \left(\frac{\delta^* + t}{w}\right)^2 \tag{2.23}$$

The base pressure coefficient, C_{pb}, incorporates the effects of the region of very low pressure directly behind the trailing edge and is approximately 0.1 to 0.2. The other terms are due to the mixing of the boundary layer and the combined blockage

of the trailing edge thickness and the boundary layer.

In this work, entropy generated inside the boundary layer has only been evaluated by the above equation 2.21 and graphically presented for most of the suction side test cases. It is clear from our calculation how the PSCD blade design method contributes to decrease the entropy generation inside the boundary layer and as result less mass-weighted average stagnation pressure loss and high efficiency blades can be achieved.

2.8 Surface-curvature and surface-velocity distributions

According to previous published work [2–9] it is clear that the surface curvature as well as the slope of curvature of the blade surface has a dominant effect on boundary layer characteristics and overall aerodynamic and heat transfer performance of the blade. The theoretical and experimental impacts of their effects are described in the previous publications, and are summarized below.

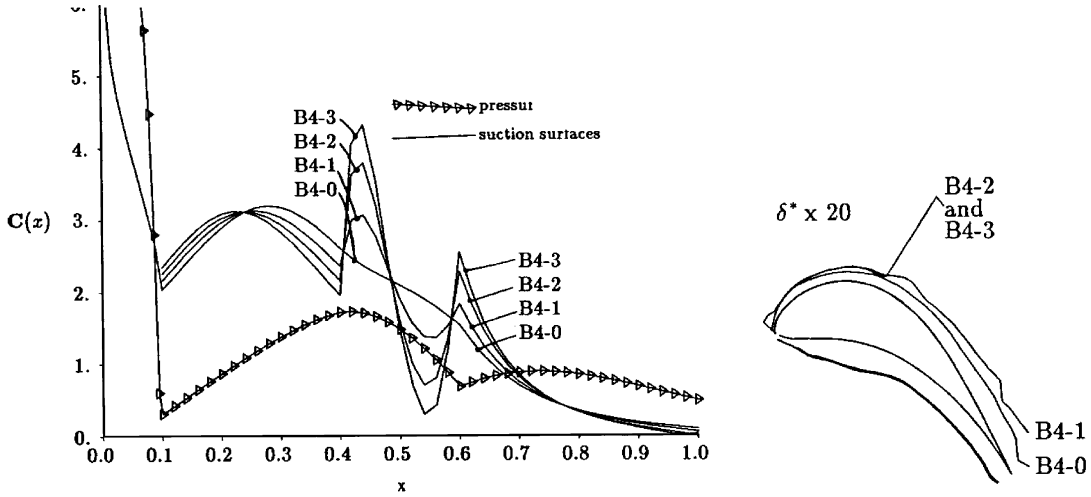

Figure 2.14: Performance of typical turbine cascade; Left, surface-curvature distributions. Right, boundary-layer displacement thickness (freestream turbulence 15%) (from [5, 12])

2.8.1 Theoretical evidence

Applying the compressible-flow Navier-Stokes equations to the limiting case of cylindrical co-ordinates (r, θ, z), results in equations that clearly show that the flow depends on the curvature distribution of the flow, which on the blade surface is equal to the curvature of the blade surface. This leads us to concentrate on the effects of surface curvature distribution.

Before the role of surface curvature distribution on the design of the blade has been explained, the equations of mass and momentum in polar coordinates (r, θ) are presented, which show how the local radius (i.e. radius of curvature) affects the turbomachinery blade performance via its effects on the behavior of the boundary layer. This same curvature distribution is useful in the stacking of 2D designs in the generation of the 3D geometry. The following equations are taken from [5, 98]:

$$\frac{\partial \rho}{\partial t} + \frac{1}{r}\frac{\partial}{\partial r}(\rho r C_r) + \frac{1}{r}\frac{\partial}{\partial \theta}(\rho C_\theta) = 0$$

$$\rho\left(\frac{\partial C_r}{\partial t} + C_r\frac{\partial C_r}{\partial r} + \frac{C_\theta}{r}\frac{\partial C_r}{\partial \theta} - \frac{C_\theta^2}{r}\right) = -\frac{\partial p}{\partial r} - \left(\frac{1}{r}\frac{\partial}{\partial r}(r\tau_{rr}) + \frac{1}{r}\frac{\partial \tau_{r\theta}}{\partial \theta} - \frac{\tau_{\theta\theta}}{r}\right) + \rho g_r$$

$$\rho\left(\frac{\partial C_\theta}{\partial t} + C_r\frac{\partial C_\theta}{\partial r} + \frac{C_\theta}{r}\frac{\partial C_\theta}{\partial \theta} + \frac{C_r C_\theta}{r}\right) = -\frac{1}{r}\frac{\partial p}{\partial \theta} - \left(\frac{1}{r^2}\frac{\partial}{\partial r}\left(r^2\tau_{r\theta}\right) + \frac{1}{r}\frac{\partial \theta\theta}{\partial \theta}\right) + \rho g_\theta$$

where r and θ is the local curvature and angle of the point on the blade surface, and p is the static pressure.

There are similar equations for incompressible flow [12] in cylindrical co-ordinates and it is clear that the incompressible flow is dependent on the local radius (i.e radius of curvature). In the above equations, both terms $\frac{1}{r}$, and $\frac{1}{r^2}$ show that there are strong relationships between local pressure, velocity distribution and local curvature. In the blade geometry C_u and r are functions of blade length, for instance along b_x or c. The above equations imply that in order to control C_u as a function of length one must control r as a function of length. The experimental and numerical evidence from blade designs presented later in this work further justify this assertion.

Turbine blade performance depends on the behavior of the boundary layer. The boundary layer behavior of the flow is affected by the surface discontinuities and the slope of velocity distributions. Korakianitis [5] indicated that the boundary layer and its behavior are affected by local radius r of the surface. It means that smooth velocity distributions along the surface of the blade require smooth surface-curvature distribution (continuous slopes of velocity and slopes of curvature along the blade surface). Slope of curvature continuity means that the surface curvature C, as well as its slope along axial distance x, $C' = dC/dx$ along the blade profile length, must both be continuous. This requires continuous third derivatives of the splines $y(x)$, i.e. continuous $y''' = d^3y/dx^3$, as illustrated in the previous equations for curvature and its slope (2.5, 2.6).

2.8.2 Experimental evidence

The blade designer has a lot of freedom to choose among many methods to describe the blade surfaces, for instance cubic, B-splines, Bezier splines etc. Among all this methods it is important to choose ones that have continuity of first, second and third spline derivatives at the spline knots. The continuity in the slope of curvature at the knots of those lines result in smooth surfaces of the blade, as well as smooth Mach number and pressure distributions along the blade surface. Generally, there are two types of discontinuities for the curvature [12]. The first one comes from the surface roughness and fouling that would affect the performance of the blade but with which the turbine must operate. The second one is the slope of curvature discontinuity which comes from the joint points between the segments of the blade surfaces. This curvature-discontinuity problem causing aerodynamic problems is evident in the tested performance of several blades published in the open literature. These curvature discontinuities result in unexpected local perturbations in surface Mach number and pressure distributions, which give rise to unexpected variations in local blade loading, and to local separation bubbles or increased-loss regions. The

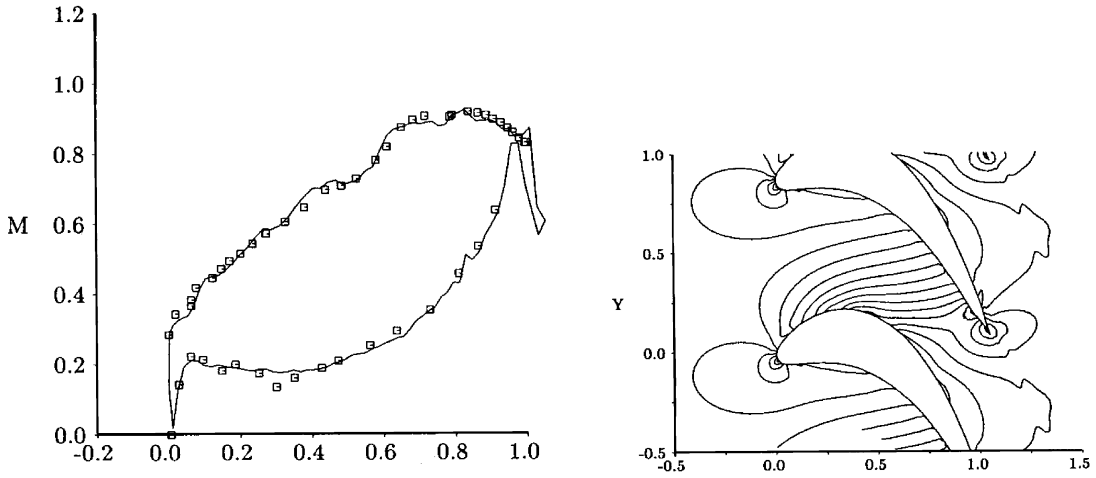

Figure 2.15: Tested and computed Mach-number distributions: a- Surface Mach number distributions, b- Computed Mach number contours (increment 0.05) (from [6, 12])

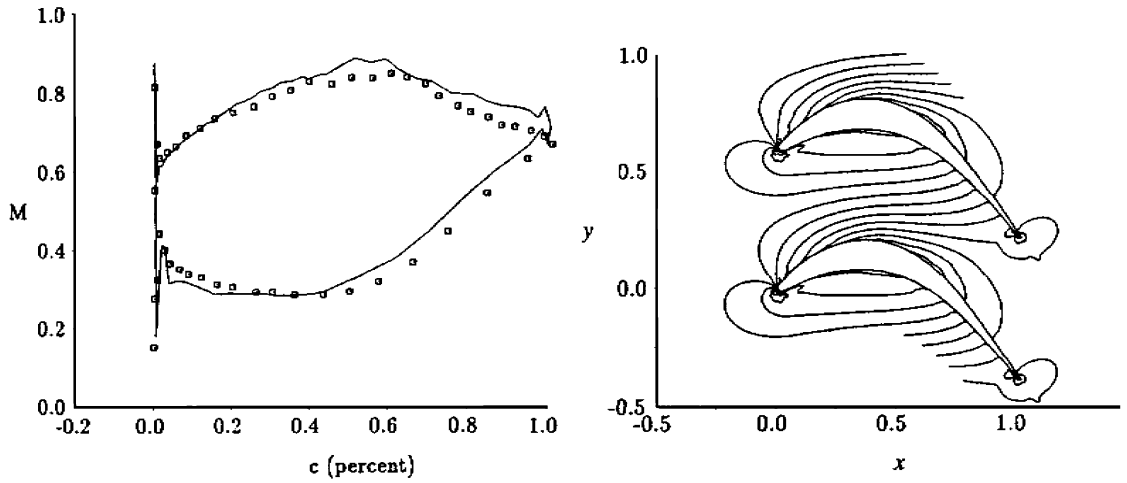

Figure 2.16: Effect of curvature discontinuity caused by the leading edge circle. Tested and computed Mach number distributions for HD turbine cascade (from [6, 12])

curvature discontinuities on the blade surfaces are invisible to the eye, as shown in the blade geometries in Figure 2.14 and produce unusually loaded blades and thicker wakes. Figure 2.14 has illustrated that the curvature distribution is a "mirror" of the Mach number distribution. Any small change in the value of the curvature affects the value of the surface Mach number distribution around the blade. These are the reasons to use the blade surface curvature distribution as a controller of the local Mach number distribution in the prescribed-curvature direct blade-design method.

In addition, the resulting design method is more flexible than the inverse design method.

Experimental data published in [99–105] clearly indicate local kinks in the surface pressure or Mach number distribution of blades, which, as will be illustrated later, is the result of surface curvature discontinuities. These "kinks" affect boundary-layer performance and blade efficiency, and they could be solved by blade design methods with slope of curvature continuity at the spline knots. There are several experimental [36–38, 99, 106] and several computational [2, 8, 27, 35, 105] works that explain how the curvature distribution affects the aerodynamic properties around the blade, illustrated in figures 2.15 and 2.16. (The same two sample cases are used in the following). The work in this thesis confirmed that the discontinuity in the surface curvature has a significant effect on the blade performance and the overall efficiency of the engine. The discontinuity between the circle and the rest of the blade still exist [105] in most of blade geometries that using direct and inverse methods, but this thesis found a unique solution for this problem and produce high efficiency blades for turbomachinery and wind turbine airfoil for the first time.

2.9 The 2D PSCD blade design method

2.9.1 Introduction

There are a number of key issues that need to be addressed in the design of blade geometries that affect the choice of implementation methods. The first issue is the flexibility of any revised method to represent a wide range of different blade shapes, and ability to work on other similar shapes such as turbine, compressor, fan and wind turbine blades. The second issue is the accuracy or the optimizing objective functions which must be compared with experimental data. The accuracy should be accounted for in both geometric and aerodynamic sense. Methods using fewer variables may not be capable of generating blade shapes with high accuracy. For

example the only major defining parameters in the inverse design method is the pressure distribution or velocity distribution to design blade geometry. However, in direct design method there are many major defining parameters of choice to design the blade geometry. Therefore, the direct design method is more flexible than the inverse design method.

The original publications on the PSCD blade design method had used Euler solvers and therefore the blades were designed with pointed or cusped trailing edges [2–7]. Later the method was modified to include leading and trailing edge circles or ellipses [8, 9]. In this thesis:

1. the description of the leading and trailing edge shapes has been modified to simplify the design of airfoils with inlet flow angles around 0°;

2. the exponential polynomial functions connecting the blade surfaces with the leading and trailing edge circles are similar but modified functions to those presented in [8]; and

3. the number of Bezier points describing the main part of the blade surface has been increased from four to six, allowing additional flexibility.

The following subsections use material from [2–9] and summarize the PSCD blade design method. The suction and pressure surfaces are separated into three major segments: the segment near the trailing edge; the main part of the blade; and the segment near the leading edge. The first segment is joined to the trailing edge shape (circle or ellipse or other shape. The last segment is joined to the leading edge shape (circle or ellipse or other shape. The method is summarized below. The method has been illustrating by the redesign of the Hodson-Dominy (HD) [37] and Kiock [107] blades, and others in the following chapters. The HD redesign case illustrates removal of the suction and pressure surface leading edge separation bubbles [27, 37, 104]. These are illustrated in the figures 2.17 and 2.18.

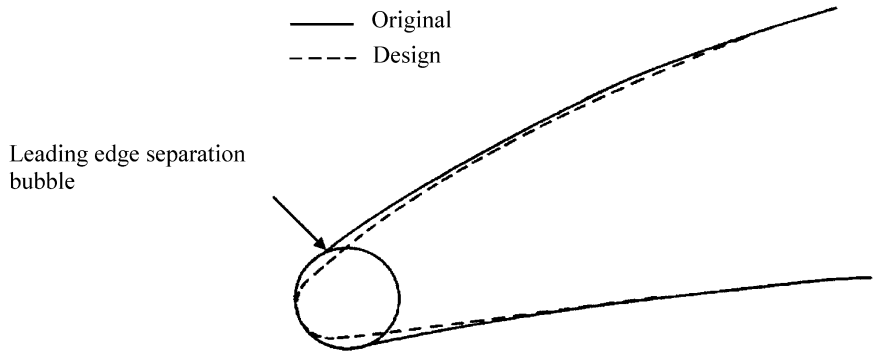

Figure 2.17: Change in blade shape to resolve leading edge spike (from [27])

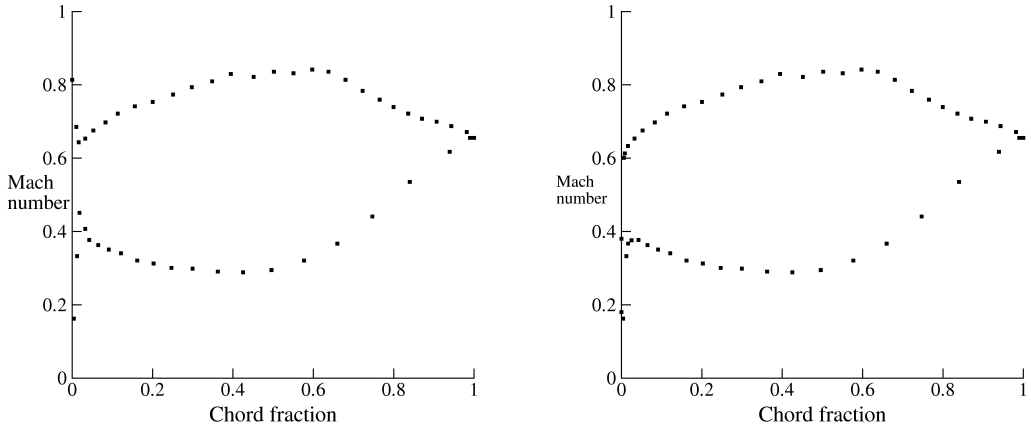

Figure 2.18: Mach number distributions for HD and redesign of the blade with inverse method including spikes, dips (from [27])

2.9.2 Trailing edge thickness - the trailing edge circle

The trailing edge thickness assumes that a trailing edge circle is used, though any other shape can also be implemented. The radius of the circle, r_{te}, is an important parameter in the blade design process. Usually, the radius should be around 1-2 % of the blade length. The location of the center of the trailing edge circle is determined by two lines: one is the vertical line when $b_x = 1$; and the other is the chord of the blade, which is described as a straight line from the origin (0,0) with a stagger angle λ to the x-axis (fig. 2.19). The stagger angle is an input parameter, and in our convention it has a negative value. The value of the stagger angle dictates the distribution of the turning of the flow along the passage and the distribution

of aerodynamic loading along the blade [5]. The trailing edge circle is made to be tangent to both of these lines, and it has a radius of r_{te},

$$x_{tc} = b_x - r_{te}$$

$$y_{tc} = b_x \tan\lambda + \frac{r_{te}}{tan\left(\frac{\pi}{4} + \frac{\lambda}{2}\right)}$$

where b_x stands for the non-dimensionalized axial blade length, $b_x \equiv b/X = 1$.

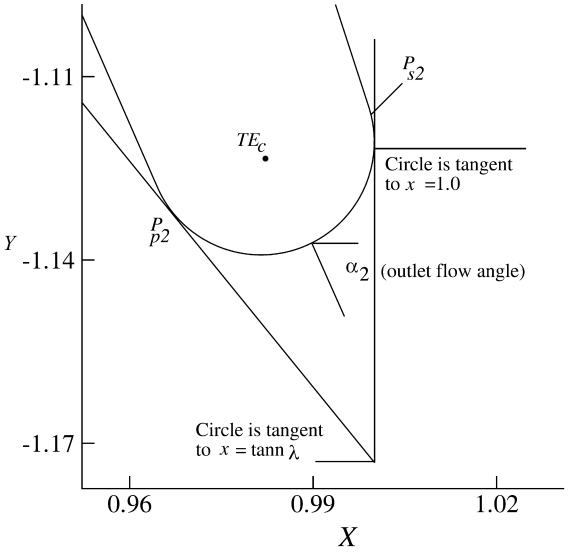

Figure 2.19: The nominal stagnation point on the trailing edge which is from outlet flow angle

Figure 2.19 shows two points (P_{s2} and P_{p2}) and two local angles around the trailing edge circle: point P_{s2} is the point joining the circle and the trailing edge suction side of the blade; β_{s2} is a local angle for the trailing edge suction side; P_{p2} is the point joining the circle and the trailing edge pressure side; and β_{p2} is a local angle for the trailing edge pressure side. These local angles are used to control the wedge angles of the trailing edge of the blade.

The point P_{s2} is specified by an equation which includes the local angle β_{s2} and the trailing edge radius r_{te}. The angle β_{s2} is given as an input parameter, and it is associated with the outlet flow angle α_2. Generally, the value of β_{s2} is around (5-8)^o less than the value of the outlet flow angle α_2. This gives the direction for the first guess of the value of β_{s2}. The end of the trailing edge circle can be calculated as follows,

$$x_{s2} = x_{tc} + r_{te} \sin(-\beta_{s2})$$

$$y_{s2} = y_{tc} + r_{te} \cos(-\beta_{s2})$$

where β_{s2} is the local angle, and conventionally has a negative value. Once the center of the circle and the beginning/end points are determined, the trailing edge circle can be constructed as follows,

$$x_i = x_{tc} + r_{te} \cos(\theta_i)$$

$$y_i = y_{tc} + r_{te} \sin(\theta_i)$$

where θ_i is a local variable and $0 < \theta_i < \beta_{s2}$, and this angle is used to manage the shape of the blade near the trailing edge. The thickness of the blade around the trailing edge depends on the trailing edge radius and the local angles. To specify the other point P_{p2} on the pressure side of the blade, the above equation is also used, but it includes different value of local angle which is β_{p2}. The angle between β_{p2} and β_{s2} is usually around (6-10)^o .

Since the curvature of a circle is the reciprocal of its radius at every point on the circle, the curvature in the trailing edge circle is a constant, and becomes

$$C = \frac{1}{r_{te}}$$

2.9.3 Trailing edge polynomial (y_3)

The suction-side trailing-edge segment is from the trailing-edge circle to the throat of the passage, where at the throat the location of the point and slope of the suction surface line at that location is used. For the pressure surface there is no corresponding guiding throat location, so a geometrically-sensible point and its slope are prescribed on the (x, y) plane of the blade. The pressure-side trailing-edge segment is from the trailing-edge circle to the pressure-surface point described above. Essentially these two suction and pressure line segments, the blade-surface "departing" angles from the trailing edge circles, and the throat and pressure points and their slopes chosen as inputs, prescribe the trailing-edge region "wedge" angle of the blade, and it's thickness for manufacturing and stress considerations.

The specification of the trailing edge segment of the blade, from the throat point to the trailing edge circle, is crucial in minimizing flow diffusion in this "unguided" (by a pressure-surface shape on the opposite side of the passage) flow region. Less deceleration (diffusion) means better designs. If the flow decelerates too much, then the blade wake will be thicker, the boundary layer may separate, and the resulting blade shape will have poorer performance (lower efficiency). The trailing edge suction side is controlled by the throat diameter o. A first approximation [12] is

$$\frac{o}{S} = \cos \alpha_2 \tag{2.24}$$

but various approximations from Ainley-Mathieson data have also been used. In the present study the data from the equation in [12] has been used to specify the throat of the blade for the direct blade design method.

In the 2D design, the throat diameter o is calculated by an input parameter of throat/chord (o/S), the tangential lift coefficient (C_L), inlet flow angle α_1, and outlet flow angle α_2:

$$\frac{S}{b} = \frac{C_L}{2\cos^2 \alpha_2 \left(\tan \alpha_1 - \tan \alpha_2\right)} \tag{2.25}$$

where C_L is the tangential lift coefficient and its value is determined by the number of the blades in the annulus. Wilson and Korakianitis [12] pointed out that tangential lift coefficient typically is between 0.8 and 1.2. In the early blade designs the value of tangential lift coefficient was low, but in modern cascades the value of C_L has been gradually increasing. Design of high efficiency cascades are difficult with keeping both high value of tangential lift coefficient, C_L, and high values of deflection ($\alpha_1 - \alpha_2$) in blades.

The parameter b_x is used to specify the blade length, and for a non-dimensional blade $b_x = 1$. The subscript 1 denotes parameters of the inlet flow and 2 denotes those of the outlet flow.

Figure 2.20 explains the relationship between the trailing edge suction side and the point of P_{p2} on the neighbouring blade on the other side. Once the control

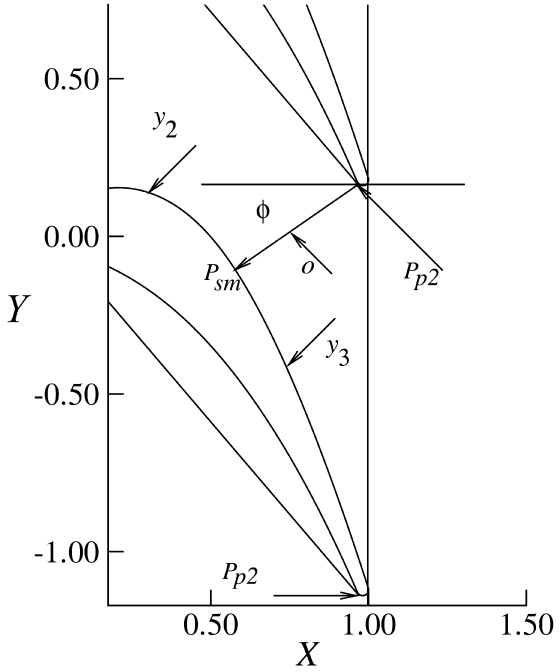

Figure 2.20: Relationship between the throat o parameter and the neighbouring blade

circle diameter o is determined, and the value of the angle ϕ is read as an input, we are able to calculate the end of the polynomial, point P_{sm}. The start point of the diameter, where the throat is drawn, can be located at point P_{p2} (Fig. 2.20) of the neighbouring blade. The value of the point P_{sm} is obtained by

$$x_{sm} = x_{p2} - o\cos\phi$$

$$y_{sm} = (y_{p2} + S) - o\sin\alpha$$

The above formula is shown that the coordinates of the point P_{p2} on the neighbouring blade are given as $(x(P_{p2}), y(P_{p2}) + S)$. These specify the last point of the trailing edge suction side, P_{sm}. Thus, the start point and end point of the trailing edge polynomial, P_{s2} and P_{sm}, have been specified. Continuous slope of curvature requires continuous third derivative as illustrated in the equations in [4–8].

The trailing edge region of the blade, between points P_{s2} and P_{sm} in fig. **??**, is specified by a polynomial function of the form:

$$y_3 = a_0 + a_1x + a_2x^2 + a_3x^3 + a_4x^4e^{k_1}\left(x - x(P_{s2})\right) + a_5x^5e^{k_2}\left(x - x(P_{s2})\right)$$

where the polynomial parameters are evaluated from the conditions of point and first derivative continuity at P_{sm}; and point, first, second and third derivative con-

tinuity at P_{s2}. With the exponential terms, the effects of $a_4 e^{k_1 (x - x(P_{s2}))}$ and $a_5 e^{k_2 (x - x(P_{s2}))}$ in the polynomial formula over most of the length of y_3 are negligible. The exponential terms do not significantly differentiate y_3 from a third-order polynomial except near the trailing edge circle (near point P_{s2}).

The procedure is similar on the pressure side polynomial, between the trailing edge circle and point P_{pm}. Instead of throat diameter and blade angle at throat diameter (point P_{sm}), the user specifies the (X, Y) location and the blade surface angle at point P_{pm}.

2.9.4 Main curvature-mapped part of the blade (y_2)

The main part of the blade is the mid portion of the surface that connects the trailing and leading edge segments of the blade. As in the previous approaches in [4–9], Bezier splines have been used to prescribe the surface curvature of this part of the blade. The original PSCD code used four points on the Bezier curve; and in this work it has been modified to use six points on the Bezier curve. Bezier curves are optimal from the point of view of geometric modeling aiming to control the inner location of the points and the degree of its differentiability [35, 57, 108–110]. The surface-curvature distribution of this part of the blade is prescribed as shown in the example of fig. 2.21, where the example shown the curvature of the main part of the blade is controlled by a five-segment Bezier curve controlled by the six control points $C_{1s}, \ldots C_{6s}$. The blade surface points on the (x, y) plane are derived from the prescribed curvature points in the (C, y) plane, where the latter is illustrated in fig. 2.21.

From the trailing edge polynomial, y_3, the curvature and slope of curvature at point P_{sm}, where the main part y_2 of the blade begins, are determined. The six-point Bezier curve ($C1s$ to $C6s$) prescribes the curvature distribution C_s of the suction surface. An iterative method is used to compute each successive (X, Y) point on the blade as described in [4–9]. The iterative process starts from blade point P_{sm}

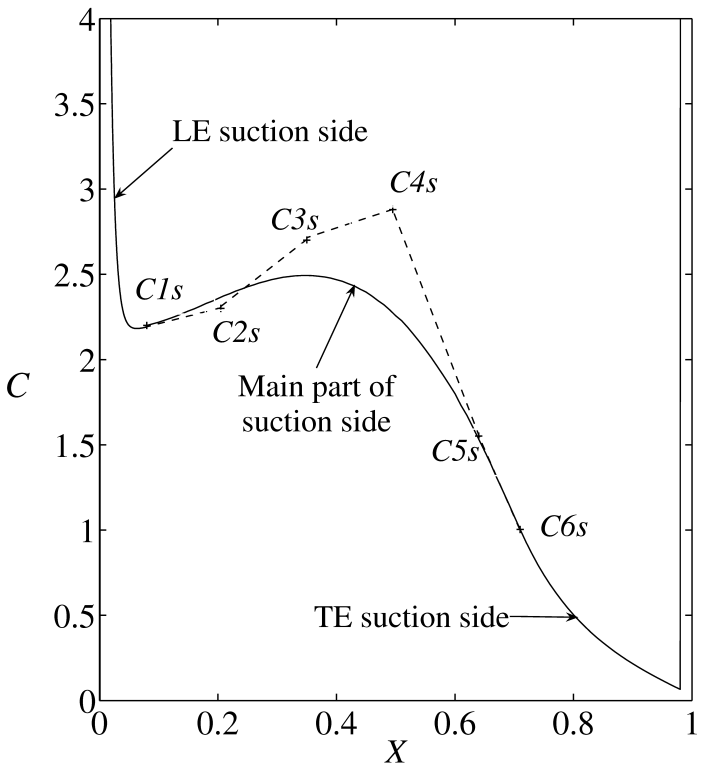

Figure 2.21: Sample of curvature distribution of the whole suction side of the blade.

and ends by calculating blade point P_{sk} (fig. 2.22, i.e. throughout segment y_2.

2.9.5 The leading edge circle and front part of the blade (y_1)

These are illustrated in figures 2.22 and 2.23. Any consistent shape can be used at the leading edge. Some manufacturers use circles, other ellipses, and others use different shapes. Without loss of generality, the PSCD blade design method uses a leading edge circle, which is the most constrained case. The PSCD method initially used a thickness distribution around a construction line [2–7] and later used a leading edge circle and a construction line [8, 9]. In this thesis the parabolic construction line (related to the the leading edge circle and the front part of the blades y_1) has been modified to simplify the design of blades with inlet flow angles around 0°.

The radius of the leading edge circle r_{le} is an input parameter, and has the most important effect on the leading edge shape. Normally, r_{te} is between (2-5) % of the blade length. Larger radius gives a relatively fat blade, sometimes favored in US and

UK designs; while blades designed with a small radius become thinner, sometimes favored by German designs. The center of the leading edge circle is determined by the blade stagger angle and the vertical line drawn at $x = 0$. The center of the leading edge circle is at:

$$x_{lc} = r_{le}$$

$$y_{lc} = \frac{r_{le}}{tan\left(\frac{\pi}{4} + \frac{\lambda}{2}\right)}$$

Figure 2.22 illustrates the following parameters: the specified points on the circle, P_{s1} and P_{p1}; the local angles, β_{s1} and β_{p1}, which are used to control the inlet wedge angle; the stagger angle, λ; and the leading edge segments y_1 for the suction and pressure sides.

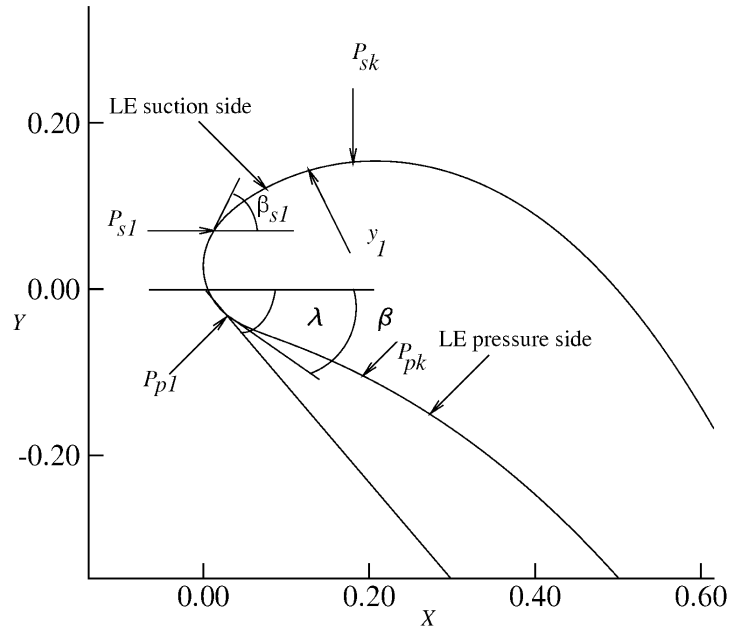

Figure 2.22: Some parameters near the leading edge of the blade

The local angle βs_1 is determined where the circle and the polynomial y_1 meet each other. It is again the tangential relationship that determines the joint point between the circle and the leading edge polynomial, named as point P_{s1}.

$$x_{s1} = x_{lc} - r_{le} \sin(-\beta_{s1})$$

$$y_{s1} = y_{lc} + r_{le} \cos(-\beta_{s1})$$

After obtaining the point P_{s1}, the leading edge circle shape can be constructed

by the following equations,

$$x_i = x_{lc} + r_{le}\cos(\theta_i)$$

$$y_i = y_{lc} + r_{le}\sin(\theta_i)$$

Similarly, point P_{p1} on the pressure side of the circle can be determined by the tangential relationships between the circle and the leading edge pressure side.

Blade segments y_1 on the suction and pressure sides affect significantly the aerodynamic and heat transfer performance of the blade; the result is significantly affected by small changes in the blade shape. Joining the leading edge circle or other shape to the main blade results in flow separation bubbles, and local accelerations and decelerations in the pressure and Mach number distributions. All blade geometries designed by both direct and inverse design methods (e.g. [28, 105, 111, 112]) have difficulties around this area.

In the present PSCD method a mixture of the previous approaches has been used. This involves a parabolic construction line similar to [2–6] coupled to a leading edge circle of [8, 9]. This PSCD approach has removed the leading-edge separation-bubble difficulties of other blade design methods.

The thickness distribution y_1 from the joint with the leading edge circle (point P_{s1}) to the joint with line segment y_2 (point P_{sk}) is given by a thickness distribution d around a parabolic construction line of the form:

$$\begin{aligned} d =& a_0 + a_1 x + a_2 x^2 + a_3 x^3 + a_4 x^4 e^{k_1 (x - x_{s1})} + \\ & a_5 x^5 e^{k_2 (x - x_{sk})} + a_6 x^6 e^{k_3 (x - x_{s1})} + a_7 x^7 e^{k_4 (x - x_{sk})} \end{aligned} \tag{2.26}$$

where thickness d is added perpendicularly to the parabolic construction line, in the manner described in [2–6]. This thickness distribution is essentially a third order polynomial, which is significantly affected by the exponential terms near points P_{s1} and P_{sk}. The eight polynomial coefficients are determined by the conditions of point, first, second and third derivative continuity at points P_{s1} and P_{sk}.

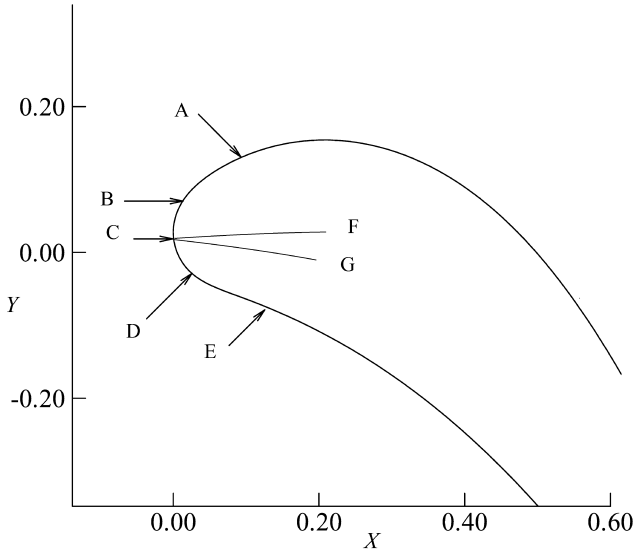

Figure 2.23: Leading edge circle, leading edge suction and pressure surfaces of the blade and construction lines. A= Leading edge suction side, B= Point P_{s1}, C= Starting point of construction line, D= Point P_{p1}, E=Leading edge pressure side F= Construction line for suction side, G= construction line for pressure side

The procedure is similar for the pressure side of the blade.

2.9.6 Procedures of the executable program

The method, used to describe all parts of the blade, has been discussed in the above sections. The code, in its executable form, has been written in an easy way for designers to make their own blades. The program requires only the input file, which consists of blade geometric and flow parameters such as inlet and outlet flow angles, stagger angle and so on. The steps to design blade segments are named after each part of the blade: trailing edge suction surface; main part suction surface; leading edge suction surface; trailing edge pressure surface; main part pressure surface; leading edge pressure surface. The blades are constructed one line after the other in sequence, or all together, which gives the designer more flexibility to change any parameter at any stage.

2.9.7 Validation, reproduction and redesign with the PSCD blade design method

A common aerodynamic shape design problem is the reproduction of an existing turbomachine airfoil to improve its performance. Aerodynamic shape redesigned for an existing blade requires that a number of constraints are enforced. These constraints are as follows. The original and new blades should have the same axial chord, so that they may fit into the existing turbomachine. The inlet and outlet flow angles should be the same in the reproduction blade as in the original one, otherwise the velocity triangles will not match with the neighboring blade rows. The mass flow rate through the new blades must be the same. Finally, the spacing between the blades must be kept fixed to give the same total number of blades. In this thesis, firstly, the Hodson-Dominy [37] blade has been reproduced, and then the same blade has been redesigned with the direct design method, which will be discussed in details in chapter 3, to improve its performance. The performance of sample turbine blades has been evaluated with the inviscid and viscous steady version of FLUENT software. The accuracy of the computations was checked by comparing the results of the Navier-Stokes computations with two test cases of known output. The first case was a comparison of inviscid and viscous computations with the experimental results from the subsonic turbine cascade obtained at Cambridge University by Hodson and Dominy [36–38]. For this case the inlet Mach number 0.496, the exit Mach number 0.710, the inlet flow angle 38.8° and the outlet flow angle -53.5° were used. Mesh generator GAMBIT and flow solvers (FLUENT and ANSYS12) have been used in the computations. A reasonably high number of computational mesh elements is required for reasonably accurate calculations. The exact numbers depend on the geometry of the blade and its model. The mesh elements used for the HD and I1, I4 and I9 blades are: 19,705 quadrilateral cells; 38,967 2D interior faces; and 20,148 nodes for all zones. A 2D O-mesh and a Pave-unstructured mesh have been used in the viscous calculations. The Pave mesh consisted of a combination

of structured and unstructured regions. The mesh around the airfoil consisted of twelve structured clustered O-grid layers with y^+ less than 5 (quadrilaterals), and the remaining majority of the flow field was descritized with quadrilateral and a small numbers of triangular cells. The $k-\omega$ SST transition turbulence model has been used to calculate aerodynamic blade performance. The experimental data was taken from the Stow [27]. The PSCD blade design method has been used to reconstruct the original blade which is called I1 blade. The results, shown in figs. 2.24, indicate very good agreement between the experimental data and computations for the HD and I1 blades. Hodson has analyzed the experimental data to show the leading-edge laminar separation bubbles on both surfaces, caused by blending a leading-edge circle with the rest of the blade. The numerical solution predicts the leading edge surface Mach number spikes. This thesis confirmed that these difficulties around the leading edge of the original blade is a function of the discontinuity in the surface curvature. The spikes and dips are also exist around the reproduction blade. These spikes and dips in the surface Mach number distribution are removed and discussed in details in the following chapters.

The results shown in fig. 2.25, indicate excellent agreement with experiments. The experimental results have been transformed from data along percentage of chord c to data along percentage of axial chord b, along x. The numerical solution shows the local kinks in different position on the suction and pressure surfaces. The figure 2.25 confirmed that removing the discontinuity in the surface curvature is essential not just between the circle and the rest of the blade but for the entire surface of the blade.

The second test case is a comparison of viscous computations with experimental results from the subsonic turbine cascade obtained at DFVLR Braunschweig by Kiock et al. [107]. For this case the inlet Mach number 0.260, exit Mach number 0.782, the inlet flow angle 30° and outlet flow angle -67.33° were used. The same type and detail of grid as for the above HD case has been used. The ability of the PSCD method was again tested to design blade geometries of the original and

redesigned S1 blades as shown in figure 2.26. With very small changes in some parts of the blade, which is not obvious to the eye, there are significant changes in aerodynamic performance, such as removing spikes and dips in the surface Mach number distribution along the blade surface.

Figure 2.27 shows the surface curvature distributions for the original blade (jagged line, evaluated numerically from the original data points) and the curvature distribution for the redesigned S1 blade. The surface curvature distribution for the redesigned S1 blade is much smoother than the original blade. The spikes and dips in the surface Mach number were completely removed as shown in fig. 2.28 (a).

Mach contours for the original and redesigned S1 blades have been shown in figure 2.29. From these figures, it is obvious how the surface curvature plays an important role to produce high smoothness of surface Mach number distribution which resulted in producing high efficiency blades. This improvement is hard to achieve with the rest of the turbomachinery blade design method in the open literature. The boundary layer of the flow around both design and redesign, S1, blades have been analyzed to show how much surface curvature contributes to the improvement of the aerodynamic blade performance such as pressure distribution or surface Mach number distribution. This parameter, δ^*, was obtained using the compressible form of the appropriate expression or integral. Figure 2.28 (b) shows the comparison between the displacement boundary layer calculations, δ^*, for the original and redesign S1 blades. The results showed that the boundary layer of the original blade is thicker than the redesigned S1 blade and this results in producing more losses inside the boundary layer. Figure 2.30 shows the computed rate of total entropy creation in the blade boundary layers on the suction side of the original and redesigned S1 blades using equation 2.21 (from [94]), indicating that the thicker boundary layer the more entropy is generated. This improvement in the surface boundary layer distribution contributes to decrease of the mass-averaged stagnation pressure losses. The mass-weighted average stagnation pressure loss for the Kiock blade is 0.0134; and for the S1 blade is 0.00967.

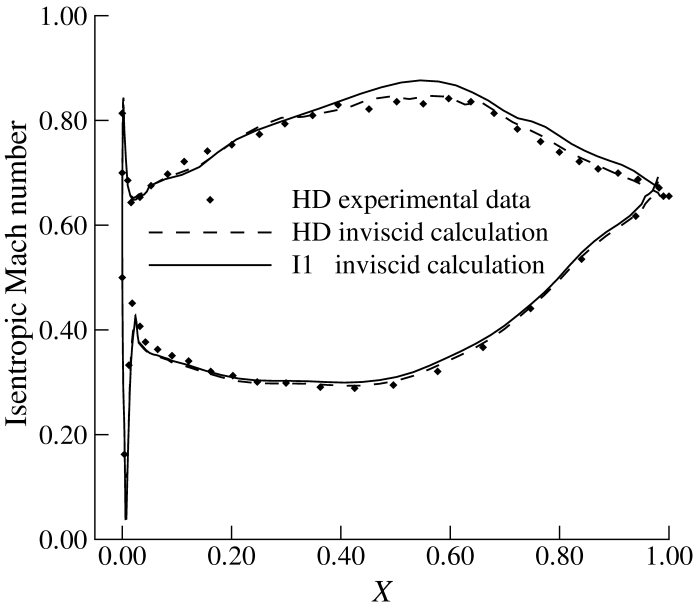

Figure 2.24: Isentropic Mach number test results for both of the original and reproduced HD blade

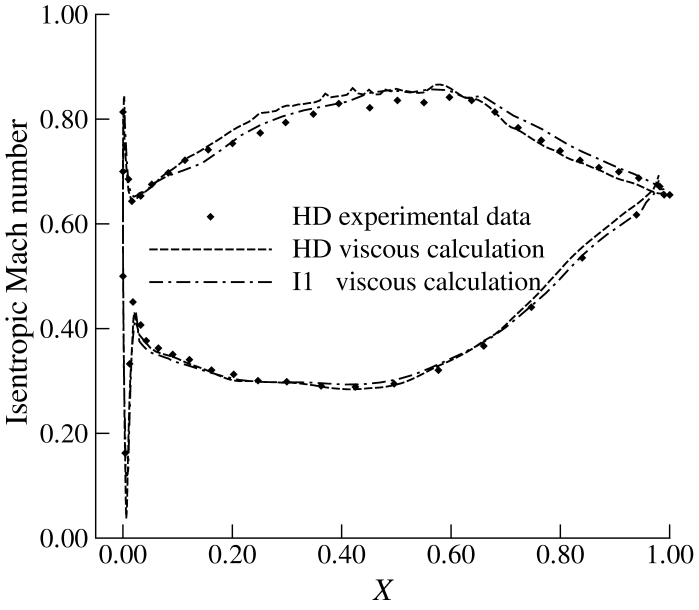

Figure 2.25: Isentropic Mach number distributions from viscous calculations for both the HD and reproduced blades

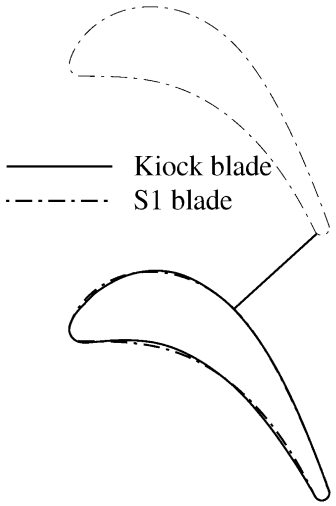

Figure 2.26: Blade geometries for the original cascade (from [107]) and redesigned S1 blade

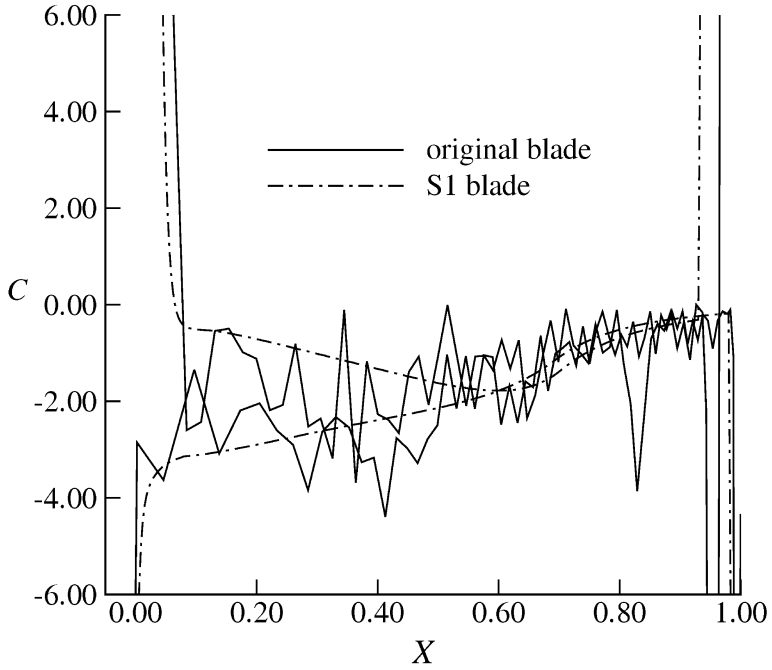

Figure 2.27: Surface curvature distributions for the original cascade investigated by Kiock (from [107]) and reproduced S1 blade

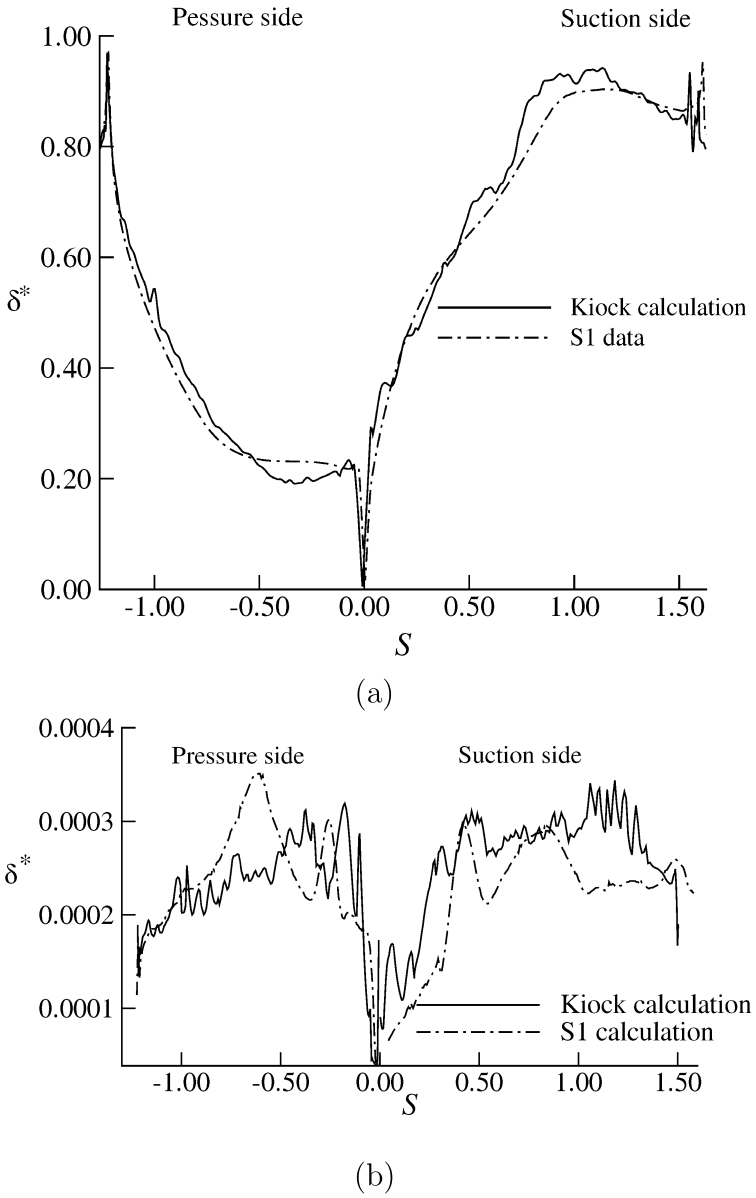

Figure 2.28: a-Surface Mach number distributions for the Kiock(from [107]) and redesigned S1 blades. b-Boundary layer displacement thickness calculations

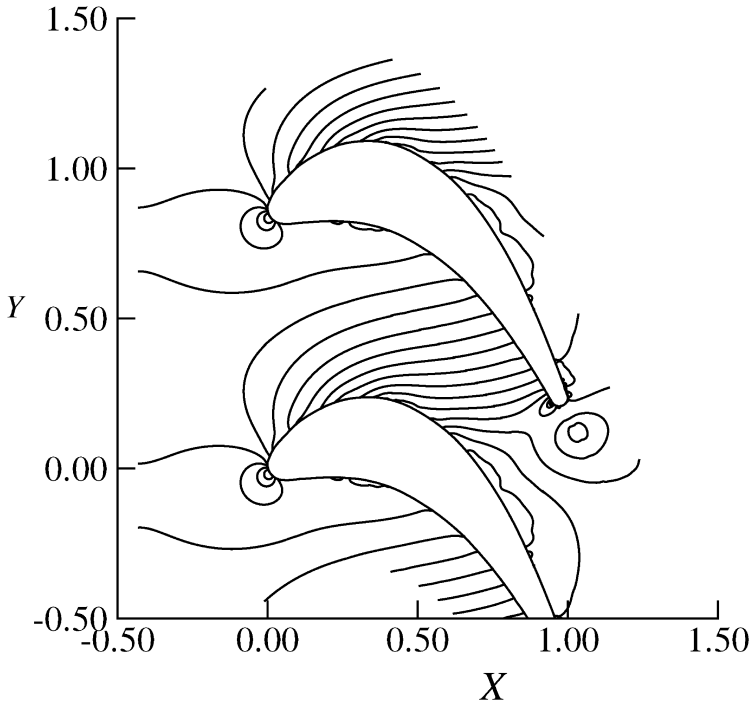

(a)

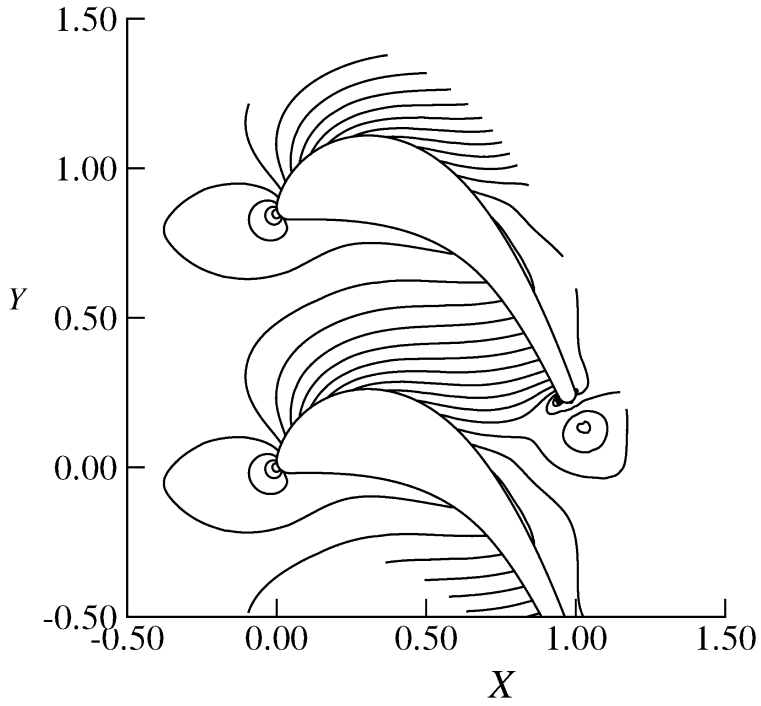

(b)

Figure 2.29: a- Mach contours for original cascade investigated by Kiock (from [107]) . b- Mach contours for the redesigned S1 blade

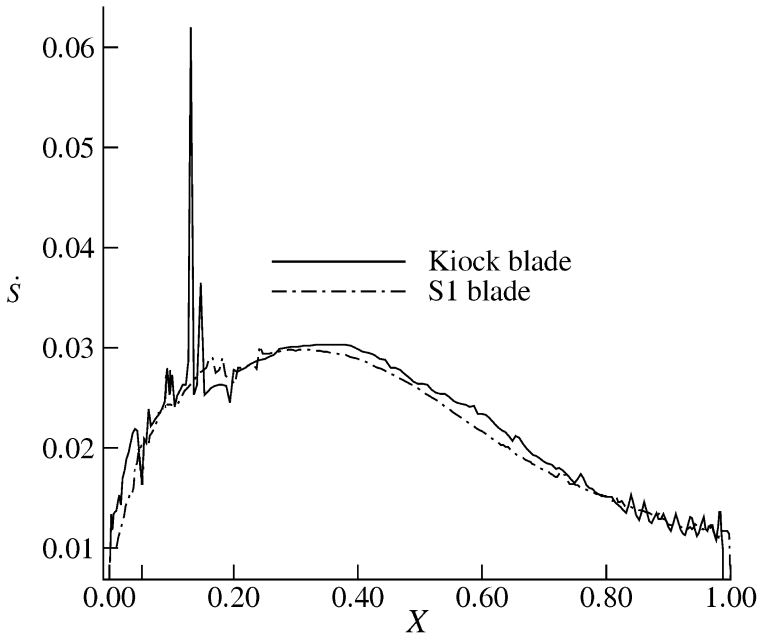

Figure 2.30: Distributions of the total rate of entropy creation on the suction side of the Kiock and redesigned S1 blades

Chapter 3

Leading edge effects in gas turbine expander blades

3.1 Introduction

This part of the blade has significant effect on the aerodynamic and heat transfer performance of the blade, and the result is significantly affected by small changes in the blade shape. Joining the leading edge circle or other shape to the main blade results in flow separation bubbles, and local accelerations and decelerations in the pressure and Mach number distributions. Most of blade geometries with both direct and inverse design methods have difficulties around this area (e.g. [28, 105, 111, 112]). The leading edge shape is critical in the blade design process, and it is quite difficult to completely control with inverse, semi-inverse or other direct-design methods. The effort is concentrated on smoothly blending the leading edge shape (circle or ellipse etc) with the main part of the blade surface, in a manner that avoids leading-edge flow-disturbance and flow-separation regions. Specifically in the leading edge region the second-order (parabolic) construction line coupled with a new smoothing polynomial equation between the leading-edge shape and the main part of the blade. Corral and Pastor [35] used a parametric design method to remove the leading-edge separation bubbles in a turbine blade geometry for which

extensive experimental data have been published (the Hodson-Dominy blade (HD blade) [36–38], which is also used as an example later on in this chapter). Corral and Pastor [35] failed to remove the leading-edge difficulties while keeping the leading edge region similar to the original shape. Specifically they report "...it is specially difficult to match the original geometry because of i.e. discontinuity in the airfoil, which is not explicitly take into account in our method. The isentropic Mach number distributions computed with MISES...". (MISES is a well known inverse design method). As will be shown later in this chapter, the PSCD blade design method can be used in a direct design method to remove the leading edge separation regions from the HD and other blades.

In consequence, the goal of this chapter is to modify the polynomial used in the thickness distribution in the leading edge region of the blade in order to enhance the PSCD method's ability to remove leading edge separation bubbles. The leading edge shape, such as a circle or ellipse, is joined to the remaining main part of the blade by thickness distributions of the form given by equation 2.26. Again the polynomial matches point, first, second and third derivative at its two ends with the remaining blade shape, thus resulting in continuous curvature and slope of curvature at these crucial locations. A similar technique is used to blend a trailing-edge circle to the blade surfaces while maintaining curvature and slope of curvature continuity at these locations.

The Hodson-Dominy blade has been used as an example to show the ability of this blade-design method to remove leading-edge separation bubbles in gas turbine blades and other airfoil shapes in the following chapters. An additional gas turbine blade example has been used to illustrate the ability of this method to design leading edge shapes that avoid leading-edge separation bubbles at off-design conditions. This gas turbine blade example has inlet flow angle 0°, outlet flow angle -64.3°, and tangential lift coefficient 1.045, in a region of parameters where the leading edge shape is critical for the overall blade performance. Computed results at incidences of $-10°$, $-5°$, $+5°$, $+10°$ are used to illustrate the complete removal of leading-edge

flow-disturbance regions, thus minimizing the possibility of leading-edge separation bubbles, while concurrently minimizing the stagnation pressure drop from inlet to outlet. These improvements on the prescribed-curvature-distribution blade-design method provide direct control for the overall blade geometry, eliminating the problems of inverse method. The boundary layer displacement thickness has been found and compared with the successive improvements of the surface curvature for the above incidences. Results showed that the modified blade, B3, is thinner than the B1 blade. This is contributed to produce high efficiency blades with minimum loss.

3.2 Aerodynamic effects of leading edge geometry

Data in this section have been presented in [141]. Experimental data published in [99–103] clearly indicate local kinks in the surface pressure or Mach number distribution of blades, which, as will be illustrated later, is the result of surface curvature discontinuities. These "kinks" affect boundary-layer performance and blade efficiency, and they could be smoothed by the prescribed surface-curvature blade design method.

Hodson [36] experimentally detected the presence of the leading edge spike as a result of a curvature discontinuity in the blending point between the circle and the rest of the blade. Hodson and Dominy experimentally tested this blade (which is designated as the HD blade) extensively [36–38]. Several authors have computationally confirmed this spike [2, 8, 27, 35] around the leading edge of the same blade. Stow [27] illustrated the removal of the leading edge spike locally using an inverse design method.

In this section the use of the PSCD blade design technique is illustrated: first to reproduce a blade (designated I1) designed with the prescribed-curvature distribution direct design method (not locally, but from trailing edge to leading edge) that has geometry and leading edge spike similar to those of the HD blade; then to redesign the blade shape with the prescribed-curvature blade-design method (again

from trailing edge to leading edge) in a series of successive improvements (blades I4 and I9 are shown) that remove the leading edge separation spikes. The details of the computations are included below. The design parameters and representatives data are in the QMUL-EGR-2010-01 confidential report (available from Professor Korakianitis).

Figure 3.1 shows the leading-edge geometry of the original HD blade (which coincides with the I1 blade) and of blades I1 and I9. The geometry to use the same leading-edge circle diameter has been restricted, and in order to maintain the same blade chord from $x = [0, 1]$, as the blade became progressively thinner near the leading edge the reduction in the leading edge wedge angle is limited so that the foremost point on the blade did not move forward from $x = 0$ to values $x > 0$. Thus the foremost point on blade I9 is at $(x, y) = (0.0000, 0.006723)$ as shown in figure 3.1.

The HD blade profile is a thin, hollow, castable root section from the rotor of a low-pressure turbine. It was designed to operate at air inlet flow angle 38.8° relative to the axial direction and to provide approximately 93° of flow turning. The design velocity ratio across the cascade is equal to 1.41. The nominal aspect ratio was 1.8. The test Reynolds number is 2.3×10^5 and the test inlet and outlet Mach numbers are 0.496 and 0.702. Further details can be found in references [27, 36–38].

Figure 3.2(a) shows the surface-curvature distribution for the HD blade (jagged line, evaluated numerically from the original data points) and the curvature distributions of blades I1, I4 and I9. The surface curvature distributions of blades I1, I4 and I9 are smoother lines, as these blades have been reproduced with the prescribed-curvature-distribution blade design method. The figure also shows the curvature of blade I1 trying to follow the curvature of the HD blade in the vicinity of the leading edge "spike" on the suction side. This "spike" in the surface curvature of blade I1 (which it is not normally used in this region of a blade design) is now required in order to reproduce the flow spike for blade I1, in order to reproduce the spike in the HD blade. The "spike" is not "prescribed" in the curvature distributions of blades

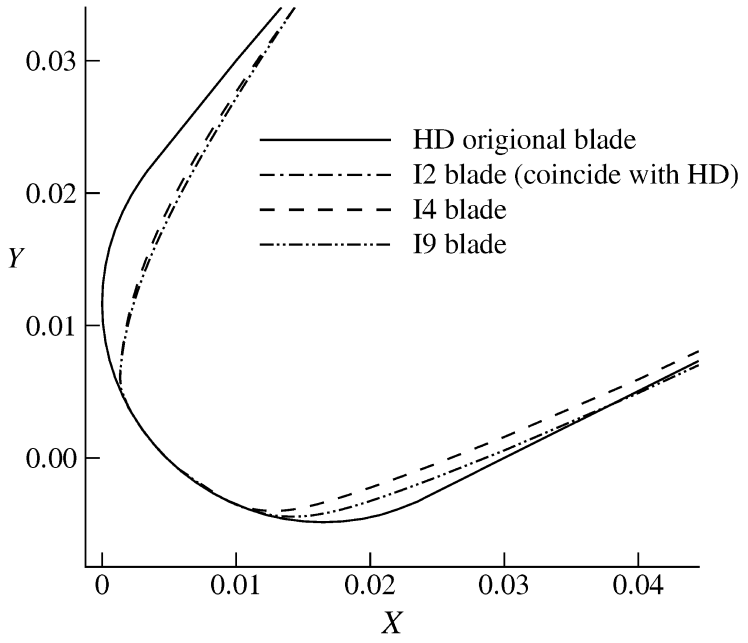

Figure 3.1: Original and redesigned leading edge for both of HD and I1, I4, and I9 blades

I4 and I9, which are by specification and design smooth. The resultant computed isentropic Mach number distributions are shown in the figure 3.2(b). The sharp local acceleration-deceleration region in the leading edge of blade I9 has also been smoothed.

Mesh generator GAMBIT and flow solver FLUENT have been used in the computations. A reasonably high number of computational mesh elements is required for reasonably accurate calculations. The exact numbers depend on the geometry of the blade and its model. The mesh elements used for the HD and I1, I4 and I9 blades are: 19,705 quadrilateral cells; 38,967 2D interior faces; and 20,148 nodes for all zones. A 2D O-mesh and a Pave-unstructured mesh have been used in the viscous calculations. The Pave mesh consisted of a combination of structured and unstructured regions. The mesh around the airfoil consisted of twelve structured clustered O-grid layers with y^+ less than 5 (quadrilaterals), and the remaining majority of the flow field was descritized with quadrilateral and a small numbers of triangular cells. The $k-\omega$ SST transition turbulence model has been used to analyze the aerodynamic performance of the blade. Figure 3.3 shows the Mach number

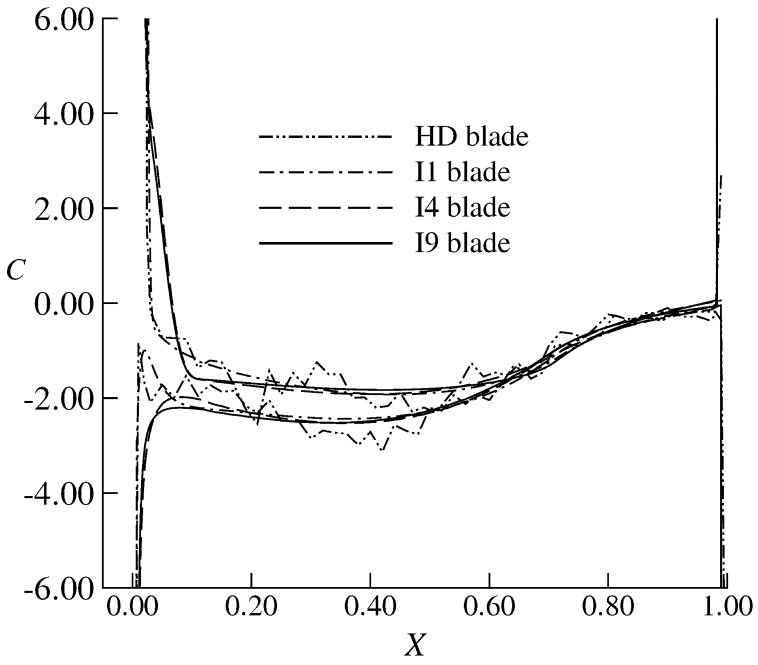

(a)

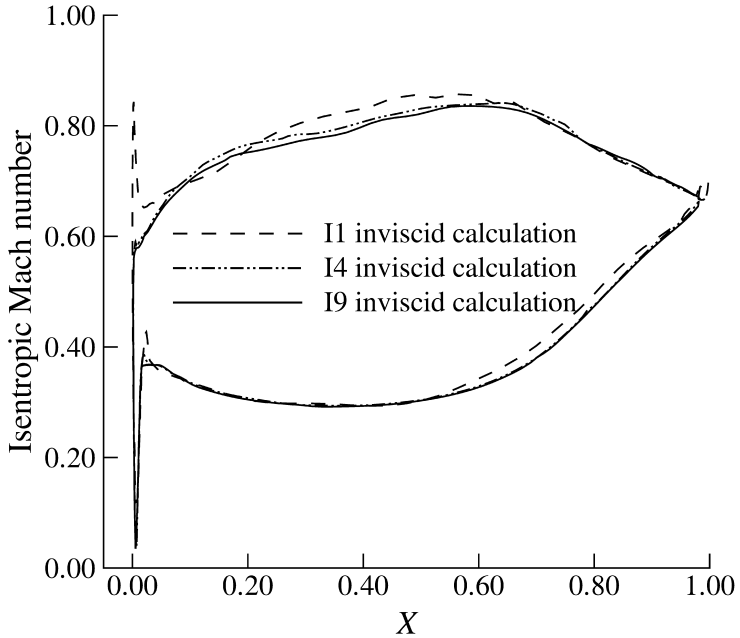

(b)

Figure 3.2: a- Surface curvature distributions for all blades (HD, I1, I4, I9). b- Isentropic surface Mach number distributions of the reproduced HD blade and redesigned I4 and I9 blades

contours around the leading edge of the HD and I9 blades, and shows the success of the prescribed-curvature distribution method to remove the local deceleration regions (and the resultant separation bubbles) at the edges of the leading-edge circle region.

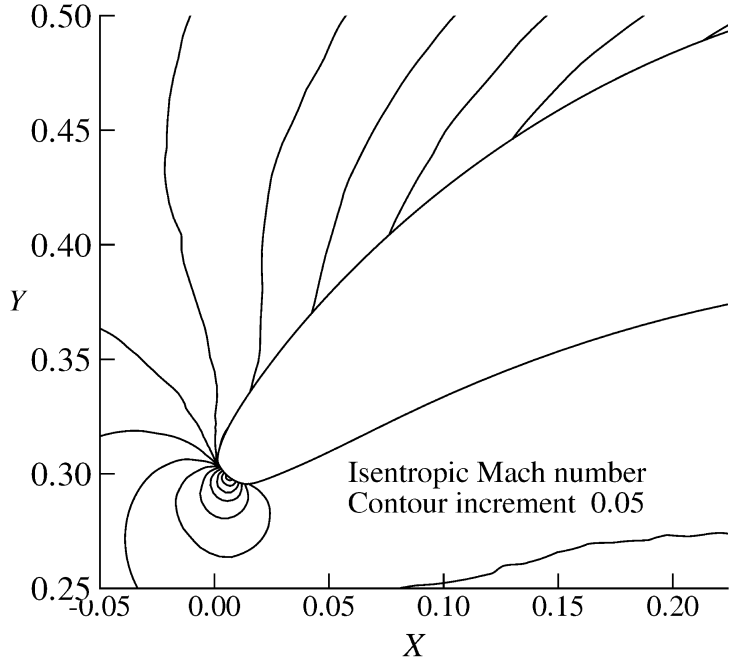

(a)

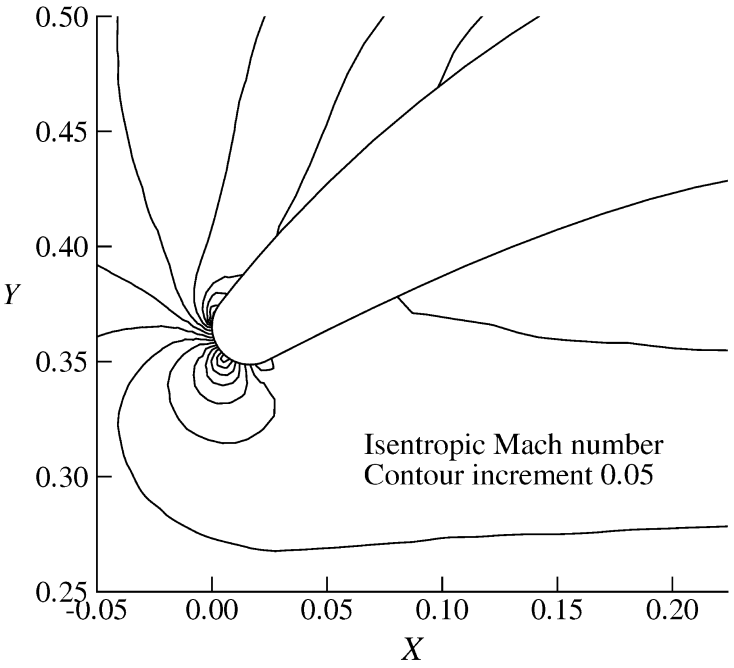

(b)

Figure 3.3: a- Mach contours for the original HD blade. b- Mach contours for the redesigned I9 blade

Figure 3.4 shows the comparison of the experimental data for the HD blade with the results of viscous calculations for blades HD, I1, I4 and I9.

The boundary layer of the flow around both HD and redesign, I9, blades have

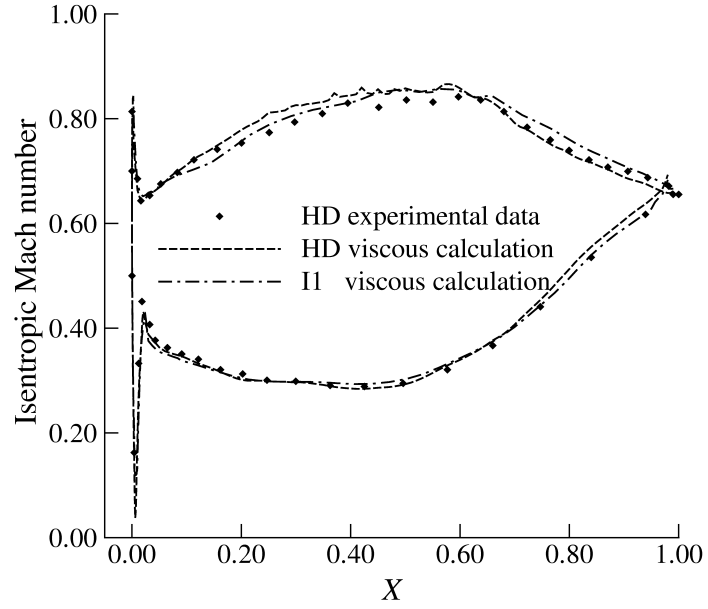

(a)

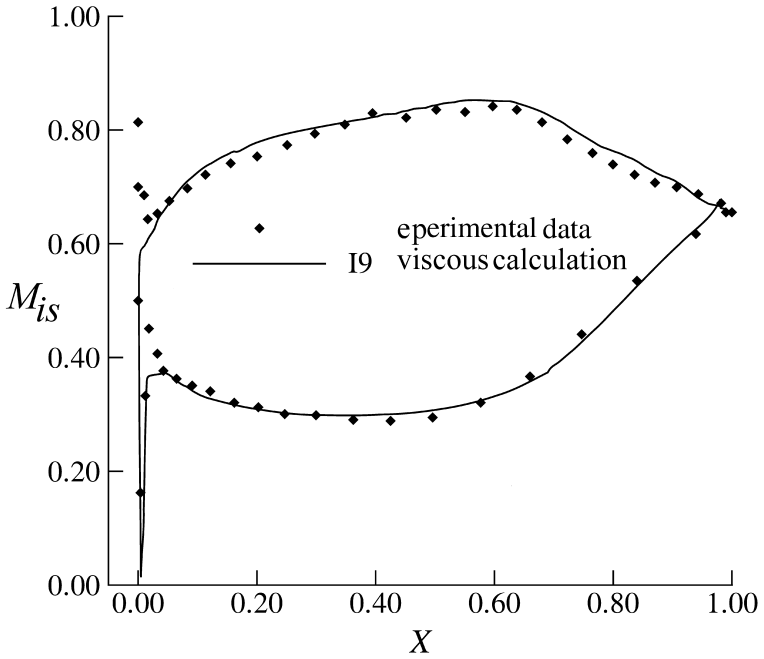

(b)

Figure 3.4: a- Isentropic surface Mach number distributions of the HD and I1 blades. b- Viscous Mach number distributions for the HD and I9 blades

been analyzed to show how much surface curvature contributes to the improvement of the aerodynamic blade performance such as pressure distribution or surface Mach number distribution. Figure 3.5 (a, b) show the comparison between the surface Mach number distributions and the displacement boundary layer calculations, δ^*,

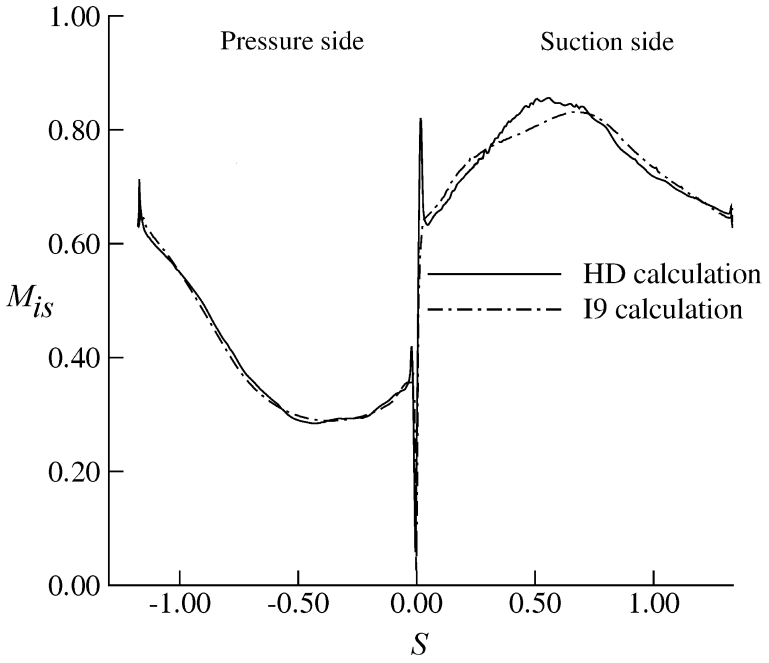

(a)

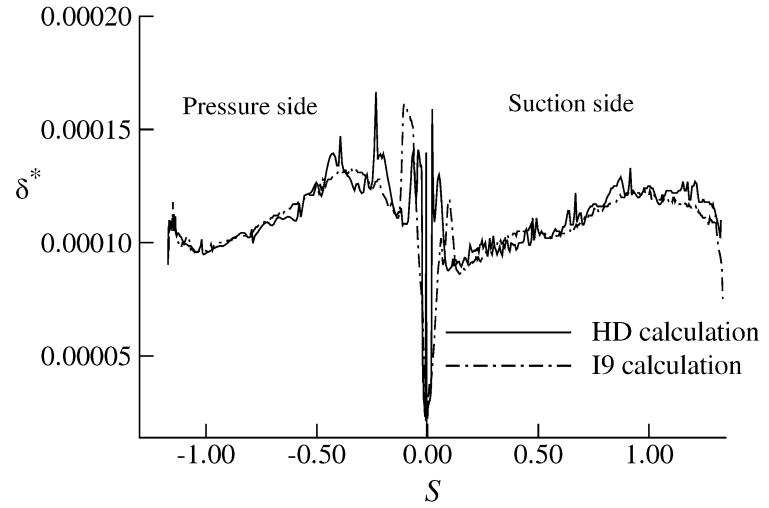

(b)

Figure 3.5: a-Surface Mach number distributions for the HD and redesigned I9 blades. b-Boundary layer displacement thickness calculations

for the HD and redesign I9 blades. The results showed that the boundary layer of the HD blade is thicker than the redesigned I9 blade and this results in producing more losses inside the boundary layer. The rate of total entropy creation [94] in the blade boundary layers has been evaluated on the suction side of the HD and redesigned I9 blades to show that the thicker boundary layer the more entropy generated. Figure 3.6 (a) shows the comparison between the total rate of entropy

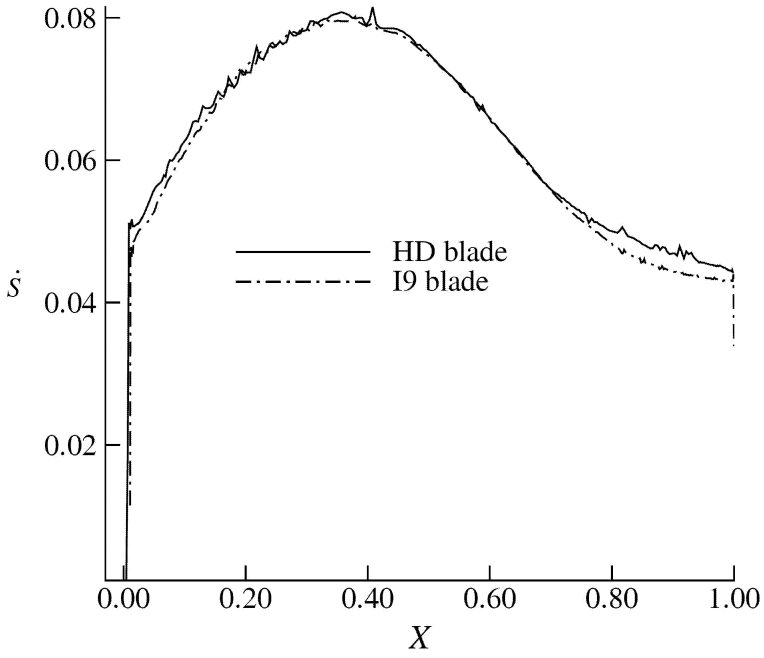

(a)

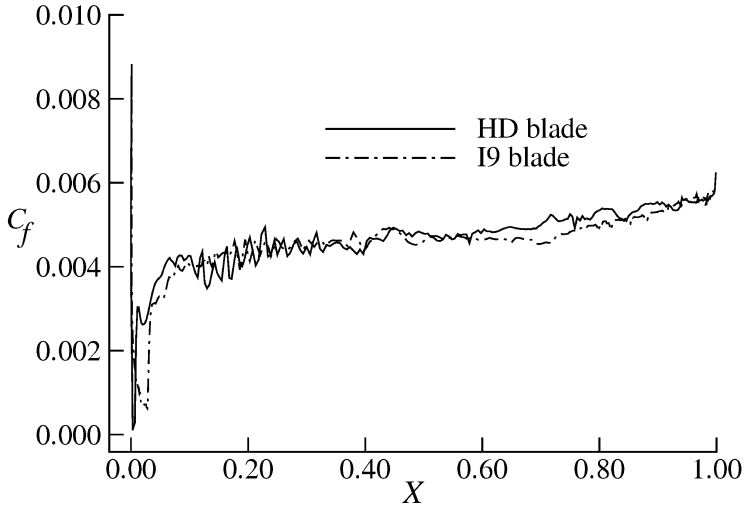

(b)

Figure 3.6: a-The rate of entropy creation on the suction side of the HD and I9 blades. b- Skin friction calculations on the suction side of the HD and I9 blades

creation inside the boundary layer of the suction side of the HD and the redesigned I9 blades. This improvement in the surface boundary layer distribution contributes to decrease of the mass-averaged stagnation pressure losses. The mass- averaged stagnation pressure losses for the HD which is $Z = 0.00316$ and $Y = 0.0132$; and for the redesigned I9 which is $Z = 0.00220$ and $Y = 0.0113$. The separation and reattachment points have been predicted accurately by the SST transition model. Figure 3.6 (b) shows the skin friction calculations, C_f, for the HD and redesigned I9

blades. The turbulence model predicts the separation point at $X/b_x = 0.29\%$ and reattachment point at $X/b_x = 0.88\%$. The main transition around $X/b_x = 60\%$ on the suction side has also been predicted.

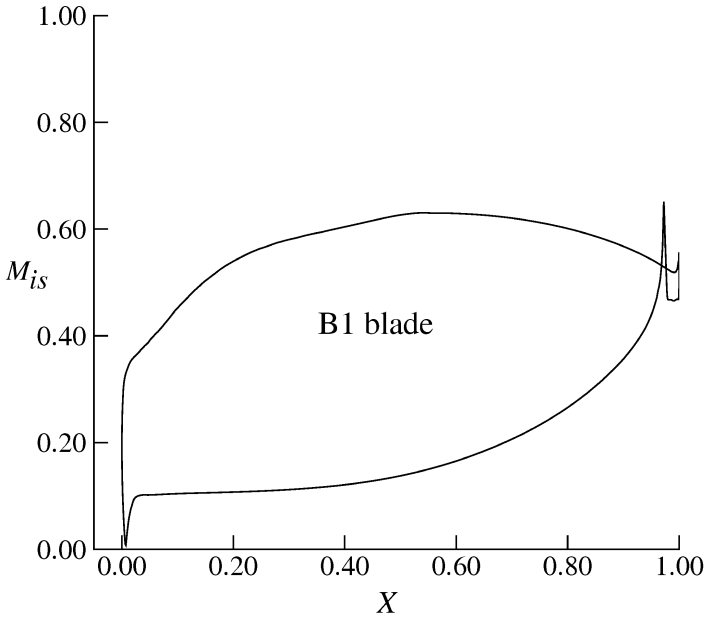

(a)

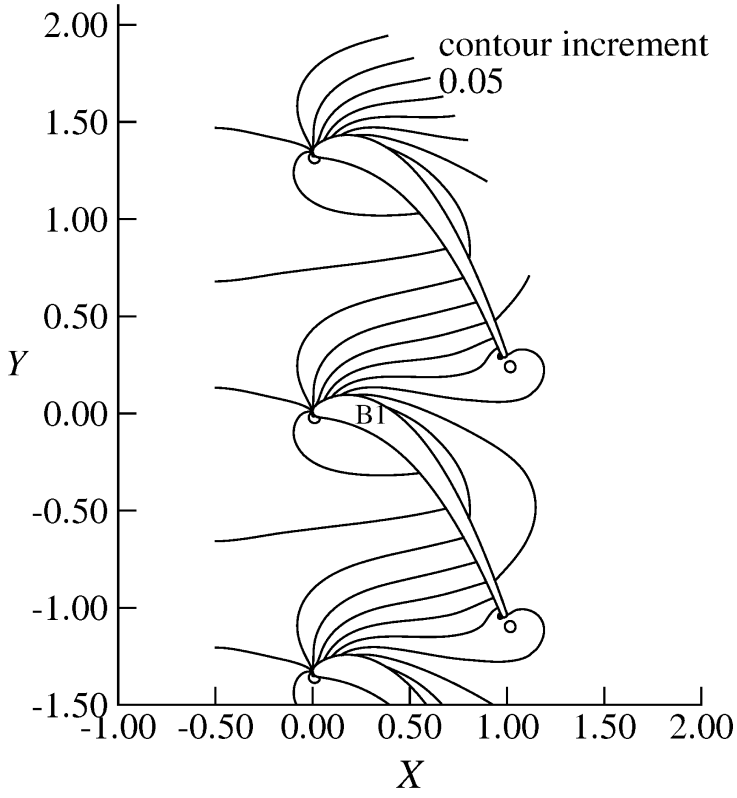

(b)

Figure 3.7: a- Isentropic surface Mach number distribution at design condition 0°. b- Mach contours at design condition 0°, increment 0.05

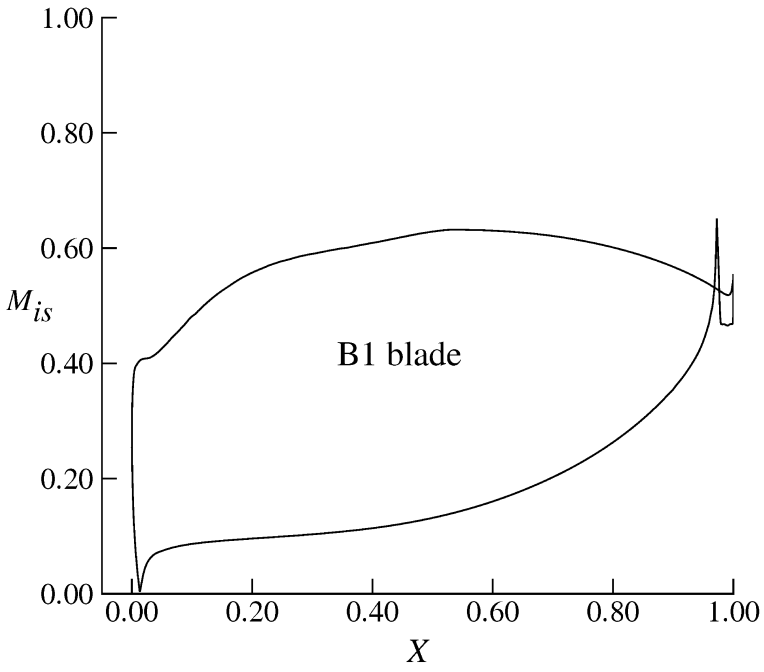

(a)

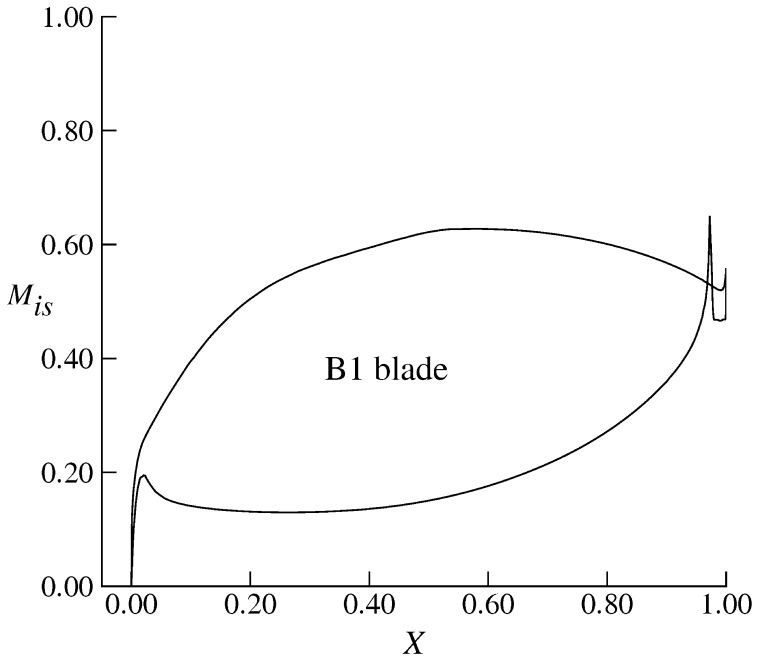

(b)

Figure 3.8: a- Isentropic surface Mach number distribution at off-design condition +5°. b- Isentropic surface Mach number distribution at off-design condition -5°

3.3 Design and off-design performance

Curvature discontinuities have a more severe impact around the leading edge at design and off-design conditions because at least one of the discontinuities takes place in a region of a high velocity. Benner [104] mentioned that the discontinuity

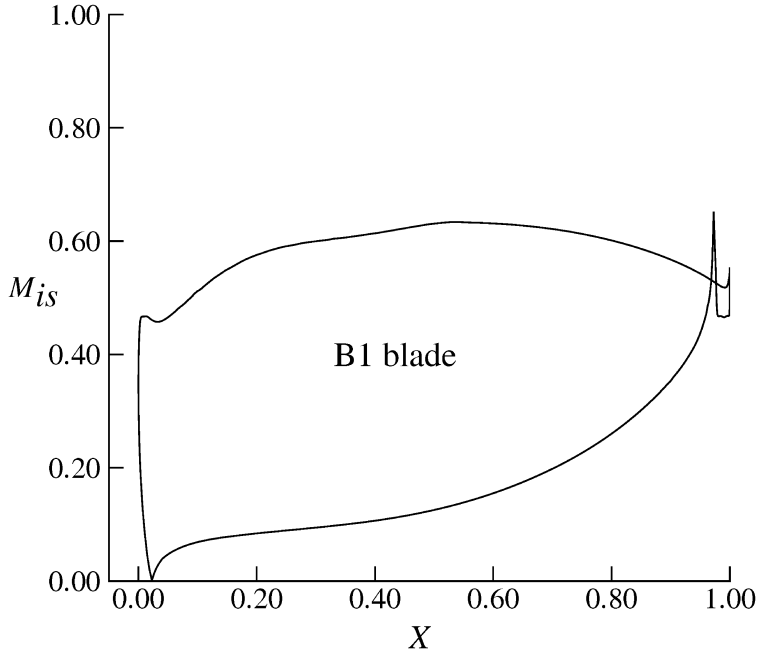

(a)

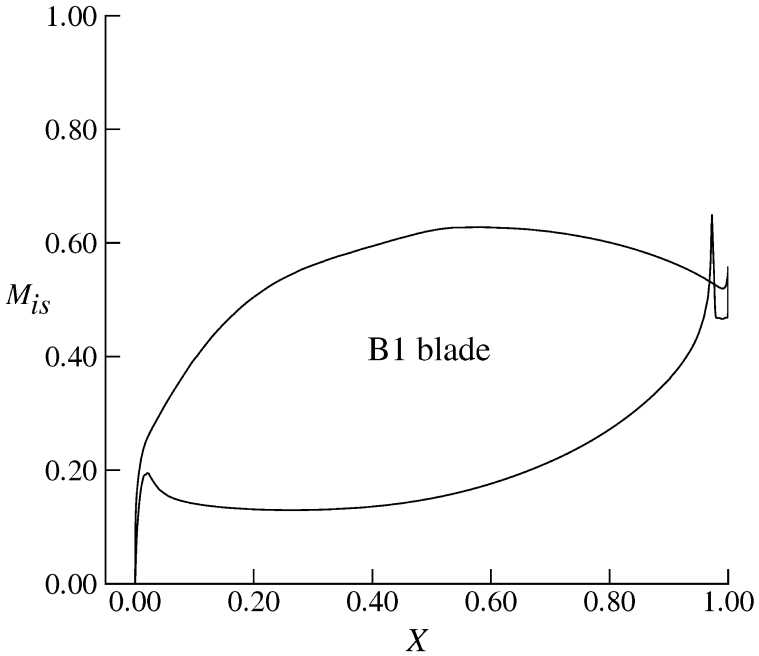

(b)

Figure 3.9: a- Isentropic surface Mach number distribution at off-design condition +10°. b- Isentropic surface Mach number distribution at off-design condition -10°

in the (flow) curvature is increased at off design conditions, and he argued that the off-design behavior of the blade is influenced by the magnitude of the discontinuity in the surface curvature between the circle and the rest of the leading edge part of the blade.

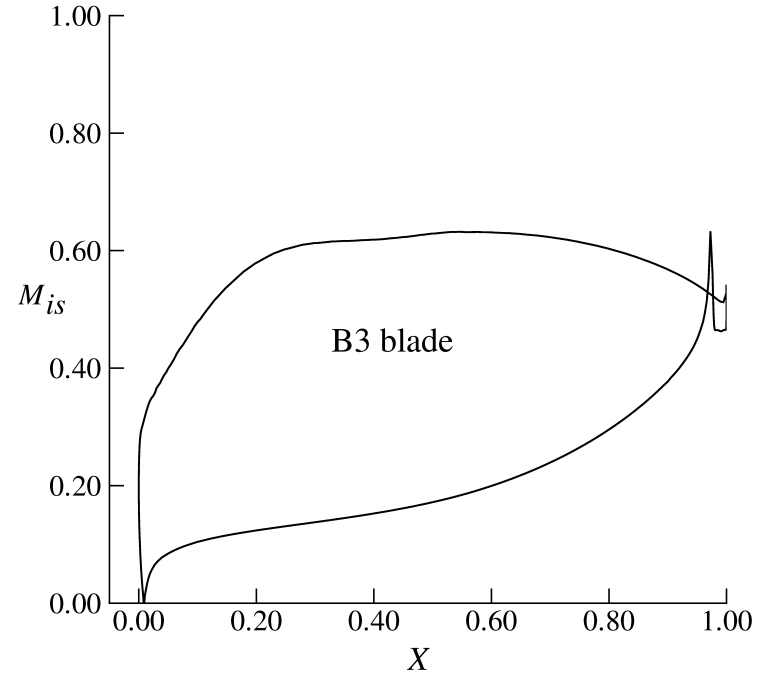

(a)

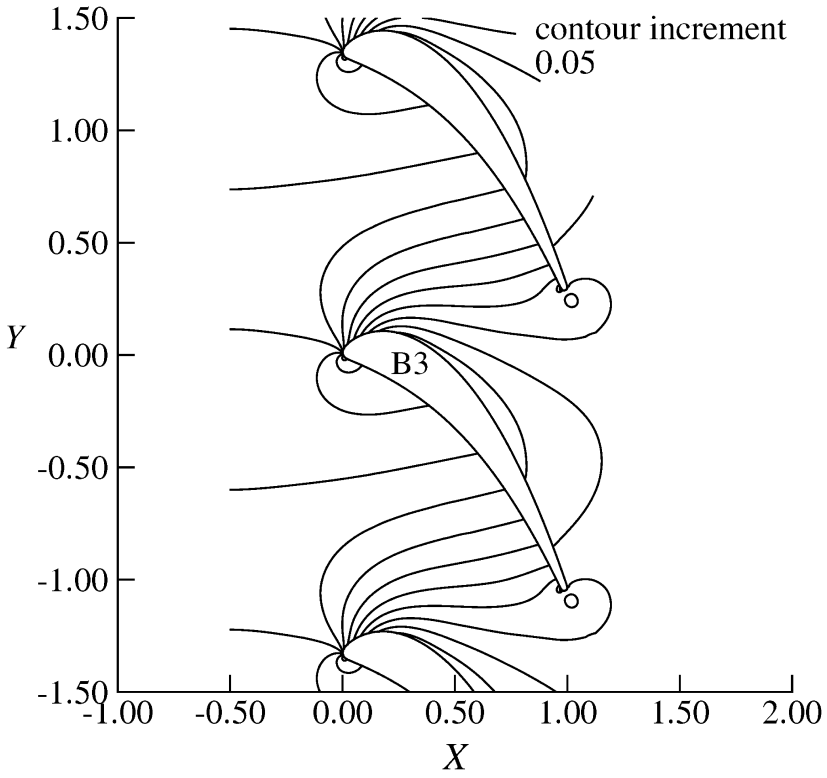

(b)

Figure 3.10: a- Isentropic surface Mach number distribution at design condition 0°. b- Mach contours at design condition 0° of the B3 blade, increment 0.05

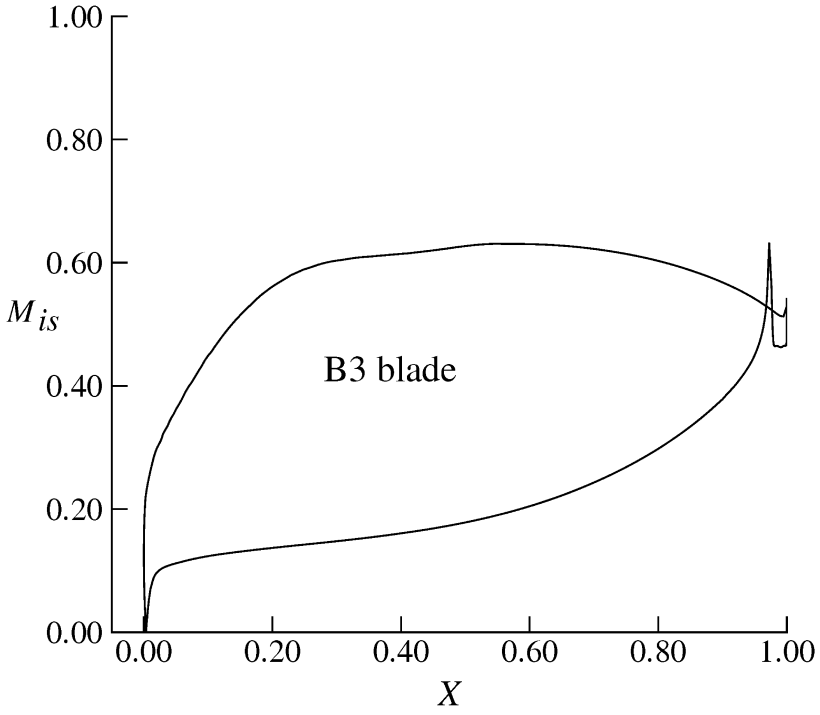

(a)

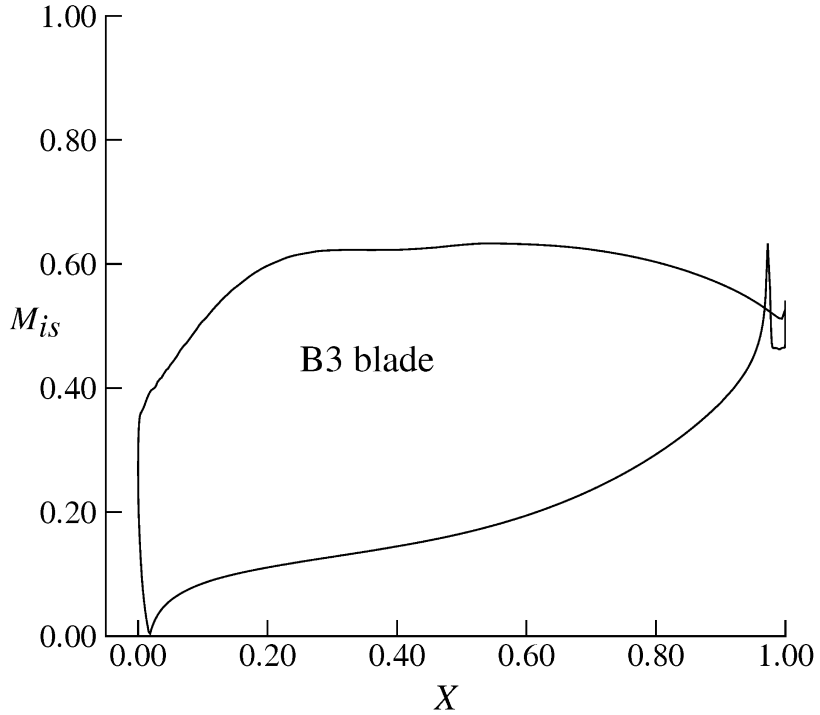

(b)

Figure 3.11: a- Isentropic surface Mach number distribution at off-design condition -5°. b- Isentropic surface Mach number distribution at off-design condition +5°

The prescribed-curvature blade design technique has been used to design three example blades, designated B1, B2 and B3, to illustrate the effect of the surface-

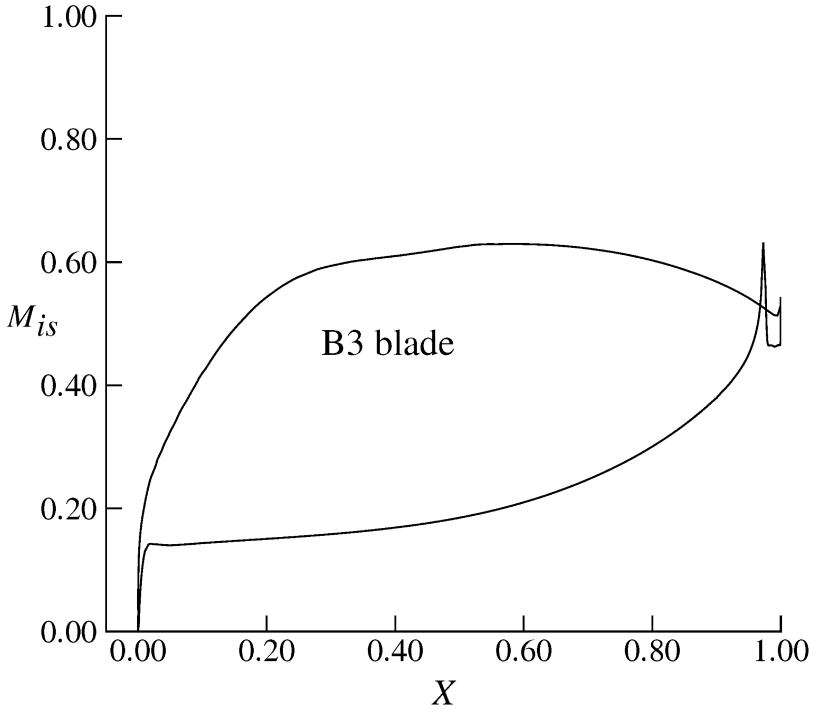

(a)

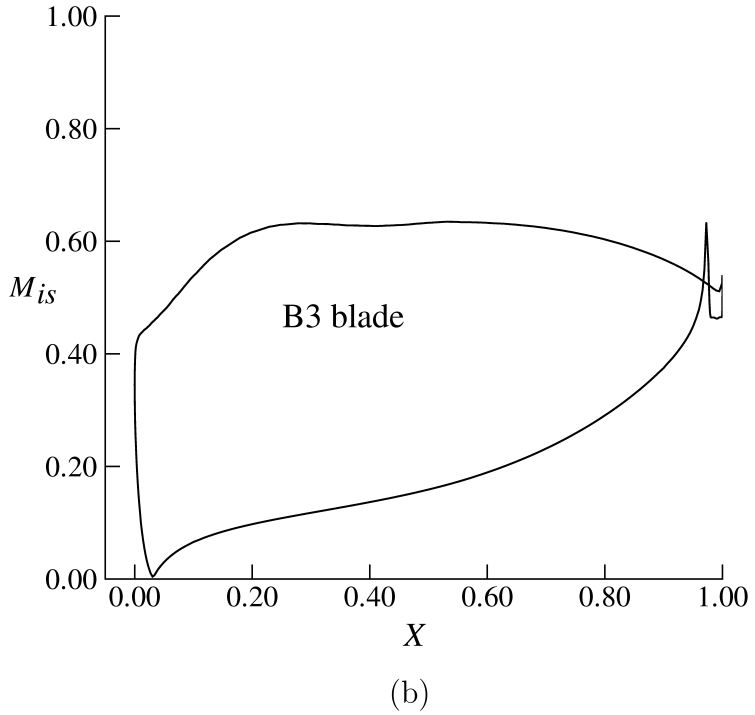

(b)

Figure 3.12: a- Isentropic surface Mach number distribution at off-design condition -10°. b- Isentropic surface Mach number distribution at off-design condition +10°

curvature distribution at design and off-design conditions. Three dimensional blade designs B1, B2 and B3 have been obtained, but the representative mean-line results

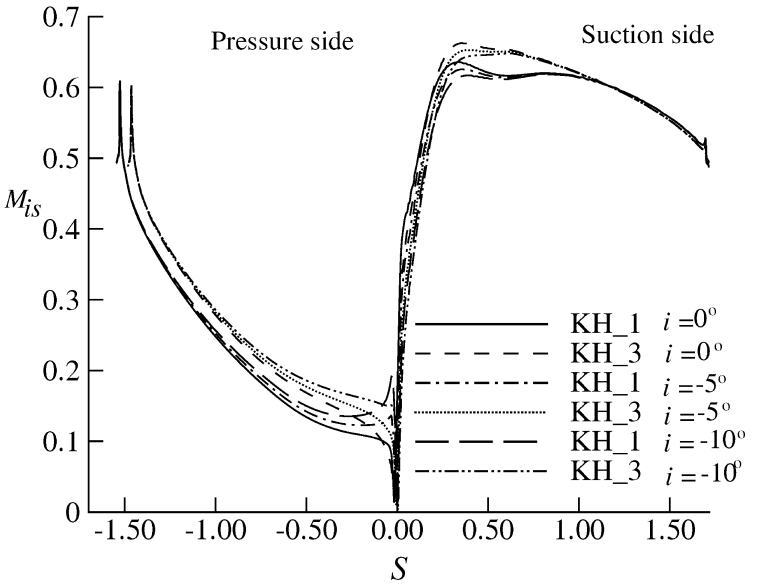

(a)

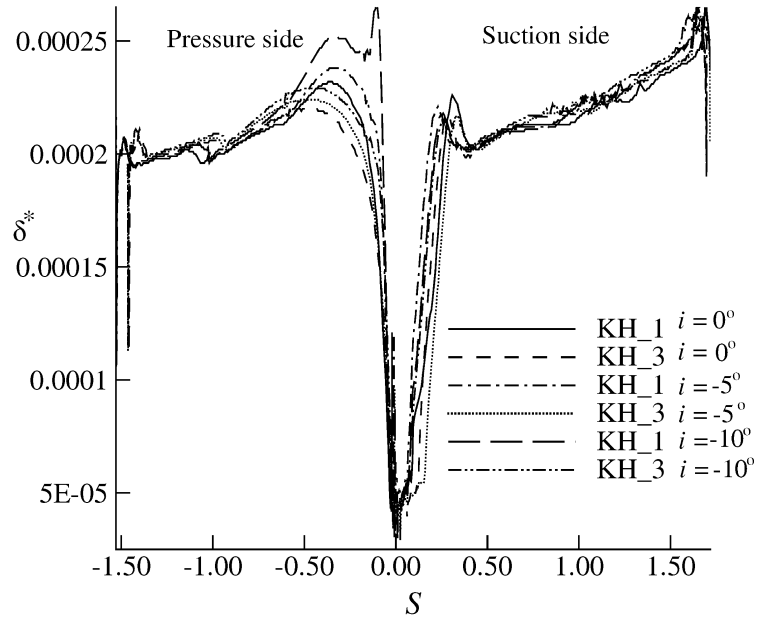

(b)

Figure 3.13: a- Surface Mach number distributions for B1 and B3 blades. b- Boundary layer displacement thickness calculations

are reported. The design parameters and representative data points for blade B3 are obtained from QMUL-EGR-2010-01 confidential report (available from Professor Korakianitis). Blades B1, B2 and B3 have been designed for the following conditions:

inlet total temperature 1000 K;

inlet total pressure 532 kPa;

inlet flow angle (design point) 0.00^o

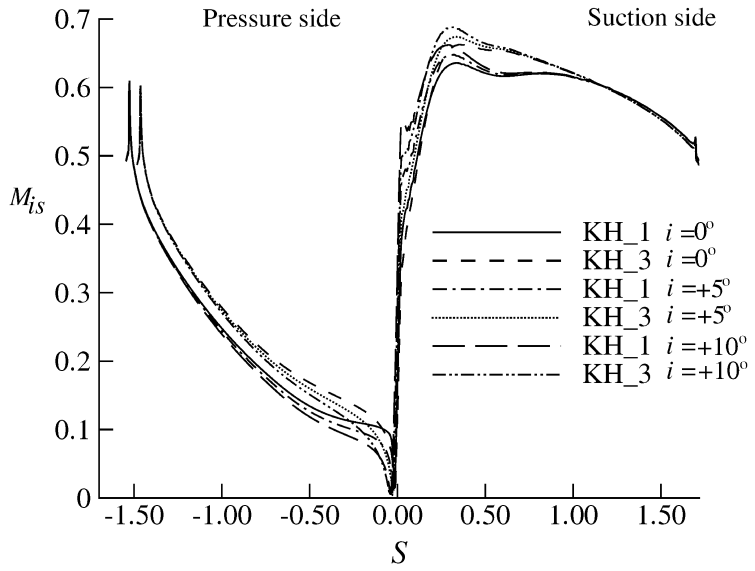

(a)

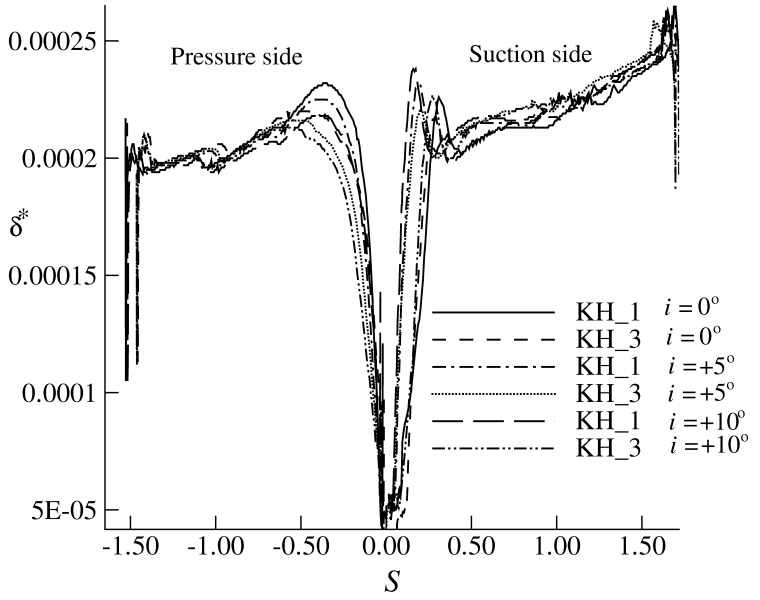

(b)

Figure 3.14: a- Surface Mach number distributions for B1 and B3 blades. b- Boundary layer displacement thickness calculations

outlet flow angle (design point) 64.30^o

Pitch to axial chord ratio $S/b = 1.3371$

Throat diameter to pitch ratio $o/S = 0.441$

Tangential loading coefficient (at mean line) $C_L = 1.04500$

Stagger angle λ = -47^o

Leading edge circle radius to axial chord ratio $r_{le}/b = 0.0300$

Trailing edge circle radius to axial chord ratio $r_{te}/b = 0.0150$

Inlet Mach number 0.2052

Outlet Mach number 0.5346

Inlet Reynolds number of $1.7 * 10^5$

Outlet Reynolds number of $3.7 * 10^5$

These specifications have been specifically chosen around inlet flow angles of zero degrees (to illustrate the effect of positive and negative inflow angles from this value). The flow solutions have been obtained with FLUENT [60] specifying free-stream turbulence intensity of 10% and using the $k - \omega$ SST transition turbulence model. The solutions have been obtained for design point conditions as well as for incident angles of -5°, +5°, -10°, and +10°.

The computational meshes are: 25,076 quadrilateral cells; 49,604 2D interior faces; and 25,624 nodes for all zones. A 2D O-mesh and a Pave-unstructured mesh have been used in the viscous calculations. The same procedure for the HD blade have been used to generate mesh around the B1 B2 and B3 blades.

Figure 3.7 illustrates the isentropic surface Mach number distributions and the Mach contours of blade B1 at design conditions. Figures 3.8, and 3.9 illustrate the off design conditions. Figure 3.10 illustrates the surface Mach number distributions and the Mach contours of blade B3 at design conditions. Figures 3.11 and 3.12 illustrate the off-design conditions. The surface curvature distribution of blades B1 and B3 is shown in figure 3.15. Figure 3.13 (a, b) show the surface Mach number distributions and boundary layer displacement thickness calculations for B1 and B3 at design condition and incident angles of $-5^o, -10^o$. Figure 3.14 (a, b) show the surface Mach number distributions and boundary layer displacement thickness calculations for B1 and B3 at design condition and incident angles of $+5^o, +10^o$. These results show that the thicker boundary layer the more entropy generated and these resulted in producing more losses in the boundary layer of the blade which contributes to increase the mass-averaged stagnation pressure losses.

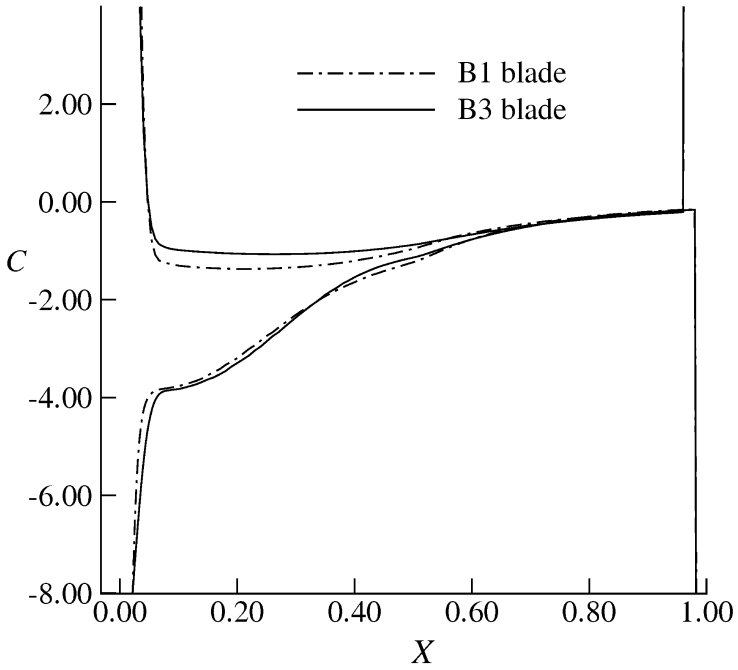

Figure 3.15: Surface curvature distributions of blades B1 and B3

Table 3.1: Stagnation pressure losses Z at design and off-design conditions

Blade names	Design and off design conditions				
	-10	**-5**	**0**	**+5**	**+10**
B1	0.002430	0.002450	0.002480	0.002518	0.002560
B2	0.002424	0.002446	0.002474	0.002508	0.002552
B3	0.002357	0.002404	0.002433	0.002467	0.002512

Table 3.2: Stagnation pressure losses at design and off-design conditions,$Y_t = \frac{P_{01}-P_{02}}{P_{02}-P_2}$

Blade names	Design and off design conditions				
	-10	**-5**	**0**	**+5**	**+10**
B1	0.01314	0.01323	0.01334	0.01348	0.01388
B3	0.01291	0.01314	0.01328	0.01343	0.01374

Table 3.3: Suction-side diffusion ratio at design and off-design conditions

Blade names	Design and off design conditions				
	-10	**-5**	**0**	**+5**	**+10**
B1	0.87110	0.869975	0.86985	0.86772	0.86780
B2	0.849743	0.84831	0.84685	0.84538	0.843875
B3	0.838995	0.836926	0.834855	0.832745	0.83042

At design point conditions blade B1 exhibits perfectly acceptable behavior, without any leading-edge flow disturbances at the joining points of the blade surface with

the leading edge circle. At +5° a small disturbance is shown on the suction surface at the location of joining the leading edge circle with the blade surface. At -5° a small acceleration-deceleration region is shown on the pressure surface at the location of joining the leading edge circle with the blade surface. These flow disturbances are made worse at +10°, and -10°.

These disturbances at off-design conditions are progressively improved in blades B2 and B3 by small changes in the blade surface curvature distribution, as illustrated in figure 3.15. Furthermore these flow effects have consequences in the flow deceleration regime in the region of unguided diffusion, and the resultant computed total pressure losses on the blade. For the purposes of discussion the suction-side diffusion ratio are defined as the maximum isentropic Mach number on the surface of the suction side divided by the Mach number at the trailing edge.

The results show that with the PSCD blade-design method the effect of joining the leading edge circle to the blade surfaces has been minimized not only at design conditions, but also at relatively large angles of incidence. The computed stagnation pressure losses from inlet to outlet at design and off-design conditions are shown in table 3.1. Table 3.3 shows the resultant suction-side diffusion ratios at design and off design conditions. There is a direct correlation between increases in suction-side diffusion ratio and stagnation pressure losses.

3.4 Conclusion

Redesign of the HD blade to remove the leading edge problems had been attempted before with inverse design methods [27], but this is the first reported attempted to remove the leading edge spikes with a surface-curvature direct blade design method. It is noted that suction-surface spike and the pressure-surface region of diffusion near the leading edge have been completely removed. The results show that the prescribed surface curvature distribution blade design method is a robust tool for blade design, providing a manageable and accurate way to control the blade surface

and the aerodynamic properties around the blade.

The prescribed surface curvature blade design technique results in smoother boundary layer flows, affecting aerodynamic as well as heat transfer performance. Sample blades B1, B2 and B3 have been designed to show the capability of the method to eliminate the spike and dips in the surface Mach number distribution at design and off-design conditions in the vicinity of the leading edge circle at both design and off-design conditions. Stagnation pressure losses decrease with smoothing the blending of the circle with the blade surfaces, as predicted by Benner [104]. The boundary layer displacement calculations showed that how the surface curvature distributions contribute to produce high smooth surface and reflects to control the development of the boundary layer. This resulted in producing high efficiency blades with less mass-averaged stagnation pressure losses.

It is concluded that the prescribed surface curvature blade design technique can be used to provide accurate guidance and control for the design of blade shapes. Furthermore the method can be used to eliminate the flow problems resulting from blending a leading edge circle or other shape with the blade surfaces at design and off-design conditions.

The prescribed-curvature blade design technique has been used to design stacked 3D turbine blades, compressor and fan blades, isolated airfoils, and wind turbines. These will be reported in other chapters.

Chapter 4

3D stacking effects in gas turbine expander blades

4.1 Introduction

The flow field inside a turbine is highly three dimensional and extremely complex. Numerical optimization methods have been successfully used for a variety of design problems. However, application to aerodynamic blade shape optimization problem still remains as a hard challenge. The application of three dimensional blade-to-blade and through flow calculation methods in design process of turbomachine are restricted to consideration of limited Mach numbers, minimizing the number of stages, or maximizing work per stage while keeping high efficiencies. In most turbomachinery design systems a meridional through flow calculation is the backbone of the design process. It is fast, reliable and easy to use to design multi-stage blade rows for turbomachinery. Initial blade design components are based on the assumption of steady quasi-three-dimensional axisymmetric flow in a series of meridional planes (through-flow analysis in the axial-radial directions). These analysis are based on the general S1/S2 theory of Wu [43]. Blade shapes are then designed by quasi-three-dimensional analysis in a series of meridional-tangential planes. In the design process of turbomachinery blades, the design of annuals passage and blade shapes with both

methods are crucial points before analyzing three-dimensional(3D) Navier-Stokes simulations. The through flow [44,45,47–49] and blade-to-blade [50,51] design methods treat the three dimensional (3D) flow through a series of second dimensional blade sections and stacked based on the center of gravity [51–57] or trailing and leading edge positions [57–59] to build up three dimensional blade geometry. Design of blade geometry sections, using quasi-three-dimensional, is a typical way to design 3D blade geometry, and it is quite efficient when it compares to fully-3D Navier-Stokes simulations [51]. Through flow streamline method gives velocity diagrams from hub to tip to a designer which are based on the three major non-dimensional parameters such as work coefficient, reaction and flow coefficient. Based on these velocity diagrams from hub to tip, 3D turbine blades are generated by stacking 2D designs using rules of center of gravity of the 2D sections and the shape of leading and trailing edges and resulting blade surfaces.

Most of the design methods including inverse method and parameterization methods [52, 56, 57, 59] still could not produce a smoothed surface for all type of blades (controlling the shape of the leading edge with the rest of the surfaces), according to their published data to present aerodynamic performances such as Mach number or pressure distributions around the specified blade geometry, that remove disturbances and separation bubbles around the leading edge of the blade at design and off-design conditions or from hub to tip blade profiles. Their blade design methods based on different type of polynomials such as Bezier curve, B-spline and non-uniform rational B-spline to prescribe the whole surface of the blade including leading and trailing edges

The use of stacking three dimensional has been the source of large number of investigations including experimental and numerical calculations over recent years. Stacking line modifications has been described by a variety of terms (e.g. dihedral, sweep, bow, skew) and different nomenclature has been used from these investigations. Therefore, there is a need to describe these terms in this work. The dihedral can be defined as the movement of blade normal to the airfoil section chord line,

and the lean can be defined as the movement of blade parallel to the camber line of the blade. There are two techniques of stacking blade profiles from hub to tip which are the radial stacking and non radial staking lines. The first group incorporates the average of radial stacking of individual center of gravity of blade sections on a radial line. The second group of stacking blade profiles includes sweep, dihedral and skew shapes of the blade. Many research efforts [97, 113–126], for compressor and turbine, have been spent to reduce end-wall losses through leaned and dihedral lines of stacking, and a result of these modifications the overall increased efficiency and elimination of corner stall can be achieved. Gallimore and his groups [127, 128] investigated the advantages of the sweep and dihedral staking in multistage axial compressor for the first time and they explained that their modifications through leaned and dihedral staking lines are important to the designer at an early stage in the design so that efficiency and surge margin goals can be achieved. Thaler [129] pointed out that the shape and extend of the secondary flow mainly depend of flow parameters (e.g. incidence angle, the boundary layer thickness and the turbulence) and geometric parameters (e.g. distribution of the blade load, shape and radius of the leading edge, dihedral and sweep of the blade). Non radial stacking [119,130,131] offers increased capability of near-endwall, tip clearance losses, control of secondary flows, radial migration of high loss fluid and as well as provides a unique means for rotor noise reduction [132]. Pullan and Harvey [133, 134] investigated the consequences of sweep for turbine blade profile losses and they argued that the necessity of achieving a high blade speed and reducing the number of required stages, for a large bypass in turbofan, through sweeping blades, and they concluded that the mixedout midspan profile loss was measured to be %20 grater for the swept blade than for unswept one. D'lppolito [135] reported that the blade lean angle leads to grow the secondary vorticity in regions where secondary losses and blade loading decrease. Biollo and Benini [136–139], in several attempts, reported out that the use of swept and leaned blades can considerably influence the internal flow structures in transonic compressor-rotor blades, and they confirmed the possibility of

improving overall efficiency of the engine. The advantages of sweep and skew to improve efficiency, performance and extension of stall-free operating range at design condition were discussed in the review paper by Vad [140] as well. In this thesis, the previous streamline curvature solution [8, 10] with extensions has been chosen to design three dimensional velocity diagrams for axial turbomachinery blades. This method still requires the iteration loop for mass flow balance, but for solving radial momentum equation at each flow stations Korakianitis and Zou [10] used a one pass numerical predictor-corrector technique, which substantially reduces the computational effort and takes into account an axial slope of streamlines. There are three non-dimensional parameters found to be useful in turbomachinery design to prescribe velocity diagram for the flow through turbomachinery blades. One, which expresses the work capacity of a stage, is called the work coefficient or temperature drop coefficient . Another useful parameter is the degree of reaction or simply the reaction . The third dimensionless parameter is the flow coefficient ϕ.

The objective of this chapter is to apply the method first described in [8] for the radial variation of PSCD blade-design parameters through Bezier curves as a relation between non-dimensional radial direction, (along $r' = r/r_m$), and other design parameters, which include throat diameter o, stagger angle λ, radius of leading and trailing edge, the tangential space of the blade S. The output parameters from the streamline method are presented through Bezier curve relations from hub to tip, and the designer selects the number of blade sections to present 3D blade geometry. These parameters from the Bezier relations are used as input information to the quasi-2D direct PSCD blade design method. This technique combined with through flow calculation enables designers easily make an efficient blade from hub to tip. In addition to that, this quasi 3D technique with Bezier description of parameters in the radial direction minimizes the number of 3D blade design parameters.

4.2 3D flow analysis

The flow analysis is performed for each profile section separately. The streamline curvature method, which was presented in [8, 10], has been used. Korakianitis and Zou [10] solved this method numerically by McCormak's explicit predictor corrector method at each flow station (blade inlet and outlet rows) along discrete streamlines in the r direction. The performance of each stage was analyzed by assuming models for the total pressure drops in stator, and total to total polytropic efficiencies for each stage. Korakianitis and Zou [10] pointed out that these losses can be applied in each individual streamline, accounting for losses as a function of geometry. They also assumed that the radial components of velocity do not contribute to friction. Further details of the derivation of radial equilibrium with streamline curvature can be found in references [10, 12]. In this thesis, this method is reused with modifications and some extensions to solve radial- axial variation of blade geometry sections and combined with the PSCD blade design method through Bezier radial variation relations of blade sections from hub to tip to present 3D blade geometry.

In the preliminary design stage, velocities are specified by three velocity diagram parameters: flow coefficient ϕ; work coefficient ψ; and R_n reaction. In general the absolute (and relatives) velocities at any flow station between blade rows have axial C_x, tangential C_u and radial C_r component of velocities. In the radial direction $C_r = C_x tan\mu$ and in the tangential direction $C_u = C_x tan\alpha$, where at inlet and outlet flow angles of the blade will be the ones used to specify blade geometries. In the simple 2D velocity diagram the flow is assumed adiabatic, two dimensional, radial changes in streamline location through the stage are neglected, and the axial component of velocity is assumed constant. With these assumptions, the three major parameters [12, 13] are described as follows:

$$\phi \equiv \frac{C_x}{u} \Rightarrow \phi_{si} = \frac{C_x}{u}$$

$$\psi = \frac{-\Delta h_0, stage}{u^2} \Rightarrow \psi_{si} = \frac{-\left(C_{u,2} - C_{u,1}\right)}{u}$$

$$R_n \equiv \left(\frac{\Delta h_{st}}{\Delta h_0}\right)_{rotor} \Rightarrow R_{nsi} = 1 - \frac{C_{u,1} - C_{u,2}}{2u}$$

In the blade design process, simple and repeating velocity diagrams can be used as a first choice to specify three non-dimensional through flow parameters but in this thesis a general 3D velocity diagram has been used. It means the axial and peripheral velocities are not constant (C_x and u). In three dimensional through-flow velocity diagram with radial velocity variation C_r both values of work coefficient and flow coefficient are different at each inter-blade plane, and the diagram is not repeating. The selection of an acceptable velocity diagram is complex and affected by considering different performance and operation conditions. Wilson and Korakianitis [12] prefer a typical value of ϕ is about 0.6 and the work coefficient is between 1.0 and 2.0 for turbines, but the work coefficient is between -0.5 and -0.35 for compressor stages.

In this thesis, a 2D Navier-Stokes compressible and viscous calculations have been used for all blade sections from hub to tip, which is essential for blade shape optimization due to viscous effects such as boundary layer separations, shock wave and flow interactions. Mesh generator GAMBIT and flow solver FLUENT have been used in the computations. A reasonably high number of computational mesh elements is required for reasonably accurate calculations. The exact numbers depend on the geometry of the blade and its model. The mesh elements used for the sample section blades are: 25,076 quadrilateral cells; 49,604 2D interior faces; and 25,624 nodes for all zones. A 2D O-mesh and a Pave-unstructured mesh have been used in the compressible and viscous calculations. The Pave mesh consisted of a combination of structured and unstructured regions. The mesh around the airfoil consisted of twelve structured clustered O-grid layers with y^+ less than 5, and the remaining majority of the flow field was descritized with quadrilateral and a small numbers of triangular cells. The $k - \omega$ SST transition turbulence model has been used. The

PSCD method is highly flexible, accurate and robust to design all type of blades.

4.3 Blade shape parameterization

Aerodynamic performance of a turbomachinery blades is very sensitive to its shape (i.e surface curvature). Therefore, generally blade shapes must be parameterized with a large number of parameters. The sample blade from the combined method has been used to show the ability of the direct-surface-curvature method to design blade profiles from hub to tip and to build up three dimensional blade geometry. The 3D blade shape is represented by eleven blade sections, respectively at 0-100% (increment 10%). Each of these sectional profiles can be defined by a major parameters: throat to pitch diameter o/S; stagger angle λ; tangential lift coefficient C_L; control points of blade suction sides Xc_s, Yc_s; and control points for blade pressure sides Xc_p, Yc_p. All of these are presented through a third order Bezier spline curve from hub to mean and another third-order Bezier from mean to tip of the blade. Parameterization using Bezier spline is one of the most popular approaches for blade design geometries. This idea has been previously used by [8].

The method begins with solving radial momentum equation to obtain design parameter variations such as inlet flow angles, stagger angle, tangential lift coefficient and etc from hub to tip. Presenting the output parameters through the Bezier curve is an excellent guidance to reduce iterations and computational time for both direct and inverse design methods. Based on these modifications and the powerful direct surface-curvature method the blade geometry sections can be easily specified and do not need any previous experience to design blade sections through direct surface curvature method. The presenting variation of properties through a Bezier curve have been specified with three given data points, which are data points at hub mean and tip, two inputs data and one out put. Table 4.1 shows the 3D output variations from hub to tip for the sample blade. These data presented in this table have been calculated from the 3D streamline curvature method for the stator blade.

Table 4.1: Output parameters for stator from 3D streamline curvature (hub-tip)

Sections	α_1	α_2	ϕ_{in}-ϕ_{ex}	ψ	R_n	C_L
Hub	0.00000	68.29000	0.82000-0.75000	2.55000	0.39000	0.83661
1	0.00000	66.60000	0.80000-0.77000	2.41000	0.42000	0.90421
2	0.00000	65.94000	0.78000-0.77000	2.31000	0.44000	0.94045
3	0.00000	65.45000	0.76000-0.75000	2.21000	0.46000	0.97162
4	0.00000	64.88000	0.75000-0.74000	2.13000	0.48000	1.00504
Mean	0.00000	64.30000	0.73000-0.73000	2.08000	0.50000	1.03864
6	0.00000	64.00000	0.72000-0.72000	2.00000	0.51000	1.06401
7	0.00000	63.59000	0.70000-0.70000	1.93000	0.53000	1.09245
8	0.00000	63.22000	0.69000-0.69000	1.86000	0.55000	1.119631
9	0.00000	62.87000	0.68000-0.68000	1.74000	0.56000	1.1461
Tip	0.00000	62.47000	0.67000-0.67000	1.71000	0.58000	1.17393

Figure 4.1 (a, b) shows the variations of both non-dimensional throat to pitch ratio and stagger angle of the blade sections from hub to tip.

Figures 4.2 $(a, b, c, d, e$ and $f)$ show non-dimensional surface curvature control points of the main part of the suction side of the blade which are $XC2s$, $YC1s$, $YC2s$, $YC3s$, $YC4s$ and $XC5s$ respectively. Figures 4.3 $(a, b, c$ and $d)$ show non-dimensional surface curvature control points of the main part of the pressure side of the blade which are $YC1p, YC2p, YC3p$ and $XC5p$ respectively. With these informations for the suction and pressure sides of the blade the designer is easily able to built up the 2D blade profiles from hub to tip. In addition to that, the blade geometry sections have been prescribed while keeping the tangential lift coefficient variations from hub to tip especially the high value of this parameter which is 1.174 at the tip section of the blade. keeping the high value of this parameter or variation has a great effect on the shape of the blade from hub to tip and it is reflected to improve efficiency of the turbomachinery blades. However, all of the previous blade design geometry methods have difficulty to keep the tangential lift coefficient as high as possible, which is based on the number of blades, the outlet angle and the pitch of the blade, from hub to tip. In the open literature, the value of the tangential lift coefficient is kept between (0.8 -1.0) for all blade design methods.

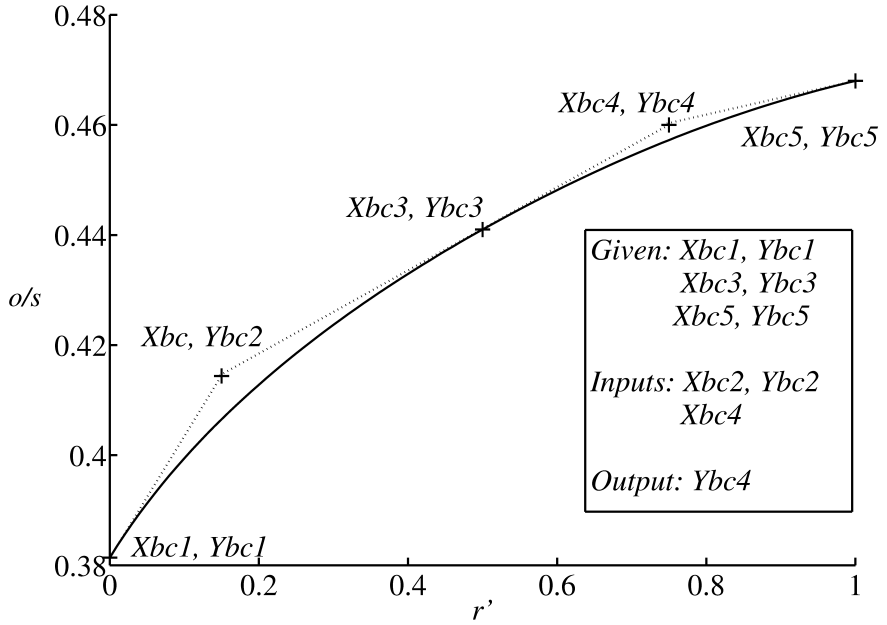

(a)

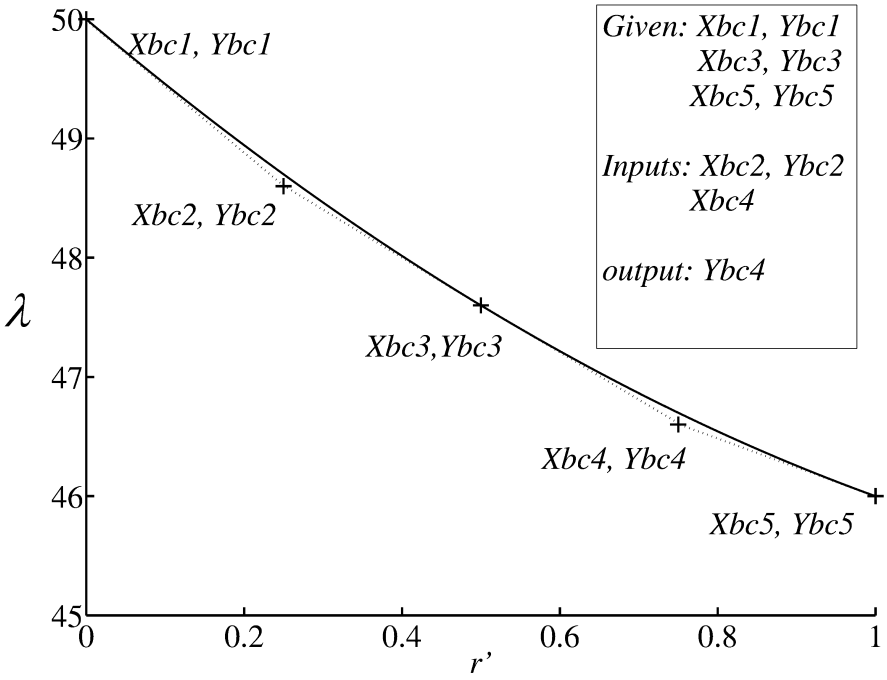

(b)

Figure 4.1: a- Throat to pitch ratio from hub to tip. b- Stagger angle variation from hub to tip

4.4 Blade stacking, design and off-design performances

Three dimensional of turbomachinery blade is also challenging to understand flow properties around the blade. This demands to create a fully three dimensional or

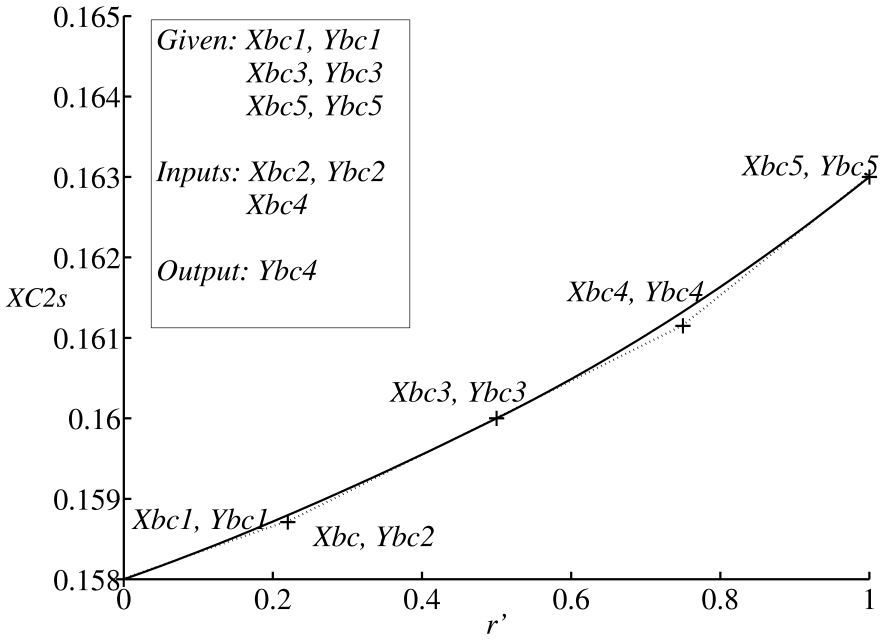

(a)

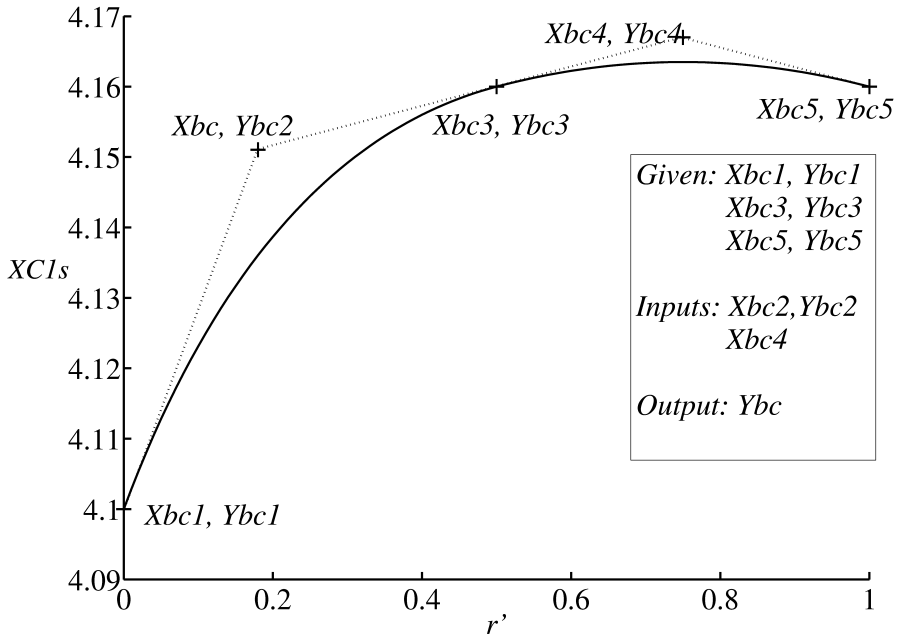

(b)

stacking 2D blade sections to analyze aerodynamic performance and heat transfer.

Three dimensional blade sections can be stacked through a center of gravity, trailing edge or leading edge of the blade as well. Blade example has been used and stacked according to different center of gravity (non-radial stacking) of each blade instead of taking an average value of all of them (radial stacking), which is

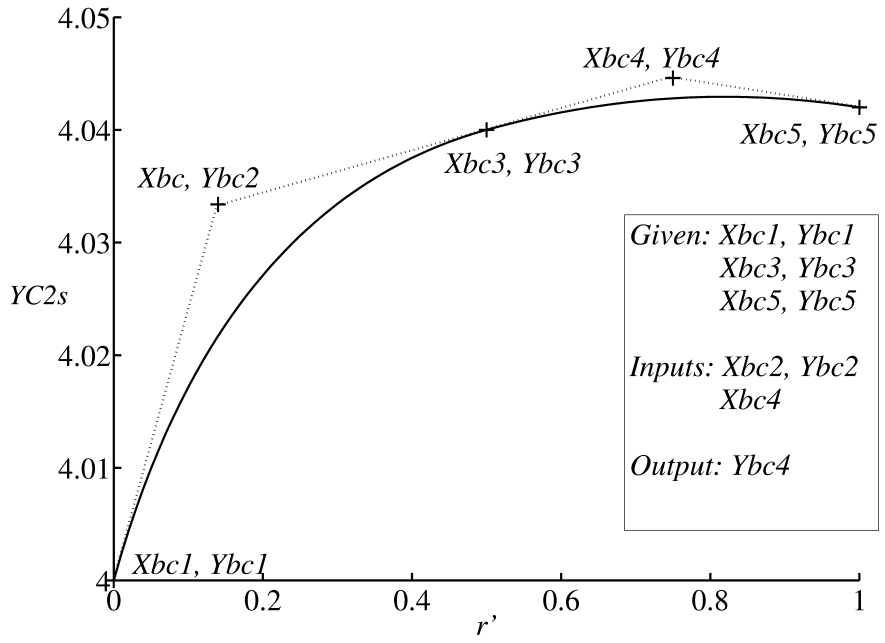
4.05
4.04
4.03
4.02
4.01
4
YC2s
0
0.2
0.4
0.6
0.8
1
r'
Xbc4, Ybc4
Xbc5, Ybc5
Xbc3, Ybc3
Xbc, Ybc2
Xbc1, Ybc1
Given: Xbc1, Ybc1
Xbc3, Ybc3
Xbc5, Ybc5
Inputs: Xbc2, Ybc2
Xbc4
Output: Ybc4

(c)

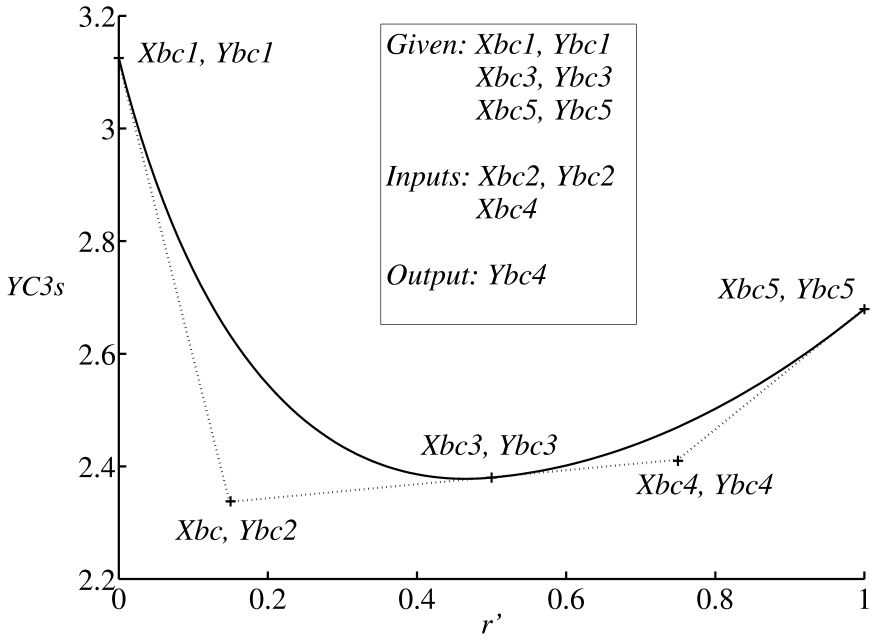
3.2
3
2.8
2.6
2.4
2.2
YC3s
0
0.2
0.4
0.6
0.8
1
r'
Xbc1, Ybc1
Xbc5, Ybc5
Xbc3, Ybc3
Xbc4, Ybc4
Xbc, Ybc2
Given: Xbc1, Ybc1
Xbc3, Ybc3
Xbc5, Ybc5
Inputs: Xbc2, Ybc2
Xbc4
Output: Ybc4

(d)

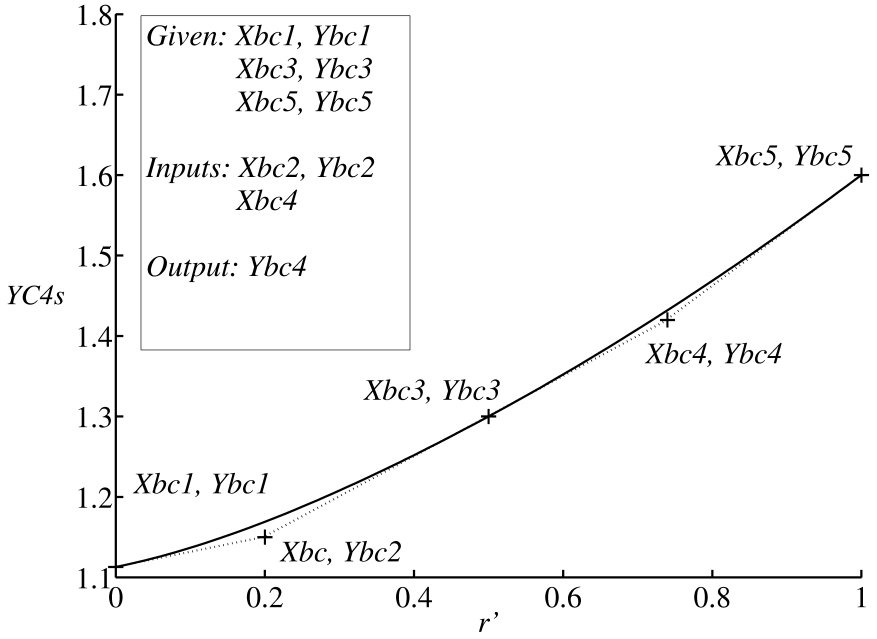

(e)

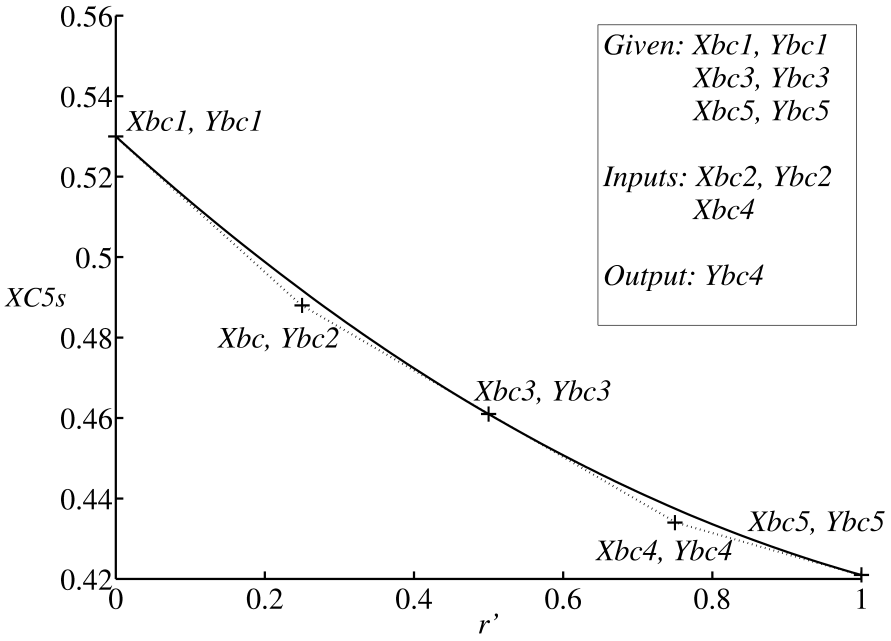

(f)

Figure 4.2: Hub to tip non-dimensional surface curvature control points of the suction side of the blade, a- $XC2s$, b-$YC1s$, c-$YC2s$, d-$YC3s$, e-$YC4s$, f-$XC5s$

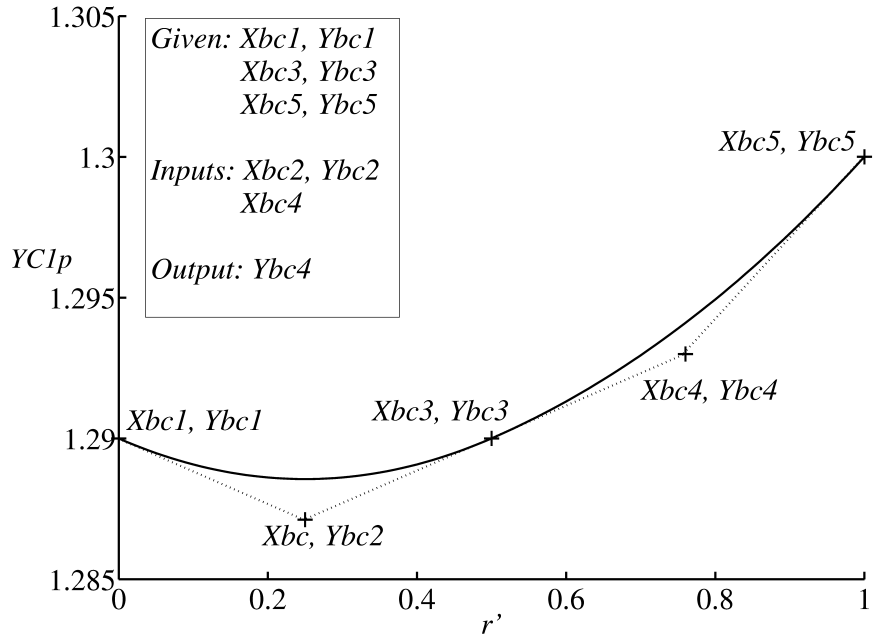

(a)

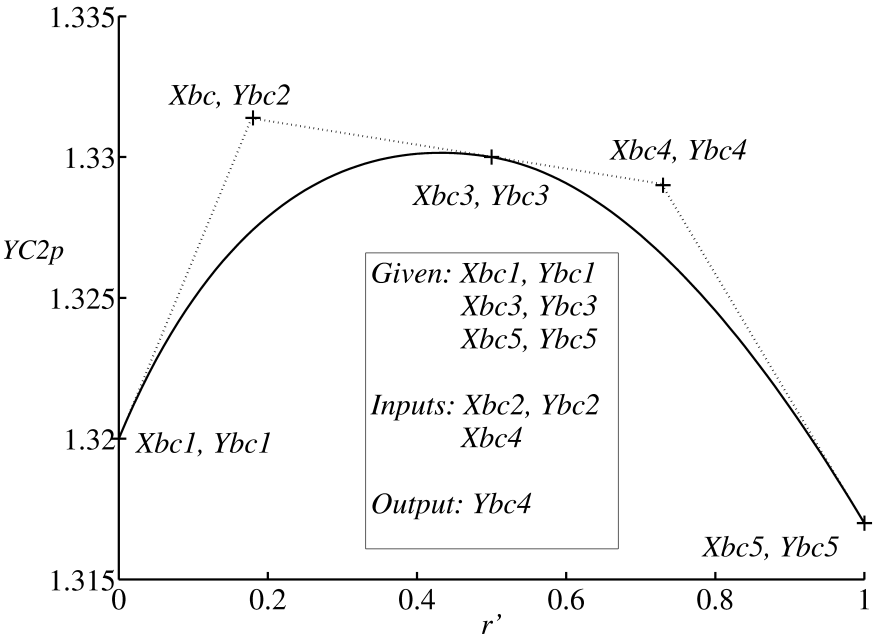

(b)

turned out with the irregular blade shape (e.g. lean and dihedral) across the span. Blade parameters have been used to design eleven sections across the span of the blade. These blade sections, based on the variation of parameters from hub to tip, are able to reduce the computing time and iteration approach. The sample stator blade of the first stage has been designed at the boundary condition of the inlet

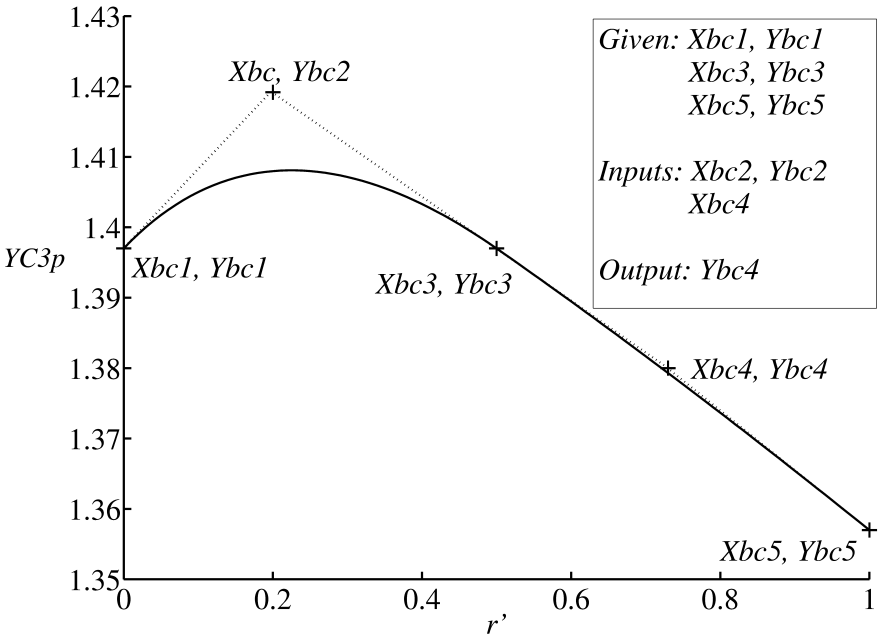

(c)

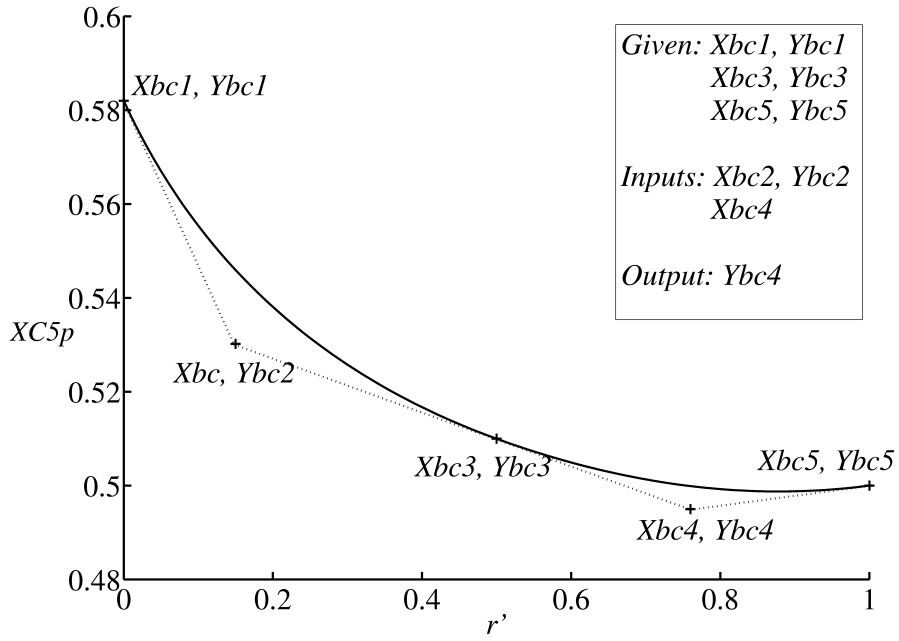

(d)

Figure 4.3: Hub to tip non-dimensional surface curvature control points of the suction side of the blade, a- $YC1p$, b-$YC2p$, c-$YC3p$, d-$XC5p$

total temperature 1000 K, the inlet total pressure of 532 kPa and the outlet static pressure of 442.678 kPa. These specifications have been specifically chosen around inlet flow angles of zero degrees (to illustrate the effect of positive and negative

inflow angles from this value for the hub, mean and tip sections) and at a different outlet flow angles from hub to tip as shown in table 4.1. The flow solutions have been obtained with FLUENT solver specifying free-stream turbulence intensity of 10% and using the $k-\omega$ SST transition turbulence model. The solutions have been obtained for design point conditions as well as for incident angles of -5°, +5°. The radial and non-radial 3D blade shapes have been presented in Figs. 4.4 (a and b). With modifications on the stacking line through Bezier variation of the parameters the resultant aerodynamic performance can be improved, which is as a result of reducing flow disturbances, secondary flows near the endwalls and removing separation bubbles around the leading edge for all sections from hub to tip at design and some range of off-design conditions.

Figures 4.5 (a, b and c) show the blade sections from hub to tip at different position from (0-100)%. Figures 4.6 (a and b) show the isentropic surface Mach number distributions and Mach contours around the blade section at the hub for design conditions. The boundary layer displacement thickness has been evaluated for the design conditions and off design incident angles of $-5^o, +5^o$ for the hub mean and tip sections of the blade respectively. At design point conditions the sample blade in figures 4.6 exhibits perfectly acceptable behavior, without any leading-edge flow disturbances at the joining points of the blade surface with the leading edge circle. Off-design conditions $\pm 5°$ has been shown in figures 4.7 (a and b). These figures also have excellent performance for positive and negative incidences. Figure 4.8 (a, b) shows the surface Mach number distributions and boundary layer displacement thickness calculations for the hub section at design and off-design conditions. Figure 4.9 shows the aerodynamic performances of the mean section of the 3D blade geometry sections, which has an acceptable value of the surface Mach number distributions and the highly smoothed distributed Mach contours around the blade section. The off-design conditions for the mean section of the 3D blade have been shown in the figures 4.10 (a and b). Figure 4.11 (a, b) shows the surface Mach number distributions and boundary layer displacement thickness calculations for the mean

section at design and off-design conditions.

Figure 4.12 (a and b) show the isentropic viscous Mach number distribution at tip section of the 3D blade geometry profiles. Off-design conditions $\pm 5^{\circ}$ has been shown in figures 4.13 (a and b). This section has been specified with high tangential lift coefficient, which is highly difficult with the rest of the blade design methods. In addition to that there is no disturbances and separation bubbles at design and off-design conditions for the tip sections around the leading edge of the blade. Figure 4.14 (a, b) show the surface Mach number distributions and boundary layer displacement thickness calculations for the tip section at design and off-design conditions. These results confirmed that how the surface curvature contributes to produce high efficiency turbomachinery blades.

4.5 Conclusion

A new design environment, which is similar to [8], presented for three dimensional turbomachinery blades based on streamline curvature method, the PSCD blade design method, with blade parameter variations from hub to tip through Bezier curve relations, and using a flow solver to analyze flow properties. Presenting the radial variation of blade profile parameters from hub to tip through a Bezier curve makes the PSCD direct blade design method more accurate and robust than the rest of the blade design methods, which require many iterations, computation time and controlling the blade geometries. The 3D velocity diagram are used as inputs for the 3D blade design method. In this method the surface curvature of the blade profiles are specified from the leading edge to the trailing edge in a way that there is no discontinuity in curvature and the slope of curvature, and this is reflected to produce highly smoothed surface. With this modification the resulting surface blade free from disturbances and separation bubble around the leading edge and aerodynamic performances are improved at design and off-design condition. In addition to that, the iteration and computational times are highly reduced to design blade sections

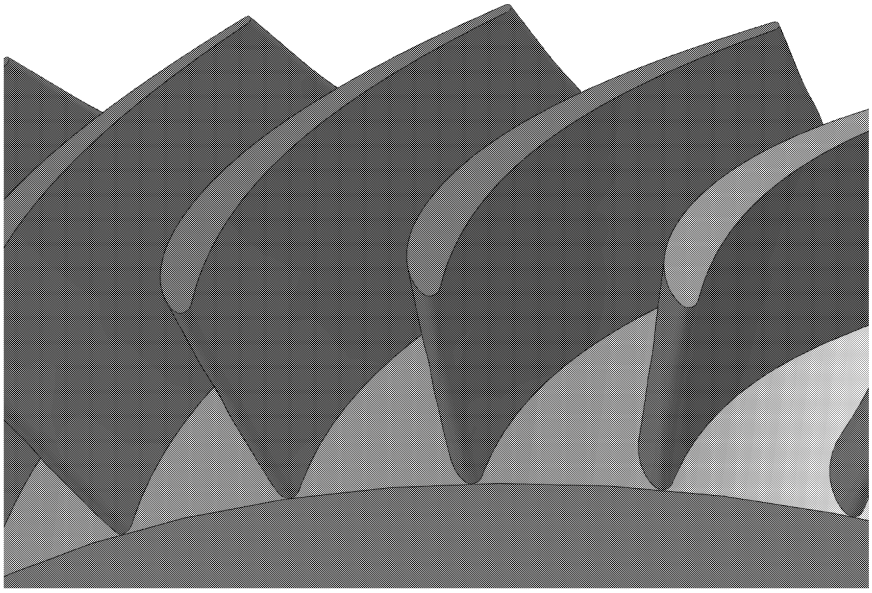

(a)

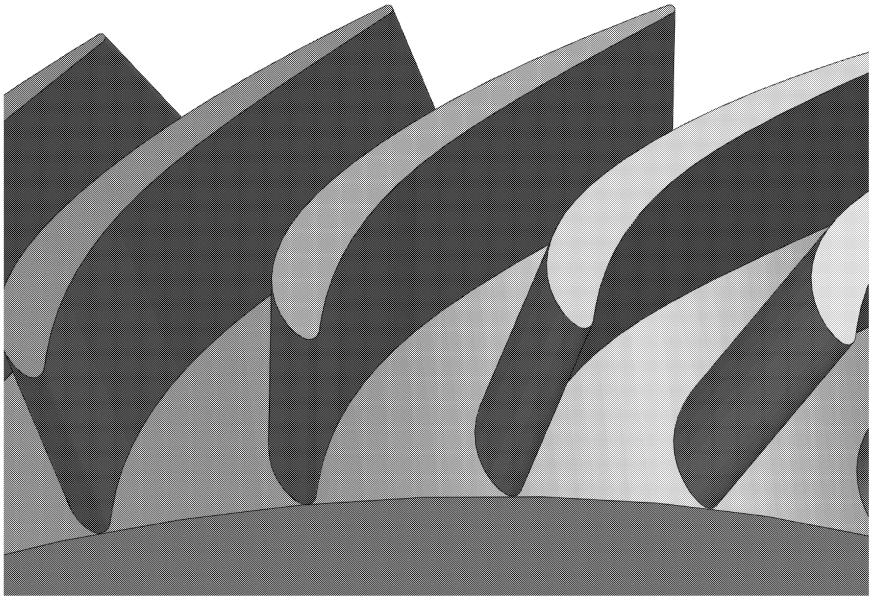

(b)

Figure 4.4: Sample of blade stacking: a- Non-radial stacking 3D blade shape. b- Radial stacking 3D blade shape

from hub to tip. The method is smoothly able to design all blade section geometries from hub to tip. The 2D center of gravity, leading edge and trailing edge are suitably stacked in the non-radial direction until the resulting blade shape has a desirable aerodynamic and structural characteristics. As known from the open literature [127, 128, 133, 134, 137–139], the possibility of improving efficiency, reducing secondary flow and increasing operation range can be achieved through the modification of the

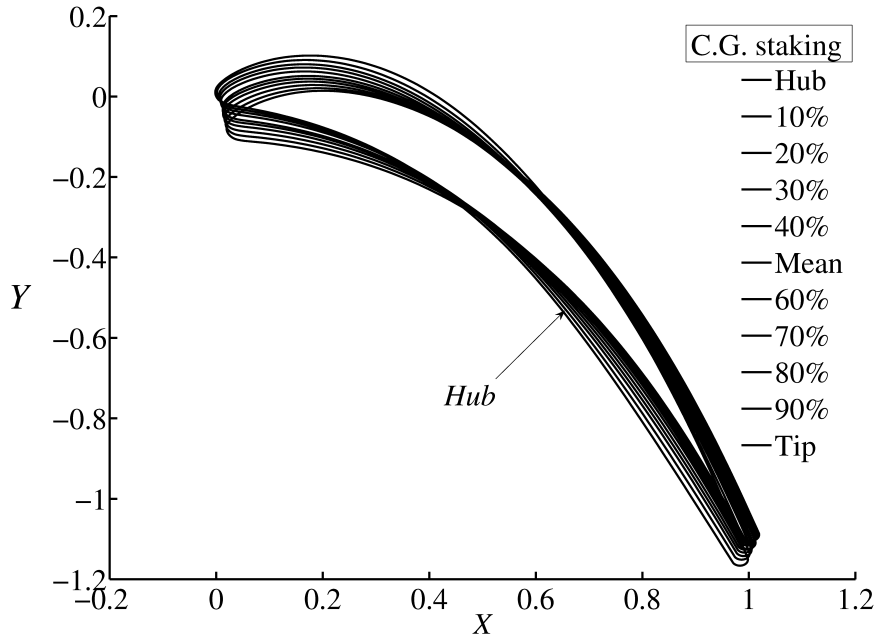

(a)

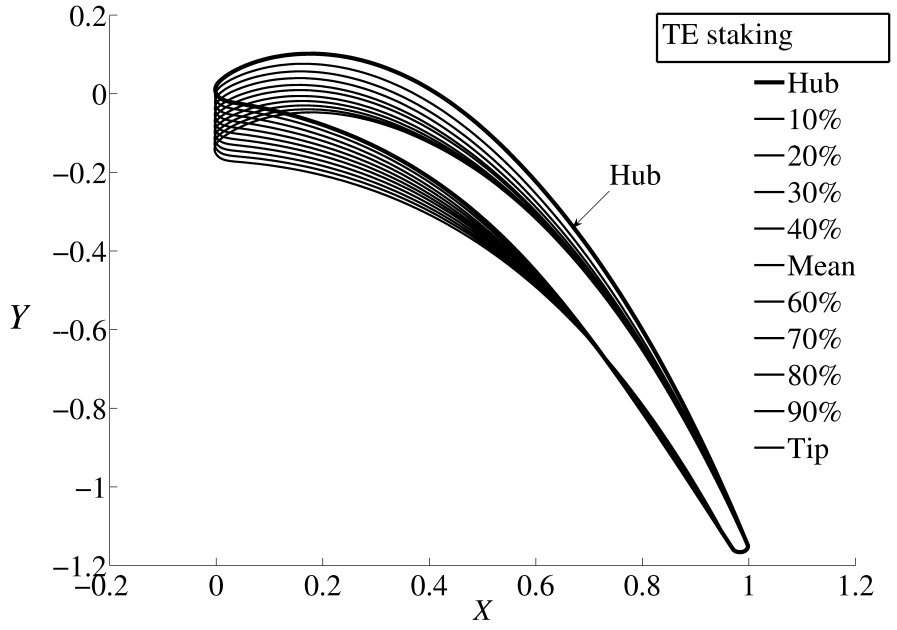

(b)

staking line of the 2D blade profiles(e.g. lean and dihedral). The three dimensional through flow method is combined with the 3DE PSCD method by varying blade parameters through Bezier curves from hub to tip. These modifications make the leaned and dihedral blade shapes are a function of these parameters. The resultant blade geometry sections have been modified and the aerodynamic performances (e.g.

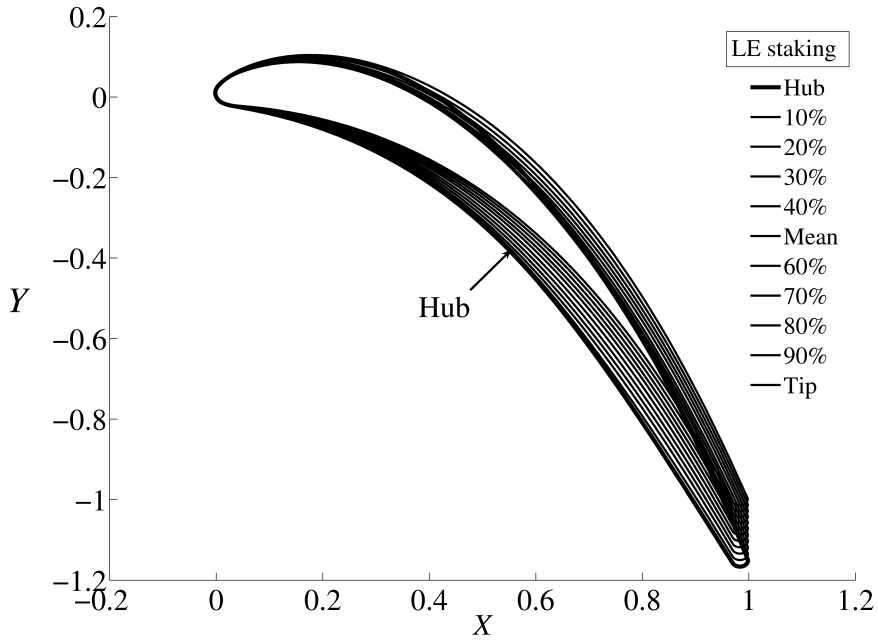

(c)

Figure 4.5: Blade stacking: a- Center of gravity, b- Trailing edge, and c- Leading edge

pressure distribution and isentropic Mach number) have been improved through removing flow disturbances, decreasing secondary flow, removing separation bubble at design and some range of off-design conditions (in this work, -5° incidence has been used).

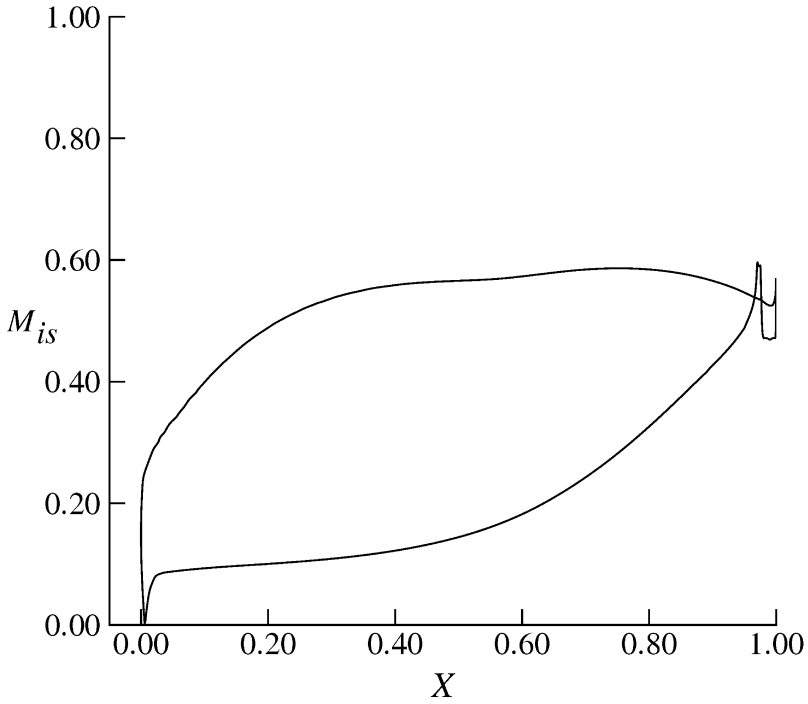

(a)

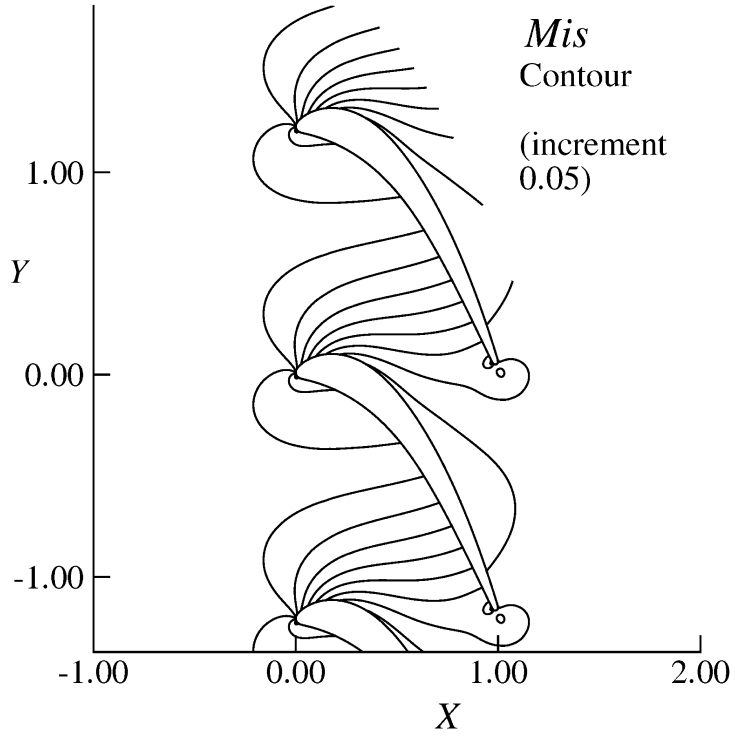

(b)

Figure 4.6: Hub: a- Isentropic surface Mach number distribution at design incidence. b- Mach contours at design condition

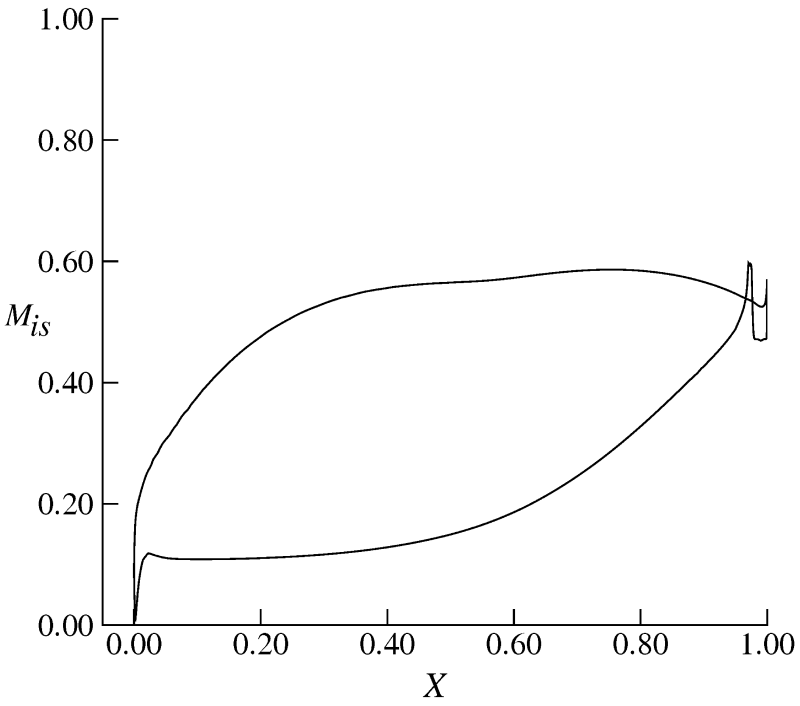

(a)

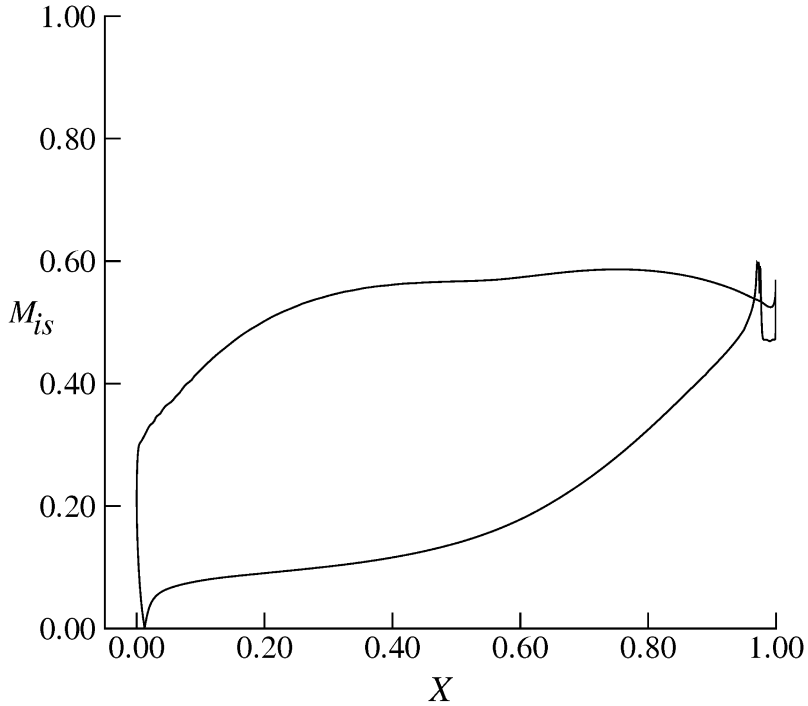

(b)

Figure 4.7: Hub: a- Isentropic Mach number distribution at off-design incidence -5°. b- Isentropic Mach number distribution at off-design incidence +5°

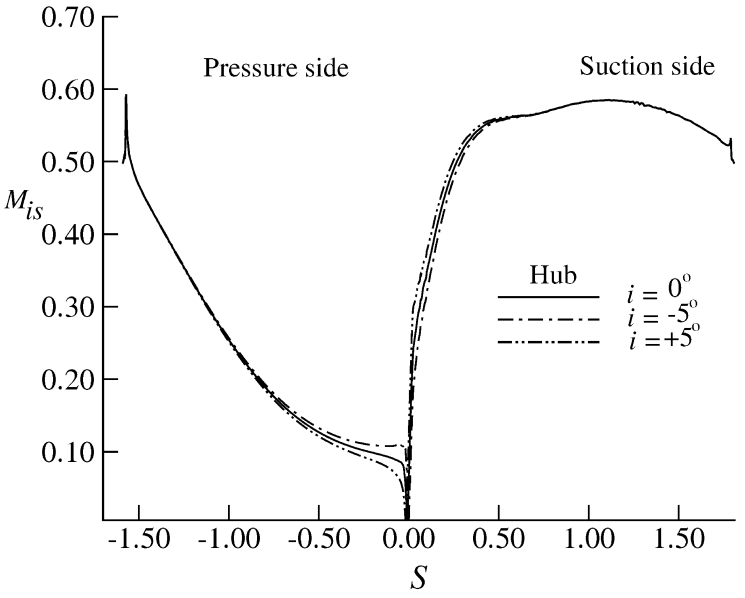

(a)

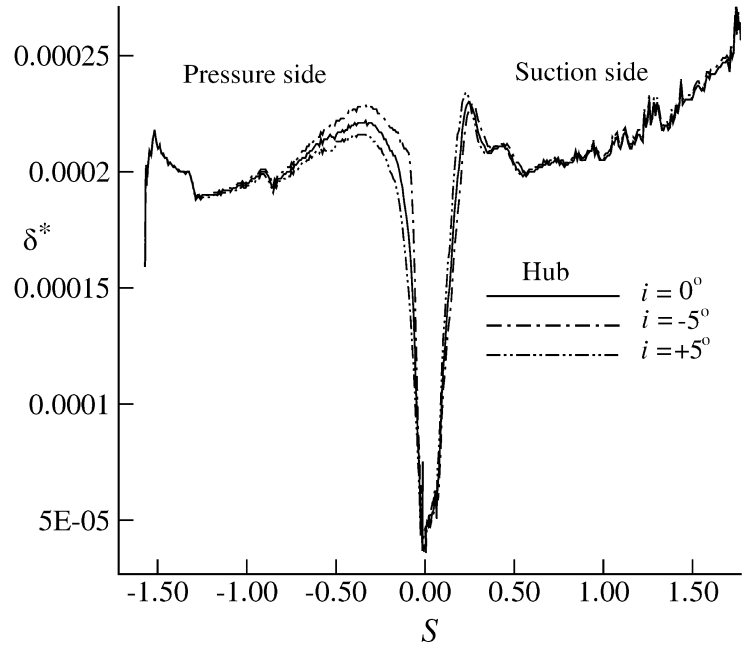

(b)

Figure 4.8: a- Surface Mach number distributions for hub at design and off-design conditions. b- Boundary layer displacement thickness calculations

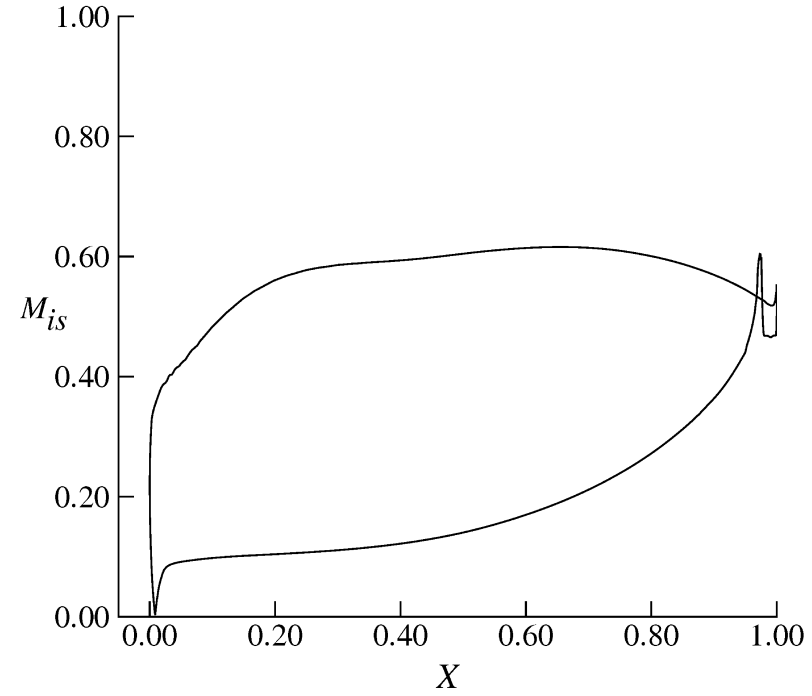

(a)

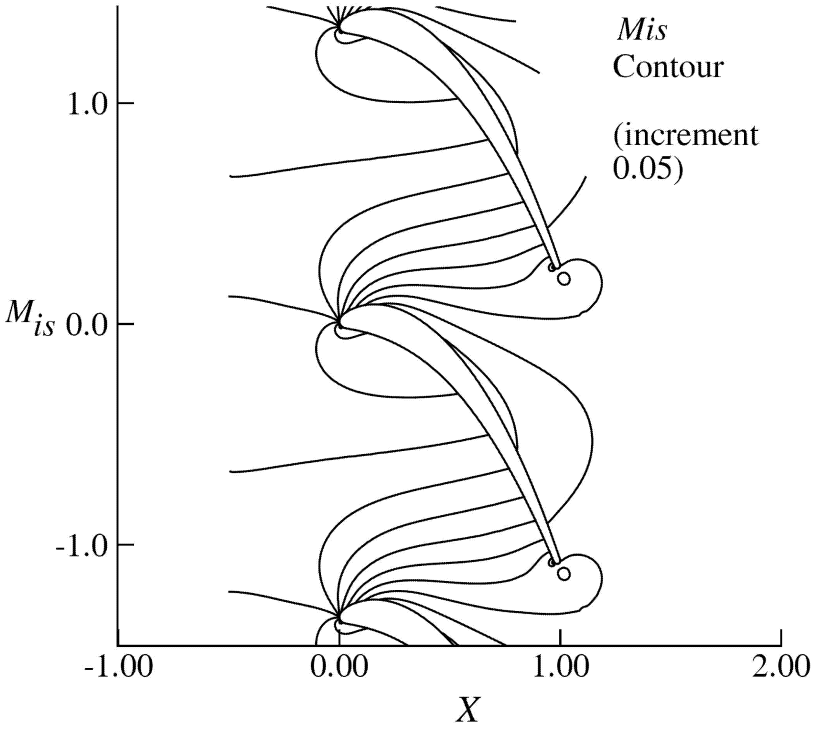

(b)

Figure 4.9: Mean: a- Isentropic Mach number distribution at design incidence. b- Mach contours at design condition

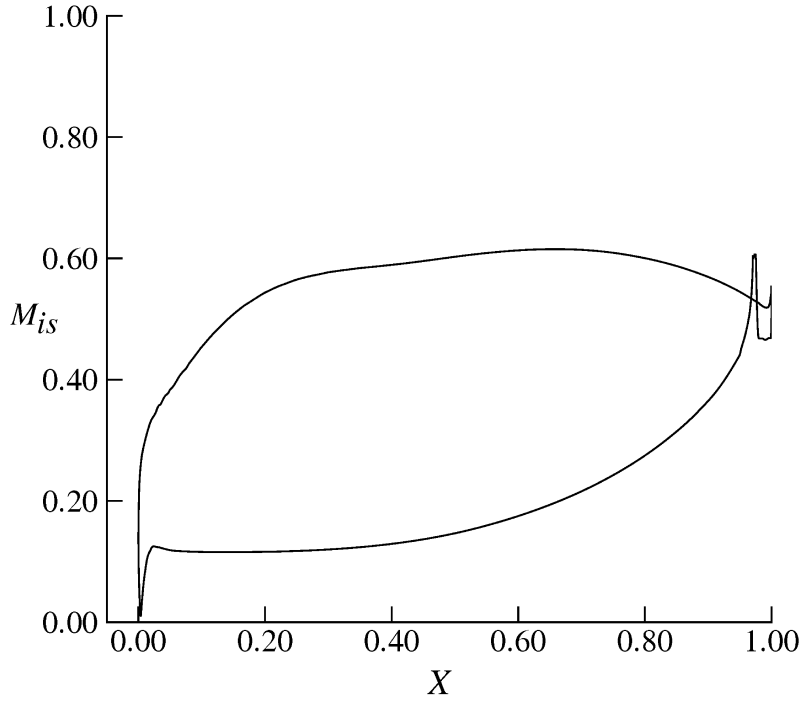

(a)

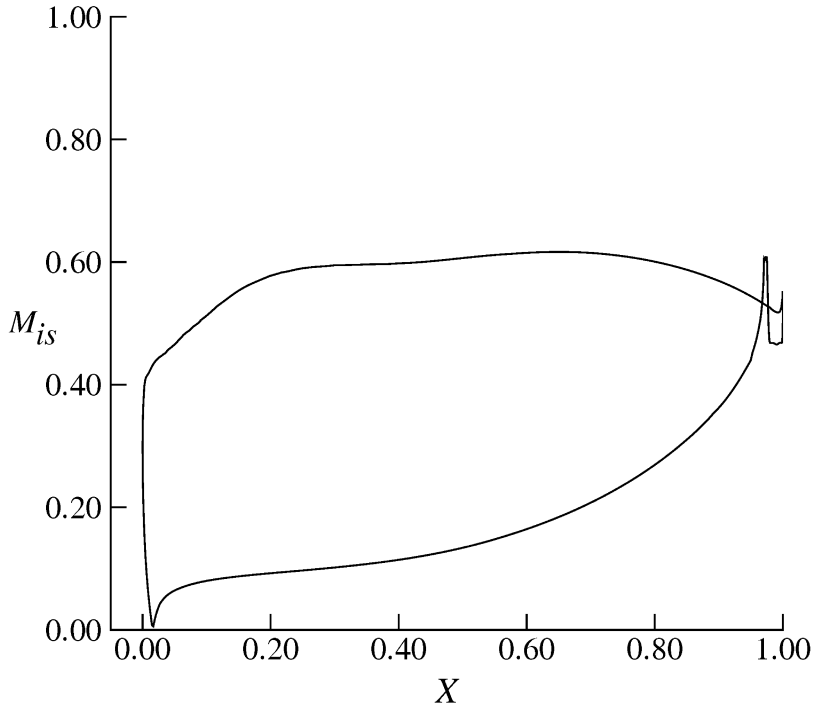

(b)

Figure 4.10: Mean: a- Isentropic Mach number distribution at off-design incidence -5°. b- Isentropic Mach number distribution at off-design incidence +5°

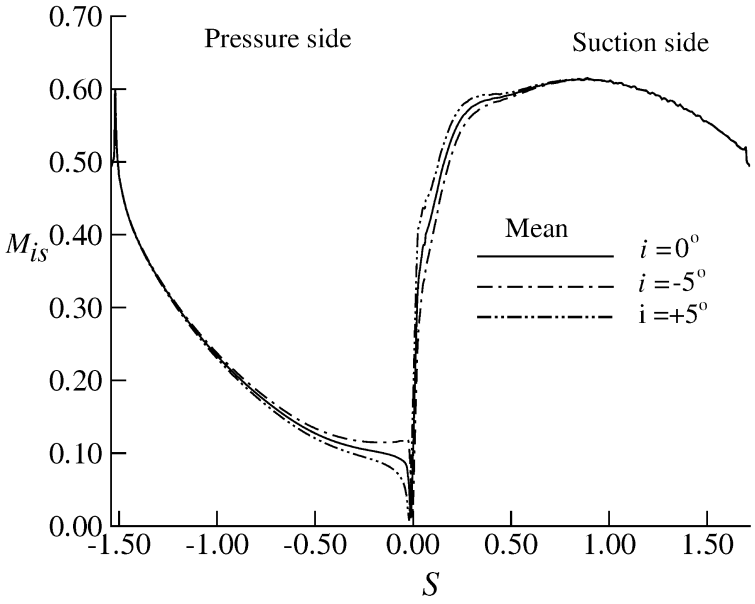

(a)

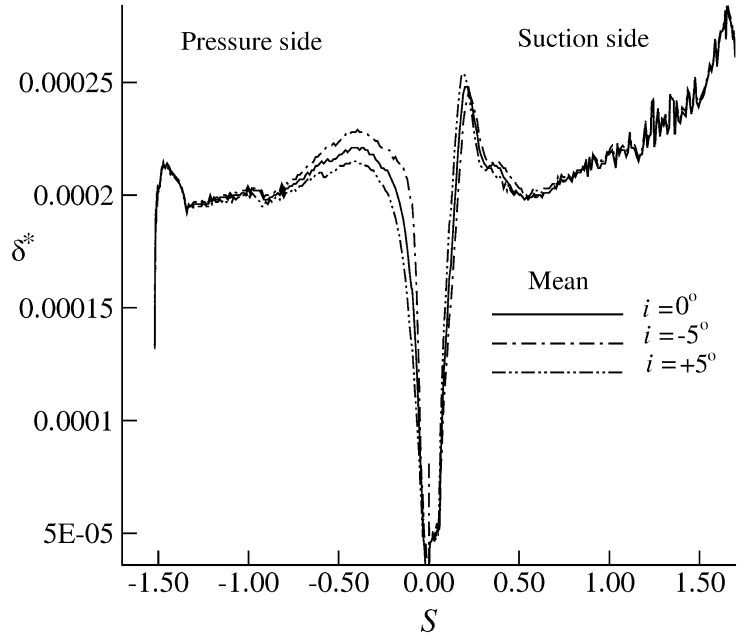

(b)

Figure 4.11: a- Surface Mach number distributions for the mean section at design and off-design conditions. b- Boundary layer displacement thickness calculations

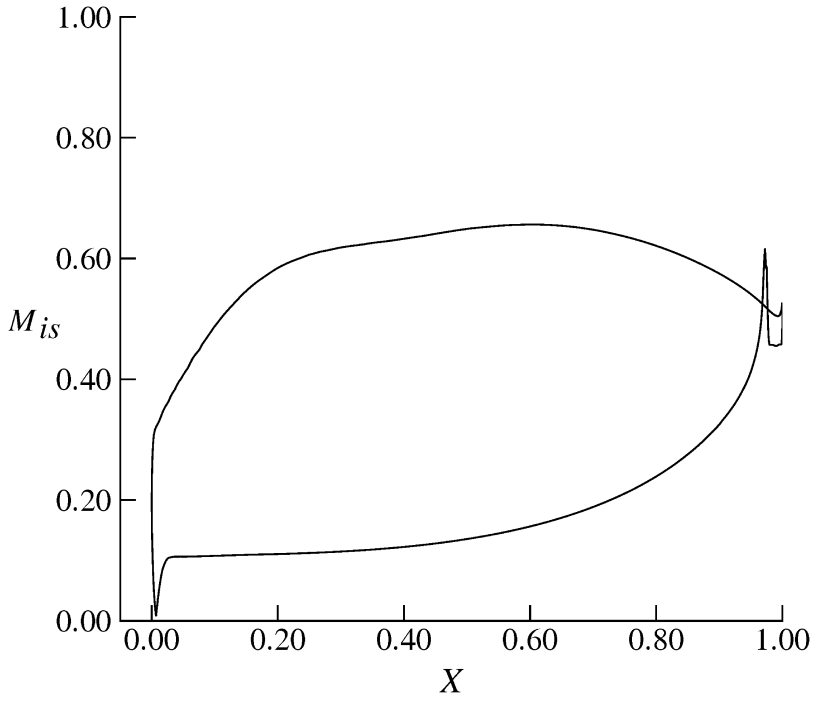

(a)

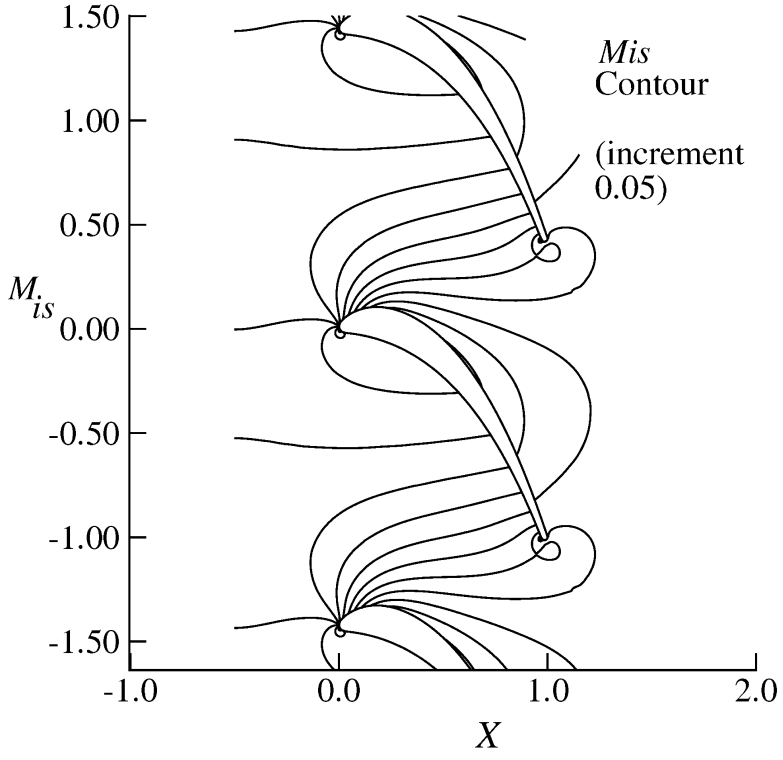

(b)

Figure 4.12: Tip: a- Isentropic Mach number distribution at design incidence. b- Mach contours at design condition

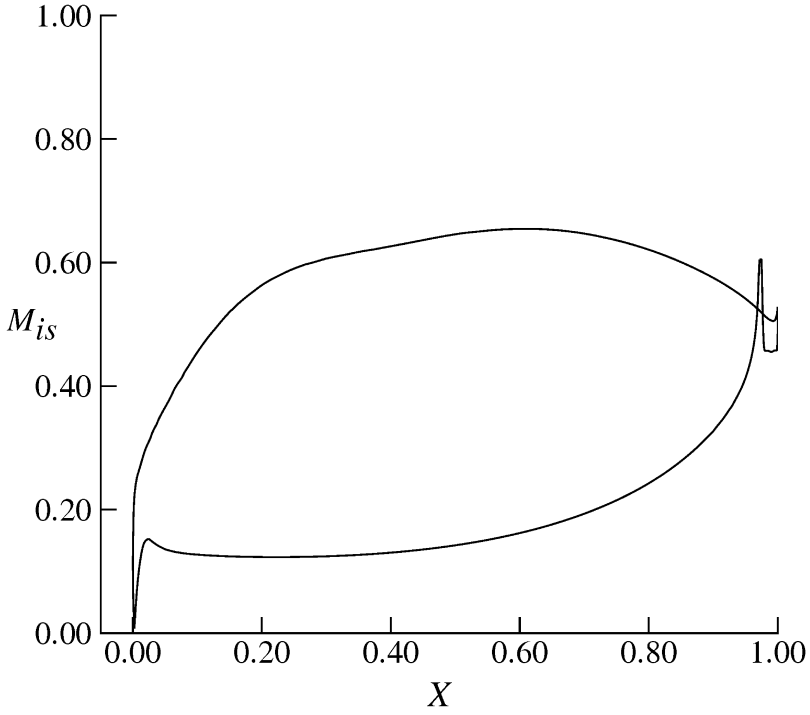

(a)

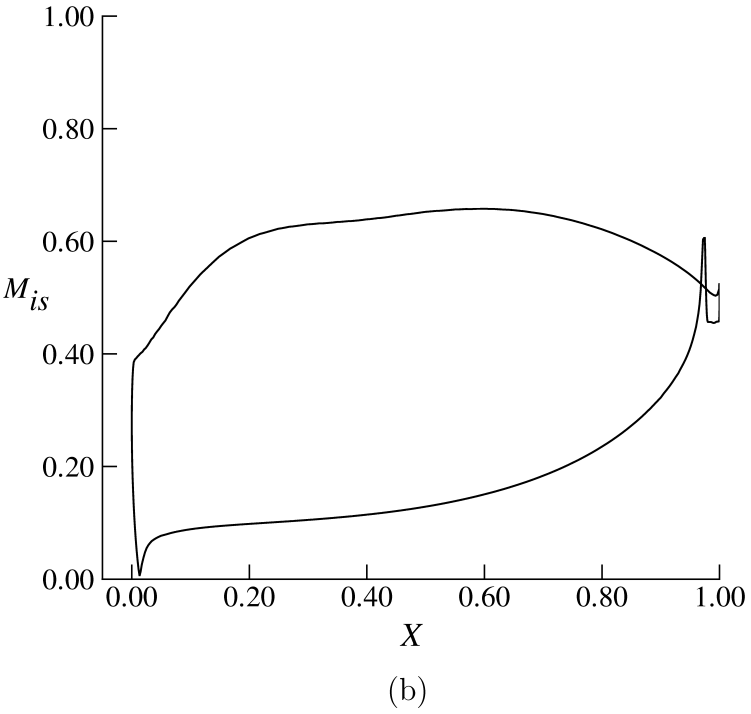

(b)

Figure 4.13: Tip: a- Isentropic Mach number distribution at off-design incidence -5°. b- Isentropic Mach number distribution at off-design incidence +5°

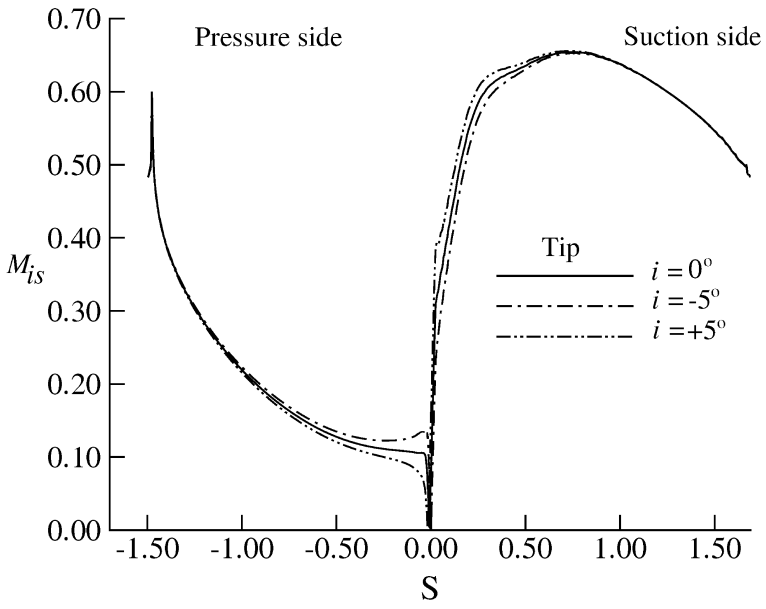

(a)

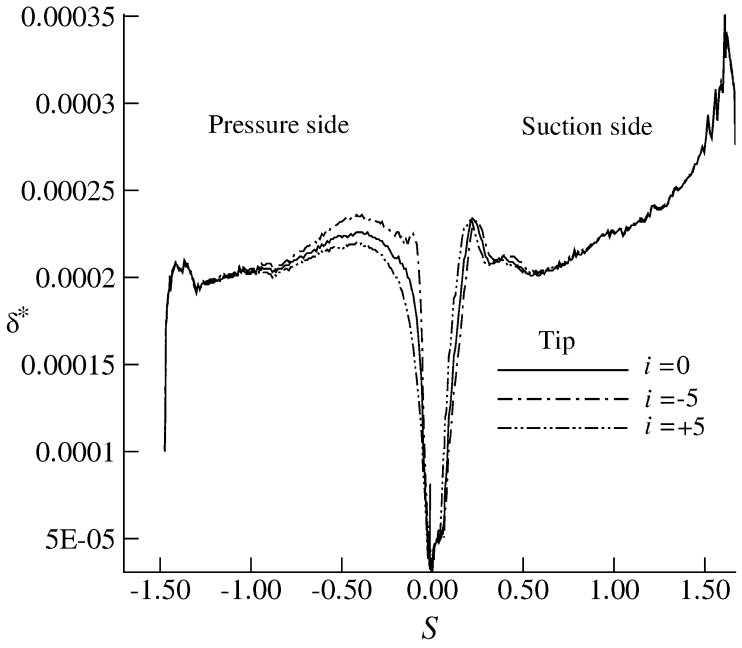

(b)

Figure 4.14: a- Surface Mach number distributions for tip section at design and off-design conditions. b- Boundary layer displacement thickness calculations

Chapter 5

Surface curvature distribution effects on heat transfer of turbine blades

5.1 Introduction

One of the main objectives in saving energy resources is to design high efficient energy conversion system. Gas turbine is one of the common device for power production and energy conversion, any improvements in its efficiency leads to a major contribution to energy resource savings. Heat transfer is an important design consideration for all parts of a modern gas turbine, but especially the combustor, turbine and exhaust nozzle. The possibility of achieving higher turbine inlet temperature, reducing profile losses, shock losses, trailing edge losses and cooling losses are directed to increase gas turbine performance. The accurate knowledge of heat transfer distribution on various engine components such as blades, end walls is of primary importance in improving the efficiency of the gas turbine engines. Documentation in this area is noticeably scare and there is a very little reliable experimental data to be found that could be used for optimization or improvements. This difficulty makes inaccurate prediction of heat transfer calculation. However, parallel to that

there is some good results of heat transfer data available in the open literature. Consigny and Richards [142] showed detailed heat transfer measurements on gas turbine rotor blade under differing conditions of Mach number, Reynolds number, inlet flow angle and flow turbulence level. They mentioned that the heating rate and its value is depend on the state of the boundary layer, and they showed several area of uncertainty in the flow behaviour such as separated boundary layers, trailing edge flow and shock boundary layer interaction. Camci and Arts [143, 144] presented the experimental and numerical calculation on a film-cooled gas turbine blade. They explained that the boundary layer development has a great effect on the connective heat transfer with and without film cooling. Arts [145, 146] explained detailed of heat transfer measurements and computational prediction for highly turbine nozzle guided van and rotor blade. He argued that the behaviour of the boundary layer is affected by the value of the Mach number and turbulence intensity as well. Many authors [147–164] have investigated measurement and computational prediction of surface heat transfer coefficients and its effects on blade performance and consequently on the overall efficiency of the engine. Overall, they explained any improvement in the boundary layer development has a significant effect on the improvement of the surface heat transfer distribution with removing spikes and dips in the Nusselt or Stanton number distribution around the cascade.

Manna [165] redesigned one test case of VKI blade under certain conditions. He used third order Bezier spline for the whole suction and pressure sides and including the circle or ellipse for the leading and trailing edges. He investigated the possibility of a well-designed existing turbine blade cascade by addressing the issue of the direct control of the thermal load which includes control points of the Bezier spline and decreasing total to total pressure losses, increasing load coefficient and reducing heat heat transfer coefficient. However, he used a first derivative to keep surface continuity between joint points and still has a difficulty to keep the continuity at second and third derivatives. In another words, there is still discontinuity in its surface curvature of the designed modified blade which is similar to the original

blade. In addition to that, with his technique he had not able to improve the original blade with keeping all design conditions as it was used in the blade design methodology for the VKI blade such as loading coefficient, inlet and outlet angles, etc. He designed his own blade with different design conditions based on VKI blade.

The objective of this chapter is to illustrate the heat transfer advantages of the PSCD blade design method described above. The blade is split into three segments for suction and pressure sides, in addition to the circles or ellipses for the leading and trailing edges. The method is used for profiles which guarantee the adequate representation of all type of blade shapes with a reduced parameter and keeping the curvature continuity, based on the curvature and the slope of the curvature, between line segments and also between the circle and the rest of the blade. To our knowledge, this is the second application of using Bezier curves to enhance the heat transfer performance of blades. This is done by reducing the local surface heat transfer coefficient by removing or eliminating the flow disturbances, spikes and dips in the surface pressure and Nusselt number distribution. In this chapter two test cases, NASA and VKI, have been redesigned to improve their aero-thermal performance. Results show excellent agreement between the experimental and calculation isothermal surface Mach number distribution and very good agreement between experimental and computational surface Nusselt number. Some discrepancies (especially for the suction side of the NASA blade) are due to limitations in the the turbulence models in predicting heat transfer calculation, and also due to limitations of the experimental data. However, the important thing is smoothing the blade surface and removing the spikes and dips using the PSCD method has a significant improvement on the blade surface Nusselt number distribution, and decreasing local heat transfer coefficient. This is another illustration of the capability of the PSCD blade design method to improve aero-thermal performance of turbomachine blades.

5.2 Blade geometry and surface heat transfer effects

Two sample blades, H1 and H2, have been redesigned and compared with the original blades, NASA and VKI, as shown in Fig. 5.1 . The figure shows small changes between the original blade and the modified blades, but there is a significant improvement in their performance and surface heat transfer distributions around the blade (they will be discussed later). Blade parameters and representative blade points for H1 and H2 are in QMUL-EGR-2010-01 confidential report (available from Professor Korakianitis). The surface curvature direct blade design method ensures the designer how it is possible to remove any flow discontinuities from the leading-edge stagnation point to the trailing edge stagnation point of the blade. Of course, it is demanded for too-high adverse pressure gradients for the flow conditions the discontinuity will still occur. These improvements are reflected to remove any spikes and dips in the surface Stanton number distribution or surface heat transfer coefficient around the blade and reflected to decrease the heating up around the discontinuity point and increased the overall performance.

Aerodynamic performance and surface heat transfer of turbomachinery blades are very sensitive to its shape (i.e surface curvature). Therefore blade shapes must be parameterized with a large number of parameters. However, the PSCD method, with fewer than 25 parameters, enables the designer to produce a very complex shape while keeping the continuity and smoothing the blade surface. In the direct blade design method, the surface curvature can be used as a mirror for the surface pressure or Mach number distribution around the blade. It means any change in the surface curvature directly reflects to the change in the surface pressure or surface Mach number and consequently on heat transfer distribution. This facility, which is only exist in the direct surface curvature method, helps the designer to analyze graphically blade performance before analyzing the flow around the blade more accurately than the rest of the blade design methods. This means before analyzing

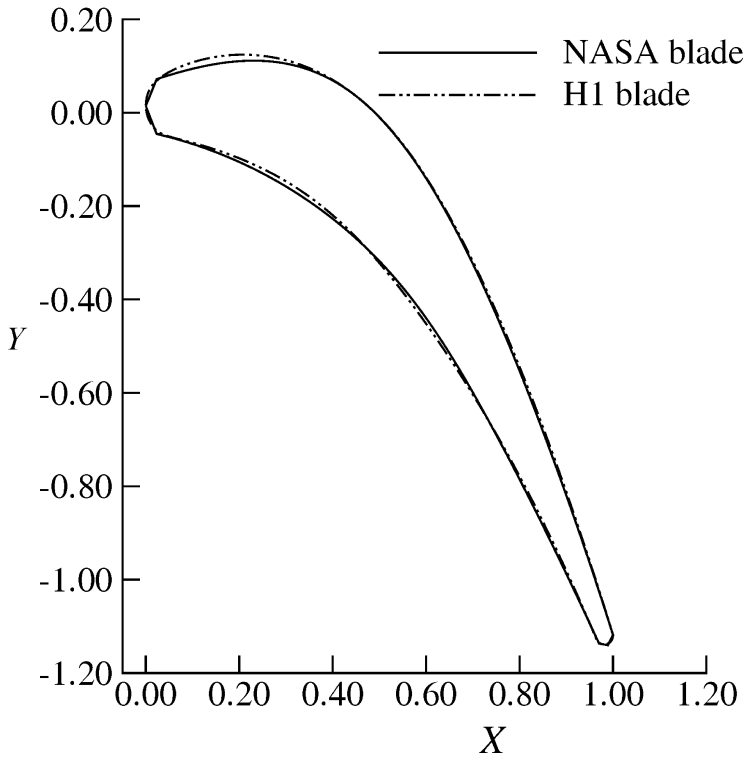

(a)

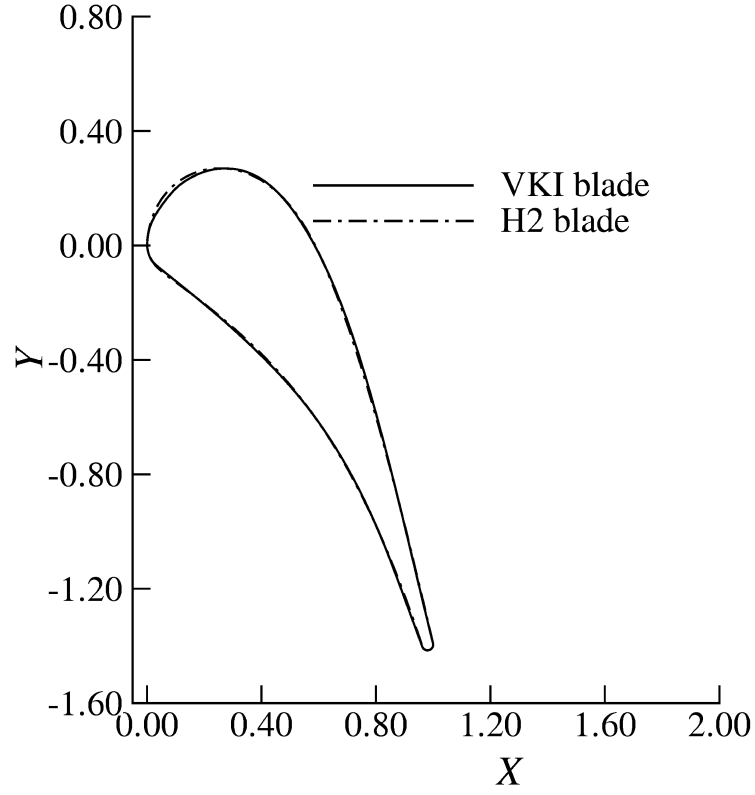

(b)

Figure 5.1: Blade geometries. a- NASA and H1 blades. b- VKI and H2 blades

the flow the designer is able to remove discontinuities in the slope of surface curvature of the blade, enabling design of high efficiency blades in reduced computer times. In addition to that these also can be used as a best guidance for the prediction of the surface heat transfer distribution around the blade. Proper aerodynamic description of the flow field, which provides the boundary conditions for the heat transfer calculation, is essential if the predicted heat transfer distribution for the surface of the specific component is to be believed.

Experimental data published in [99–103] clearly indicate local kinks in the surface pressure or Mach number distribution of blades, which is the result of surface curvature discontinuity between line segments or between the leading edge and the rest of the blade. These, "kinks" affect boundary layer performance, which is directly influence the surface heat transfer distribution around the blade, and blade efficiency. These difficulties in the surface pressure or Mach number distribution can be easily removed through the PSCD blade design method. In the following the effects of blade surface curvature smoothness on blade surface heat transfer distribution will be explained.

Two test cases have been redesigned, firstly to show the ability of the method and secondly to show how the surface heat transfer distribution can be affected by any small improvement in the surface curvature, which includes removing discontinuity between line segments and smoothing the blade surfaces. In other words, removing discontinuity (kinks) in the surface curvature are reflected to decrease heat transfer coefficient and results in increasing the overall performance.

The first test case is the United Technology Research Center(UTRC) 1.5 stages large scale rotating rig(LSRR). The stator has only been redesigned, from 1.5 stages, for aerodynamic and surface heat transfer distribution purposes. The test case was performed at the following inlet and outlet boundary conditions: inlet Mach number 0.0704; inlet Reynolds number 247,156; inlet static pressure 100,979 Pa; inlet static temperature 288.1 K ; exit static pressure 100,500 Pa, and wall average temperature 301.68 K. The surface curvature of the original blade (evaluated from the original

data points) and the H1 blade have been shown in Fig. 5.2. The figure shows the discontinuity in the leading edge part of the blade for both sides. The main part of the original suction surface curvature looks smoother as well when compared with the modified one. There is some jagged line near the leading edge pressure side and the discontinuity between the circle and the rest of the blade. The surface curvature of the modified H1 blade is highly improved for the whole section from the leading edge to the trailing edge especially near the leading edge of the blade and this reflects to remove the flow disturbances and separation bubble. However, the surface curvature is smoother than the original blade. These discontinuities affect the surface heat transfer distribution as well. The resultant computed isentropic Mach number distributions for the original and modified H1 blades are shown in the figure 5.3. The figure clearly shows the flow disturbances and separation bubble around the leading edge of the original blade. The sharp local acceleration-deceleration region in the leading edge of the original has been completely removed and smoothed. In addition to that, with removing these unwanted phenomena, the surface heat transfer coefficient or Stanton number can be smoothed and decreased when compared to the original blade. As a result of that, the blade performance can be significantly improved. Figures 5.4 (a and b) show the pressure and surface heat transfer distributions for the NASA and H1 blades. Figure 5.4 (a) represents the surface pressure distribution for the experimental, calculated and redesigned H1 blades. Excellent agreement has been achieved between the experimental data and calculation. The modified H1 blade is very similar to the original blade but the differences in the leading edge of the blade improve the smoothness of the pressure distribution on the suction side. Figure 5.4 (b) shows the surface heat transfer (Stanton number) distributions for the experimental, calculated and redesigned H1 blades. The surface heat transfer of the redesigned H1 is highly improved; the "spike" near the leading edge has been removed, and the overall Stanton number distribution has been smoothed. There is excellent agreement between the suction and pressures side of the calculated and experimental data.

The boundary layer of the flow around the NASA and redesigned H1 blades have been analyzed to show how much surface curvature contributes to the improvement of the aerodynamic blade performance and surface heat transfer predictions. Figure 5.5 (a, b) show the comparison between the surface Mach number distributions and the displacement boundary layer calculations, δ^*, for the NASA and redesign H1 blades. The results showed that the boundary layer of the NASA blade is thicker than the redesigned H1 blade and this results in producing more losses inside the boundary layer. The rate of total entropy creation [94] in the blade boundary layers has been evaluated for the suction side of the NASA and redesigned H1 blades to show that the thicker boundary layer the more entropy generated. Figure 5.6 (a) shows the comparison between the total rate of entropy creation inside the boundary layer of the suction side of the NASA and the redesigned H1 blades. This improvement in the surface boundary layer development contributes to decrease the mass-averaged stagnation pressure losses and reflects to improve the surface heat transfer distribution. The mass-averaged stagnation pressure losses for the NASA which is 0.026 and for the redesigned H1 which is 0.024. Figure 5.6 (b) shows the skin friction calculations, C_f, for the NASA and redesigned H1 blades. From the figure 5.6 (b) it is obvious the flow separated at $X/b_x = 1.4\%$ and reattached at $X/b_x = 5.2\%$ and then the main transition started approximately at $X/b_x = 42\%$ for the NASA blade. These results approximately coincided with the experimental data.

The second test case, which is the highly loaded transonic turbine nozzle guide vane (NGV), has been selected and redesigned due to a wealth of experimental data available in the open literature (Arts et al. [166]). The NGV was performed in the isentropic Light Piston Compression Tube facility in the von Karman Institute (VKI). The complete data has been digitized manually from Arts et al. [166]. The flow conditions of the VKI MUR235 test case correspond to an exist isentropic Mach number of 0.927, an exit Reynolds number of 1.25×10^6 and a free stream turbulence intensity of 6%.

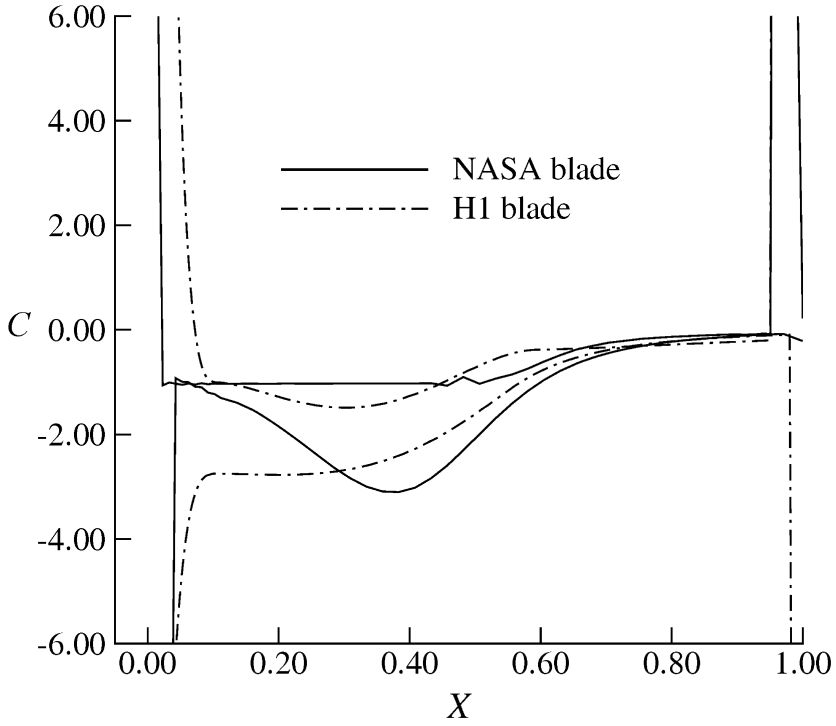

Figure 5.2: Surface curvature distributions for the NASA stator and redesigned H1 blade

Figures 5.7 (a and b) show the surface curvature distribution for the VKI blade (jagged line, evaluated from the original data points) and the H2 redesigned blade. The jagged line of the surface curvature of the original blade affects aerodynamic performance and surface heat transfer distribution, introducing local small spikes and dips in the surface Mach number and surface heat transfer distributions. There is a shock in the flow distribution, which is explained entirely by the high pressure gradient around this area [145]. However, in our understanding, the shock phenomenon is not just caused by the high velocity in this area, but to some degree encouraged by the discontinuity in the surface curvature. This is illustrated in the surface isentropic Mach number distribution and surface heat transfer coefficient distribution around the redesigned H2 blade. In addition to that, with removing surface curvature discontinuities from the trailing edge to the leading edge, the surface Mach number and heat transfer distributions have been smoothed. Figure 5.9 shows the Mach contours for the VKI and redesigned H2 blades. The figure shows that the achieved improvement on the suction side of the blade is a function of high

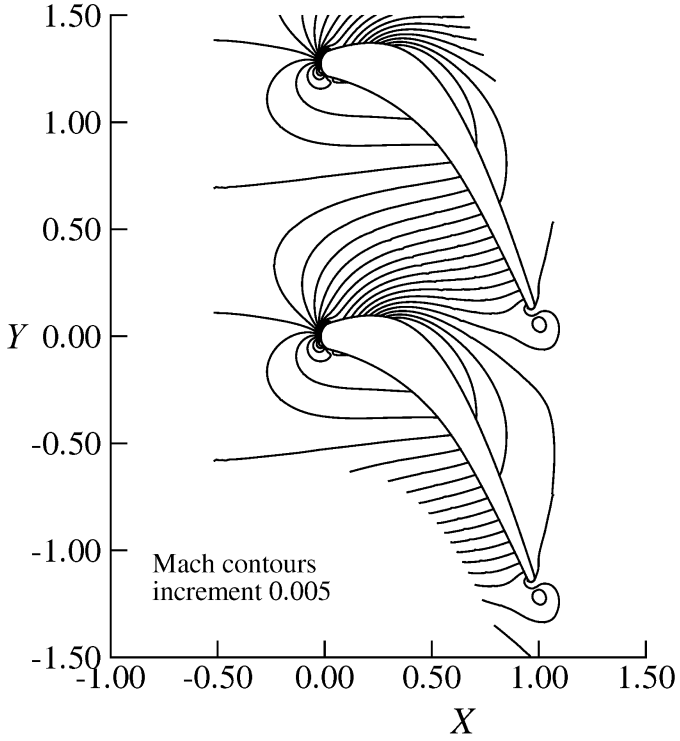

(a)

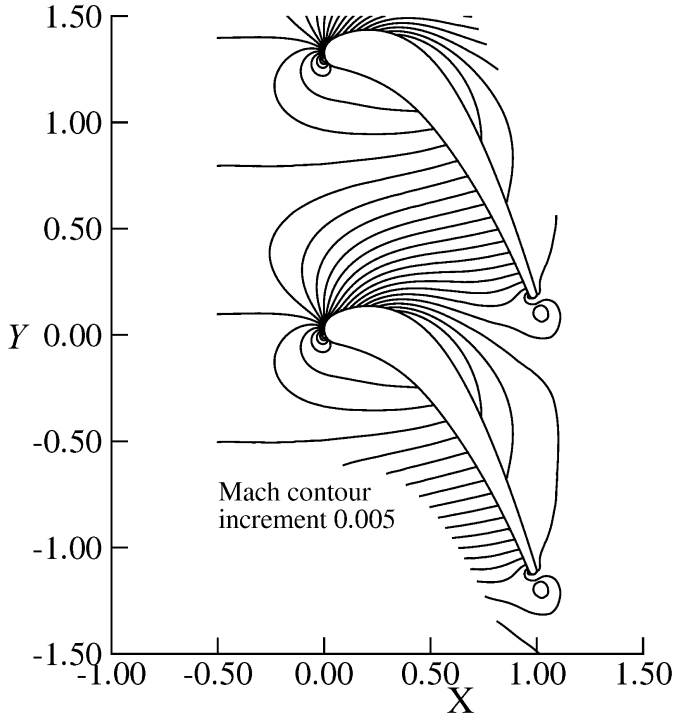

(b)

Figure 5.3: a- Mach contours for the NASA blade, increment 0.005. b- Mach contours for the H1 blade, increment 0.005

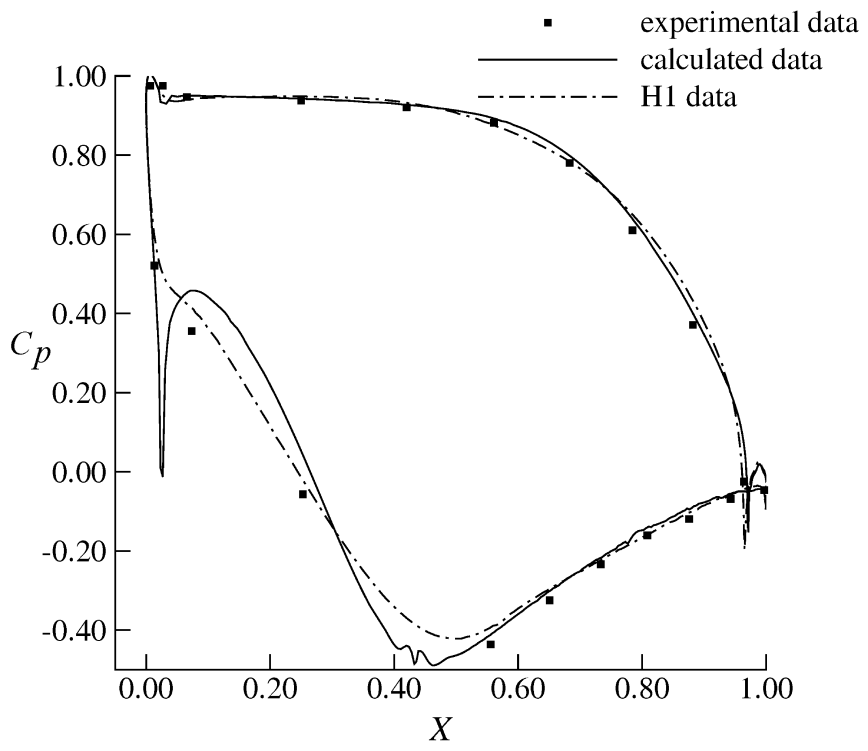

(a)

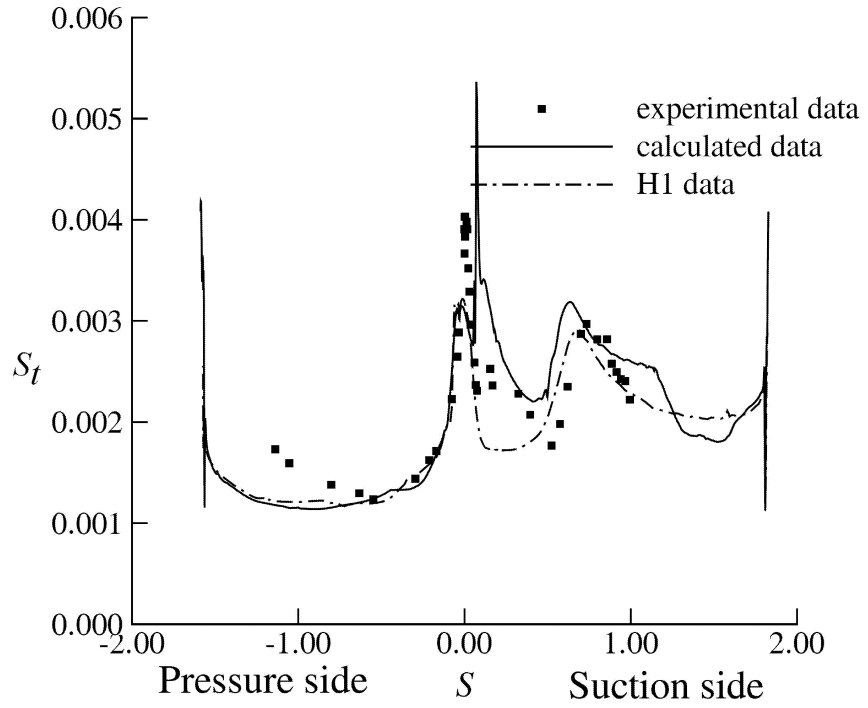

(b)

Figure 5.4: a- Surface pressure distributions. b- Surface Stanton number distributions

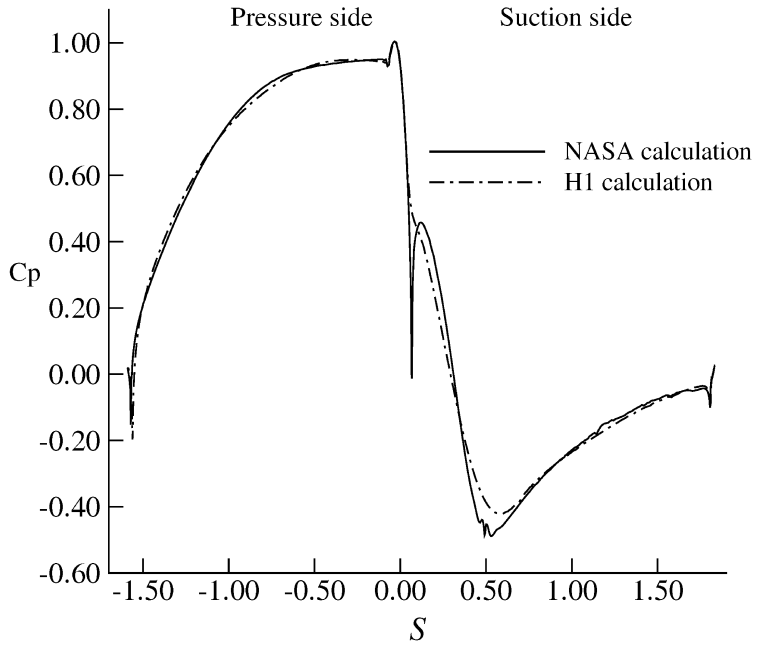

(a)

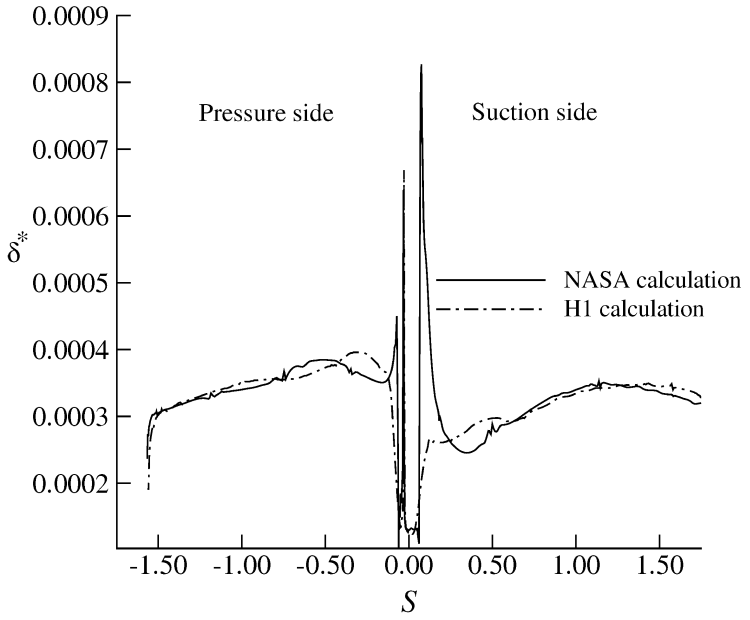

(b)

Figure 5.5: a-Surface Mach number distributions for the NASA and redesigned H1 blades. b-Boundary layer displacement thickness calculations

velocity and surface curvature together.

Figure 5.8 shows the surface isentropic Mach number and surface heat transfer distributions. Figure 5.8 (a) shows the surface isentropic Mach number distribution for the calculated VKI and modified H2 blades. However, the experimental data for

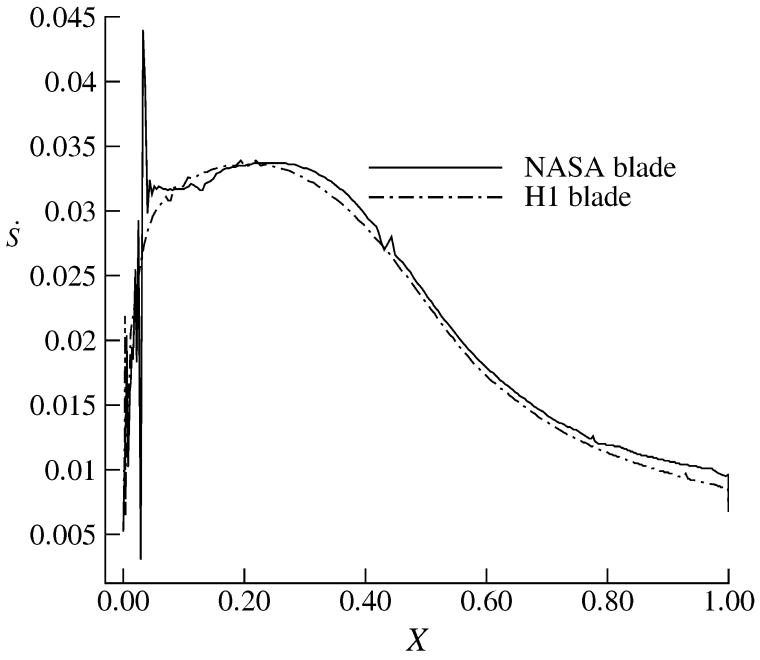

(a)

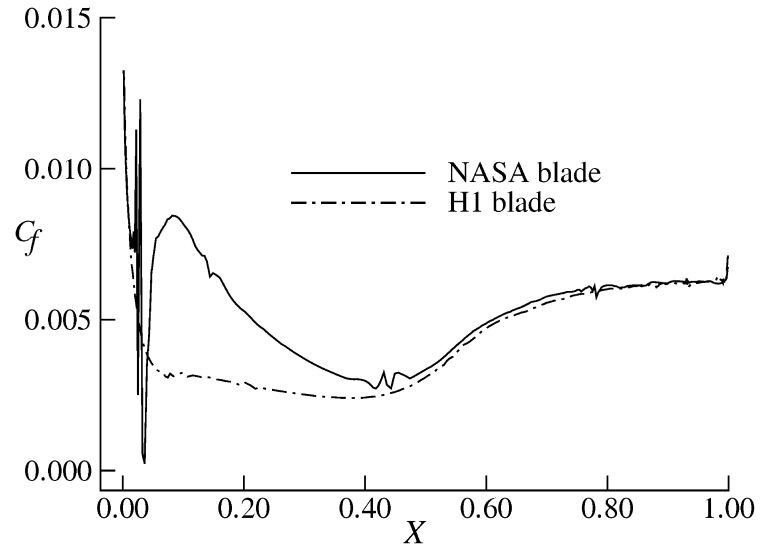

(b)

Figure 5.6: a-The rate of entropy creation on the suction side of the NASA and H1 blades. b- Skin friction calculations on the suction side of the NASA and H1 blades

the isentropic Mach number is not available in the Arts's report. The surface heat transfer data is available for these boundary conditions. The figure 5.8 (b) shows surface heat transfer coefficient distributions for the VKI and H2 blades. Producing the smoothed surface with continuous surface curvature results in producing smooth surface heat transfer distribution. This reflected to improve aero-thermal effects of the entire blade.

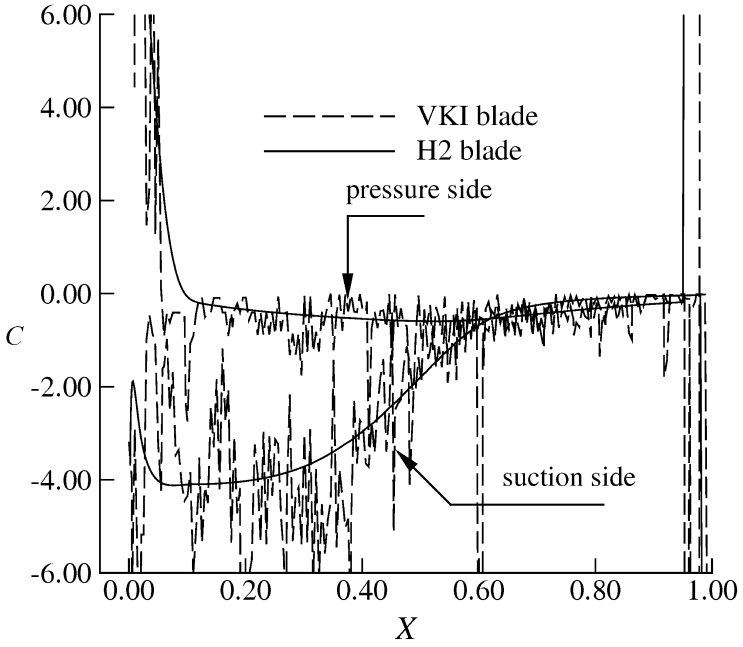

Figure 5.7: Surface curvature distributions for the VKI NGV and redesigned H2 blade

Figure 5.10 (a, b) show the comparison between the surface Mach number distributions and the displacement boundary layer calculations, δ^*, for the VKI and redesign H2 blades. The results showed that the boundary layer of the VKI blade is thicker than the redesigned H2 blade and this results in producing more losses inside the boundary layer. The rate of total entropy creation [94] in the blade boundary layers has been evaluated for the suction side of the VKI and redesigned H2 blades to show that the thicker boundary layer the more entropy generated. Figure 5.11 (a) shows the comparison between the total rate of entropy creation inside the boundary layer of the suction side of the VKI and the redesigned H2 blades. This improvement in the surface boundary layer development contributes to decrease the mass-averaged stagnation pressure losses and reflects to improve the surface heat transfer distribution. The mass-weighted average stagnation pressure losses for the VKI which is 0.063 and for the redesigned H2 which is 0.058. Figure 5.11 (b) shows the skin friction calculations, C_f, for the VKI and redesigned H2 blades. From the figure 5.11 (b) it is obvious that the turbulence model captures the overall behaviour and the onset of transition quite well. The onset off transition is coincided with the

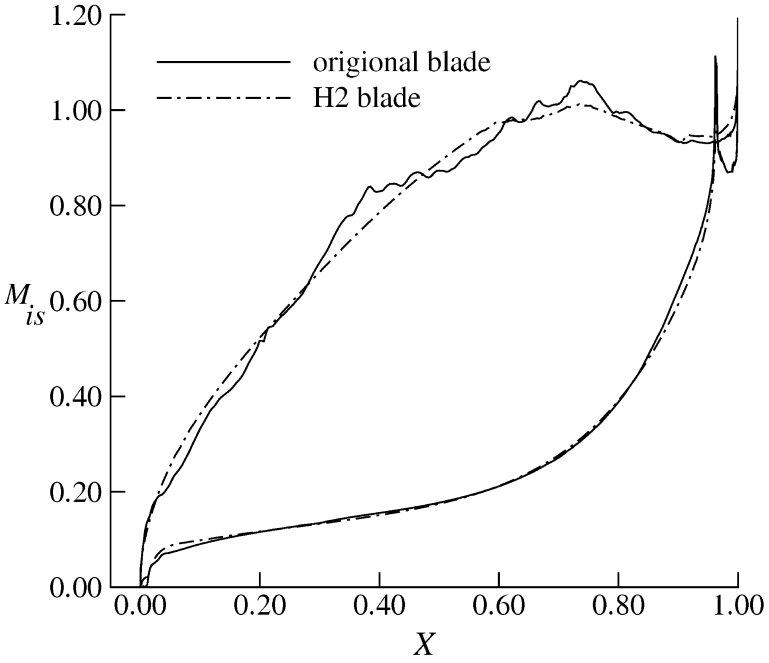

(a)

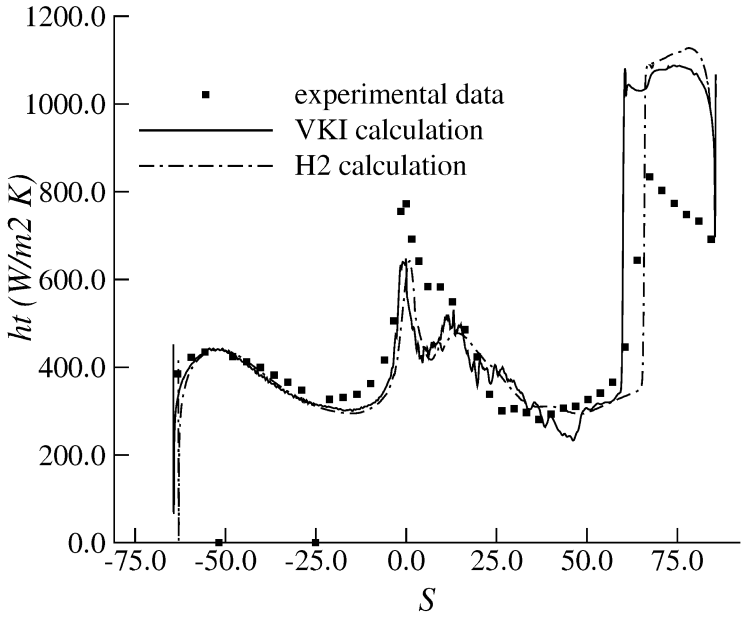

(b)

Figure 5.8: a- Isentropic surface Mach number distributions. b- Surface heat transfer coefficients,h_t ,W/m^2K

experimental data and which is about S=60 mm.

The two test cases illustrate that the PSCD blade design method provides a unique tool for blade design and that the surface curvature distribution has a great effect on development of the boundary layer on the surface of the blade, affecting

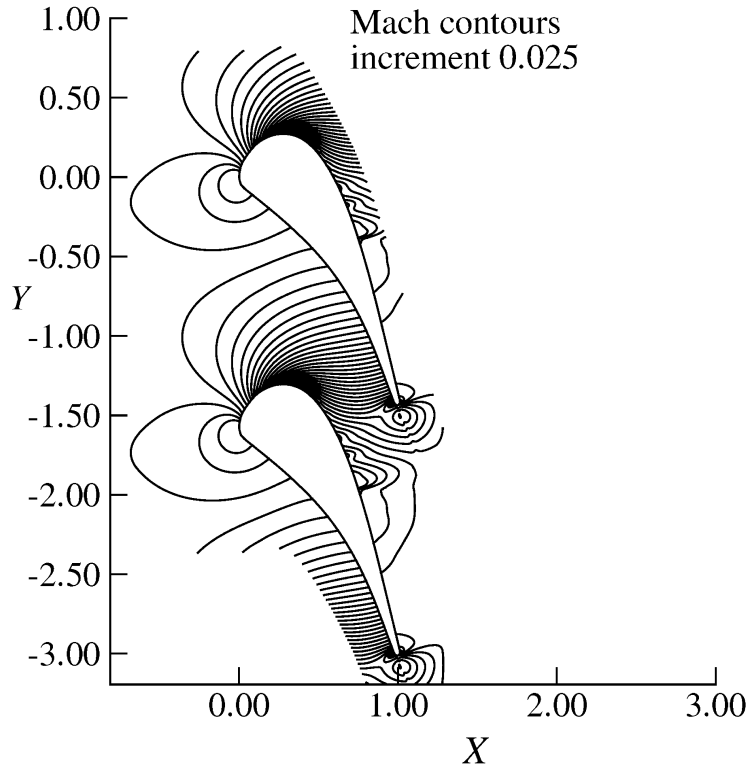

(a)

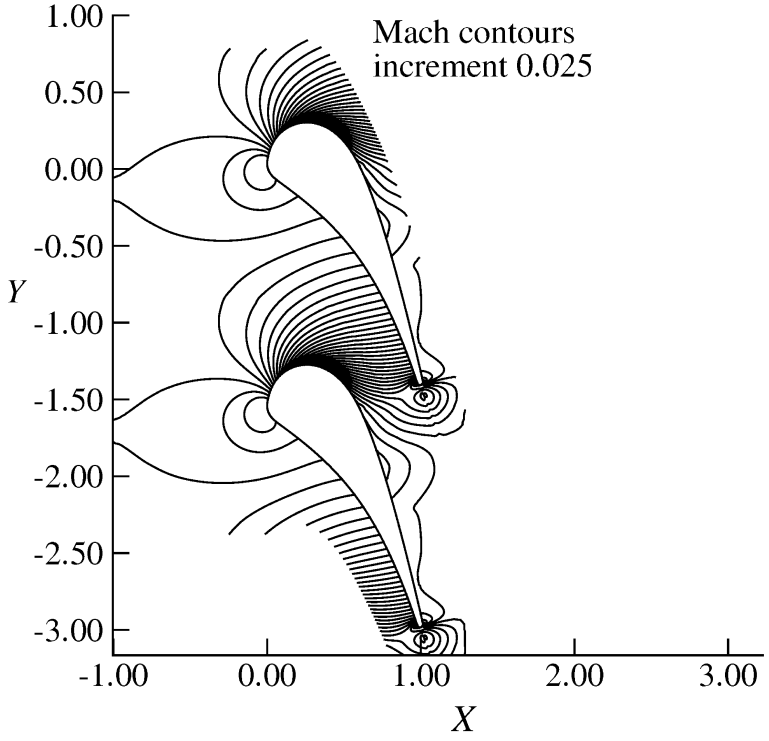

Figure 5.9: a- Mach contours for the VKI blade, increment 0.025. b- Mach contours for the redesign H2 blade, increment 0.025

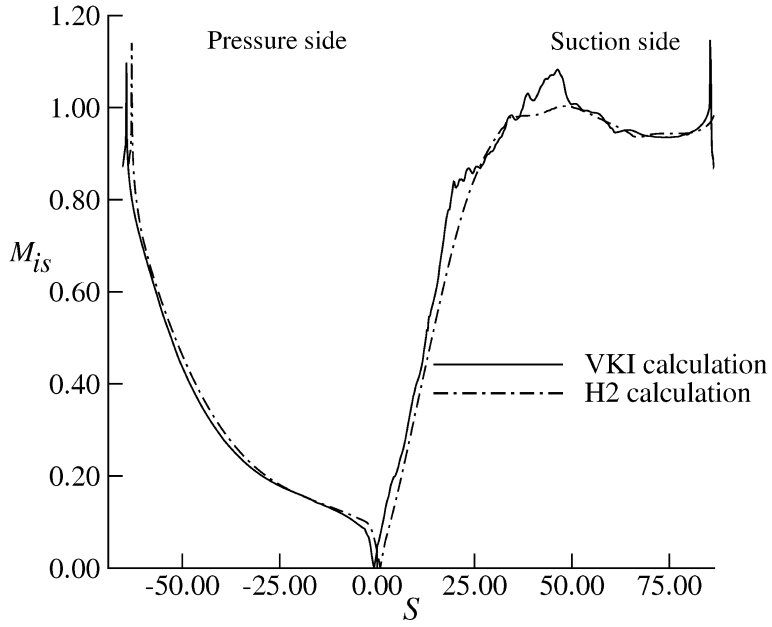

(a)

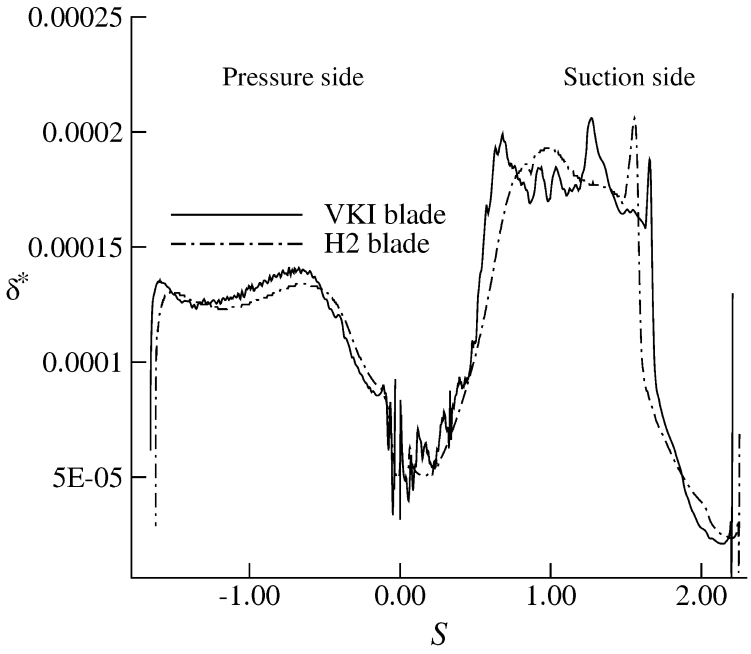

(b)

Figure 5.10: a-Surface Mach number distributions for the VKI and redesigned H2 blades. b-Boundary layer displacement thickness calculations

both aerodynamics and heat transfer performance.

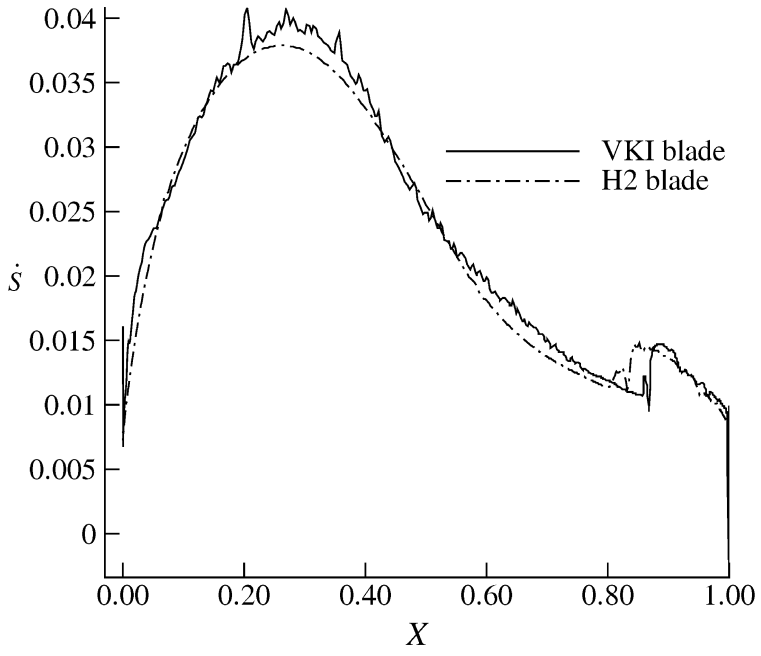

(a)

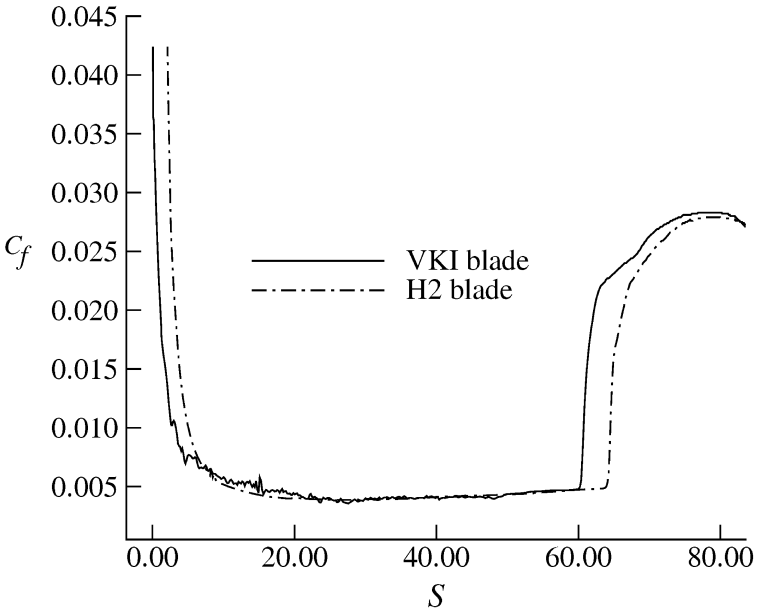

(b)

Figure 5.11: a-The rate of entropy creation on the suction side of the VKI and H2 blades. b- Skin friction calculations on the suction side of the VKI and H2 blades

5.3 Conclusions

The PSCD blade design method provides advantages not just for the aerodynamic performance but for the thermal load of blade shapes. The results of the two test cases show that surface curvature distribution plays an important role in removing

spikes and dips in the surface isentropic Mach number and surface heat transfer distribution, and can be used to avoid local shocks in high velocity regions. The associated reduction in the cooling flow rates may induce appreciable benefits to the whole gas turbine design process.

Chapter 6

PSCD applied to the design of compressor and fan blades

6.1 Introduction

The flow within a multi-stage axial turbomachine is inherently unsteady and turbulent. Due to its complexity, the blade design problem is usually reduced to a series of staked two dimensional problems and assuming the flow field is steady. The second dimension (2D) of the compressor blades are determined from the variations of flow angles from hub to tip, derivation of the radial equilibrium through flow calculations, location of center of gravity of blade sections and geometrical shape of the leading and trailing edges. These three dimensional constraints and hollow sections must be accommodated in the design and affect the performance of the compressor. The goal of any blade design method is to find a geometry that satisfies flow requirements with minimum loss, tolerable mechanical stresses, minimum disturbances downstream and upstream, and adequate stall margin, among others. The design of blade geometries is a very important step for the design of efficient turbomachine, as the blade design process directly influences the blade-row efficiency and thus the overall machine efficiency.

Design of compressor blade is quite difficult according to its nature of the flow

around the blade surfaces. All blade design methods (direct and inverse) have difficulty to control the behaving flow around the leading edge of the blade to eliminate flow disturbances and separation bubbles which are reflected to decrease total pressure losses and improve aerodynamic efficiency. Early blade design methods were based on specifying a thickness distribution around a camber line. In this method, for specifying compressor and turbine blade shapes, straight line, circular arc or parabolic camber lines were used, and then the thickness distribution was added to these camber lines for both the suction and the pressure sides of the blade. Examples of this method [12, 15] are designs of NACA compressor airfoils (NACA-65 series), C4, C5 and other series of NACA profiles for turbines by Dunavant and Erwin [23]. This method did not provide enough flexibility to control both the suction and pressure surfaces in order to obtain a desirable aerodynamic performance. In parallel early work on inverse design was performed by Stanitz [167].

After the 1950s, most turbomachinery blades have been designed by specifying the shape of the suction and pressure surfaces of the blades. Thus the passage was defined by the blades and the resultant blade thickness was obtained. In the beginning of the 1960s advances in blade to blade flows, secondary flows, through flow methods had great impact on practical compressor design approaches. Gostelow and Hobson [168] developed a two dimensional potential flow analysis for incompressible and compressible flows and provided exact solutions for blade profiles. From 1970s till now there is tremendous design methodology used in both direct and inverse design methods to produce efficiency blade for turbomachinery applications and still challenging to find a more efficient method which is able to design blades at design and off-design conditions and it is possible to apply for all type of blades at different conditions. Some of them [54, 56, 57, 59, 169–173] tried to redesign the blade at design condition and improves aerodynamic performances with either decreasing total pressure losses or producing smooth surfaces but still there is difficulty to control the leading edge and the rest of the surfaces which is caused from the discontinuity in the surface curvature [104] and it makes high deceleration and acceleration

of the flow around this area. Few attempts [105, 109, 170] have been found in the open literature, to redesign the blade at design and off design conditions together to improve aerodynamic performance. These attempts have still difficulty to eliminate or remove disturbances and separations which is the result of the discontinuity in the surface curvature of the blade especially around the leading edge, at off-design conditions. The PSCD method is easily able to eliminate these difficulties from the discontinuity problems and produced highly smoothed blade surface. These are reflected to improve aerodynamic performances and overall improved efficiency of the whole engine.

The first purpose of the present chapter is to apply the PSCD blade design method to design compressor blades at design and off-design conditions. Two test cascade cases has been redesigned. The first one is the MAN GHH 1-S1 cascade at design and off-design conditions; and the second one is Sanger's blade at design conditions. Results show that the PSCD method eliminates local flow disturbances and separation bubbles around the leading edge of the blade, and improves the overall surface of the blade. With these improvements the mass-weighted average stagnation pressure losses decrease.

The second purpose of this chapter is to design four compressor stages and to use the output from the through-flow calculation to design the stator blade of the final stage, from hub to tip. Similarly to the turbine 3D examples presented earlier, the 3D compressor blade design parameters have been prescribed with Bezier curves and third order polynomials from hub to tip to produce the 3D blade geometry. It is concluded that the PSCD blade design method is highly flexible, friendly and robust, and can be used to design all blade geometries: compressors; turbines; and (later chapter) isolated airfoils as well.

6.2 Blade design methodology

The methodology of this technique is the same at that of the PSCD blade design method described in [2–9, 141]. The only difference between compressor and turbine blades is that the throat constraint on the suction surface was moved from the outlet region of the turbines to the inlet region of the compressors. Figure 6.1 shows a sample of compressor blade that has been designed with the PSCD blade design method.

As for turbines, the compressor suction and pressure surface of the blades have been split into three major parts from the trailing edge to the leading edge of the blade. The leading and trailing edges of the blade are prescribed with circles, though ellipses and other shapes can alos be used. The trailing edge region of the blades (y_3) has been prescribed with exponential polynomials similar to those presented earlier for turbines; the main part of the blade (y_2) has been prescribed by specifying the curvature with Bezier curves similar to those used earlier for turbines; and the leading edge region of the blades (y_1) has been prescribed with polynomials similar to those used earlier for turbines.

This is the first application of compressor blade design with the PSCD method, and all the advantages discussed earlier for turbines carry over to compressor designs. Figure 6.2 shows the blade geometry of the redesigned C1 and C2 blades with the PSCD method. These blades are successive attempts to remove or eliminate the flow difficulties around the leading edge of the MAN GHH 1-S1 at design and off-design conditions. The Sanger and redesigned C3 blades are shown in figure 6.3. Blade parameters and representative blade points for C1, C2 and C3 are in QMUL-EGR-2010-01 confidential report (available from Professor Korakianitis).

The PSCD method is a new design environment decoupling the traditional maximum thickness and maximum camber discussions (used in early airfoil designs) from blade design. Similarly to inverse design methods, the design is guided by the surface pressure and surface Mach number distributions, and the output is the blade

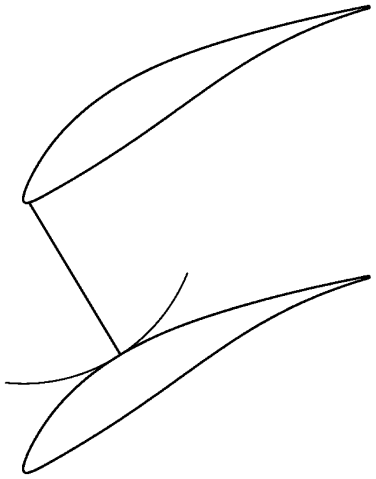

Figure 6.1: Illustration of compressor blade design with the PSCD method

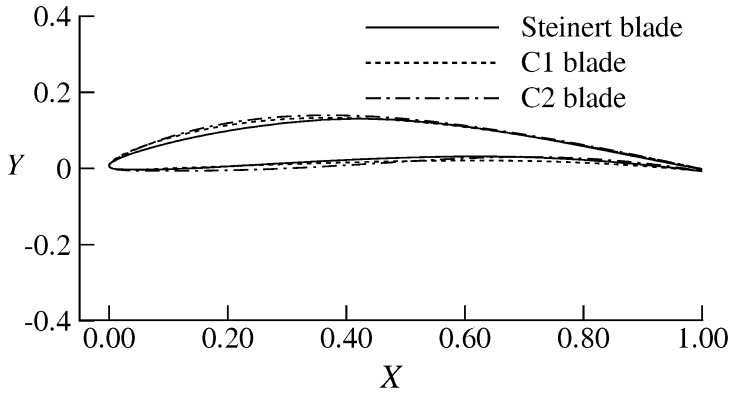

Figure 6.2: Blade geometries for MAN GHH 1-S1, C1 and C2 blades

shape. The design sequence shapes the curvature, and therefore blade surface and location of maximum loading, forwards or backwards on the blade surface.

6.3 Design and off-design condition

The main aspects of the development of the industrial compressor [29] includes requirement of large variations in pressure ratio and flow volume for adaptation to the process conditions, high efficiency for reducing energy costs and minimum size and maximized operational reliability. These requirements can be achieved with the design of various blade rows of the compressor stages to provide the largest possible working range between chocking and separation at highest possible Mach number.

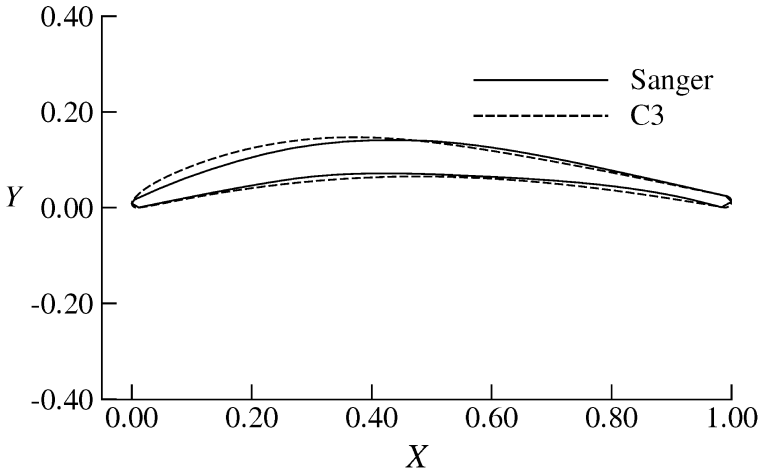

Figure 6.3: Blade geometries for Sanger and C3 blades

As part of optimization efforts of turbine blades (in the previous section) and axial-flow compressors (in the present section), a MAN GHH 1-S1 [29] compressor blade with high subsonic inlet Mach number and Elazar [174] blade have been redesigned with the PSCD blade design method to improve design and off-design performance, and improving efficiency by significantly decreasing stagnation pressure losses.

Spikes in the surface pressure distribution often exist at the leading edge of the compressor blade at design and off-design conditions. These are caused by large changes in surface curvature between the shape of the leading edge, trailing edge and the rest of the blade. Curvature discontinuity have a more severe impact around the leading edge of the blade at design and off-design conditions because at least one of the discontinuities takes place in a region of a high velocity. These spikes have potential effects on the compressor performance [175]. Carter [106] mentioned that spikes have a large effect on the blade performance. Goodhand and Miller [105] have previously studied the effect of these spikes on losses. Different shapes of the leading edge with different blade design methods have been use, in the open literature, to control the differences in the surface curvature especially between the leading edge (e.g. circle) and the rest of the blade by [56,59,109,170,172,175]. To our knowledge, there is no solution to date in the open literature to control this difficulty between the circle and the rest of the blade other than the PSCD method.

The PSCD method has been used to redesign two test cases; the first one, that has been used by Steinert [29], is redesigned at design and off-design conditions; and the second one is Elazar [174] blade which is redesigned only at design condition. The incidences for the first test case, which is called by MAN GHH 1-S1 blade, are ±4°,+5°, -7°. Two trials of redesign blades, C1 and C2, have been presented to show the ability of the method to eliminate flow disturbances, separation bubbles and increasing operating range with decreasing stagnation total pressure loss. Mesh generator GAMBIT, flow solver FLUENT and ANSYS12 have been used in the computations. A reasonably high number of computational mesh elements is required for reasonably accurate calculations. The exact numbers depend on the geometry of the blade and its model. The mesh elements used for the blades are: 30,520 quadrilateral cells; 60,558 2D interior faces; and 31000 nodes for all zones. A 2D O-mesh and a Pave-unstructured mesh have been used in the compressible and viscous calculations. The Pave mesh consisted of a combination of structured and unstructured regions. The mesh around the airfoil consisted of twenty one structured clustered O-grid layers with wall boundary parameter y^+ less than 1, and the remaining majority of the flow field was descritized with quadrilateral and a small numbers of triangular cells. The SST $k-\omega$ transition turbulence model has been used. The boundary conditions of this blade at design conditions are as follows: inlet total pressure 101,325 Pa, inlet total temperature 287.15 K, turbulence intensity 1.5, turbulence length scale, $l_m/chord = 0.0476$, inlet Mach number 0.618 and pressure ratio 1.1021. Further details can be found in [29]. The results show that the PSCD method is highly flexible, accurate and robust to design all type of blades.

Figure 6.4 (a and b) show the isentropic Mach number distribution and Mach contours at design condition. Figure 6.4 (a) shows a comparison between the experimental data and the viscous calculation of the original and C1 blades. Figure 6.4 (b) shows the Mach contours for the C1 blade as a first attempt. There is a very good agreement between the experimental data and viscous calculation. However, the spikes does not appear near the leading edge in the experimental data because

of excluding the experimental data around this area, but they appeared in the viscous calculation of [176]. Our viscous calculations also show the spikes and dips in the isentropic surface Mach number distribution around the leading edge. The C1 blade has been significantly improved at the suction side but there is still a high acceleration on the pressure side which still needs more improvements to decrease the total stagnation pressure losses. Figures (6.5 and 6.6) show the isentropic surface Mach number distributions at off-design conditions such as +4°, +5°, -4°, -7°. Again, excellent agreement can be achieved with viscous calculation between experimental and calculation at off-design incidences. In all cases, the transition point moved forward in the redesigned C1 blade and significant improvements on the suction side have been achieved, however, the pressure side of the negative incidences have the high value of acceleration but smoother than the original blade. Figure 6.7 shows the Mach contours and isentropic surface Mach number distribution at design conditions. In the second attempt, the blade C2 has significantly improved which is free from flow disturbances and separation bubbles around the leading edge and highly improved in the rest of the blade with moving the transition point toward the leading edge circle. In addition to removing these pressure distribution disturbances the mass-weighted average stagnation pressure loss is decreased and consequently the efficiency can be improved.

The off-design isentropic surface Mach number distributions have been shown in figures (6.8 and 6.9) between the experimental data and viscous calculation for C2 compressor blade. Table 6.1 shows the mass-weighted average stagnation pressure losses for the original and redesign C2 blades at design and off-design conditions. The losses are significantly decreased with keeping continuity in the surface curvature and modified blade. Based on experimental data of loss coefficients [29], with decreasing the losses the operating range can be increased. The favorable results of the low loss level is due to removing discontinuity of the surface curvature, thickening the blade, and as a result of that eliminating flow disturbances and separation bubble at design and of design incidences can be achieved.

Figure 6.10 (a, b) show the comparison between the surface Mach number distributions and the displacement boundary layer calculations, δ^*, for the Steinert and redesign C2 blades at design and negative incidences. Figure 6.11 (a, b) show the comparison between the surface Mach number distributions and the displacement boundary layer calculations, δ^*, for the Steinert and redesign C2 blades at design and positive incidences. The results showed that the boundary layer of the Steinert blade is thicker than the redesigned H2 blade and this results in producing more losses inside the boundary layer. The rate of total entropy creation [94] in the blade boundary layers has been evaluated for the suction side of the Steinert and redesigned C2 blades to show that the thicker boundary layer the more entropy generated. Figure 6.12 (a) shows the comparison between the total rate of entropy creation inside the boundary layer of the suction side of the Steinert and the redesigned C2 blades. This improvement in the surface boundary layer development contributes to decrease the mass-averaged stagnation pressure losses. Figure 6.12 (b) shows the skin friction calculations, C_f, for the Steinert and redesigned H2 blades. From the figure 5.11 (b) it is obvious that the turbulence model captures the overall behaviour and the onset of transition quite well. The separation point at $X/b_x = 1.34\%$ and the main transition at about $X/b_x = 42.43\%$. The prediction of transition is approximately coincided with the experimental data. This transition turbulence model is a more suitable to predict most of the flow behaviour around turbomachinery blades if it is provided with appropriate boundary conditions.

The second test case is the Elazar or Sanger blade which was used in the design military of aircraft gas turbine engines. The blade was designed for the following boundary conditions: inlet total pressure 1.03 atm; inlet Mach number 0.25, and inlet total temperature 294 K; the outlet static pressure 1.00 atm; Reynolds number 7×10^5. The controlled diffusion blade geometry, extra parameters for the experiment and boundary conditions can be found in [174]. The same method has been used to redesign this blade as well. Experimental and calculated surface pressure distributions and Mach contours have been shown in Fig. 6.13. The SST $k - \omega$

transition turbulence model was used to calculate surface pressure distribution. Excellent agreement was obtained between the predicted and experimental pressures at design condition. The calculated surface pressure, for the redesign C3 blade, was shown in the same figure. The Mach contour of the redesign blade was shown in Fig. 6.15 (a).

Figure 6.13 (a, b) show the comparison between the surface Mach number distributions and the displacement boundary layer calculations, δ^*, for the Sanger and redesign C3 blades at design condition. Figure 6.15 (b) shows the comparison between the total rate of entropy creation inside the boundary layer of the suction side of the Sanger and the redesigned C3 blades. This improvement in the surface boundary layer development contributes to decrease the mass-averaged stagnation pressure losses. It is concluded that removing the discontinuity problem between the circle and the rest of the blade has a significant effect in removing flow disturbances and separation bubble around the leading edge. This is another advantage of the PSCD blade design method.

Table 6.1: Stagnation pressure losses at design and off-design conditions

Blade names	Design and off design conditions				
	-7	**-4**	**0**	**+4**	**+5**
MAN GHH 1-S1, Y_c	0.0466	0.0232	0.0186	0.01760	0.04170
C2, Z	0.00286	0.00218	0.00165	0.00175	0.00278
C2, Y_c	0.01479	0.01418	0.01580	0.01710	0.01880

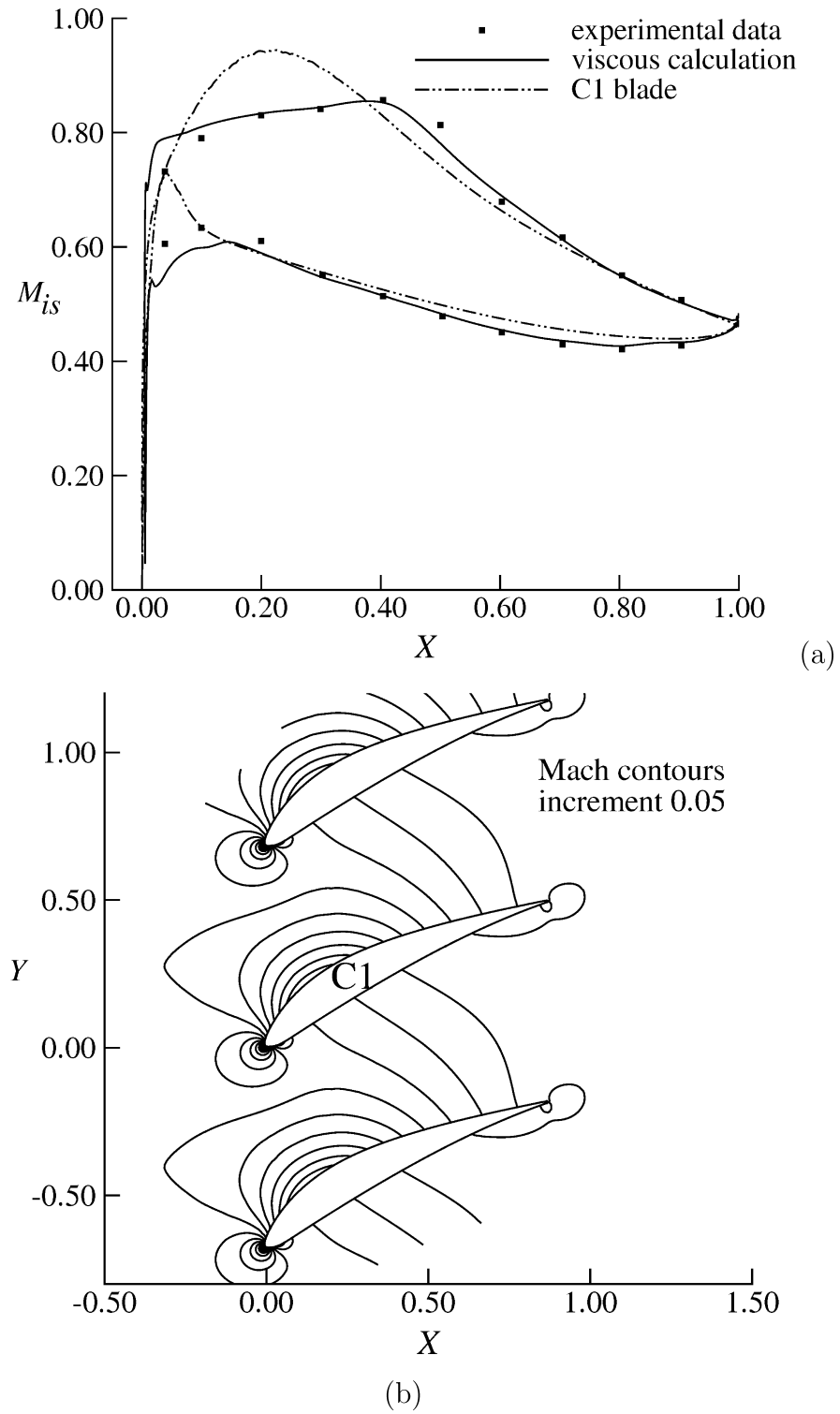

Figure 6.4: a- Isentropic Mach number distributions at design incidence. b- Mach contours at design condition

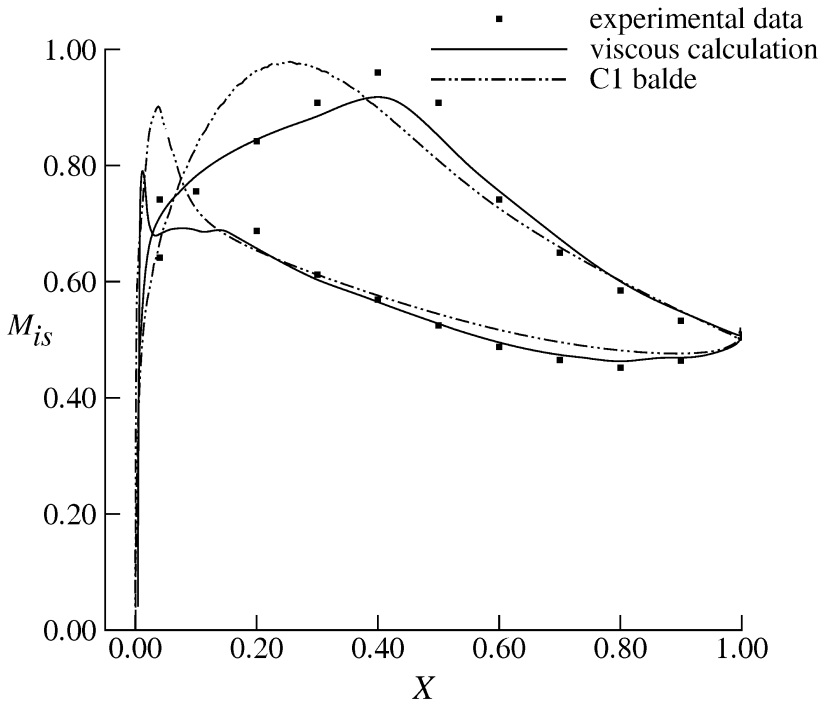

(a)

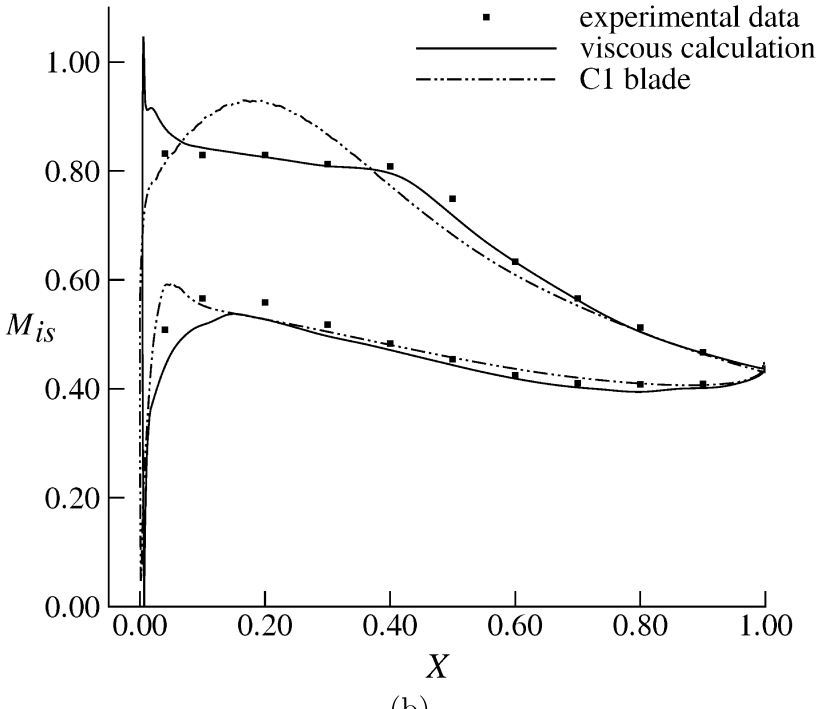

(b)

Figure 6.5: a- Isentropic Mach number distributions at off-design incidence -4°. b- Isentropic Mach number distributions at off-design incidence +4°

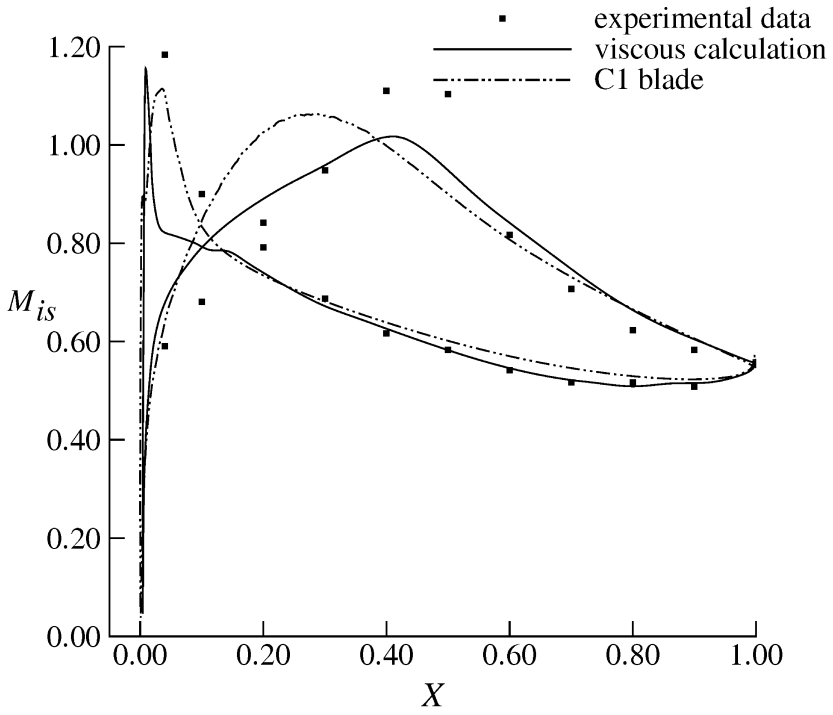

(a)

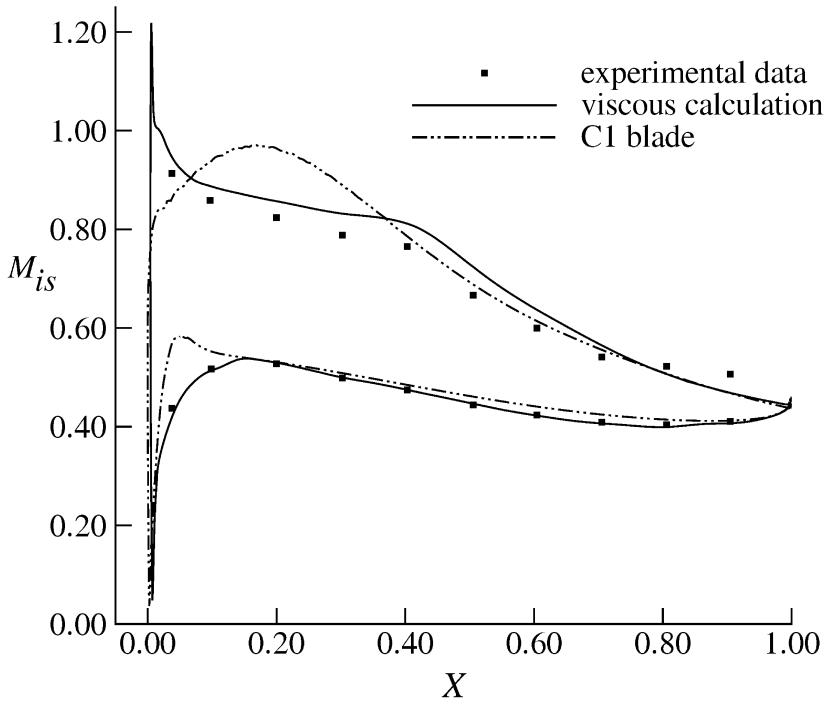

(b)

Figure 6.6: a- Isentropic Mach number distributions at off-design incidence -7°. b- Isentropic Mach number distributions at off-design incidence +5°

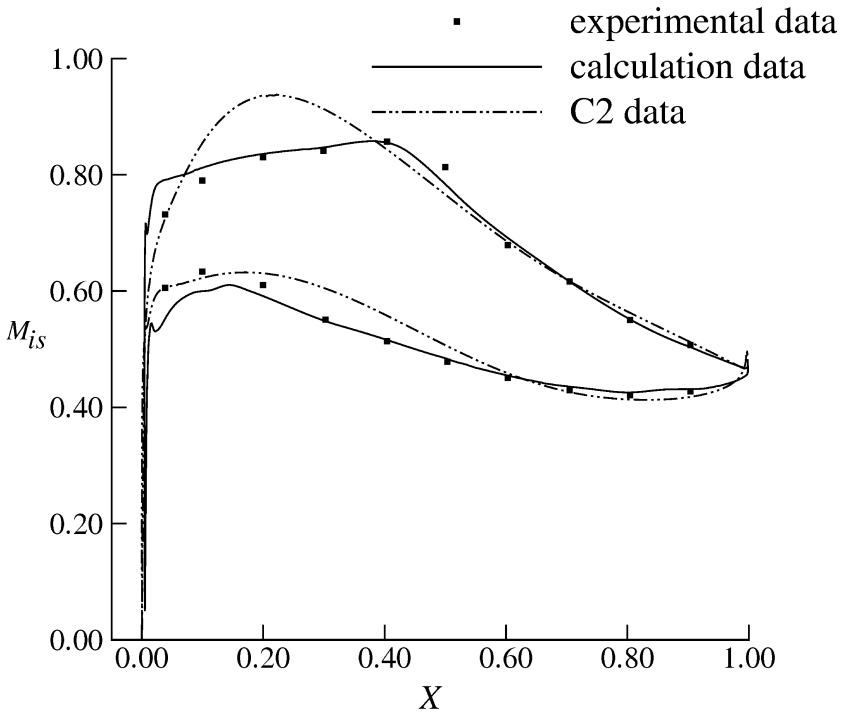

(a)

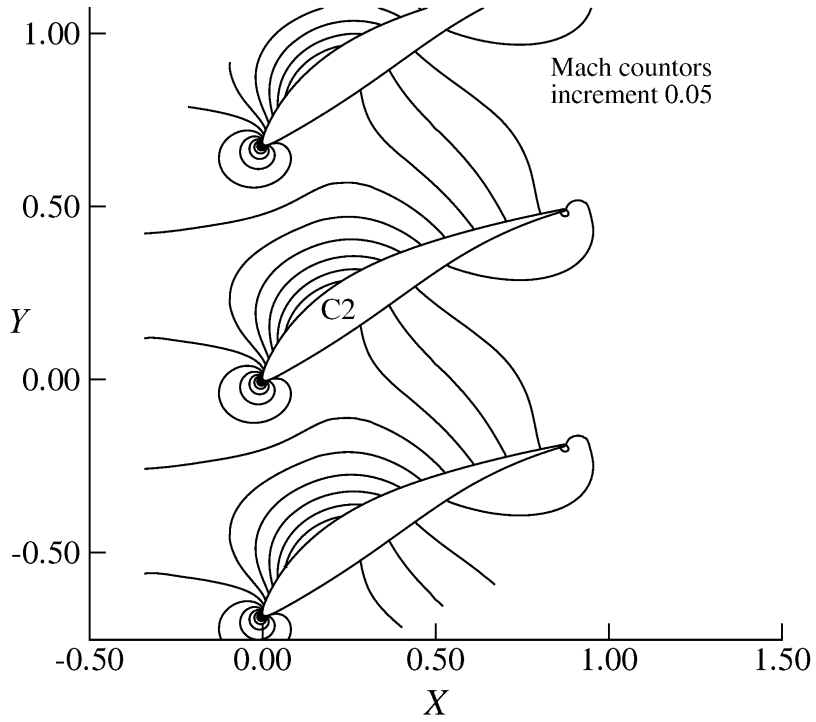

(b)

Figure 6.7: a- Isentropic Mach number distributions at design incidence. b- Mach contours at design condition

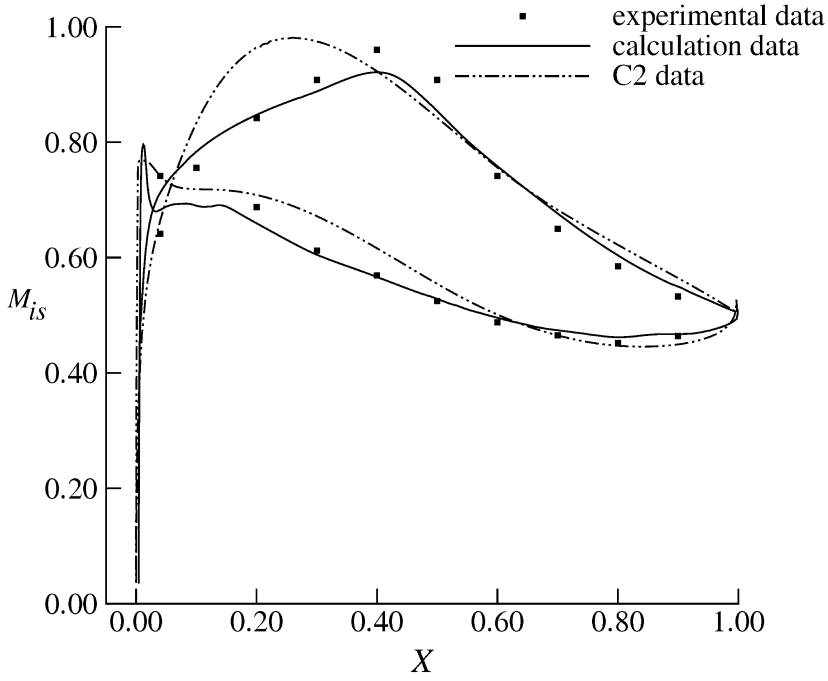

(a)

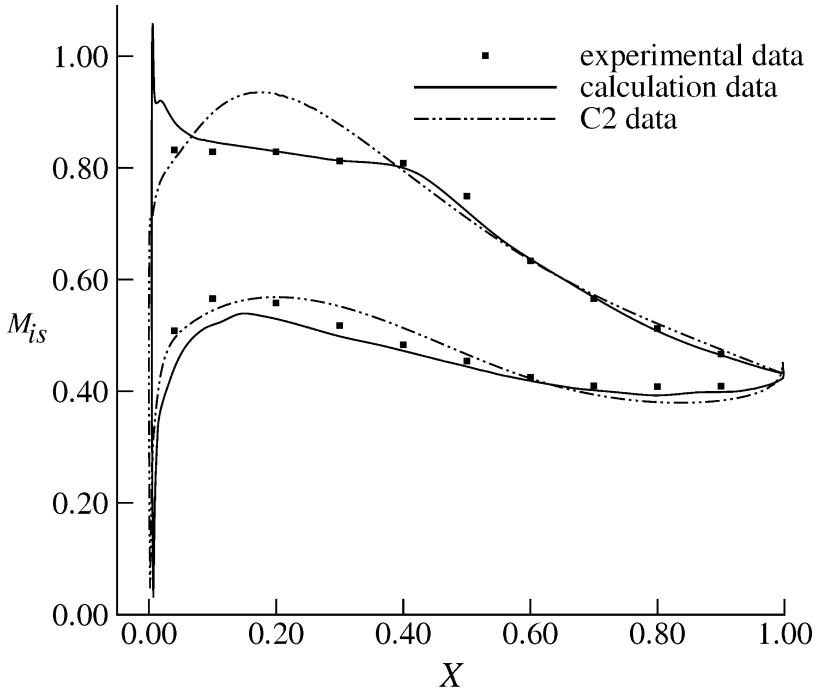

(b)

Figure 6.8: a- Isentropic Mach number distributions at off-design incidence -4°. b- Isentropic Mach number distributions at off-design incidence +4°

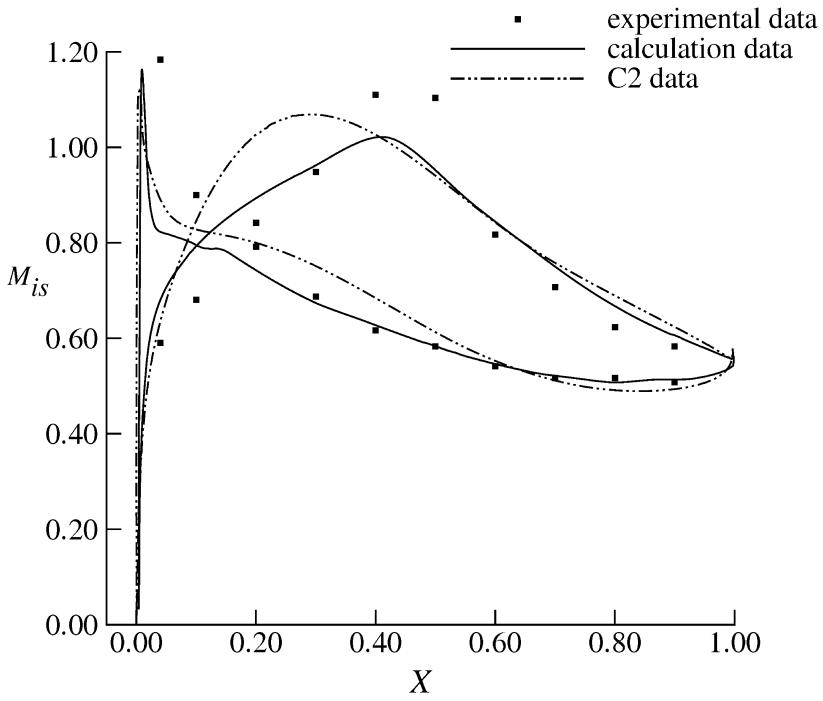

(a)

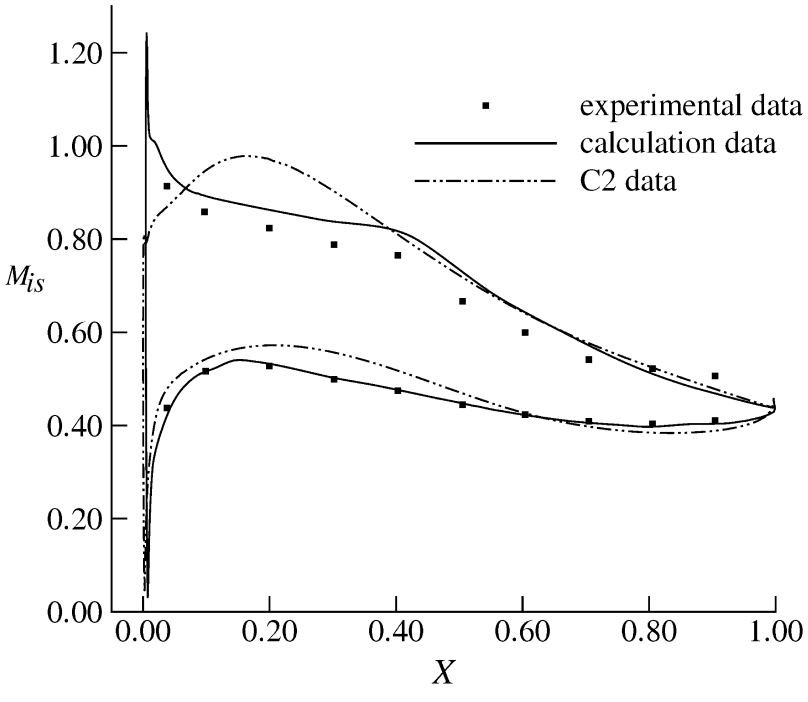

(b)

Figure 6.9: a- Isentropic Mach number distributions at off-design incidence -7°. b- Isentropic Mach number distributions at off-design incidence +5°

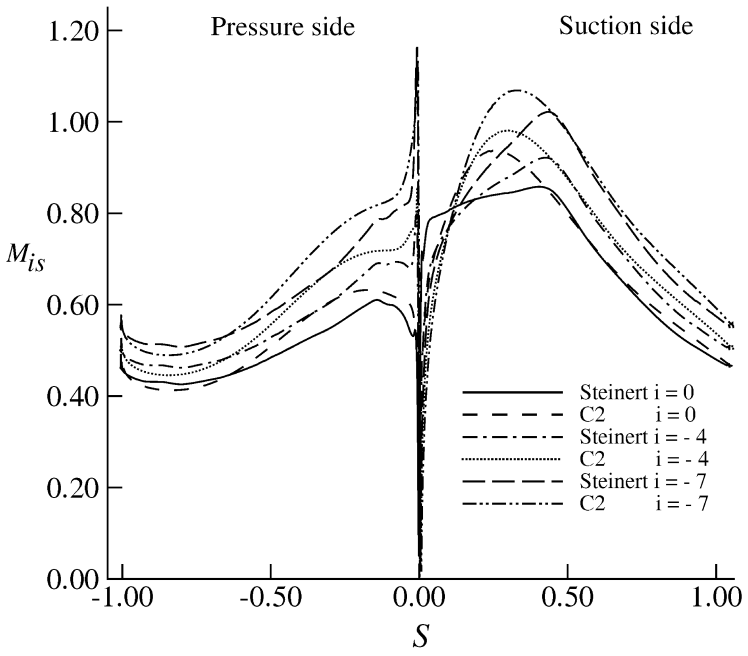

(a)

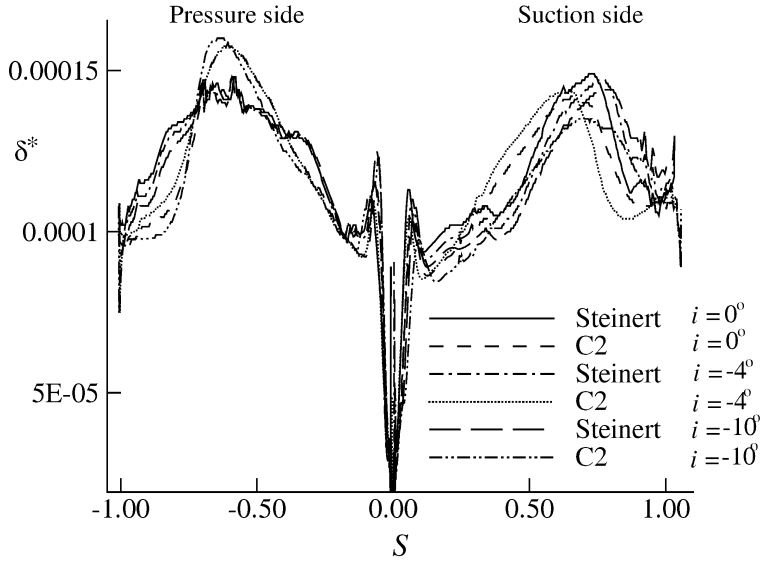

(b)

Figure 6.10: a-Surface Mach number distributions for the Steinert and C2 blades at design and negative incidences. b-Boundary layer displacement thickness calculations

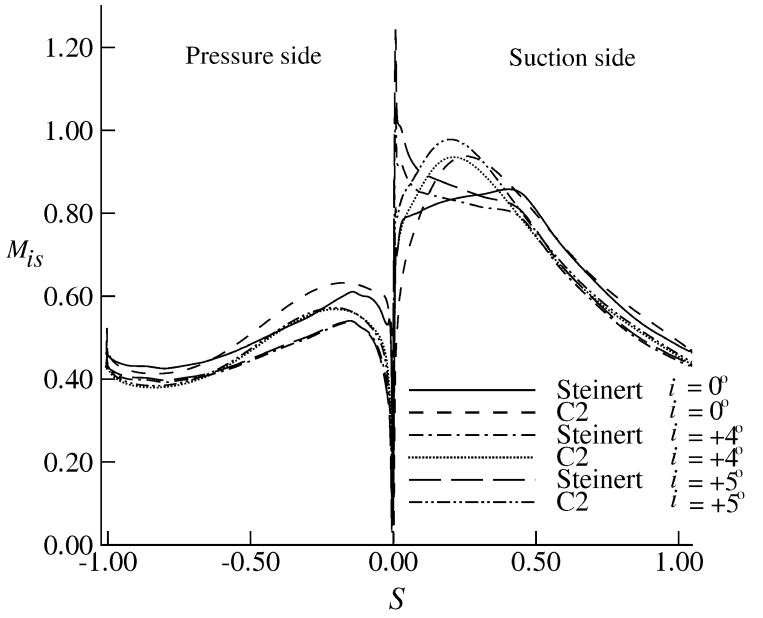

(a)

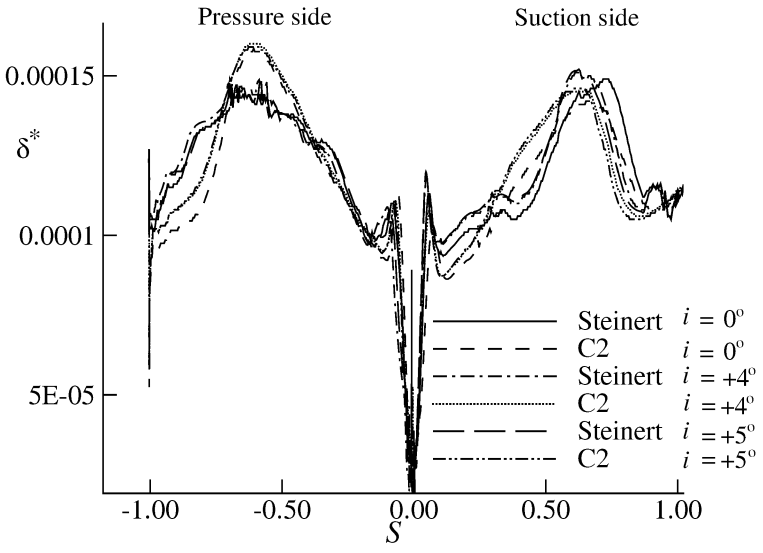

(b)

Figure 6.11: a-Surface Mach number distributions for the Steinert and C2 blades at design and positive incidences. b-Boundary layer displacement thickness calculations

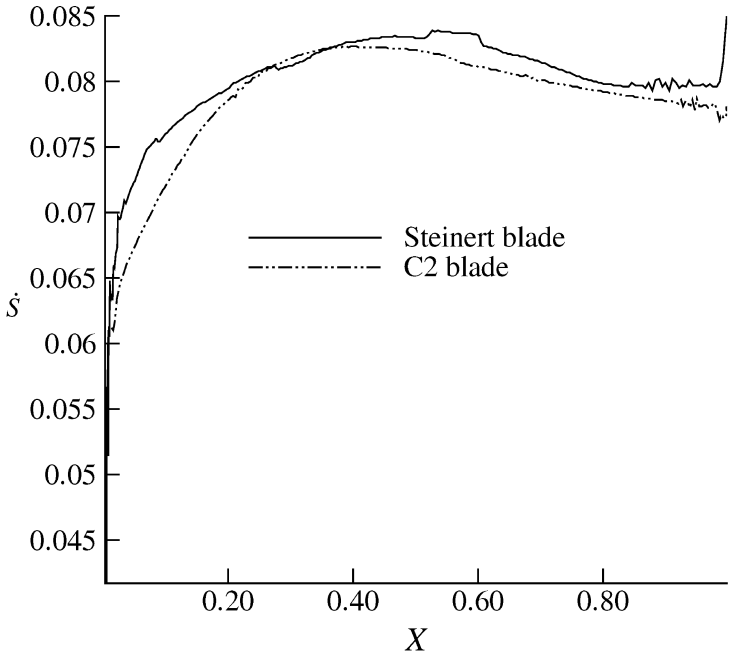

(a)

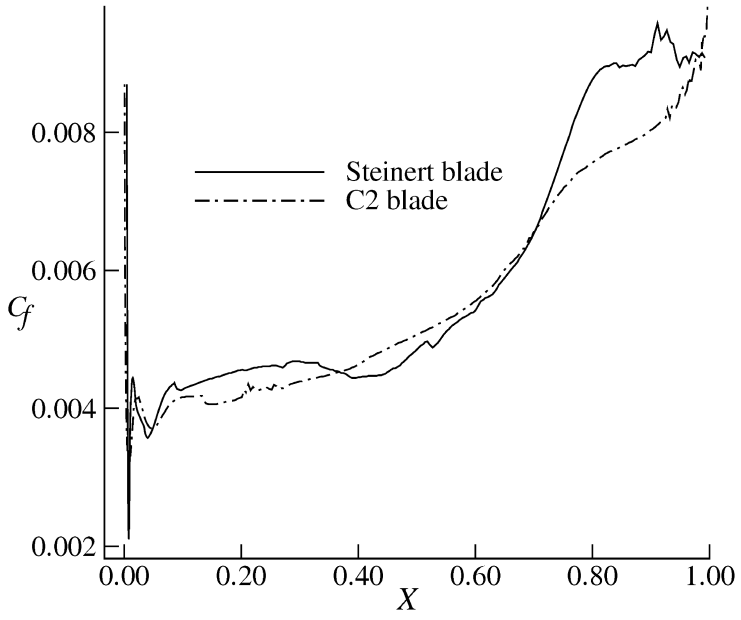

(b)

Figure 6.12: a-The rate of entropy creation on the suction side of the Steinert and C2 blades. b- Skin friction calculations on the suction side of the Steinert and C2 blades

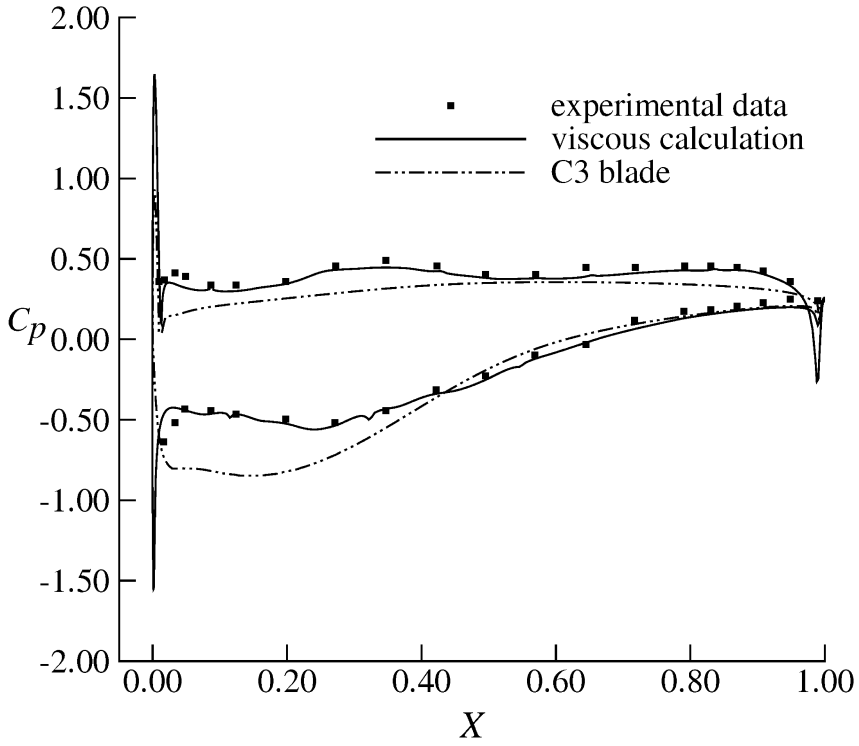

(a)

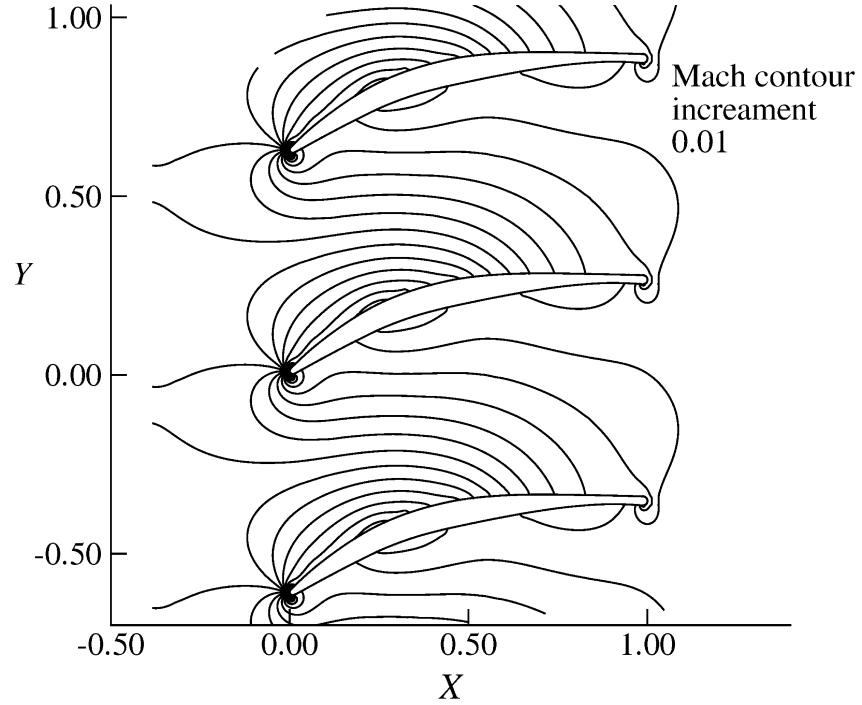

(b)

Figure 6.13: a- Isentropic Mach number distributions for design and redesign blades. b- Mach contours for Sanger cascade at design condition

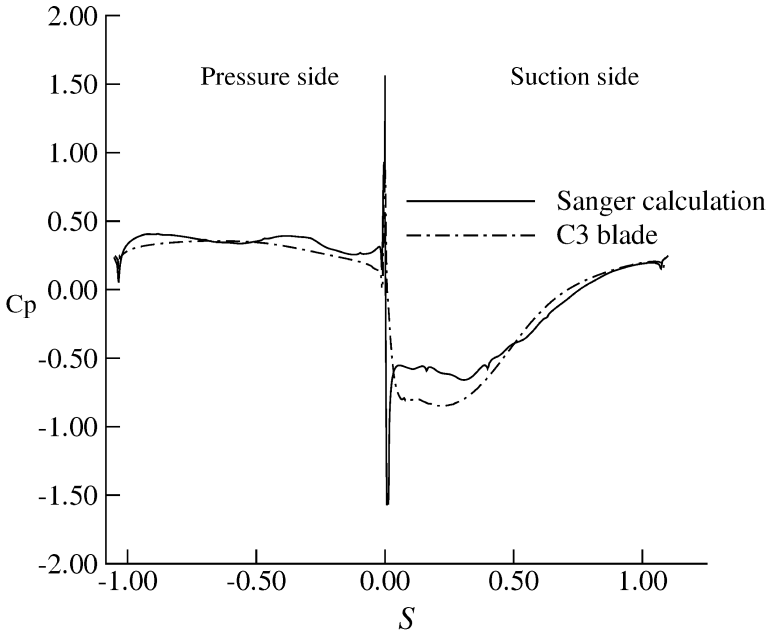

(a)

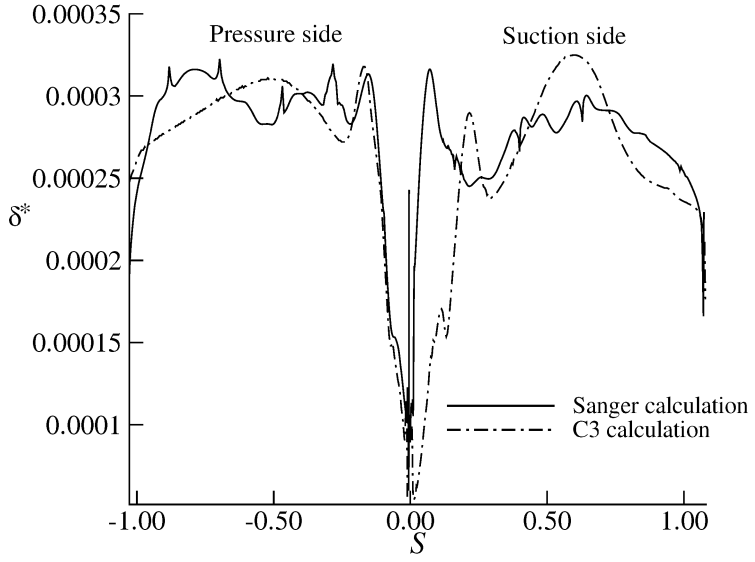

(b)

Figure 6.14: a-Surface Mach number distributions for the Sanger and C3 blades at design condition. b-Boundary layer displacement thickness calculations

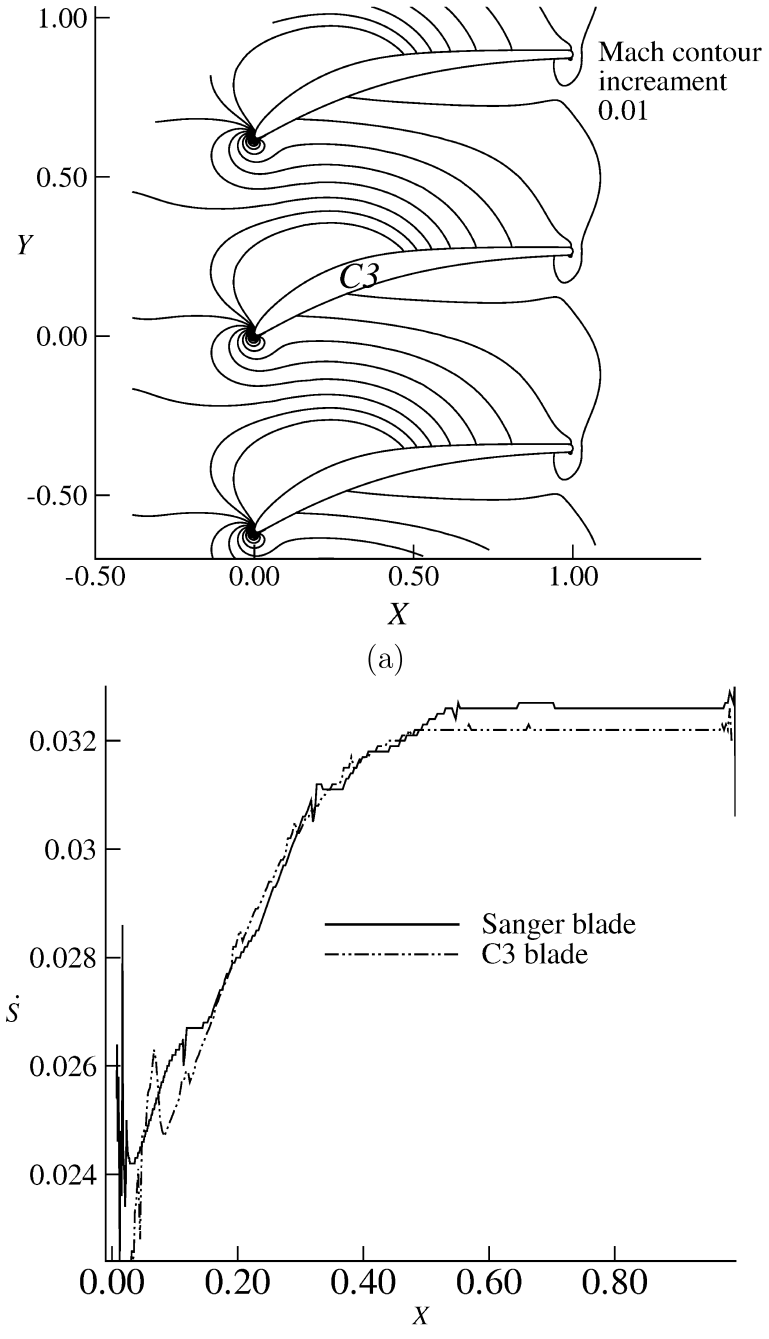

Figure 6.15: a-Mach contours for C3 blade. b-The rate of entropy creation on the suction side of the Sanger and C3 blades

6.4 Blade shape parameterization and stacking

General 3D blade shapes usually are described with a large number of parameters. A sample compressor blade has been used to show the ability of the PSCD blade design method to prescribe blade profiles from hub to tip, and to build up 3D blade geometry. Without loss of generality the 3D blade shape is represented by eleven blade sections from hub to tip in 10% increments (many more sections can be specified as the parameters are analytic functions along the radial direction). Each of these 2D sectional profiles can be defined by a few major parameters: stagger angle λ; tangential lift coefficient C_L; control points of blade suction sides Xc_s, Yc_s; and control points for blade pressure sides Xc_p, Yc_p. Similarly to the 3D design of turbines with the PSCD method in the earlier chapter, all of these are prescribed via third order Bezier spline curves from hub to tip. Parameterization using Bezier splines is one of the most popular approaches for blade design geometries.

The method begins with solving the radial momentum equation to obtain design parameter variations such as inlet flow angles, stagger angle, tangential lift coefficient etc from hub to tip. Presenting output parameters through Bezier curves is an convenient way to reduce design iterations and computational time for both direct and inverse design methods. Based on these the 3D PSCD method specifies the blade geometry sections easily, and the designer does not need any previous experience to design blade sections. The variation of 2D parameters via Bezier curves have been specified similarly to [8] with three data points at the hub, mean, and tip sections. Table 6.2 shows the output of the though-flow calculation from hub to tip for the sample stator blade.

Figures 6.17 (a, b, c and d) show non-dimensional surface curvature control points of the main part of the suction side of the blade which are $YC1s$, $YC2s$, $YC3s$ and $YC4s$ respectively. Figures 6.18 (a, b, c and d) show non-dimensional surface curvature control points of the main part of the pressure side of the blade which are $YC1p, YC2p, YC3p$ and $YC4p$ respectively. With this information for the suction

Table 6.2: Output parameters for stator from 3D streamline curvature (hub-tip)

Sections	α_1	α_2	ϕ_{in}-ϕ_{ex}	ψ	R_n	C_L
Hub	46.57000	30.88000	0.56000-0.60000	-0.36000	0.58000	0.85251
1	46.25000	30.74000	0.56000-0.59000	-0.34000	0.59000	0.85048
2	45.96000	30.61000	0.55000-0.58000	-0.32000	0.59000	0.84955
3	45.72000	30.47000	0.55000-0.57000	-0.31000	0.59000	0.85241
4	45.53000	30.34000	0.54000-0.56000	-0.29000	0.59000	0.85788
Mean	45.39000	30.19000	0.54000-0.55000	-0.28000	0.60000	0.86797
6	45.25000	30.04000	0.53000-0.54000	-0.27000	0.60000	0.87793
7	45.14000	29.89000	0.52000-0.53000	-0.25000	0.60000	0.88995
8	45.06000	29.74000	0.52000-0.53000	-0.24000	0.60000	0.90410
9	45.01000	29.60000	0.52000-0.52000	-0.23000	0.60000	0.91977
Tip	45.00000	29.46000	0.51000-0.51000	-0.22000	0.60000	0.93846

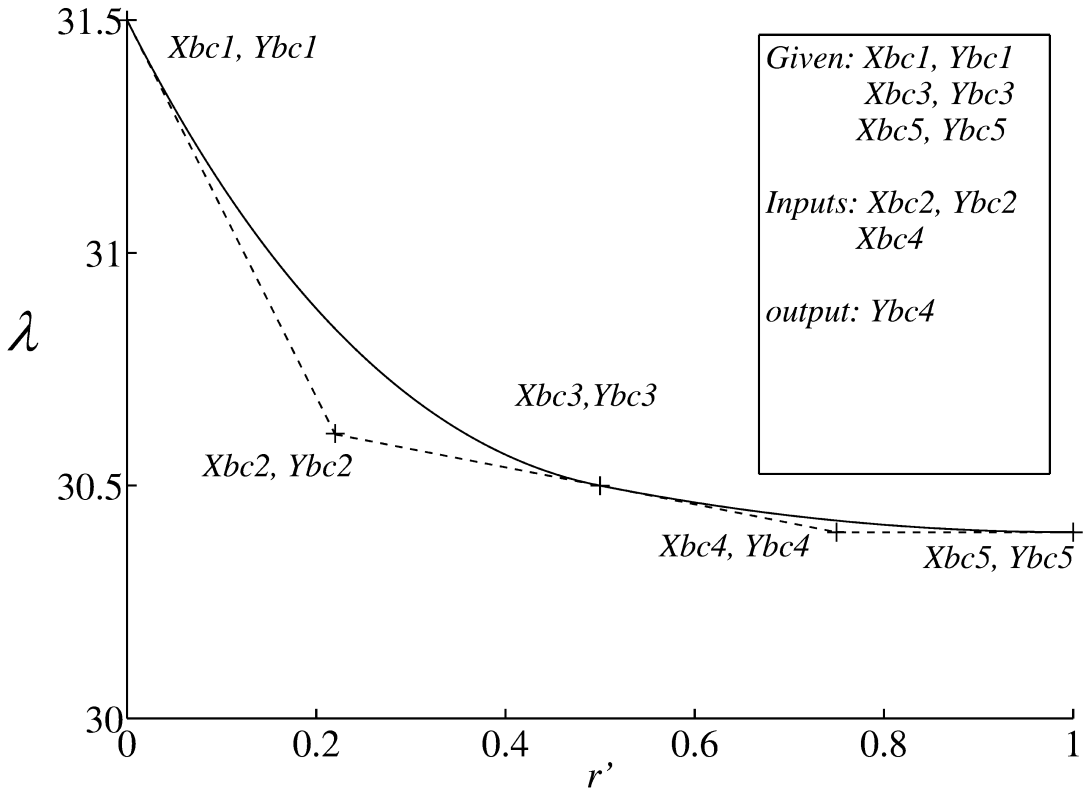

Figure 6.16: Stagger angle variations from hub to tip

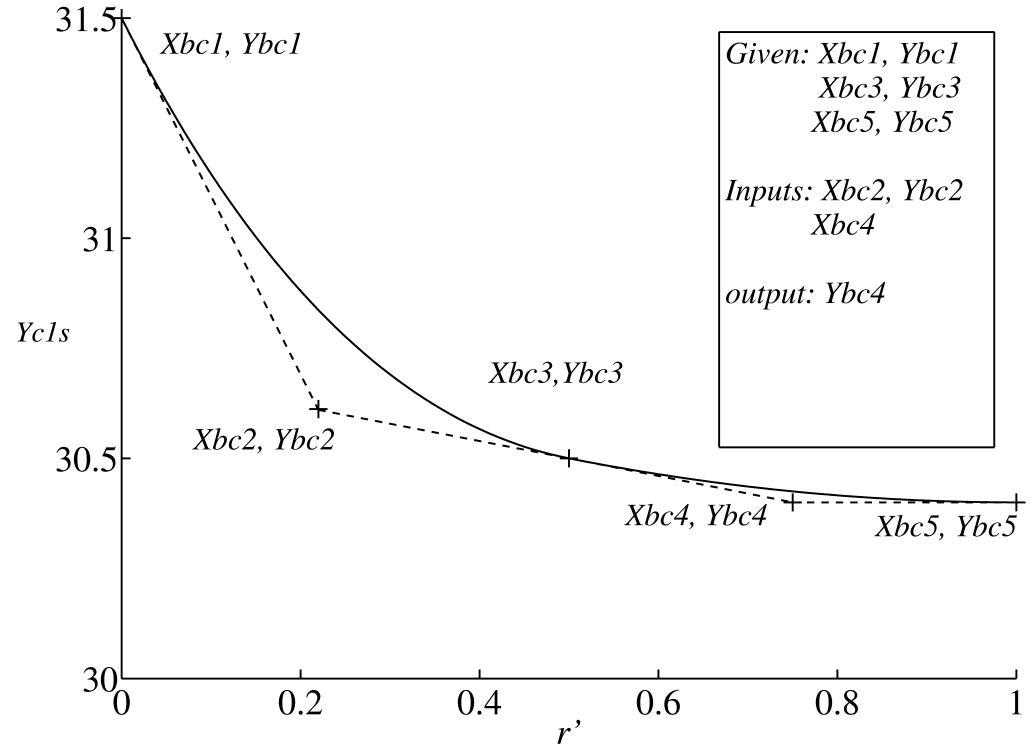
31.5
31
30.5
30
Yc1s
Xbc1, Ybc1
Xbc2, Ybc2
Xbc3,Ybc3
Xbc4, Ybc4
Xbc5, Ybc5
Given: Xbc1, Ybc1
Xbc3, Ybc3
Xbc5, Ybc5
Inputs: Xbc2, Ybc2
Xbc4
output: Ybc4
0
0.2
0.4
0.6
0.8
1
r'

(a)

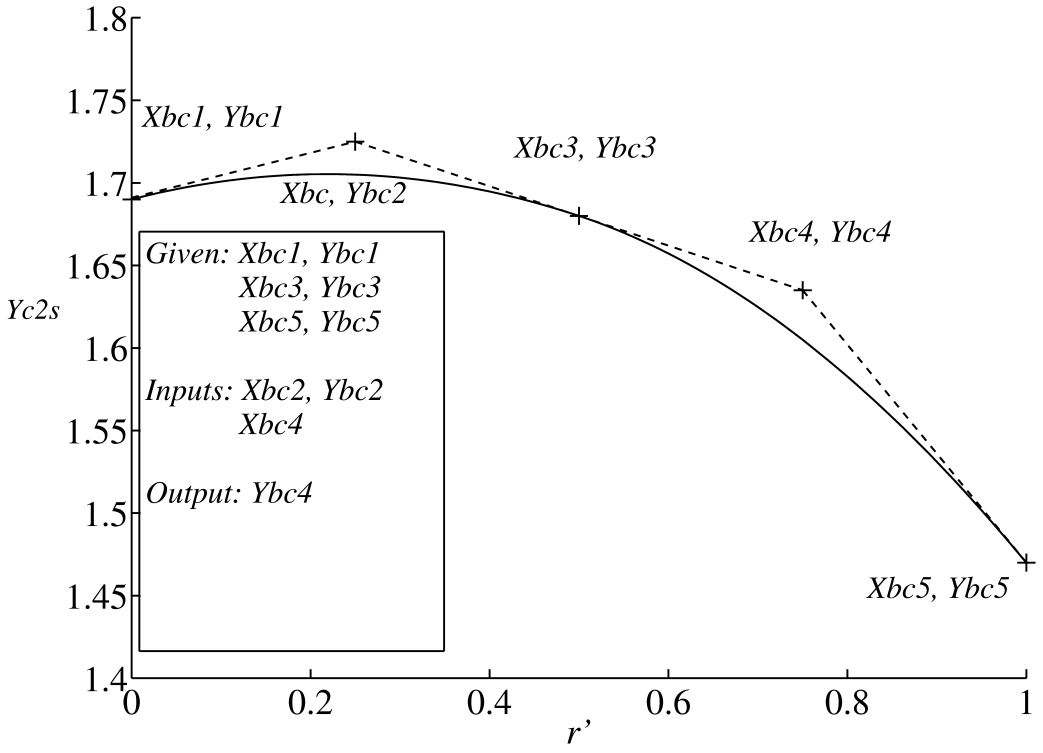
1.8
1.75
1.7
1.65
1.6
1.55
1.5
1.45
1.4
Yc2s
Xbc1, Ybc1
Xbc, Ybc2
Xbc3, Ybc3
Xbc4, Ybc4
Xbc5, Ybc5
Given: Xbc1, Ybc1
Xbc3, Ybc3
Xbc5, Ybc5
Inputs: Xbc2, Ybc2
Xbc4
Output: Ybc4
0
0.2
0.4
0.6
0.8
1
r'

(b)

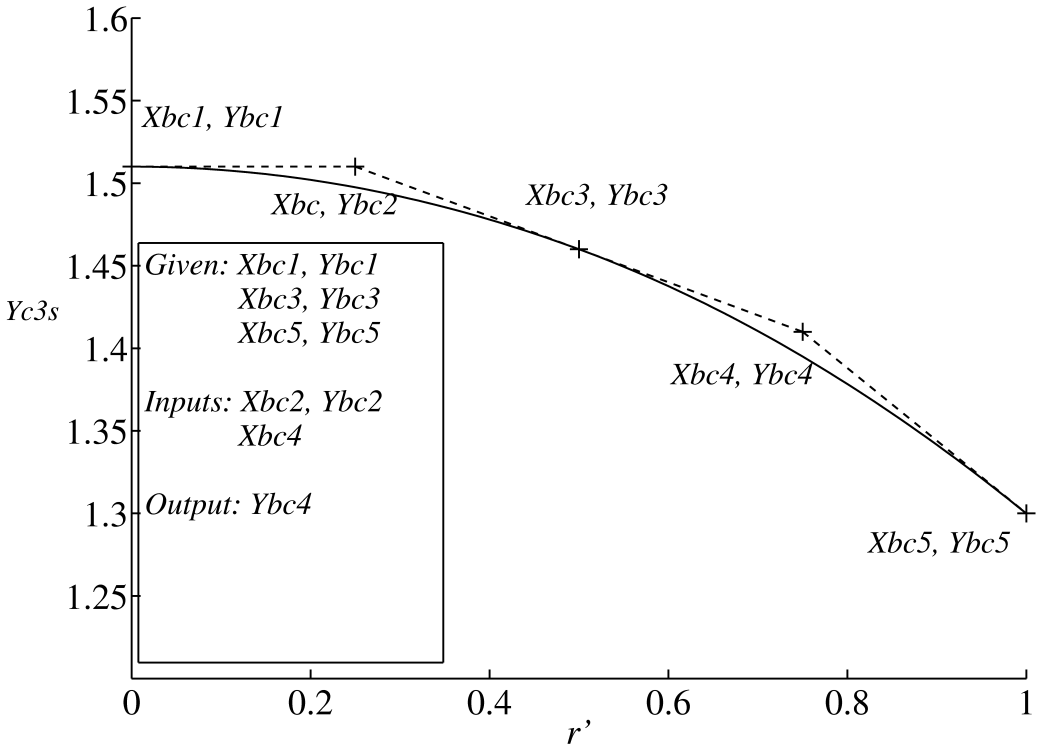

(c)

and pressure sides of the blade the designer is easily able to built up the 2D blade profiles from hub to tip. Three dimensional blade sections can be stacked through a center of gravity, trailing edge or leading edge of the blade as well. The sample blade has been stacked along the leading edge, along the trailing edge, and along the centers of gravity of the 2D sections. It can also be stacked with lean or dihedral along the span. Blade parameters have been used to design eleven sections across the span of the blade. These blade sections, based on the variation of parameters from hub to tip, are able to reduce the computing time and iteration approach. The stator cascade of the stage four of the compressor has been designed at the boundary condition of the inlet total temperature 442.857 K, the inlet total pressure of 460.665 kPa and the outlet static pressure of 336.249 kPa. These specifications have been chosen at different inlet flow and outlet flow angles from hub to tip as shown in table 6.2. Figure 6.19 shows the blade sections from hub to tip at different position from (0-100)%. The 3D blade shape stacked along the center of gravity is presented in Fig. 6.20.

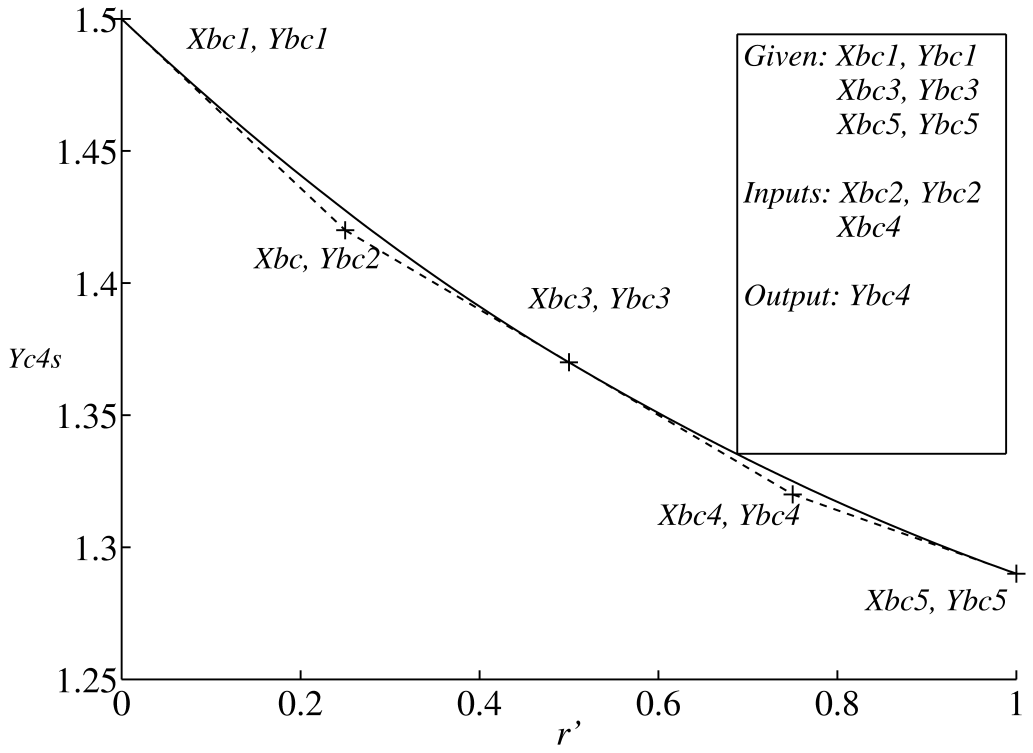

(d)

Figure 6.17: Hub to tip non-dimensional surface curvature control points of the suction side of the blade, a- $YC1s$, b-$YC2s$, c-$YC3s$, d-$YC4s$

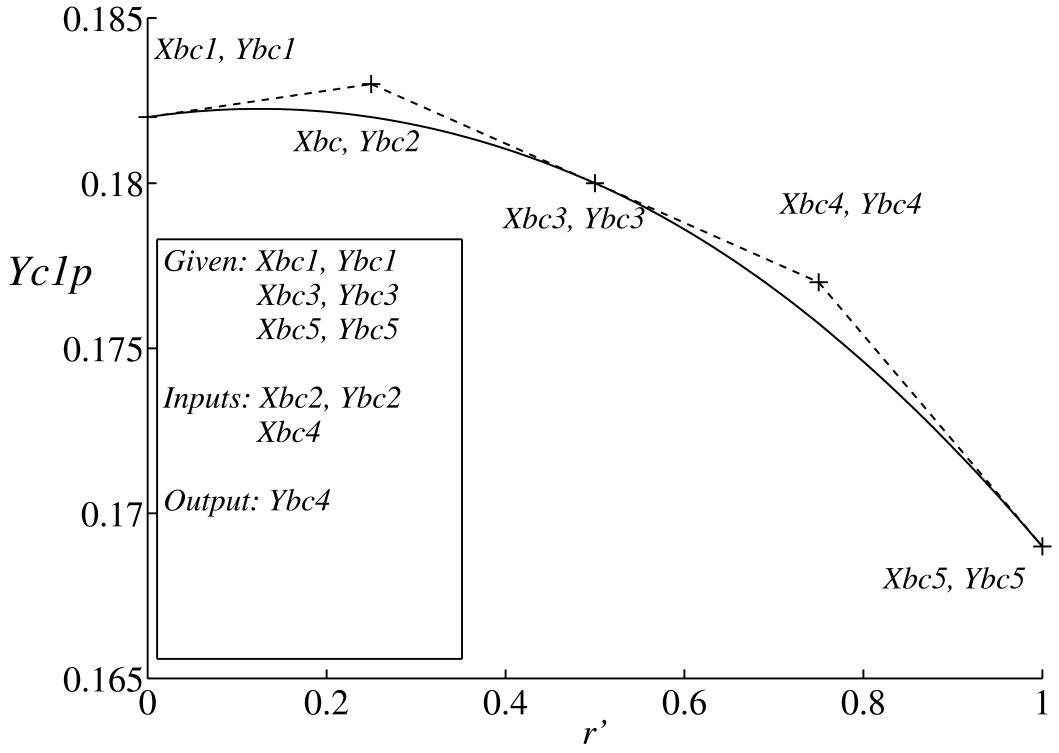
0.185
0.18
0.175
0.17
0.165
Yc1p
Xbc1, Ybc1
Xbc, Ybc2
Xbc3, Ybc3
Xbc4, Ybc4
Xbc5, Ybc5
Given: Xbc1, Ybc1
Xbc3, Ybc3
Xbc5, Ybc5
Inputs: Xbc2, Ybc2
Xbc4
Output: Ybc4
0
0.2
0.4
0.6
0.8
1
r'

(a)

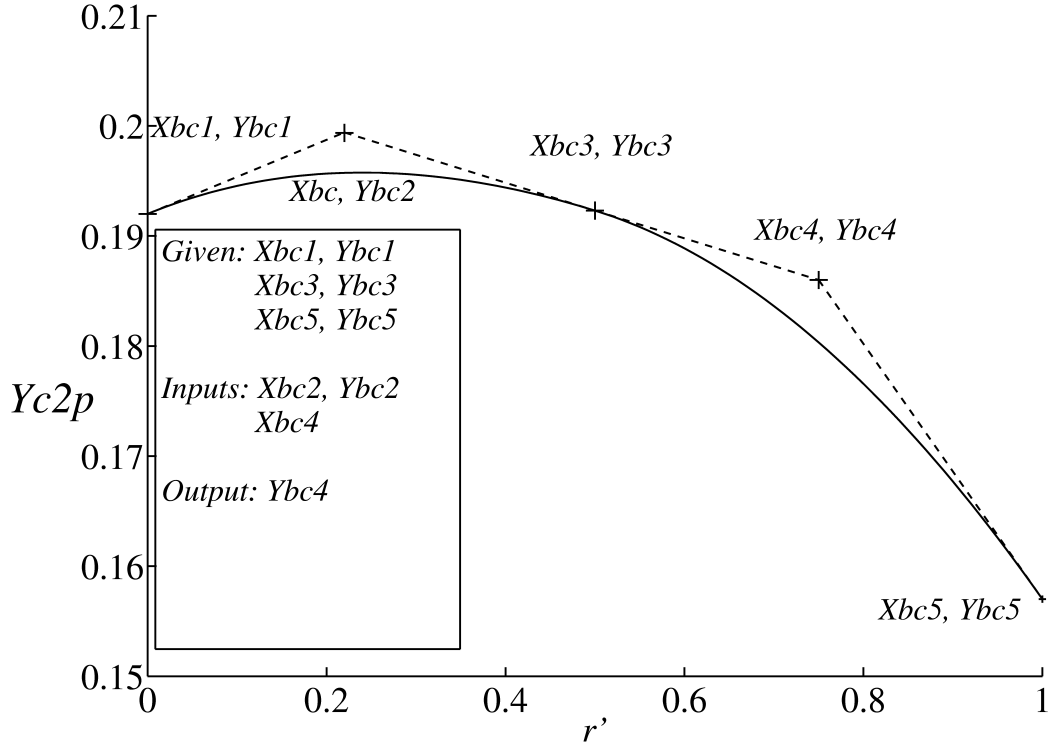
0.21
0.2
0.19
0.18
0.17
0.16
0.15
Yc2p
Xbc1, Ybc1
Xbc, Ybc2
Xbc3, Ybc3
Xbc4, Ybc4
Xbc5, Ybc5
Given: Xbc1, Ybc1
Xbc3, Ybc3
Xbc5, Ybc5
Inputs: Xbc2, Ybc2
Xbc4
Output: Ybc4
0
0.2
0.4
0.6
0.8
1
r'

(b)

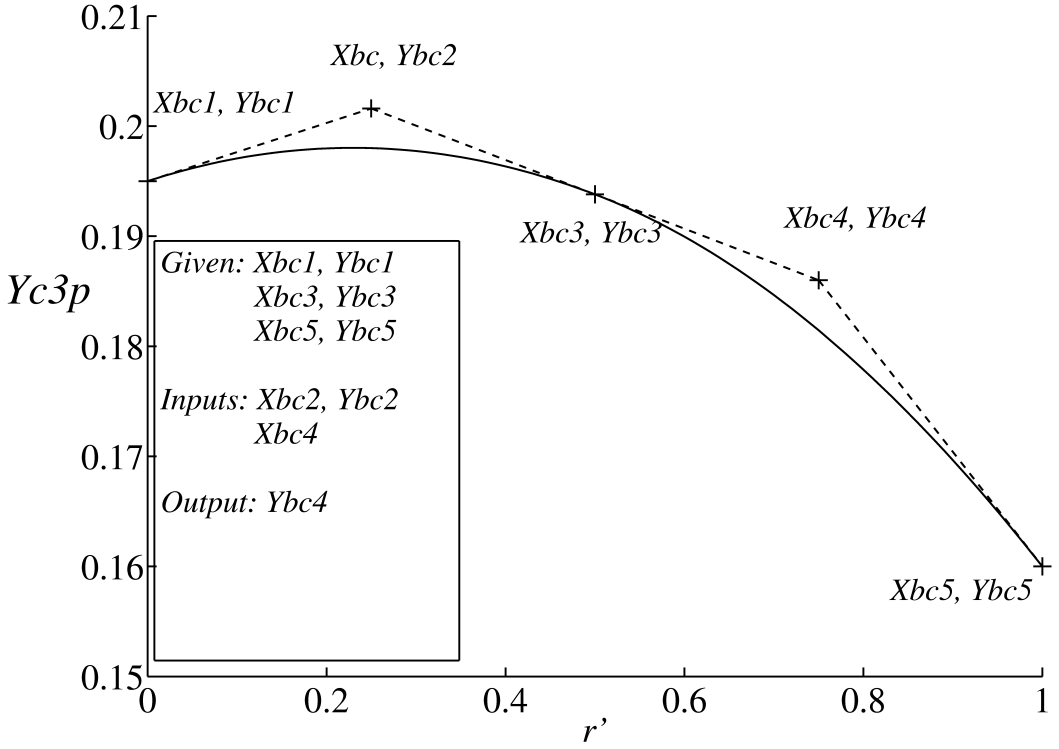

(c)

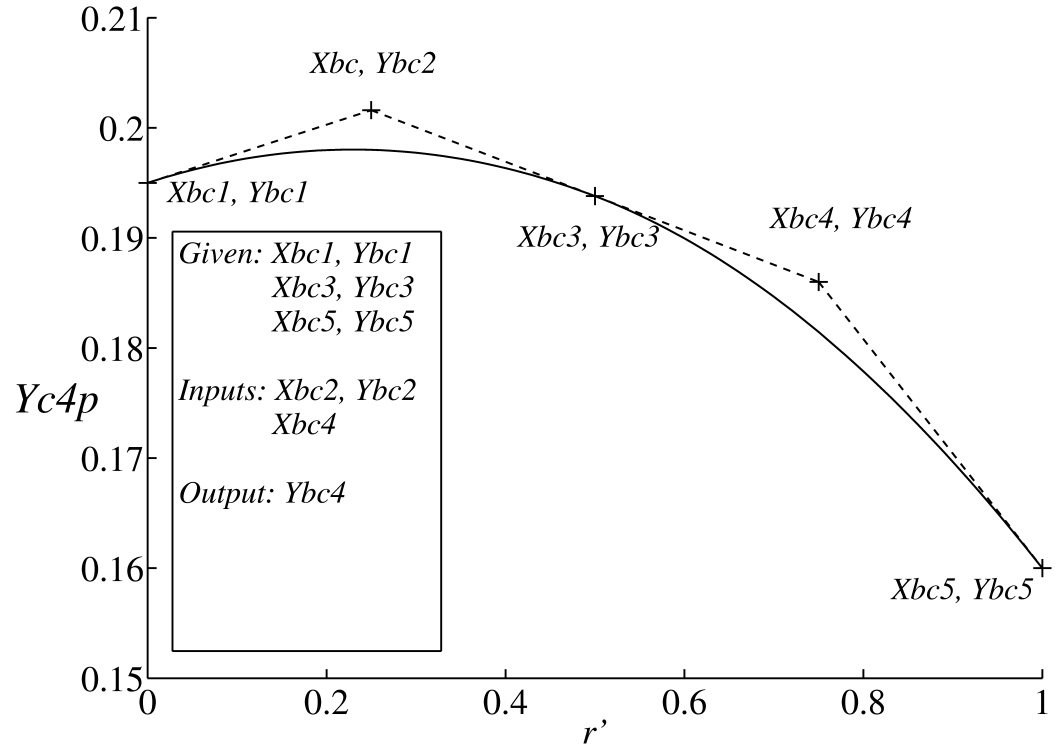

(d)

Figure 6.18: Hub to tip non-dimensional surface curvature control points of the pressure side of the blade, a- $YC1p$, b-$YC2p$, c-$YC3p$, d-$YC4p$

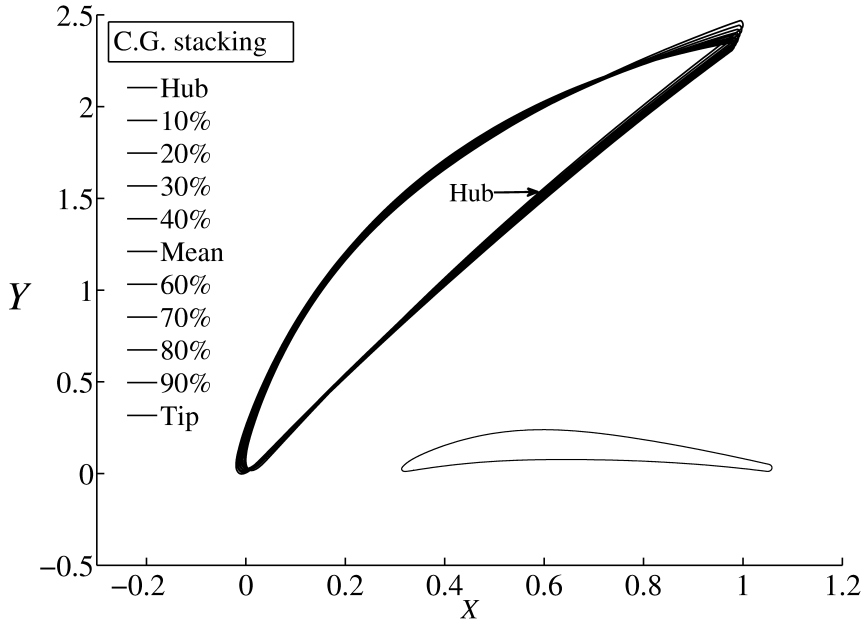

(a)

6.5 Conclusions

The PSCD blade design method has been used to redesign and optimize the MAN GGH 1-S1 blade with aim to reduce losses. The viscous prediction of the surface Mach number distribution agrees very well with the original-blade experimental results at design and positive conditions. At the negative incidence -7° some differences were observed. The PSCD method enables removal of the curvature discontinuity between the circle and the rest of the blade near the leading edge, and the redesigned blade moves the transition point upstream towards the leading edge. The computed stagnation pressure losses of the redesigned blade have been significantly decreased as compared with the original MAN GHH 1-S1 blade. Redesign of the Elazar cascade with the same method has also been illustrated. Excellent agreement was achieved between the experimental and calculated surface pressure distribution. It is now clear that how the discontinuity in the surface curvature affects the flow behavior around the leading edge and consequently the rest of the blade.

As known from the open literature [127, 128, 133, 134, 137–139], the possibility of improving efficiency, reducing secondary flow and increasing operation range can be

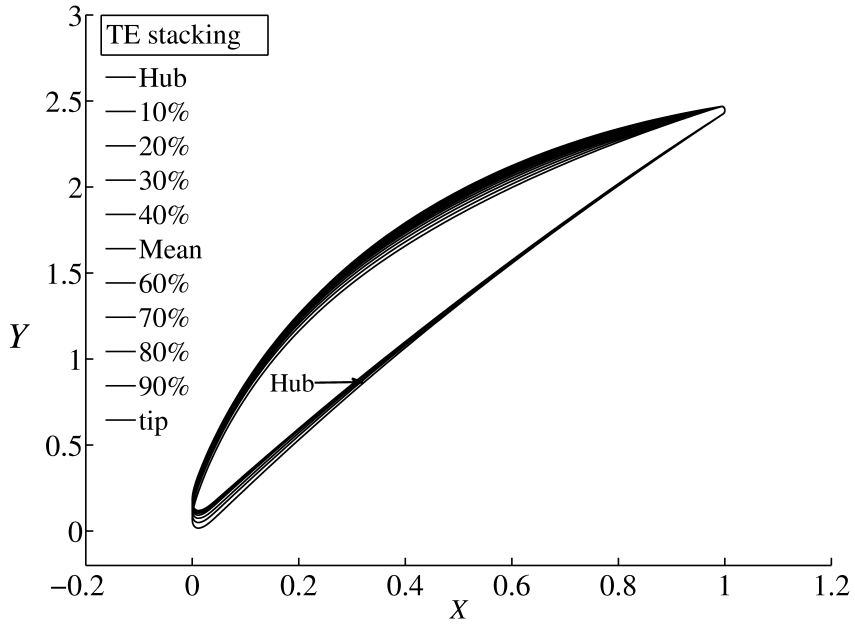

(b)

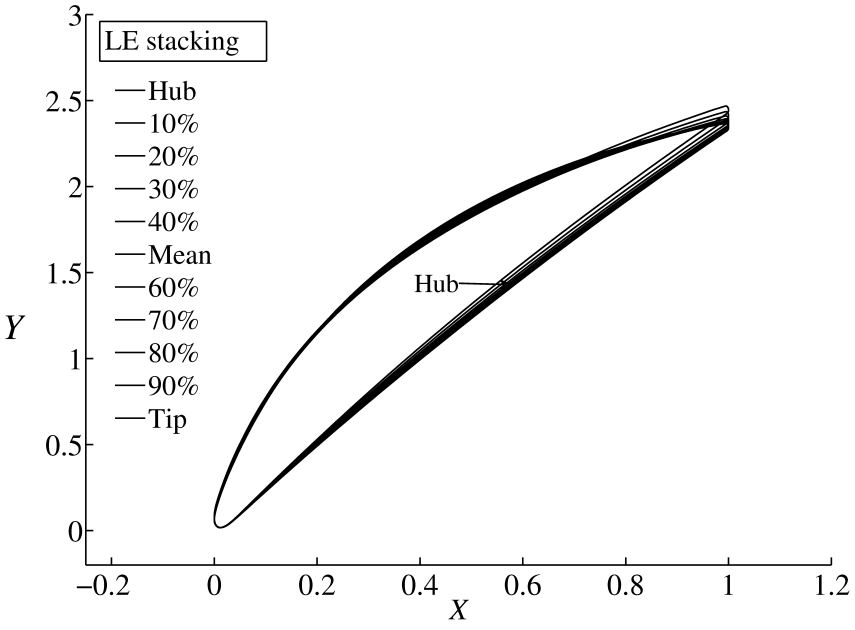

(c)

Figure 6.19: Blade stacking : a- Center of gravity, b- Trailing edge, and c- Leading edge

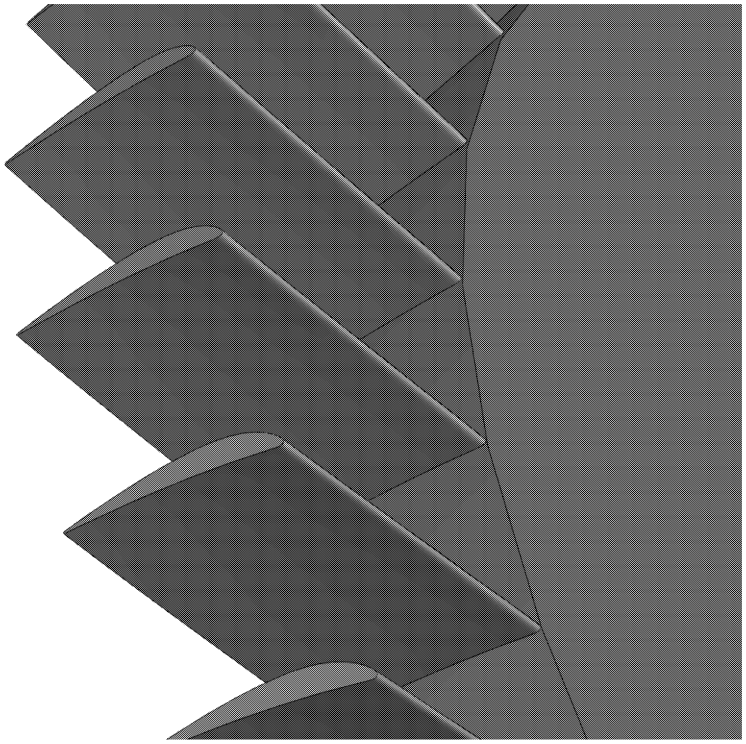

Figure 6.20: Stacking of the 3D compressor stator blade along the center of gravity achieved through the modification of the staking line of the 2D blade profiles(e.g. lean and dihedral). In this chapter the 3D PSCD environment of varying the hub to tip blade input parameters with Bezier curves, originally presented in [8], has been applied to compressor design from hub to tip. The resultant blade geometry sections have been modified and the aerodynamic performances (e.g. pressure distribution and isentropic Mach number) have been improved through removing flow disturbances and removing separation bubbles at the design condition. The PSCD method is highly flexible and robust to design all type of turbomachinery blades as well as the wind turbine airfoils (which will be discussed in the next chapter).

Chapter 7

Wind turbines and isolated airfoils

7.1 Introduction

Development of wind turbine technology requires an efficient wind turbine airfoil to generate electricity. Studies on an optimization of airfoil shape design methods show that the suitable shape of the blade are important to further reduce the cost of the produced energy and improving aerodynamic performances [177]. In addition to that when designing a wind turbine, the goal is to attain the highest possible power output under specified atmospheric conditions. From the technical point of view, this depends on the shape of the blade. The change of the shape of the blade is one of the methods to modify smoothness, stiffness and stability, and it influences aerodynamic efficiency of the wind turbine.

Early blade design methods were based on specifying a thickness distribution around a camber line. In this method, for specifying turbomachinery blade shapes, straight line, circular arc or parabolic camber lines were used, and then the thickness distribution was added to these camber lines for both the suction and the pressure sides of the blade. Examples of this method [12,15] are designs of NACA compressor airfoils (NACA-65 series), other series of NACA profiles for turbines by Dunavant and Erwin [23] and the most commonly used airfoil families for horizontal axis wind turbines have included the NACA 44xx, NACA23-xxx, NACA63-xxx, and NASA LS

airfoil series [178, 179]. This method did not provide enough flexibility to control both the suction and pressure surfaces in order to obtain a desirable aerodynamic performance.

Many methods have been developed to aid the designer in attaining optimum airfoil sections: traditional inverse method, full inverse approach, mixed-inverse method and direct method [180, 181]. In the traditional inverse design method the flow surface of the blade is prescribed at specified operational conditions and a geometry is found that will generate these surface flow conditions. Full-inverse methods determine the airfoil geometry form the overall surface pressure distribution whereas mixed-inverse methods determine parts of the airfoil contour while holding the rest unchanged. In this chapter, the direct design has been defined as a process in which the blade geometry is specified and the resultant aerodynamic performance on that geometry is calculated. Generally, the capability of the traditional inverse design method is limited for multiple design points when there is the only target pressure distribution has been used at a single design point. However, an inverse method was developed for the multi-point airfoil design method [182]. This method is able to allow different segments for the airfoil shapes by different flow constraints and limited off-design considerations but can not treat multidisciplinary design problems involving aerodynamics, structural dynamics, stability and control, manufacturing and maintenance considerations. These matters are most often taken care of manually by the designer in a cut and try process [183]. The direct design method [183] based on numerical optimization provide basically a rational multidisciplinary design procedure where several design parameters can be improved and multiple constraints can be imposed. However, all these methods have still limitations to control flow disturbances, separation around the leading edge and keeping continuity for the entire shape of the blade from the trailing edge to the leading edge. The PSCD blade design has been applied to the case of isolated airfoil in a manner similar to that for turbine and compressor blade design.

Aerodynamics of wind turbine has based on theory of airplane (NACA airfoil

series) and helicopter rotor [183]. However, performance characteristics (design and off-design) and thickness desirable for airplane airfoils are not necessarily good for wind turbine airfoils [184]. In the mid 1980's the development of wind turbine airfoils has been started and a large efforts were done by Tangler and Somers [185].

Airfoil design still requires a sensitive method to design highly smooth geometry surfaces and which is reflected to improve aerodynamic performance (pressure and Mach number distributions). In addition to that, most of the published data of designed wind turbine airfoil [183, 186–189] have separations and disturbances around the leading edge, pressure or suction surfaces of the airfoil.

The main purpose of this chapter is to illustrate the advantages of using the PSCD blade design method for the design of isolated airfoils, wing sections, and wind turbine blades. The redesign of the Eppler 387 airfoil [190] has been used as an example to illustrate the ability of the PSCD method to design isolated airfoils and wind turbine blades.

7.2 The PSCD method applied to isolated airfoils

Optimization results always requires a smooth airfoil shape. In principle, any physically realistic shape should be possible to allow design from scratch. An acceptable shape and computational costs are based on the flexibility of the design method which is based on few design variables to produce an effective and representative airfoil shape. It is important that the design space dose not limit by geometric description too much a priori. Different approaches can be used. Hicks [191] describes the airfoil thickness by a polynomial where the coefficients are design variables. Others such as [183, 188, 192, 193] used polynomials to present airfoil shapes. All the airfoil wind turbine design methods have difficulties to produce a smooth surface and control discontinuities in the surface curvature of the blade. These reflected to produce unwanted flow disturbances near the leading edge and leads to separate the flow around this area. In addition to that, the discontinuity produce kinks in surface

pressure or Mach number distribution and again leads to reduce the aerodynamic performance. All of these difficulties make the blade inefficient to produce power. The PSCD blade design method has unique advanatges for the design of turbine and compressor blades, and the same advantages carry over to the design of isolated airfoils and wind turbine blades. The effect of surface curvature discontinuity on the blade performance has been explained by Manner [104]. He explained that most of the kinks and dips in the surface pressure or Mach number distribution are a function of the discontinuity between the leading edge and the rest of the blade at design and off-design conditions. The discontinuity in the surface curvature between line segments and between the leading edge and the rest of the blade are a najor performance concern.

The application of the PSCD method to airfoils is straight forward: there is no throat restriction, so both the suction and pressure surfaces are designed in a manner identical to the pressure surfaces of compressor and turbine blades.

The Eppler 387 airfoil was chosen because of the importance of an airfoil geometry to most lifting devices and the availability of detailed experimental measurements [190]. The original Eppler 387 and redesigned A1 blade are shown in figure 7.1. There are small differences between their geometries, but they have substantially different aerodynamic performance because of the removal of a slope of curvature discontinuity on the suction surface, and also because of improvements in blending the leading edge circle to the main part of the airfoil. Blade parameters and representative blade points are in QMUL-EGR-2010-01 confidential report (available from Professor Korakianitis).

7.3 Results and discussion

The Eppler 387 airfoil has been used as a test case to show the ability of the PSCD method to design the "same" airfoil but with removing its flow disturbances from curvature effects through the entire blade geometry from the leading edge to the

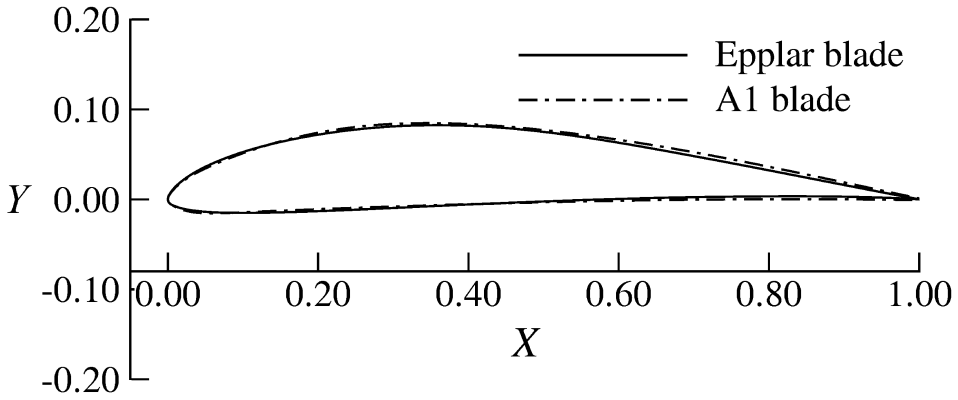

Figure 7.1: Blade geometries for the Eppler 238 and redesigned A1 blades

trailing edge. The flow performance shows (minor) disturbances near the leading edge and also a more-significant disturbance on the suction surface at $X \approx 0.7$ at the experimentally-tested angle of attack of $+4°$. These difficulties are separation bubbles, which are the result of high pressure gradient near the leading edge; and the shedding of vortices around the middle part of the suction surface, as published by many authors [194–196]. The laminar Navier-Stokes solver, which has been used by [195], can predict the flow behavior till the transition point and then the flow becomes fully turbulent. All of the existing turbulence models such as $k-\epsilon$, $k-\omega$ and $S-A$, are not able to precisely predict the transition point and flow re-attachment for this case including the existing $k-\epsilon$ Low- Reynolds turbulence models. The modified low Reynolds $k-\epsilon$ model, developed by Chen [61], has been implemented by the commercial code developers into FLUENT (version 6.3.26), and has been used in the computations discussed below.

Mesh generator (GAMBIT), flow solvers (FLUENT and ANSYS12) have been used in the computations. A reasonably high number of computational mesh elements is required for reasonably accurate calculations. The exact numbers depend on the geometry of the blade and its model. An example of the grid used for the Eppler 387 airfoil is shown in figure 7.2. A C-type mesh, produced by GAMBIT grid generator, is used in the present airfoil computation. The grid contains 730 points wrapped over the airfoil and 164 normal to the airfoil. The computational domain extends to 15 chord lengths in all directions. Grid resolution studies showed that

the high-velocity-gradient regions about the leading edge and primary separation required grid clustering.

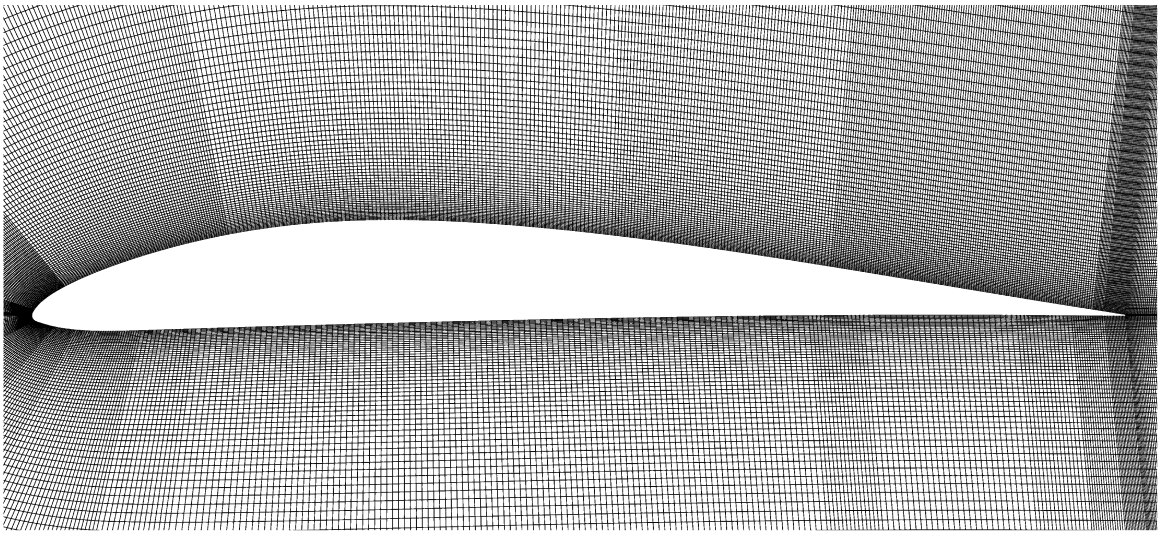

Figure 7.2: Part of the structured grid for the Eppler 387

The boundary conditions of this airfoil are as follows. At the outer boundaries, the free stream velocity was prescribed, matching the desired Reynolds number 1×10^5, and turbulence intensity was 0.5%. Further details can be found in [190, 194, 195]. The Eppler 387, redesigned A1 airfoils and their surface curvature distributions are shown in figure 7.3. The figure shows the flow separation for the leading edge and around the middle part of the original airfoil. It also obvious the modified A1 blade is free from those disturbances. The pressure coefficients for both airfoils, Eppler 387 and A1, have been shown in figure 7.4. The proposed turbulence model can accurately predict the transition point and also re-attachment flow after separation. In addition to that, with removing the discontinuity in the surface curvature from the leading edge to the trailing edge of the airfoil, there is no separation flow around the modified A1 blade. It means the surface curvature gives the guidance to the designer, prior to the analyzing the flow, to predict the difficulty which is the result of the discontinuity in the surface of the blade. The Mach contours of the Eppler around the whole blade and the middle part of the airfoil are shown in figure 7.5. The laminar separation bubble is quite clear around this area of the Eppler airfoil

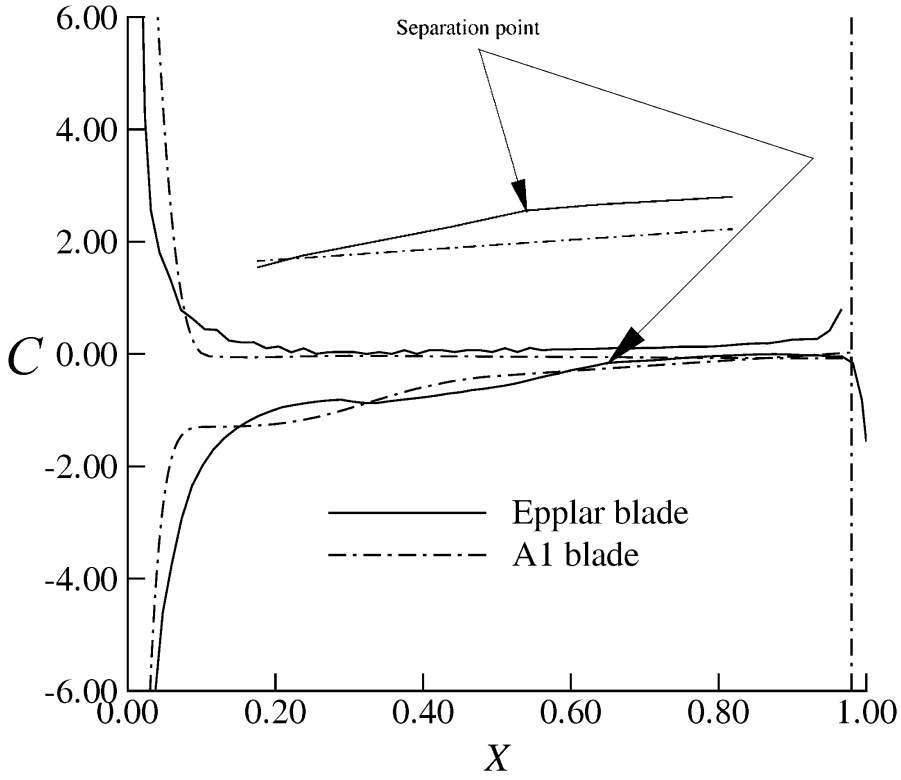

Figure 7.3: Sample of curvature distributions for the Eppler 387 and redesigned A1 airfoils

and can accurately predicted by using of the modified Chen's model to the k-e turbulence model. Figure 7.6 shows the Mach contours of the whole modified A1 airfoil and around its middle part. The flow computations indicate that the modified A1 blade is free from flow disturbances and separation bubbles. This is the result of removing discontinuities in the surface curvature. The results show that the PSCD blade design method is highly flexible, accurate and robust, and provides unique advantages to the design of all types of blades and flow passages.

7.4 Conclusions

The PSCD method is an efficient, robust and flexible method, and in addition to turbine and compressor 2D and 3D blade sections, it can be used to design high

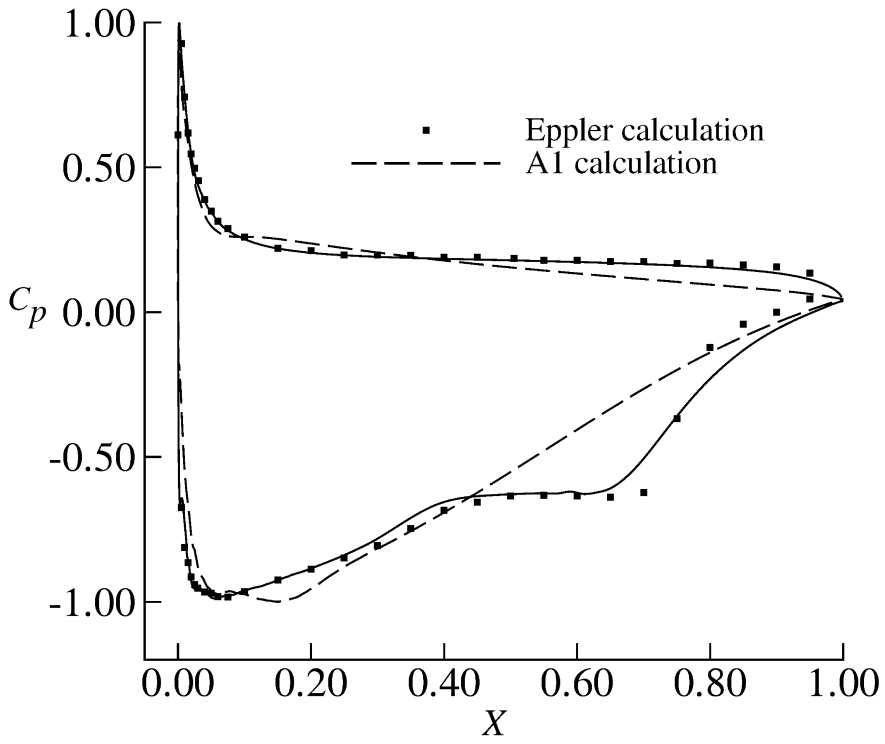

Figure 7.4: Pressure distributions for the Eppler 387 and redesigned A1 airfoils

efficiency 2D and 3D airfoils and wing sections, and wind turbine blades. The surface curvature distribution effects on aerodynamic performance is a major guidance parameter, which must be taken into account prior to flow analysis. The modified low Reynolds $k-\epsilon$ turbulence model has a good response to predict the separation phenomena and re-attachment of the flow on the blade surface. The discontinuity of the surface curvature of the Eppler blade is a source of the laminar separation around the leading edge and the rest of the blade. Results obtained for the Eppler 387 and the redesigned A1 blade (pressure distribution and Mach contours) show excellent agreement with the experimental data and other published calculation results. It is concluded that the PSCD blade design method is a unique tool to eliminate flow disturbances and separation bubbles in airfoil performance.

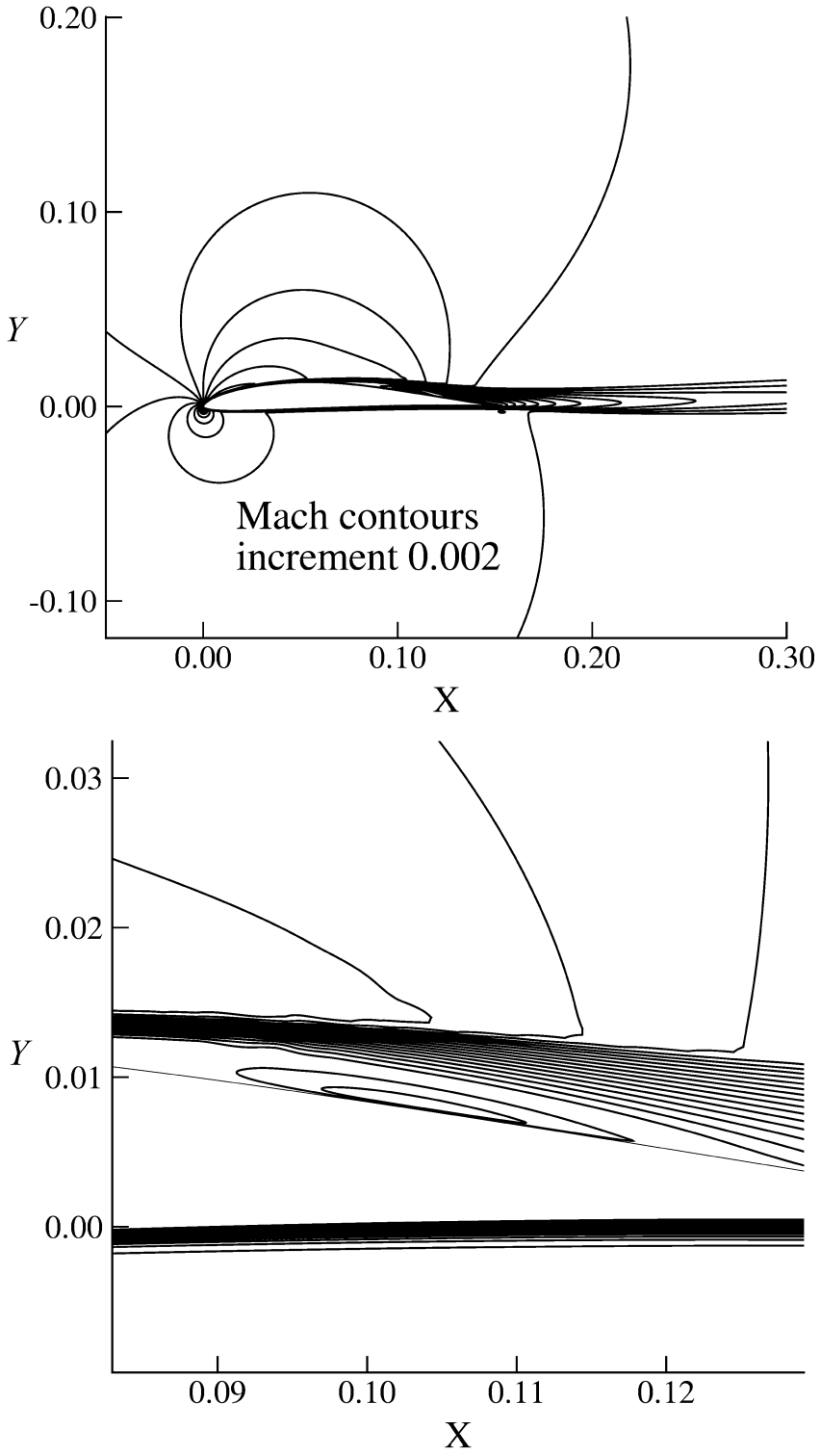

Figure 7.5: Mach contours around the whole blade and the shown separated area of the Eppler 387

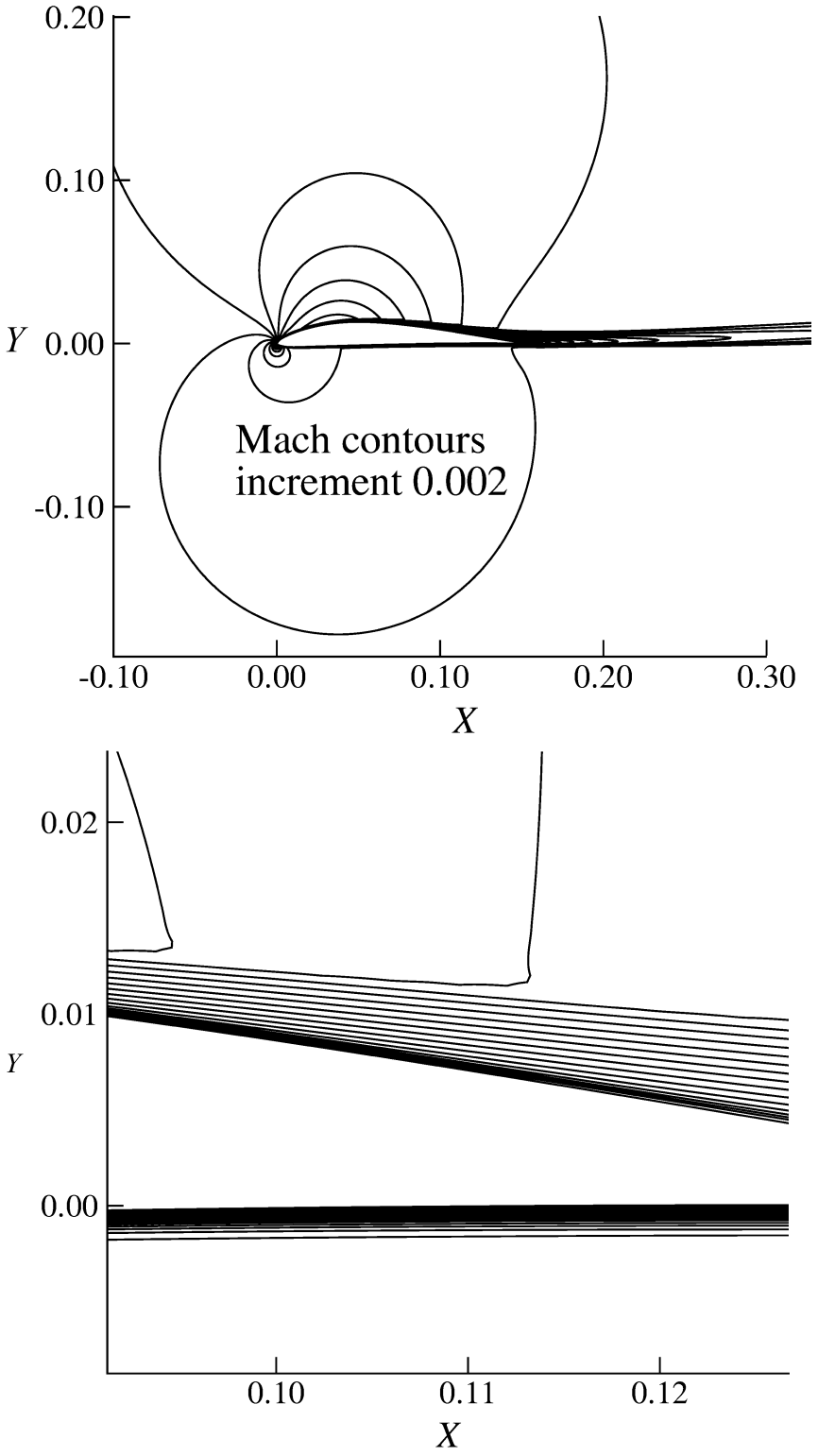

Figure 7.6: Mach contours around the whole blade and the shown separated area of the redesigned A1 airfoil

Chapter 8

Conclusions

The PSCD blade design method has been used with several 2D and 3D turbine, compressor, and airfoil examples to illustrate its aerodynamic performance and heat transfer advantages over other blade design methods. Blade surface curvature distribution is a key criterion for blade design. Smoothing the surface curvature distribution removes surface discontinuities between line segments of the blade and produces high efficiency blades. The various polynomials and construction lines used to join the surfaces with the leading and trailing edge shapes presented in [2–9] have been further investigated, and improved forms of the polynomials and construction lines have been introduced in the latest version of PSCD, albeit of the same general nature as those proposed in [8].

The results of seven test cases and several sample blades show the advantages of the PSCD blade design method in removing over-speed regions (high acceleration and deceleration in surface Mach number distribution or surface pressure distribution) near the leading edge and in smoothing blade surfaces from the stagnation point at the leading edge to the stagnation point at the trailing edge of the blades. The results of these test cases confirm that surface curvature distribution affects aerodynamic as well as heat transfer performance via the effects it has on the local boundary layer.

The computational results have been obtained by running commercial codes

GAMBIT (mesh generator), FLUENT and ANSYS 12 (flow solvers) with modeling inviscid, viscous two dimensional compressible flows for a series of test cases. The validity of the results is insured by comparing the computational output with sample blade geometries that have been experimentally tested in the open literature.

Significant recent advances have been made in direct and inverse blade design methods for the design of airfoils and blades. Most of the existing blade geometries in the open literature up to date, which are designed with those methods, have difficulties around the leading edge, trailing edge and most of the suction and pressure surfaces. These methods usually result in streamwise blade surface curvature disturbances (or sometimes curvature discontinuities). Acceleration-deceleration regions and occasionally separation bubbles near the leading edge are hard to remove with these methods. The PSCD blade design method resolves these difficulties. It can produce high efficiency blade shapes for the direct or inverse design of subsonic or supersonic isolated airfoils and turbomachinery blades.

The computed results of the turbomachinery blades and Eppler airfoil re-designed using the PSCD blade design method suggest the following. The mass-weighted average stagnation pressure losses are decreased with removing the spikes and dips in the surface Mach number distribution near the leading edge circle (which are the result of discontinuities in the slope of surface curvature). The PSCD method results in improved leading edge geometries, which improve off-design aerodynamic performance at positive an negative angles of incidence. This increases the range of operation by removing the leading edge flow disturbances at off-design conditions. Removing the spikes and dips in the surface heat transfer coefficient distribution or Stanton number distribution decreases the local heat transfer rate on the surface of the blade.

Complex blade shapes and all type of turbomachinery blades can be easily designed with the PSCD blade-design method. Highly smooth surfaces for blades can be achieved to improve aerodynamic performance and surface heat transfer distribution. Thin or thick blades, and high turning blades can be easily designed with

this method. The possibility of improving efficiency, secondary flow effects, and increasing operating range may be achieved through the modifications of the stacking line of the two-dimensional blade profiles (lean and dihedral). Shock waves are also partially a function of surface curvature discontinuity and they can be reduced with producing a smooth surface. Blade parameters and representative blade points for all redesigned blades are in QMUL-EGR-2010-01 confidential report (available from Professor Korakianitis).

Chapter 9

Recommendations

The PSCD blade design method is a significant contribution to turbomachine design because it can be used to remove the spikes and dips in the surface pressure distribution in blade shapes, which are the result of discontinuities in the slope of surface curvature. The PSCD method is highly flexible and efficient, robust, and it can be used to design 2D and 3D turbomachinery blades, isolated airfoils, and wind turbine airfoils. It is recommended that the PSCD method is used to produce high efficiency blades, and that it may replace other direct and inverse blade design methods. It is highly recommended to use this blade design method for practical applications. It is recommended to study the effect of surface curvature on aeromechanical integrity. A frequent cause of turbomachinery blade failures is the high cycle fatigue failure (HFC) resulting from cyclic loads. For turbomachinery blades the most common cyclic excitation source is a non-uniform flow field generated by upstream wakes, inlet distortion and flow disturbances (e.g. separation bubble) stemming from the blade surface and pressure interaction on adjacent rows. It is quite necessary to lower the vibration stresses to an acceptable level to avoid HFC failures by producing a highly efficient blade.

The ability of the method has been explained in the design of 2D and 3D blade profiles from hub to tip for turbomachinery blades. It is recommended the method is applied to 3D wind turbine airfoils.

The advantages of the off-design effects on the continuity in the surface curvature of the blade has been presented. It is recommended to use the PSCD blade design method to study the effect of surface curvature at off-design conditions for wind turbine airfoils. Using the PSCD blade design method as a platform, we can address the overall blade design industry.

Bibliography

[1] A. G. Gerber, R. Sigg, L. Völker, M. V. Casey, and N. Sürken. Prediction on non-equilibrium phase transition in a model low pressure steam turbine. *Transactions of the ASME, Journal of Engineering for Power and Energy*, 221(A6):735–744, September 2007.

[2] T. Korakianitis. *A design method for the prediction of unsteady forces on subsonic, axial gas-turbine blades.* Doctoral dissertation (Sc.D., MIT Ph.D.) in mechanical engineering, Massachusetts Institute of Technology, Cambridge, MA, USA, September 1987.

[3] T. Korakianitis. Design of airfoils and cascades of airfoils. *AIAA Journal*, Vol.27(4):455–461, April 1989.

[4] T. Korakianitis. Hierarchical development of three direct-design methods for two-dimensional axial-turbomachinery cascades. *Transactions of the ASME, Journal of Turbomachinery*, 115(2):314–324, April 1993.

[5] T. Korakianitis. Prescribed-curvature distribution airfoils for the preliminary geometric design of axial turbomachinery cascades. *Transactions of the ASME, Journal of Turbomachinery*, 115(2):325–333, April 1993.

[6] T. Korakianitis and P. Papagiannidis. Surface-curvature-distribution effects on turbine-cascade performance. *Transactions of the ASME, Journal of Turbomachinery*, 115(2):334–341, April 1993.

[7] T. Korakianitis and G. Pantazopoulos. Improved turbine-blade design techniques using fourth-order parametric spline segments. *Computer Aided Design (CAD)*, 25(5):289–299, May 1993.

[8] T. Korakianitis and B. H. Wegge. Three dimensional direct turbine blade design method. AIAA paper 2002-3347. AIAA 32nd fluid dynamics conference and exhibit, St. Louis, Missouri, June 2002.

[9] T. Korakianitis. Surface curvature driven robust design and optimization of turbomachinery blades. Euromech Colloquium 482, London, September 2007.

[10] T. Korakianitis and D. Zou. Through-flow analysis for axial-stage design including streamline-slope effects. ASME paper 93-GT-56, 1993.

[11] B. Lakshminarayana. *Fluid dynamics and heat transfer of turbomachinery.* John Wiley and Sons, Inc., 1996.

[12] D. G. Wilson and T. Korakianitis. *The design of high-efficiency turbomachinery and gas turbines.* Prentice Hall, 2nd edition, 1998.

[13] H. Cohen, GFC Rogers, and HIH Saravaamuttoo. *Gas turbine theory.* 4^{th} edition Cornwall press, 1996.

[14] D. G. Wilson. *The design of High-efficiency turbomachinery and gas turbines.* The MIT Press, 1984.

[15] J. D. Mattingly. *Elements of gas turbine propulsion.* McGraw-Hill, Inc., 1996.

[16] Ruolong Ma., Scott C. Morris, and Thomas C. Corke. Design of a transonic research turbine facility. *AIAA 2006-1311*, 2006.

[17] R. I. Lewis. *Turbomachinery performance analysis.* Arnold, 1996.

[18] O. Zweifel. The spacing of turbomachine blading, especially with large angular deflection. *Brown Boveri Review*, 32(12), 1945.

[19] D. G. Aniley and G. C. R. Mathieson. An examination of the flow and pressure losses in blade rows of axial flow turbines. British ARC R and M 2891, 1951.

[20] Stewart and Glassman. Turbine design and application. NASA-SP-290, 1973.

[21] S. C. Kacker and U. Okapuu. A mean-line prediction method for axial-flow turbine efficiency. ASME paper 81-GT-58, 1981.

[22] J. H. Horlock. *Axial flow turbines.* Krieger publishing copmany, Huntington, New york, 1973.

[23] J. C. Dunavant, Tannehill J., and Erwin R. Investigation of a related series of turbine blade profiles in cascade. NACA TN 3802, Washington, 1956.

[24] J. Dunham. A parametric method of turbine blade profile design. ASME, 74-GT-119, 1974.

[25] L. J. Pritchard. An eleven parameter axial turbine airfoil geometry model. ASME, 85-GT-219, 1985.

[26] G. Meauze. Overview on balding design methods. In AGARD, editor, *Blading design for axial turbomachines, AGARD Lecture Series 167, AGARD-LS-167.* AGARD, 1989.

[27] P. Stow. Blading design for multi-stage hp compressors. In AGARD, editor, *Blading design for axial turbomachines, AGARD Lecture Series 167, AGARD-LS-167.* AGARD, 1989.

[28] B. Phillipsen. A simple inverse cascade design method. ASME, 2005-GT-68575, 2005.

[29] W. Steinert, B. Eisenberg, and H. Starken. Design and testing of a controlled diffusion airfoil cascade for industrial axial flow compressor application. *Transaction of the ASME, Journal of Turbomachinery*, 113:583–590, 1991.

[30] G-L Liu. A new generation of inverse shape design problem in aerodynamics and aero-thermoelasticity: concepts, theory and methods. *An International Journal of Aircraft Engineering and Aerospace Technology*, 72(4):334–344, April 2000.

[31] Oguz U. and Camci C. Aerodynamic loss characteristics of a turbine blade with trailing edge coolant ejection: Part 2- external aerodynamics, total pressure losses, and predictions. *Transaction of the ASME, Journal of Turbomachinery*, 123:249–257, 2001.

[32] A. M. O. Smith. High lift aerodynamics. *Journal of Aircraft*, 12(6), 1975.

[33] W. T. Tiow and M. Zangeneh. A three-dimensional viscous transonic inverse design method. 2000-GT-0525, 2000.

[34] M. P. C. van Rooij, T. Q. Dang, and L. M. Larosiliere. Improving aerodynamic matching of axial compressor blading using a 3D multistage inverse design method. *Transactions of the ASME, Journal of turbomachinery*, 129(1):108–118, 2007.

[35] R. Corral and G. Pastor. Parametric design of turbomachinery airfoils using highly differentiable splines. *Journal of Propulsion and Power, Vol. 20, No. 2, pp. 335-343*, March-April 2004.

[36] H. P. Hodson. Boundary-layer transition and separation near the leading edge of a high-speed turbine blade. *Transactions of the ASME, Journal of Engineering for Gas Turbines and Power*, 107:127–134, 1985.

[37] H. P. Hodson and R. G. Dominy. Three dimensional flow in a low pressure turbine cascade at its design condition. *Transactions of the ASME, Journal of Turbomachinery*, 109(2):177–185, April 1987.

[38] H. P. Hodson and R. G. Dominy. The off-design performance of a low-pressure turbine cascade. *Transactions of the ASME, Journal of Turbomachinery*, 109(2):201–209, April 1987.

[39] A. Massardo, A. Satta, and M. Marini. Axial-flow compressor design optimization. 1. Pitchline analysis and multivariable objective function influence. *Transactions of the ASME, Journal of Turbomachinery*, 112(3):399–404, 1990.

[40] A. Massardo and A. Satta. Axial-flow compressor design optimization. 2. Throughflow analysis. *Transactions of the ASME, Journal of Turbomachinery*, 112(3):405–410, 1990.

[41] A. F. Massardo and M. Scialò. Thermoeconomic analysis of gas turbine based cycles. *Transactions of the ASME, Journal of Engineering for Gas Turbines and Power*, 122:664–671, 2000.

[42] V. Pachidis, P. Pilidis, F. Talhouarn, A. Kalfas, and I. Templalexis. Thermoeconomic analysis of gas turbine based cycles. *Transactions of the ASME, Journal of Engineering for Gas Turbines and Power*, 128(3):579–584, 2006.

[43] C. H. Wu. A general theory of three-dimensional flow in subsonic and supersonic turbomachines of axial-radial and mixed-flow type. NACA TN 2604, 1952.

[44] C. H. Wu and L. Wolfenstein. Application of radial-equilibrium condition to axial flow compressor and turbine design. NACA Report 955, (also 1949 NASA TN 1795), 1950.

[45] L. H. Smith. The radial-equilibrium equation of turbomachinery. *Transactions of the ASME, Journal of Engineering for Power*, 88:1–12, January 1966.

[46] R. A. Novak. Streamline curvature computing procedures for fluid-flow problems. *Transactions of the ASME, Journal of Engineering for Power*, 89:478–490, October 1967.

[47] H. Marsh. A digital computer programme for the through-flow fluid mechanics in an arbitrary turbomachine using a matrix method. ARC R& M 3509, 1968.

[48] J. D. Denton. Throughflow calculations for transonic axial flow turbines. *Transactions of the ASME, Journal of Engineering for Power*, 100(2):212–218, April 1978.

[49] R. P. Dring and H. D. Josyln. Through-flow analysis of a multistage compressor: part i - aerodynamic input. *Transactions of the ASME, Journal of Turbomachinery*, 108(3):17–22, July 1986.

[50] D. Buche, G. Guidati, and P. Stoll. Automaited design optimization of compressor blades for stationary, large-scale turbomachinery. ASME Turbo Expo 2003, GT2003-38421, 2005.

[51] F. Sieverding, B. B. Ribi, M. Casey, and M. Meyer. Design of industrial axial compressor blade sections for optimal range and performance. *Transactions of the ASME, Journal of Turbomachinery*, 126:323–331, April 2004.

[52] J. Z. Xu and C. W. Gu. Anumerical procedure of three dimensional design problem in turbomachinery. *Transaction of the ASME, Journal of Turbomachinery*, 114:79–90, 1992.

[53] P. L. Miller IV, J. H. Oliver, D. P. Miller, and D. L. Tweedt. Turbine design and application. NASA-TM-107262, 1996.

[54] A. Oyama, M-S Liou, and S. Obayashi. Transonic axial-flow blade shape optimization using evolutionary algorithm and three-dimensional navier-stokes solver. AIAA 2002-5642, 2002.

[55] V. Richard, G. Paniagua, H. Kato, and M. Thatcher. Design and testing of the contra-rotating turbine for the scimitar precooled mach 5 cruise engine. IAC-08-C4.5.3, 2008.

[56] Ki-S. Lee, K-Y. Kim, and A. Samad. Design optimization of low-speed axial flow fan blade with three-dimensional rans analysis. *Journal of Mechanical Science and Technology*, 22:1864–1869, 2008.

[57] G. N. Koini, S. S. Sarakinos, and I. K. Nikolos. A software tool for parametric design of turbomachinery blades. *Advances in Engineering Software*, 40:41–51, 2009.

[58] J. Bergner, D. K. Hennecke, M. Hoeger, and K. Engel. Darmstadt rotor no.2, ii : Design of leaning rotor blades. *International Journal of Rotating Machinery*, 9(6):385–391, 2003.

[59] B. Chen and X. Yuan. Advanced aerodynamic optimization system for turbomachinery. *Transactions of the ASME, Journal of Turbomachinery*, 130:021005–0210017, April 2008.

[60] Fluent Inc. *Fluent 6.3.26 User's Guide*. FluentInc, 2008.

[61] S. Chen, J. Lai, J. Milthorpe, and N. Mudford. A new modified low-reynolds-number $k - \epsilon$ model. AIAA paper 1998-2553. AIAA 29^{th} fluid dynamics conference, Albuquerque, NM, June 15-18 1998.

[62] F. R. Menter. Two-equation eddy-viscosity turbulence models for engineering applications. *AIAA Journal*, 32:1598–1605, August 1994.

[63] F. R. Menter and R. B. Kuntz, M. langtry. Ten years of industrial experience with the SST turbulence model . Turbulence, Heat and Mass Transfer 4: K. Hanjalic, Y. Nadano, and M. Tummers, Begell House, Inc., 2003.

[64] F. R. Menter, R. B. langtry, S. R. Likki, Y. B. Suzen, P. G. Huang, and S. Volker. A correlation-based transition model using local variables Part I: Model formulation. *Transaction of the ASME, Journal of Turbomachinery*, 128:413–422, July 2006.

[65] Y.B. Suzen and P.G. Huang. Predictions of separated and transitional boundary layers under low pressure turbine airfoil conditions using an intermittency transport equation. AIAA 2001-0446,39th AIAA Aerospace Sciences Meeting and Exhibit, Reno, Nevada, January 8-11, 2001.

[66] H. Schlichting. Boundary-layer theory. McGrow-Hill, NewYork, 1979.

[67] R.E. Mayle. The role of laminar-turbulent transition in gas turbine engines. *Transactions of the ASME, Journal of Turbomachinery*, 113(4):509–537, 1991.

[68] R. E. Mayle and A. Schulz. The path to predicting bypass transition. *Transactions of the ASME, Journal of Turbomachinery*, 119(3):405–411, 1985.

[69] E. Malkiel and R. E. Mayle. Transition in a separation bubble. *Transactions of the ASME, Journal of Turbomachinery*, 118(4):752–759, 1996.

[70] R. B. Langtry, F. R. Menter, S. R. Likki, Y. B. Suzen, P. G. Huang, and S. Volker. A correlation-based transition model using local variables Part II: Test cases and industrial applications. *Transaction of the ASME, Journal of Turbomachinery*, 128:4423–434, July 2006.

[71] R.B. Langtry and F.R. Menter. A correlation-based transition model using local variables for unstructured parallelized cfd codes. *AIAA Journal*, 47(12):2894–2905, 2009.

[72] C. K. G. Lam and K. Bremhorst. A modified form of the $k - \epsilon$ model for predicting wall turbulence. *Transactions of the ASME, Journal of Turbomachinery*, 103:456–460, 2006.

[73] R. C. Schmidt and S. V. Patankar. Simulating boundary layer transition with low-reynolds number k_ϵ turbulence models: Part 2-an aaproach to improving the predictions. *Transactions of the ASME, Journal of Turbomachinery*, 113:18–26, 1991.

[74] S. Fan and Lakshminarayana B. Low-reynolds number k_ϵ model for unsteady turbulent boundary-layer flows. *AIAA Journal*, 31(10):1777–1784, 1993.

[75] J. Luo and Lakshminarayana. Numerical simulation of turbine blade boundary layer and heat transfer and assessment of turbulence models. *Transaction of the ASME, Journal of Turbomachinery*, 119:794–801, Oct. 1997.

[76] Reza T. Z., Mahmood S., and Amir K. Prediction of boundary layer transition based on modeling of laminar fluctuations using rans approach. *Chinese Journal of Aeronautics*, 22:113–120, 2009.

[77] S.G. Baek and M.K. Chung. $k-\epsilon$ model for predicting transitional boundary-layer flows under zero-pressure gradient. *AIAA Journal*, 39(9):1699–1705, 2001.

[78] S. Dhawan and R. Narasimha. Some properties of boundary layer during the transition from laminar to turbulent flow motion. *Journal of Fluid Mechanics*, 3:418–436, 1958.

[79] J. Steelant and E. Dick. Modelling of bypass transition with conditioned navier-stokes equations coupled to an intermittency transport equation. *International Journal for Numerical Methods in Fluids*, 23(3):193–220, 1996.

[80] F. R. Menter, T. Esch, and S. Kubacki. Transition modelling based on local variables. in Rodi, W. and Fueyo, N. (Eds.):5^{th} International Sympsium on Turbulence Modelling and Measurements, Mallprca, Spain, pp. 555-564, 2002.

[81] F. R. Menter R. Langtry S. Völker. Transition modelling for general purpose CFD codes. *Flow Turbulence And Combustion*, 77:277303, Aug. 2006.

[82] Y.B. Suzen and P.G. Huang. Modeling of flow transition using an intermittency transport equation. *Journal of Fluids Engineers*, 122:273–284, 2000.

[83] K. Lodefier, B. Merci, C. De Langhe, and E. Dick. Transition modeling with the sst turbulence model and intermittency transport equation. ASME Turbo Expo,Atlanta, Georgia, USA, June 16-19, 2003.

[84] B. J. Abu-Ghannam and R. Shaw. Natural transition of boundary layers- the effects of turbulence, pressure gradient, and flow history. *Journal of Mechanical Engineering Science*, 22(5):213–228, 1980.

[85] K. Lodefier, B. Merci, C. De Langhe, and E. Dick. Intermittency based rans bypass transition modelling. *Progress in Computational Fluid Dynamics*, 6(1/2/3):68–78, 2006.

[86] H. K. Myong and N. Kasagi. A new approach to the improvement of $k-\epsilon$ model for wall bounded shear flows. *JSME International Journal, Series II*, 33(1), 1990.

[87] R. Pecnik, W. Sanz, A. Gehrer, and J. Woisetschl äger. Transition modelling using two different intermittency transport equations. *Flow, Turbulence And Combustion*, 70:299–323, 2003.

[88] K. Maaroofi, M. R. H. Nobari, and E. Shirani. A numerical simulation of external heat transfer around turbine blades. *Journal of Heat and Mass Transfer*, 2(1), 2007.

[89] E. Wiltod. Transition modelling in turbomachinery. *Journal of theoretical and applied Mechanics*, 45(3):539–556, 2007.

[90] Tominaga Y., Mochida A., S. Murakami, and S. Sawaki. Comparison of various revised $k-\epsilon$ models and les applied to flow around a high-rise building model with 1:1:2 shape placed within the surface boundary layer. *Journal of Wind Engineering and Industrial Aerodynamics*, 96:389–411, 2008.

[91] S. Piotrowski W. Elsner W. Drobniak. Transition prediction on turbine blade profile with intermittency transport equation. *Transactions of the ASME, Journal of Turbomachinery*, 132:011020–29, 2010.

[92] D. C. Wilcox. Turbulence modeling for cfd. DCW Industries, Inc., 1993.

[93] V. C. Patel, W. Rodi, and G. Scheuerer. Turbulence model for near-wall and low-reynolds-number flow. *Transactions of the ASME, Journal of Turbomachinery*, 119(5):1308–1319, 1985.

[94] J.D. Denton. Loss mechanisms in turbomachines. *Transactions of the ASME, Journal of Turbomachinery*, 115(4):621–656, 1993.

[95] A.M. Howatson, P.G. Lund, and J.D. Todd. *Engineering Tables and Data*. Chapman and Hall, 1991.

[96] A.H Shapiro. *The dynamics and thermodynamics of compressible fluid flow: Volume 1*. Wiley and Sons, 1953.

[97] J. D. Denton and L. Xu. The effects of lean and sweep on transonic fan performance. Proceedings of ASME Turbo Expo GT2002-30327: Power for Land, Sea and Air, Amsterdam, The Netherlands, Jun 3-6 2002.

[98] R. B. Bird, W. E. Stewart, and Lightfoot E. N. *Transport Phenomena*. John Wiley & Sons, 1960.

[99] U. Okapuu. Some results from tests on a high work axial gas generator turbine. ASME paper 74-GT-81, New York, NY, 1974.

[100] J. P. Gostelow. A new approach to the experimental study of turbomachinery flow phenomena. *Transaction of the ASME, Journal of Engineering for Power*, 99(1):97–105, 1977.

[101] J. H. Wanger, R. P. Dring, and H. D. Joslyn. Inlet boundary layer effects in an axial compressor rotor: part 1- blade-to-blade effects. *Transaction of the ASME, Journal of Engineering for Gas Turbine and Power*, 107(2):374–386, 1985.

[102] J. Hourmouziadis, F. Buckl, and P. Bergmann. The development of the profile boundary layer in a turbine environment. *Transaction of the ASME, Journal of Engineering for Gas Turbines and Power*, 109(2):286–295, 1987.

[103] O. P. Sharma, G. F. Pickett, and R. H. Ni. Assessment of unsteady flows in turbines. *Transaction of the ASME, Journal of Turbomachinery*, 114:79–90, 1992.

[104] S. A. Sjolander M. W. Benner and S. H. Moustapha. Influence of leading-edge geometry on profile losses in turbines at off-design incidence:experimental results and an improved correlation. *Transactions of the ASME, Journal of Turbomachinery*, 119:193–200, April 1997.

[105] M. N. Goodhand and R. J. Miller. Compressor leading edge spikes. Proceedings of ASME Turbo Expo GT2009-59205: Power for Land, Sea and Air, Orlando, Florida, USA, Jun 8-12 2009.

[106] A D S Carter. Blade profiles for axial flow fans, pumps and compressors etc. *Proc Inst Mech Eng*, 175(15):775–806, 1961.

[107] R. Kiock, F. Lehthaus, N. C. Baines, and C. H. Sieverding. The transonic flow through a plane turbine cascade as measured in four european wind tunnels. *Transaction of the ASME, Journal of Engineering for Gas Turbines and Power*, 108:277–284, 1986.

[108] K. G. Giannakoglou1. A design method for turbine blades using genetic algorithms on parallel computers. Computational fluid dynamics 98;Proceedings of the 4th European Computational Fluid Dynamics Conference, Athens, Greece; Uinted Kingdom;, 7-8 Sept. 1998.

[109] F. Sieverding, B. Ribi, M. Casey, and M. Meyer. Design of industrial axial compressor blade sections for optimal range and performance. *Transaction of the ASME, Journal of Turbomachinery*, 126(2):323–331, 2004.

[110] M. Hoffmann, Y. J. Li., and G. Z. Wang. Paths of C-Bezier and C-B-spline curves. *Computer Aided Geometric Design*, 23(5):463–475, Jul. 2006.

[111] R. E. Walraevens and N. A. Cumpsty. Leading edge separation bubbles on turbomachine blades. *Transactions of the ASME, Journal of Turbomachinery*, 117:115–125, January 1995.

[112] S. A. Wheeler and A. P. S. Miller. the effect of leading-edge geometry on wake interactions in comprressors. *Transaction of the ASME, Journal of Turbomachinery*, 131(4):041013–041022, 2009.

[113] L. H. Smith and H. Yeh. Sweep and dihedral effect in axial flow turbomachinery. *Transaction of the ASME, Journal of Basic Engineering*, 85, 1963.

[114] F. A. H. Breugelmans, Y. Carels, and M. Demuth. Influence of dihedral on the secondary flow in a two dimensional compressor cascade. *Transaction of the ASME, Journal of Engineering for Gas Turbines and Power*, 106:578–584, 1984.

[115] D. C. Wisler. Loss reduction in axial-flow compressors through low speed model testing. *Transactions of the ASME, Journal of Engineering for Gas Turbines and Power*, 107:354–363, April 1985.

[116] D. L. Tweedt, T. H. Okiishi, and M. D. Hathaway. Stator end-wall leading-edge sweep and hub shroud influence on compressor performance. *Transaction of the ASME, Journal of Turbomachinery*, 108:224–232, 1986.

[117] S. Harrison. The influence of blade lean on turbine losses. *transaction of the ASME, Journal of Turbomachinery*, 114(1):184–190, Jan. 1992.

[118] M. A. Howard, P. C. Ivey, J. P. Barton, , and K. F. Young. Endwall effects at two tip clearances in a multistage axial flow compressor with controlled diffusion blading. *Transaction of the ASME, Journal of Turbomachinery*, 116(4):635–645, Oct. 1994.

[119] T. Sasaki and F. Breugelmans. Comparison of sweep and dihedral effects on compressor cascade performance. *Transaction of the ASME, Journal of Turbomachinery*, 120(3):454–463, July 1998.

[120] A. R. Wadia, P. N. Szucs, and D. W. Crall. Inner workings of aerodynamic sweep. *Transaction of the ASME, Journal of Turbomachinery*, 120(4):671–682, Oct. 1998.

[121] V Gümmer, U Wenger, and HP Kau. Using sweep and dihedral to control three-dimensional flow in transonic stators of axial compressors. *Transaction of the ASME, Journal of Turbomachinery*, 123(1):40–48, Jan. 2001.

[122] P. Lampart and S. Yershov. Direct constrained computational fluid dynamics based optimization of three-dimensional blading for the exit stage of a large power steam turbine. *Transaction of the ASME, Journal of Engineering for Gas Turbines and Power*, 125(1):385–390, Jan. 2003.

[123] G .S. McNulty, J. J. Decker, B. F. Beacher, and S. A. Khalid. The impact of forward swept rotors on tip clearance flows in subsonic axial compressors. *Transaction of the ASME, Journal of Turbomachinery*, 126:317–327, April 2004.

[124] T. H. Shieh and W. Riess. Investigation of an axial turbine stage with tangentially curved guide vanes - Part 1: Flow structure in the blade channel. *Forschung im Ingenieurwesen- Engineering Research*, 69(3):151–162, July 2005.

[125] D. A. Bagshaw, G. L. Ingram, D. G. Gregory-Smith, M. R. Stokes, and N. W. Harvey. The design of three-dimensional turbine blades combined with profiled endwalls. *Proceedings of the Institution of Mechanical Engineers, Part A: Journal of Power and Energy*, 222:93–102, 2008.

[126] D. A. Bagshaw, G. L. Ingram, D. G. Gregory-Smith, and M. R. Stokes. An experimental study of three-dimensional turbine blades combined with profiled endwalls. *Proceedings of the Institution of Mechanical Engineers, Part A: Journal of Power and Energy*, 222:103–110, 2008.

[127] S. J. Gallimore, J. J. Bolger, N. A. Cumpsty, M. J. Taylor, P. I. Wright, and J. M. M. Place. The use of sweep and dihedral in multistage axial flow compressor blading - Part I: University research and methods development. *Transaction of the ASME, Journal of Turbomachinery*, 124(4):521–532, Oct. 2002.

[128] S . J. Gallimore, J. J. Bolger, N. A. Cumpsty, M. J. Taylor, P. I. Wright, and J. M. M. Place. The use of sweep and dihedral in multistage axial flow compressor blading - Part II: Low and high-speed designs and test verification. *Transaction of the ASME, Journal of Turbomachinery*, 124(4):533–541, Oct. 2002.

[129] G. Thaler, K. Kuhn, and H. Jaberg. Secondary flow in cascades with leaned and swept blades - a literature study. *Forschung im Ingenieurwesen-Engineering Research*, 65(8):236–246, Feb. 2000.

[130] S-J Seo, S-M Choi, and K-Y Kim. Design optimization of a low-speed fan blade with sweep and lean. *Proceedings of the Institution of Mechanical Engineers, Part A: Journal of Power and Energy*, 222:87–92, 2008.

[131] B. Rosic and Xu L. Blade lean and shroud leakage flows in low aspect ratio turbines. Proceedings of ASME Turbo Expo GT2008-50565: Power for Land, Sea and Air, Berlin, Germany, Jun 9-13 2008.

[132] A. J. Cooper and N. Peake. Rotor-stator interaction noise in swirling flow: Stator sweep and lean effects. *AIAA Journal*, 44(5):981–991, May 2006.

[133] G. Pullan and N. W. Harvey. Influence of sweep on axial flow turbine aerodynamics at midspan. *Transaction of the ASME, Journal of Turbomachinery*, 129(3):591–598, Jul. 2007.

[134] Graham Pullan and Neil W. Harvey. The influence of sweep on axial flow turbine aerodynamics in the endwall region. *Transaction of the ASME, Journal of Turbomachinery*, 130(4), Oct. 2008.

[135] G. D'Ippolito, V. Dossena, and A. Mora. The influence of blade lean on straight and annular turbine cascade flow field . Proceedings of the ASME Turbo Expo GT2008-51199: Power for Land, Sea and Air, Berlin, Germany, June 9-13 2008.

[136] E. Benini. Three-dimensional multi-objective design optimization of a transonic compressor rotor. *Journal of Propulsion and Power*, 20(3):559–565, 2004.

[137] E. Benini and R. Biollo. Aerodynamics of swept and leaned transonic compressor-rotors. *Applied Energy*, 84(10):1012–1027, Oct. 2007.

[138] R. Biollo and E. Benini. Aerodynamic behaviour of a novel three-dimensional shaped transonic compressor rotor blade . Proceedings of the ASME Turbo Expo GT2008-51397: Power for Land, Sea and Air, Berlin, Germany, June 9-13 2008.

[139] R. Biollo and E. Benini. Shock/boundary-layer/tip-clearance interaction in a transonic rotor blade. *Journal of Propulsion and Power*, 25(3):668–677, May-June 2009.

[140] J. Vad. Aerodynamic effects of blade sweep and skew in low-speed axial flow rotors at the design flow rate: an overview. *Proceedings of the Institution of Mechanical Engineers; Part A, Journal of Power and Energy*, 222:69–85, Feb. 2008.

[141] I. A. Hamakhan and T. Korakianitis. Aerodynamic performance effects of leading edge geometry in gas turbine blades. *Applied Energy*, 87(5):1591–1601, May 2010.

[142] H. Cosigny and B. E. Richards. Short-duration measurements of heat-transfer rate to a gas turbine rotor blade. *Transaction of the ASME, Journal of Engineering for Power*, 104:542–551, July 1982.

[143] C. Camci and T. Arts. Experimental heat transfer investigation around the film cooled leading edge of a high pressure gas turbine rotor blade. *Transaction of the ASME, Journal of Engineering for Gas Turbines and Power*, 107:1016–1021, 1985.

[144] C. Camci and T. Arts. Short-duration measurements and numerical simulation of heat transfer along the suction side of a film-cooled gas turbine blade. *Transaction of the ASME, Journal of Engineering for Gas Turbines and Power*, 107:991–997, 1985.

[145] T. Arts. Aero-thermal performances of a two-dimensional highly loaded transonic turbine nozzle guide vane: A test case for inviscid and viscous flow computations. *Transactions of the ASME, Journal of Turbomachinery*, 114:818–827, October 1992.

[146] T. Arts, J.-M. Duboue, and G. Rollin. Aero-thermal performance measurements and analysis of a two-dimensional high turning rotor blade. *Transactions of the ASME, Journal of Turbomachinery*, 120:494–499, July 1998.

[147] R. P. Dring, Blair M. F., and Joslyn H. D. An experimental investigation of film cooling on a turbine rotor blade. *Transactions of the ASME, Journal of Turbomachinery*, 102:81–87, January 1980.

[148] R. A. Graziani, M. F. Blair, J. R. Taylor, and R. E. Mayle. An experimental study of endwall and airfoil surface heat transfer in a large scale turbine blade cascade. *Transactions of the ASME, Journal of Engineering for Power*, 102:257–267, April 1980.

[149] D. A. Nealy, M. S. Mihelc, L. D. Hylton, and H. J. Galdden. Measurements of heat transfer distribution over the surfaces of highly loaded turbine noz-

zle guide vanes. *Transactions of the ASME, Journal of Engineering for Gas Turbine and Power*, 106:149–158, January 1984.

[150] M. G. Dunn, W. J. Rae, and J. L. Holt. Measurement and analysis of heat flux data in a turbine satge: Part ii- discusion of results and comparison with predictions. *Transactions of the ASME, Journal of Engineering for gas Turbine and Power*, 106:234–240, January 1984.

[151] D. A. Ashworth, J. E. LaGraff, D. L. Schultz, and K. J. Grindord. Unsteady aerodynamic and heat transfer processes in a transonic turbine stage. *Transactions of the ASME, Journal of Engineering for Gas Turbine and Power*, 107:1022–1030, October 1985.

[152] S. A. Hippensteele, L. M. Russell, and F. J. Torres. Local heat-transfer measurements on a large scale-model turbine blade airfoil using a composite of a heater element and liquid crystals. *Transactions of the ASME, Journal of Engineering for Gas Turbine and Power*, 107:953–960, October 1985.

[153] R. P. Dring, Blair M. F., and Joslyn H. D. The effects of inlet turbulence and rotor stator interactions on the aerodynamics and heat transfer of a large-scale rotating turbine model. NASA CP 179467, May 1986.

[154] M. F. Blair, P. R. Dring, and Joslyn D. H. The effects of turbulence and stator/rotor interactions on turbine heat transfer: Part i, design operating conditions. *Transactions of the ASME, Journal of Turbomachinery*, 111:87–103, January 1989.

[155] M. G. Dunn. Phase and time-reolved measurements of unsteady heat transfer and pressure in a full stage rotating turbine. *Transactions of the ASME, Journal of Turbomachinery*, 112:531–538, July 1990.

[156] N. V. Nirmalan. An experimental study of turbine vane heat transfer with leading edge and downstream film cooling. *Transaction of the ASME, Journal of Turbomachinery*, 112:477–487, July 1990.

[157] R. S. Abhari, G. R. Guenette, A. H. Epstein, and M. B. Giles. Comparison of time-resolved turbine rotor blade heat transfer measurements and numerical calculations. *Transactions of the ASME, Journal of Turbomachinery*, 114:818–827, October 1992.

[158] R. S. Abhari and A. H. Epstein. An experimental study of film cooling in a rotating transonic turbine. *Transactions of the ASME, Journal of Turbomachinery*, 114:147–154, January 1992.

[159] M. G. Dunn, J. Kim, K. C. Civinskas, and R. J. Boyle. Time-averaged heat transfer and pressure measurements and comparison with prediction for a two-stage turbine. *Transactions of the ASME, Journal of Turbomachinery*, 116:14–22, January 1994.

[160] V. K. Garg and R. S. Abhari. Comparison of predicted and experimental Nusselt number for a film-cooled rotating blade. *International Journal of Heat and Fluid flow*, 18(5):452–460, Oct. 1997.

[161] R. S. Bunker, J. C. Bailey, and A. A. Ameri. Heat transfer and flow on the first stage blade tip of a power generation gas turbine part 1: Experimental results. NACA TM 209152, 1999.

[162] M. G. Dunn. Convective heat transfer and aerodynamic in axial flow turbines. *Transactions of the ASME, Journal of Turbomachinery*, 123:637–686, October 2001.

[163] T. Korakianitis, P. Papagiannidis, and N. Vlachopoulos. Unsteady-flow / quasi-steady heat transfer computations on a turbine rotor and comparison with experiments. *Transactions of the ASME, Journal of Turbomachinery*, 124(1):152–159, January 2002.

[164] Camci C. Experimental turbine aero-heat transfer studies in rotating research facilities. International Symposium on Heat Transfer in Gsa Turbine Systems, Antalya, Turkey, 9-14 August 2009.

[165] Manna M. improving the aero-thermal characterestics of turbomachinery cascades. *Transaction of the ASME, Journal of Turbomachinery*, 125(4):445–454, Oct. 2003.

[166] T. Rouvroit L. de Arts and M. Rutherford. Aero-thermal performances of a two-dimensional highly loaded transonic turbine nozzle guide vane cascade. VKI technical Note 174, von Karman Institute for Fluid dynamics, Belgium, 1990.

[167] J. D. Stanitz. Design of two dimensional channels with prescribed velocity distributions along the channel walls. NASA-TN-2594-2595, 1952.

[168] J. P. Gostelow. *Cascade aerodynamics*. Pergamon press, 1984.

[169] W. T. Tiow and M. Zangeneh. Application of a three dimensional viscous transonic inverse method to nasa rotor 67. *IMechE*, 216:243–255, 2002.

[170] D. Buche, G. Guidati, and P. Stoll. Automated design optimization of compressor blades for stationary, large-scale turbomachinery. Proceedings of IGTI03 ASME Turbo Expo 2003: Power for Land, Sea and Air, Atlanta, Georgia, USA, June 13-16 2003.

[171] CH-M Jang, P. Li, and K-Y Kim. Optimization of blade sweep in a transonic axial compressor rotor. *JSME International Journal, Series B*, 48(4):793–801, 2005.

[172] H-D Li, L. He, Y. S. Li, , and R. Wells. Blading aerodynamics design optimization with mechanical and aeromechanical constraints. Proceedings of ASME Turbo Expo, GT2006-90503: Power for Land, Sea and Air, Barcelona, Spain, May 8-11 2006.

[173] D. Bruna and C. Cravero. A cfd suite for design and performance prediction of single and multistage axial flow compressors. Proceedings of the 8th International Symposium on Experimental and Computational Aerodynamics of Internal Flows, Lyon, July 2007.

[174] Y. Elazar and R. P. Shreeve. Viscous flow in a controlled diffusion compressor cascade with increasing incidence. *Transactions of the ASME, Journal of Turbomachinery*, 112:256–265, April 1990.

[175] N. A. Cumpsty. *Compressor aerodynamics*. Longman Scientific and Technical, 1989.

[176] Michael U. *Entwurf und Optimierung der zweimensionalen Gitterströmung axialer Turbomaschinenbeschaufelungen mit Neuronalen Netzen und Genetischen Algorithmen*. Doktor-ingenieurs dissertation (Ph.D.) im fachbereich maschinenbau, Universitaat Gesamthaochschule Kassel, Hannove, Augustr 2000.

[177] Fuglsang R. and H. A. Madesn. A numerical optimization of wind turbine rotors. European Union Wind energy Conference, Goteborg, Sweden, 1996.

[178] I. H. Abbott and A. E. von Doenhoff. *Theory of wing sections*. Dover publications, Inc., 1959.

[179] James L. Tangler. Nrel airfoil familis for hawts. Golden, CO : National Renewable Energy Laboratory, January 1996.

[180] Henne P. A. E. *Applied computational aerodynamics*. American Institute of Aeronautics and Astronautics, Inc., 1989.

[181] G. S Dulikravich. Taerodynamic shape design and optimization:status and trends. *Journal of Aircraft*, 29(6):1020–1026, Nov.-Dec. 1992.

[182] M. S. Selig and M. D. Mughamer. Multipoint inverse airfoil design method based on conformal mapping. *AIAA Journal*, 30(5), 1992.

[183] Kristian S. D. and Fuglsang P. Design of the wind turbine airfoil family risϕ-a-xx. Risϕ natinal Laboratory, Roskilde, Denmark, Dec. 1998.

[184] James L. Tangler. The evolution of rotor and blade design. American Wind Energy Association Wind Power 2000 Palm Springs, California April 30 May 4, 2000.

[185] J. L. Tangler and Somers D. M. Tstatus of the special-purpose airfoil families. WINDPOWER 87, San Fransisco, 1987.

[186] Hansen A. C. and Butterfield C. P. Aerodynamics of horizontal axis wind turbines. Annu. Rev. Fluid Mechanics, 25: 115-49, 1993.

[187] T. Maeda and H. Kawabuchi. Surface pressure measurement on a rotating blade field horizontal axis wind turbine in yawed conditions. *JSME International Journal, Series B*, 48(1), 2005.

[188] B. Kamoun, D. Afungchui, and M. Abid. The inverse design of the wind turbine blade sections by the singularity method. *Renewable energy*, 31:2091–2107, 2006.

[189] T. Maeda and H. Kawabuchi. Effect of wind shear on the characteristics of a rotating blade of a field horizontal axis wind turbine. *Journal of Fluid Science and Technology*, 70:44–61, 2007.

[190] McGhee R. J. and Walker B. S. Experimental results for the epplar 387 airfoil at low Reynolds numbers in the Langley Low Turbine Pressure Tunnel. NASA-TM-4062, 1988.

[191] R. M. Hicks, E. M. Murman, and Garret N. V. An assessment of airfoil design by numerical optimization. NASA-TM-X-3092, July 1974.

[192] Chattopadhyay. A desgin otimization procedure for efficient turbine airfoil design. *An International Journal of Computers and Mathematics with Applications*, 26(4):21–31, Jan. 1993.

[193] T. Milqs and F. Gyulai. Cad technique for blade design of small power wind turbine. The International Conference on Hydraulic Machinery and Equipments, Timisoara, Romania, 1996, October 16-17 2008.

[194] J. C. M. Lin and Pauley L. L. Low-Renolds-number separation on an airfoil. *AIAA Journal*, 34(8):559–565, August 1996.

[195] Baragona M., H. Bijl, and M. V. Tooren. Bubble bursting and laminar separation unsteadiness on a multi-element high lift configuration. *Journal of Flow, Turbulence and Combustion*, 71(1-4):279–296, 2003.

[196] D. Liu and L. Tang. Proper orthogonal decomposition(pod)/response surface methodology(rsm) methodology for low renolds number aerodynamics on micro aerial vehicle(mav). AFRL/WS 06-1817, July 2006.